

*NOAA Climate Test Bed
Center for Ocean-Land-Atmosphere Studies*

CFS as a Prediction System and Research Tool

**Office of Science and Technology
NOAA's National Weather Service**

2008

Table of Content

Foreword

Wayne Higgins, Director, CTB/CPC	iii
James L. Kinter III, Director, COLA/GMU	
1. Verification of daily CFS forecasts 1981-2005	1-8
Huug van den Dool, CTB/CPC	
2. Circulation regimes in the CFS interactive ensemble: Bridging weather and climate predictability promises and challenges	9-14
David Straus, COLA/GMU	
3. MJO monitoring and assessment at the Climate Prediction Center and initial impressions of the CFS as an MJO forecast tool	15-22
Jon Gottschalck, CTB/CPC	
4. Dominant Daily Modes of the South Asian Summer Monsoon Rainfall in the NCEP Climate Forecast System	23-29
Deepthi Achuthavarier, GMU	
5. Summer season forecast experiments with the NCEP Coupled Forecast System (CFS) using different land models and different initial land states	30-41
Ken Mitchell, CTB/EMC	
6. Sensitivity of CFS mean state and ENSO variability to changes in SST bias	42-47
Julia V. Manganello, COLA	
7. Global ocean monitoring: A synthesis of atmospheric and oceanic analysis	48-53
Yan Xue, CTBP/CPC	
8. Assessment of the CFS on the predictability of the North American monsoon	54-61
Lindsey N. Long, CTB/CPC	
9. Surface latent heat flux and relationships with SST in CFS	62-67
Renguang Wu, COLA	
10. Mean, variability and the most predictable patterns in CFS over the tropical Atlantic ocean	68-72
Zeng-Zhen Hu, COLA	
11. Sensitivity of the MJO to SST: A simulation and predictability study of the MJO using the CFS and GFS	73-78
Kathy Pegion, COLA	
12. Evaluation of the stratosphere in the operational CFS and CFS-Next	79-83
Craig S. Long, CTB/CPC	

13. Multi-model ENSO prediction using CFS and CCSM3 Ben Kirtman, COLA/UM(RSMAS)	84-91
14. On the importance of horizontal resolution and initial conditions to forecasting tropical intraseasonal oscillations: the maritime continent prediction barrier Augustin Vintzileos, CTB/EMC	92-96
15. Estimation of the limit of predictability in the stratosphere versus troposphere using CFS Cristiana Stan, COLA	97-101

FOREWORD

In August 2004 the National Centers for Environmental Prediction (NCEP) implemented a new seasonal prediction system, called the Climate Forecast System (CFS) that marked a turning point in several ways. First, it systematized the operational, real-time prediction of seasonal climate using coupled general circulation models (GCMs) of the global atmosphere, world oceans, and land surface. The system was based on the operational numerical weather prediction model then in use at NCEP and the NOAA ocean GCM developed by the Geophysical Fluid Dynamics Laboratory (called the Modular Ocean Model or MOM). Importantly, it was also based on a set of retrospective forecasts that were made with the CFS to test and calibrate the prediction system. Second, the data from the retrospective forecasts were made freely and publicly available to the research community. This large data set became an invaluable tool for climate prediction research. The CFS model and the retrospective forecast data set became resources made available by NCEP through the Climate Test Bed (CTB). Third, it coincided with a new strategy put in place by the Center for Ocean-Land-Atmosphere Studies to de-emphasize the ongoing development of its own climate model in favor of the adoption of National models in use for climate prediction and climate change projection. The CFS was therefore a natural choice to be used for prediction and predictability research by COLA scientists.

As a result, a large group of scientists, both at NCEP and at COLA, began analyzing and experimenting with the CFS as a prediction system and research tool. In the course of discussions in early 2007 between COLA and NCEP, it became clear that an exchange of research results and findings would be highly beneficial to both groups and perfectly consistent with the goals of the CTB, so a joint CTB-COLA seminar series was established in Fall 2007. During 2007-2008 period, monthly seminars were held at both NCEP (by COLA scientists) and COLA (by NCEP scientists). The seminar series generated a great deal of interest at both centers and resulted in a rich and valuable exchange of information and insights about seasonal prediction in general and the CFS in particular. The outcomes have included a number of technical reports and peer-reviewed publications as well as concrete advice to the model developers and forecasters that has informed the next generation of the CFS. Recent climate prediction advances at NCEP, including implementation of the CFS, and CTB activities (such as the development of consolidation tools with CFS) have contributed to significant and sustained increases in the skill of CPC official seasonal outlooks. Activities such as this seminar series will help to ensure continued improvements in the outlooks.

We would like to thank the many individuals who made this seminar series possible through their voluntary contributions, notably Mel Gelman and Muthuvel Chelliah at NCEP and Stacey Whitlock at COLA, as well as the scientists who prepared and delivered the seminars that are summarized in this volume. We believe that this very successful inaugural joint seminar series will lead to an annual program of scientific and technical presentations among the operational and research centers of the Washington metro area. During FY09 we anticipate that the series will expand to include several CTB science priorities, including CFS improvements, evaluation of multi-model ensembles, and development of climate forecast products. Consequently, the series will build on the CTB concept to accelerate the transition of research results into operational climate services by NOAA as well as provide a robust support base for the ongoing climate research being conducted by COLA and other groups.

Wayne Higgins, Director
Climate Prediction Center
National Centers for Environmental Prediction
NOAA's National Weather Service

James L. Kinter III, Director
Center for Ocean-Land-Atmosphere Studies

Verification of daily CFS forecasts 1981-2005

Huug van den Dool¹ and Suranjana Saha²

¹*Climate Prediction Center, NOAA/National Weather Service*

²*Environmental Modeling Center, NOAA/National Weather Service*

1. Introduction

The NCEP Climate Forecast System (CFS), implemented in August 2004 and consisting of coupled global atmosphere-ocean-land components, was developed and tested with the express purpose of support for seasonal prediction for the United States (Saha *et al.* 2006), *i.e.* 90 day means. (see <http://cfs.ncep.noaa.gov/> for data download, references and documentation). Nevertheless, the model integrates through unfiltered instantaneous states, and this is the topic of study here. For each initial month during 1981-2003 (now through 2005) a 15 member ensemble had been run out to 9 months. The notion ‘ensemble’ may apply to longer lead seasonal prediction, but here we study NWP type skill and will not take ensemble averages and the like. Here we study daily data exclusively.

There is obviously a wealth of information about both forecast skill and diagnostic topics in these model daily data sets. One cannot dream to have this much data about reality. (When strung out, this data amounts to 3500 years of model integration.) Here we focus on just a number of forecast aspects. The first is skill of the CFS as if it were an NWP model for the atmosphere only, say at day 5. Data sets of retrospective forecasts of this sample size have rarely been available to study NWP skill. A second forecast aspect is the decay of skill as it tends to approach zero after weeks or months. The skill in seasonal prediction does not stand on its own, it is an amplified version (with improved signal to noise ratio) of skill that has to be there, no matter how minuscule, in the daily forecasts.

With large data sets we are also in a position to attempt to document the annual variation in skill and to explain the annual cycle in skill in terms of the standard deviation and degree of freedom. Another piece of the puzzle is correction of the model’s systematic error. The construction of the model’s climatology as a function of the lead and either the initial or the target time is very important in this context.

Obviously, the skill of NWP has been a major concern for decades at operational weather prediction centers all over the world, so these centers tend to keep track in near real time of, most famously, the extra-tropical day 5 anomaly correlation of 500 mb height prediction. This is based, naturally, on a fairly small sample as models do change frequently, and retroactive forecasts are not commonplace, not even today. Here we study a massive data set with a “constant” model over 25 years, allowing us to address in some detail questions that would normally be impossible to address because of small or inhomogeneous samples. The use of the CFS for daily operational forecasts, such as 6-10 day or week 2, has not been considered until recently because of the late cut-off time in ocean analysis, but this has changed as per January 2008. Therefore some of the questions we address here have a practical aspect immediately, and could become important for experimental week 3 and week 4 and MJO forecasts at any time of our choosing in the future.

The atmospheric component of the CFS may be described as a T62L64 NCEP (GFS) model of vintage 2003. There actually are two earlier versions of a T62L28 NCEP global spectral model which are accompanied by very large forecast or hindcast data sets. First, the global NCEP/NCAR Reanalysis (Kalnay *et al.* 1996) and its continuation CDAS (Kistler *et al.* 2001), which we label hereafter R1, launched forecasts every 5 days; later these were enhanced in frequency to daily (from 1996-present). R1 forecasts are maintained for the purpose of comparing the operational NWP model of the day (currently at T384 horizontal resolution) to a ‘frozen’ model system such as R1. Secondly, Hamill *et al.* (2006) have described so-called reforecasts with a 1998 version of nearly the same NCEP R1 model (T62L28) - they made an ensemble of reforecasts for every day from 1981 to the present - their main purpose has been to demonstrate large improvements in the probabilistic forecasts due to

calibration of probabilities and systematic error correction. Neither R1, nor the Hamill *et al.* forecasts go beyond 2 weeks, so the CFS is unique in going out to 270 days. And the CFS is the only of the three with ocean interaction. The nominal year 2003 assigned to the CFS may be flawed in that the atmospheric and land surface initial conditions are from the considerably older (late nineties) R2 global Reanalysis (Kanamitsu *et al.* 2002). At that time radiances were not assimilated and for that reason the Southern Hemisphere features rather poor predictions on account of poor initial states.

2. Definitions

2a. Anomaly Correlation

The anomaly correlation (AC) used here is given by

$$AC = \frac{\sum \sum f'(s, t) o'(s, t)}{\{ \sum \sum f'(s, t)^2 \sum \sum o'(s, t)^2 \}^{1/2}} \quad (1)$$

where $f'(s, t) = f(s, t) - climo_{mdl}(s)$ (2)

is the forecast anomaly as a function of space and verifying time at a certain lead τ (not shown)

and $o'(s, t) = f(s, t) - climo_{obs}(s)$ (3)

is the matching observed anomaly. The construction of the climatologies is described in section 2b. The double summation in (1) is over space s (say over a NH grid, with weighting (not shown)) and time t (say during 25 years 1981-2005). Besides the years there is another ‘time’ involved in t , namely the day of the year t_{day} (not shown in (1)). For instance we could evaluate (1) over all forecasts initialized from the 9th through the 13th of the month, or over all forecasts that verify at a 5 day lead in a certain calendar month.

In the procedure expressed by Eq (1) - (3) we implicitly perform a systematic error correction. This is mainly related to taking a model climatology out of the forecasts. Not applying a systematic error correction (see Section 3d) means that the observed climo is subtracted in (2).

2b. Climatologies

Given forecasts originating from 5 initial conditions centered around the 11th, the 21st of the previous month and the 1st of the current month (this is the CFS lay-out of 15 ensemble members per month, see Saha *et al.* (2006)) we can create multi-year means of $f(s, t, \tau)$ for any lead $0 < \tau < 270$ and any verifying time t . These climatologies (even when based on all years) are noisy from day to day, and we use an harmonic filter to arrive at smooth climatologies. These filters have been popular at CPC for some time (Epstein 1991, Schemm *et al.* 1998). Note that data from the entire year is thus used in the estimate of the climatology at time t . The harmonic filter has another purpose here because we have a time series of daily climatology with holes (of size 5 days), so the harmonic representation is also used to interpolate the climatologies (which can be used in real time for predictions now launched 4 times a day, all days of the year).

Johansson *et al.* (2007) prepared CFS climatologies for all 30 daily variables that have been made available. For details, see his TechNote.

3. Selected Results

3a. Time Series of Annual Scores in Mid-latitudes

Fig.1 shows the annual mean scores of 5 day NH Z_{500} forecasts by the CFS system in the extra-tropics. Each annual dot represents 180

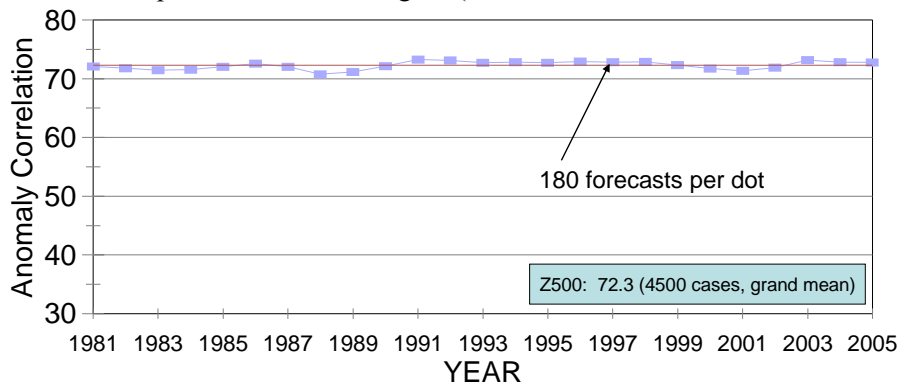


Figure 1 The day 5 anomaly correlation of 500mb height for the CFS hindcasts in the extra-tropical NH, annually aggregated for each year from 1981 through 2005. Each dot is based on 180 forecasts. The thin red line is the overall mean of 0.723.

forecasts, 15 per month. The overall mean correlation is 0.723 (4500 cases). What is most remarkable is how constant the scores are during 1981-2005, no great trend and little year to year change. Even though the flows to be predicted vary from year to year (and lore has it that some years are more difficult to predict than others), the scores come out to be very constant in the NH as annual means and vary only in the 0.71-0.74 range. The intent was to design a “constant” system, so the originators should be congratulated in achieving such constancy in their hindcasts.

A comparison should be made with Fig.2, which has been maintained in real time over 1984-present, especially with the purple line for R1/CDAS1 which is a frozen model. Indeed the scores of the forecasts off R1 initial conditions (12 mo running mean) are similar to the CFS scores off R2, and quite constant as well. Fig.2 also shows the flagship operational models (NCEP and ECMWF) pulling away slowly but surely from the R1 skill level as time progresses (in part because these centers increase resolution every few years).

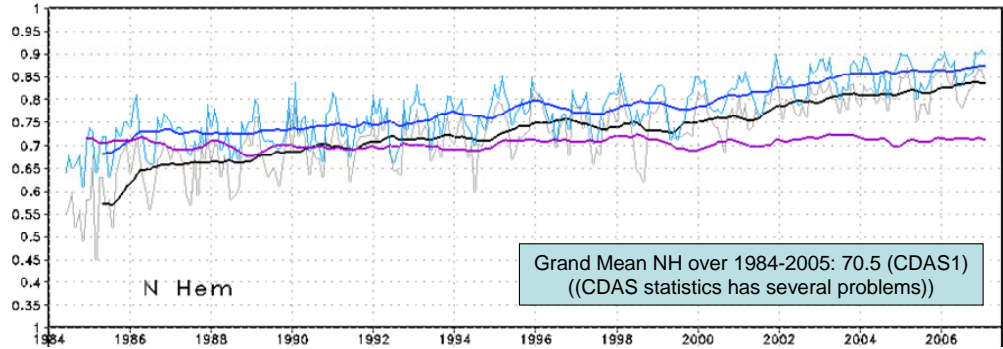


Figure 2 The same as Fig.1 but now based on real time monthly mean forecasts during 1984-present. The purple line is for the constant R1 system (hindcasts until 1996, forecasts thereafter), while the black and blue lines are for the operational model forecasts at NCEP and ECMWF, respectively. Shown are 12 mo running means. Provided by Peter Caplan/Fanglin Yang.

Fig.3 is the same as Fig.1, but now for the SH, and this tells a very different story. We first note that the grand mean score in the SH is 0.629, nearly 10 % points behind the NH. This large inter-hemispheric skill difference is typical for the pre-2000 era (of which R2 analyses are representative), when radiances were not assimilated and the SH initial states were wanting. (Off late 5 day scores in the NH and SH are much more similar for the operational models). Secondly we note a large volatility in the SH scores which vary considerably from year to year, and much more so than in the NH. There is no immediate explanation for this. Thirdly, from the SH alone we would conclude that the system is not constant at all. While the model (code) and computer are indeed constant for these 25 years worth of hindcasts, the quality of the initial conditions is not (i.e. not necessarily). Over 1981-2005 more satellite data has progressively become available (and assimilated old-fashionedly as per retrievals in R2), and this appears to boost scores in the SH (Fig.3), but not in the NH (Fig.1).

3b. Time Series of Annual Scores in the Tropics

We also verify 5-day streamfunction (ψ) and velocity potential (χ) predictions at 200mb to report on skill in the tropics. Fig.4 shows the result for ψ_{200} . The grand mean tropical scores for ψ_{200} are 0.630, i.e. at the same level as SH Z_{500} . Scores are volatile, i.e. vary considerably from year to year, in spite of having 180 forecasts per year. No upward trend is visible at all, which is of note if

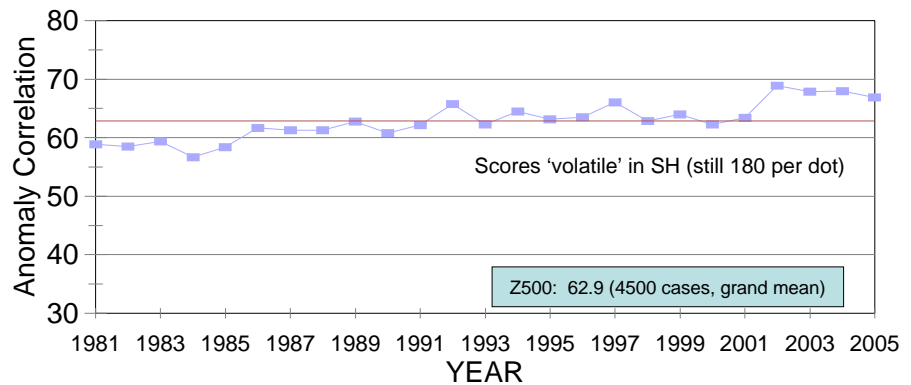


Figure 3 The day 5 anomaly correlation of 500mb height for the CFS hindcasts in the extra-tropical SH, annually aggregated for each year from 1981 through 2005. Each dot is based on 180 forecasts. The thin red line is the overall mean of 0.629.

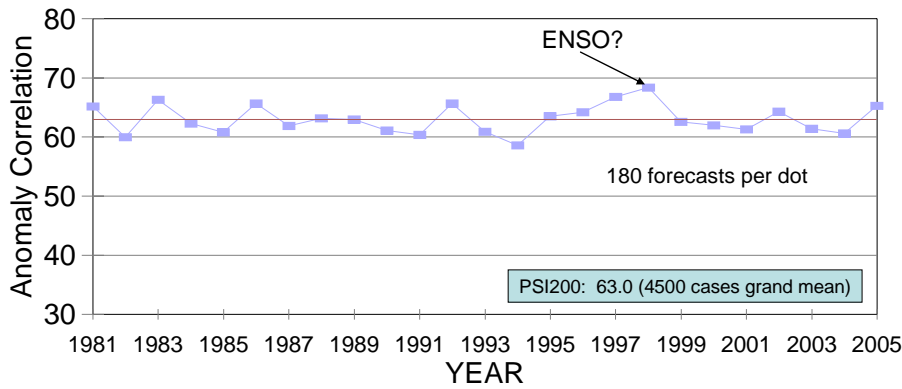


Figure 4 The same as Fig.1, but now 200mb streamfunction in the tropics. Grand mean score in 0.630.

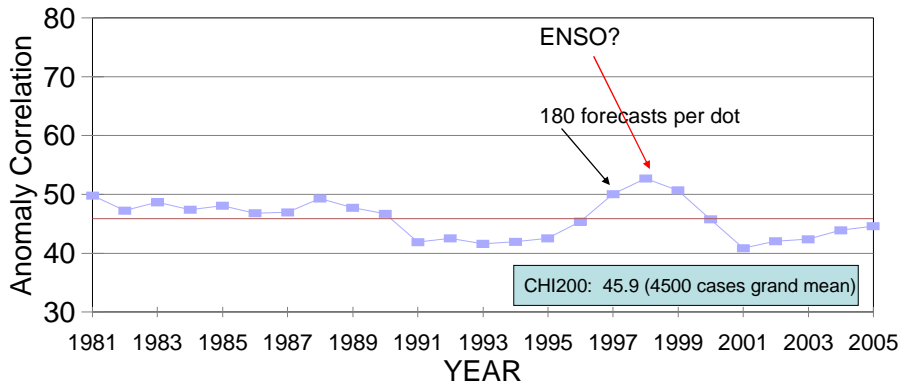


Figure 5 The same as Fig.1, but now 200mb velocity potential in the tropics. Grand mean score is 0.459.

our explanation for the upward trend in scores in the SH (more satellite data) was correct. Fig.5 is the same as Fig.4 but now for χ_{200} . The grand mean anomaly correlation sinks to a discouraging 0.459 at day 5. This is not terribly good news if MJO prediction by the CFS is a priority. Not only is there no upward trend in χ_{200} scores, there actually would have been a downward trend if it had not been for the 1997-1999 strong warm and cold events that elevated the scores for a 3 year period. The strong outflow above the quasi-stationary ENSO related convection is a juicy target (large anomalies always are!) for prediction. The somewhat elevated ψ_{200} scores in 1997-1998 may well be caused by better divergence forecasts, but one wonders why the strong 1982/83 ENSO event did not elevate scores in either χ_{200} or ψ_{200} .

On balance, the issue of the constancy of scores of the CFS hindcasts is quite complicated for the planet as a whole, and we fail to completely understand the results in Figures 1, 2, 4 and 5. Scores appear very constant in the NH, go up decidedly in the SH, and are NOT at all going up in the tropics. Non-constancy would obviously be a practical problem when scores accumulated over 1981-2005 are assigned as a-priori scores for the next real time forecasts.

Table 1 summarizes the annual mean scores for all variables/domains discussed, and also provides a quantitative comparison to R1, at least for Z_{500} . The CFS (off R2) system is just a little better than R1, but not much, and the comparison is not completely clean (see legend of Table 1).

	Z_{500} NH	Z_{500} SH	ψ_{200}	χ_{200}
CFS (R2)	0.723	0.629	0.630	0.459
R1	0.705	0.623	NA	NA

3c. Climatology of scores

With 25 years of data (from an as constant a system as possible) we may attempt to describe the climatological annual cycles in skill. Fig.6 upper left shows how the AC for Z_{500} varies sinusoidally in the NH from a maximum of 0.764 in February to a minimum of 0.677 in July. Here each dot represents 375 forecasts (25 years times 15). This variation agrees with synoptic experience of winter

Table 1 The annual mean day 5 anomaly correlation of CFS predictions for 1981-2005, for 500mb height (Z_{500}) forecasts over the domain 20 -pole (SH, NH), and 200mb streamfunction/velocity potential on the domain 20S-20N (TR). The second row shows scores of forecasts made by the Reanalysis model (R1) from R1 produced initial states. The period is 1984-2005 for R1/CDAS related forecasts, while the CFS covers 1981-2005. Climatologies used differ (between CFS and R1), the number of forecasts per year differs and CFS is bias corrected while R1 is not. NA=Not Available.

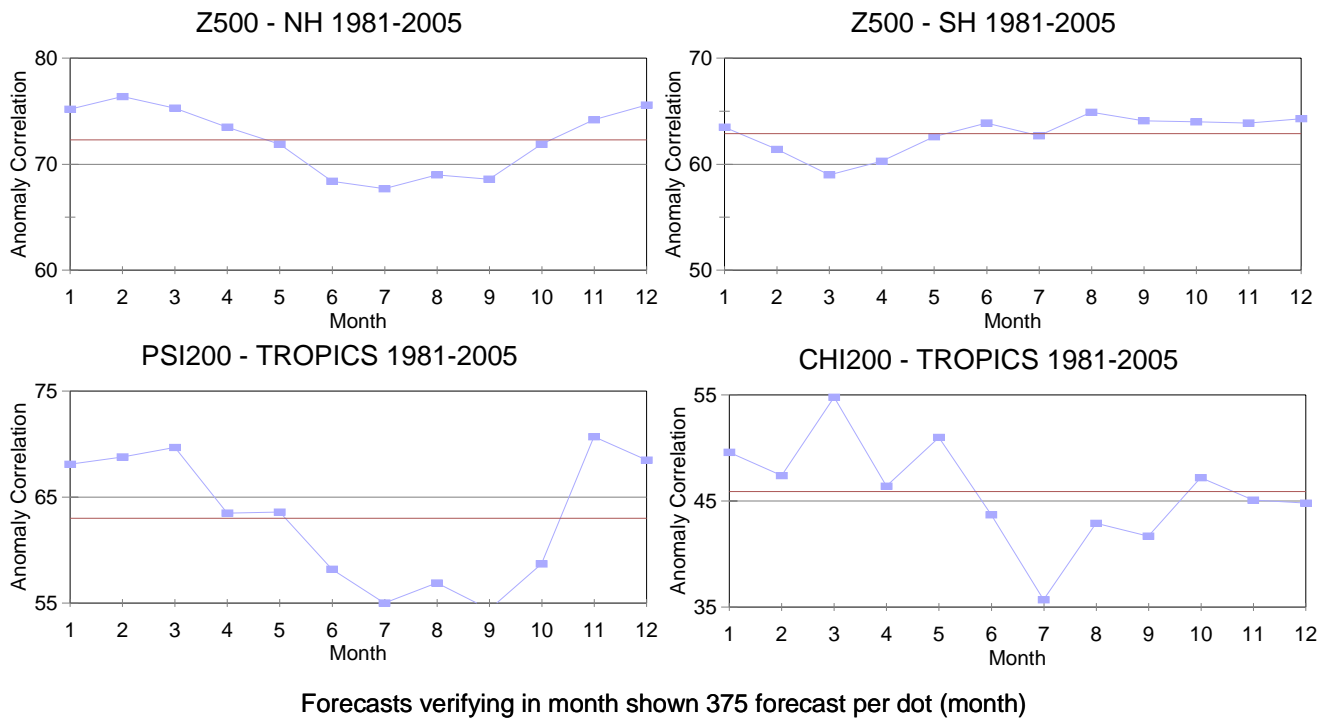


Figure 6 The climatology (=25 year mean by month) of day 5 anomaly correlation for the CFS hindcasts as a function of the month of the year for Z_{500} NH (upper left), Z_{500} SH (upper right), ψ_{200} TR (lower left) and χ_{200} TR (lower right). Each dot is based on 375 forecasts. The vertical scale covers 20 points in all 4 graphs.

being easier to forecast than summer, but puts numbers on it. We plotted 25 curves (not shown), one for each year, and Fig.6 upper left is representative for most of those 25 years. In contrast the annual variation in the SH is unclear and not very well defined with 25 years of data at hand. Fig.6 (upper right) suggests the lowest scores in the SH occur around March, but a maximum is harder to place. Moreover scores appear volatile, with an odd dip in July. The climatology of skill for the ψ_{200} and χ_{200} predictions does look somewhat like the NH's Z_{500} , i.e. higher scores in northern winter. Here again we note volatile scores in the Tropics, with odd ups and downs from month to month, in spite of having an enormous data set.

3d. Impact of bias correction

One of the stated reasons for doing all these expensive hindcasts is to perform a bias correction (or fancier calibration). Figures 1, 2, 4, 5 and 6 were all based on bias corrected forecasts, a correction achieved by subtracting out the harmonically smoothed model climatology from the forecasts. How much did we gain??? Fig.7 shows a 'die-off' curve for days 1-15 for NH Z_{500} scores in July, 375 forecasts in all. Note first of all how smooth these curves are - the reader will have rarely seen a die-off curve this smooth, since it is based on so many forecasts. As usual, the die off curve for Z_{500} is concave at first, but turns convex after passing an inflection point,

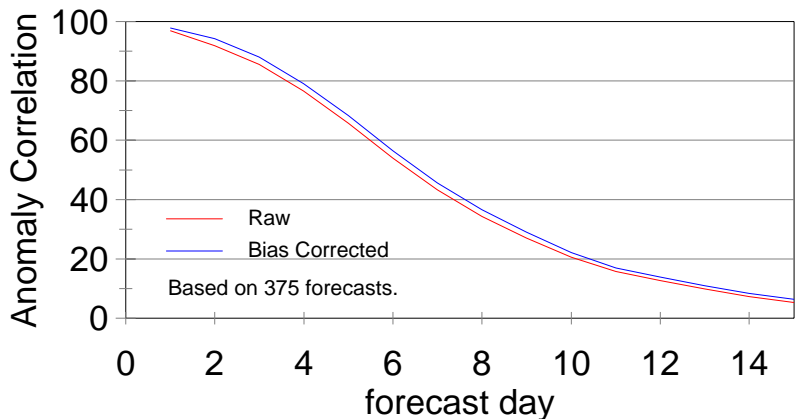


Figure 7 Die-off curve for the anomaly correlation in July for CFS Z_{500} NH, day 1-15. The red line is for 'raw' forecasts, the blue line for bias corrected forecasts. Each point is based on 375 forecasts.

situated here at a lead of about 7 days. The blue relative to the red curve shows the gain due to bias correction. There is an indisputable but rather small improvement. At day 1 the gain is small, and at long lead, when skill is small, the gain is minimal again, with a broad maximum in improvement due to bias correction between day 3 and day 8. July is typical. In most months the day 5 scores in either NH or SH do not improve more than 1 or 2 points as a result of bias correction, i.e. not all that much. It is so little because the systematic error in Z_{500} model forecasts has become small, much smaller than it once was.

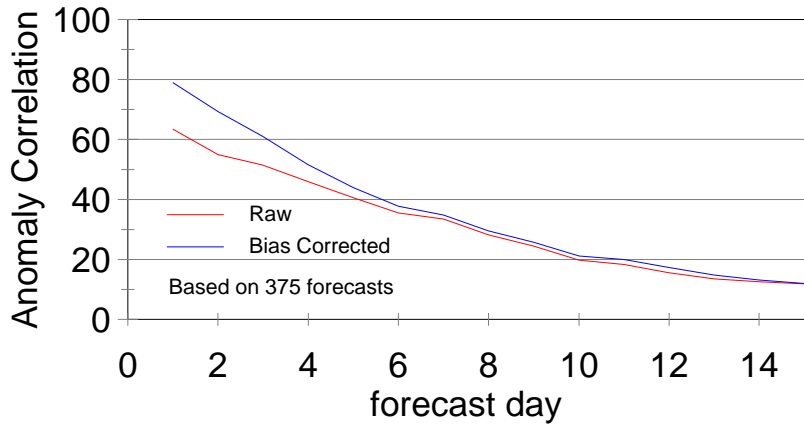


Figure 8 The same as Fig.7 but now for χ_{200} TR. Note the much lower scores, and the large gain (in anomaly correlation) at day 1 due to bias correction.

The story is very different for χ_{200} , a much more difficult variable to forecast. Fig.8 is the same as Fig.7 but now for χ_{200} in the tropics. The result is shocking. Without bias correction the day-one score is only a very modest 0.62. The effect of the bias correction is the largest at day-1, an implausible result. When day-1 forecasts are judged to be that mediocre, the initial states are likely to be poor as well. Yet we use the collection of these initial states to execute the verification and to estimate the systematic error. Regardless of bias correction, the looks of the χ_{200} die-off curve are bad in that the shape of the curve is convex right from the start. This can be taken as a sign that systematic model problems dominate the error growth, even in the random error growth (Savijärvi 1995). More than anything Fig.8 shows big and fundamental problems in the prediction of the divergent flow. The story for ψ_{200} is better in that the magnitude of the systematic error is smaller, and the day 1 scores more attractive, but the die-off curve for ψ_{200} (not shown) still looks bad in the tropics. Indications are the next CFS (CFSRR) will show improvement on two counts, both by a far improved analysis system, and by a model consistent analysis. The present CFS uses 'old' R2 initial conditions for initializing forecasts made by a more recent atmospheric model.

We have commented very little on the role of the

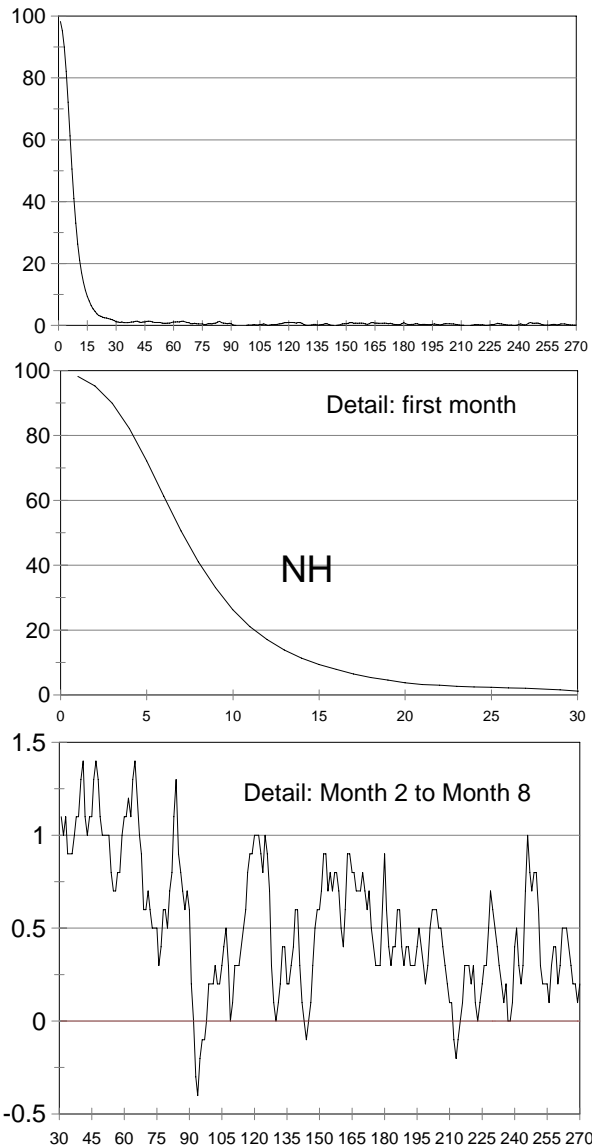


Figure 9 Die off curve for the anomaly correlation for Z_{500} forecasts by the CFS out to 270 days. Each dot is based on 4500 forecasts and all seasons aggregated. The two figures on the bottom are blow ups of the details. The one on the left for days 1-30, the one on the right (with much expanded Y scale) for months 2-8.

ocean-coupling on short-range NWP scores obtained here. On balance the impact appears small in the mid-latitude at, say, day 5. But it can not be ruled out that some of the serious problems in the tropics noted in the above are exacerbated or caused by the ocean coupling, and the initial shock thereof. Nevertheless, this is the way to go, eventually.

3e. Out to 270 days

Figure 9 shows the day-by-day die-off curve for the NH Z_{500} all the way out to 270 days. Blow ups of the first 30 days and the last 8 months (expanded Y-scale) are provided. Skill decreases smoothly at first with an integral time scale of around 8 days, then drops to a near zero level of 0.005 after 1 month, but stays positive in the mean at this very low level all the way to the end. While such skill is meaningless for the daily prediction (at day 215 say), the systematic improvement of the signal to noise ratio (by applying time means, ensemble means etc) is only possible if we accept that the correlation for the daily unfiltered data is not quite zero. Indeed the trivial skill seen in Fig.9 for months 2 through 9 can be worked upward to a better sounding 0.6 correlation or so in the PNA area for 90 day mean ensemble means in NH winter.

3f. Other results

We refer to a more extensive ppt for additional results about:

(see http://www.nws.noaa.gov/ost/climate/STIP/CTB-COLA/Huug_052808.ppt)

- Spatial distribution of the anomaly correlation at day 5 (NH, SH, summer/winter)
- The anomaly correlation as a function of EOF mode m , $1 \leq m \leq 100$.
- Some special results for week 3 and week 4
- Fits to error growth equations, such as Savijärvi's (1995) Eq (5)
- Correction of systematic errors in standard deviation (i.e. not just the mean)
- The realism of model generated flow at days 1-270 as per the strength and spatial size of the anomalies generated

4. Conclusion

We have studied forecast aspects of an unfiltered version of the 3500 years of model data generated in conjunction with the CFS hindcasts. No time means or ensemble means are taken. The short-range weather prediction capability of the CFS appears to be very close in forecast skill to that of the global spectral model (atmosphere only) used at the time of the first NCAR/NCEP Reanalysis (R1), at least in mid-latitudes. The hindcast data set created for the CFS (with R2 initial states) permits us to study in some detail scores of forecasts various variables in the tropics, the SH and the NH, in some cases in detail not seen before. The impact of bias correction is small for Z_{500} , but huge for upper level tropical divergent flow.

5. The near future

As of writing this piece the CFSRR, successor of the CFS, is already underway. Two main advances should be mentioned. First an atmospheric model benefitting from 10plus years of work on model improvements is used for analysis (@T382L64) and prediction (@T126L64). Secondly, the atmospheric initial states are consistent with the prediction model!. Other advances include the production of a guess field by the interactive ocean-atmosphere system, a novelty of unknown impact. The day 5 scores as shown for example in Table 1 for CFS appear to improve by 10 points in the NH, and even more in the SH.

Acknowledgements. We thank Cathy Thiaw for making nearly 40 reruns upon discovering errors in the CFS archives. Pete Caplan, Fanglin Yang and Bob Kistler provided data and information on the R1 predictions.

References

Epstein, E. S., 1991: Determining the optimum number of harmonics to represent normals based on multiyear data. *J. Climate*, **4**, 1047–1051.

- Hamill, T. M., J. S. Whitaker, and S. L. Mullen, 2006: Reforecasts, an important new data set for improving weather predictions. *Bull. Amer. Meteor. Soc.*, **87**, 33-46.
- Johansson, Å., Catherine Thiaw and Suranjana Saha, 2007: CFS retrospective forecast daily climatology in the EMC/NCEP CFS public server. See <http://cfs.ncep.noaa.gov/cfs.daily.climatology.doc>
- Kalnay, E., M. Kanamitsu, R. Kistler, W. Collins, D. Deaven, L. Gandin, M. Iredell, S. Saha, G. White, J. Woolen, Y. Zhu, M. Chelliah, W. Ebisuzaki, W. Higgins, J. Janowiak, K. C. Mo, C. Ropelewski, J. Wang, A. Leetma, R. Reynolds, R. Jenne, and D. Joseph, 1996: The NCEP/NCAR 40-year reanalysis project. *Bull. Amer. Met. Soc.*, **77**, 437-471.
- Kanamitsu, M., W. Ebisuzaki, J. Woollen, S-K Yang, J.J. Hnilo, M. Fiorino, and G. L. Potter, 2002: NCEP-DOE AMIP-II Reanalysis (R-2). *Bull. Amer. Met. Soc.*, **83**, 1631-1643.
- Kistler, R., E. Kalnay, W. Collins, S. Saha, G. White, J. Woollen, M. Chelliah, W. Ebisuzaki, M. Kanamitsu, V. Kousky, H. van den Dool, R. Jenne, M. Fiorino, 2001: The NCEP-NCAR 50-year reanalysis: Monthly means CD-ROM and documentation. *Bull. Amer. Met. Soc.*, **82** (2), 247-267.
- Saha, S., S. Nadiga, C. Thiaw, J. Wang, W. Wang, Q. Zhang, H. M. van den Dool, H.-L. Pan, S. Moorthi, D. Behringer, D. Stokes, M. Peña, S. Lord, G. White, W. Ebisuzaki, P. Peng, P. Xie, 2006: The NCEP climate forecast system. *J. of Climate*, **19**, 3483-3517.
- Savijärvi, H., 1995. Error growth in a large numerical forecast system. *Mon. Wea. Rev.*, **123**, 212-221.
- Schemm, J-K. E., H. M. van den Dool, J. Huang, and S. Saha, 1998: Construction of daily climatology based on the 17-year NCEP-NCAR reanalysis. *Proceedings of the First WCRP International Conference on Reanalyses*. Silver Spring, Maryland, USA. 290-293.

Circulation Regimes in the CFS Interactive Ensemble: Bridging Weather and Climate Predictability Promises and Challenges

David M. Straus^{1,2,*}

¹ *George Mason University, Fairfax VA*

² *Center for Ocean-Land-Atmosphere Studies, Calverton MD*

1. Introduction

The concept of circulation regimes represents one method of organizing the large and varied set of atmospheric circulation patterns that have been identified on time scales longer than a few days. We give a brief overview of the rich history of regimes from a dynamical point of view, and touch upon the statistical methodologies behind the identification of regimes in real and simulated data. The long history of El-Nino related changes to Pacific patterns / regimes will be summarized with reference to recent work on very large ensembles of atmospheric simulations.

Recent, preliminary results of regime structure in boreal winter for the Pacific – North American region from interactive-ensemble forecasts using the CFS are presented. Five forecasts have been carried out for early January atmosphere / ocean initial conditions for each of 11 calendar years. Each forecast uses the interactive ensemble, in which six atmospheres are coupled to one ocean. We also show some preliminary results for the probability distribution (pdf) of ideal model errors (i.e. ensemble spread) from the forecast.

Regime analysis was originally motivated by two different schools of thought. One was based on the recognition that extended periods of (possibly extreme) weather occur intermittently, and that such occurrences are related to the persistence of the large-scale flow. This led to the classification of regional weather patterns into a discrete number of types (the *grosswetterlagen*), as in Baur et al (1944), and Egger (1981) and references therein. Note that these weather patterns can be numerous. To quote Egger: “The *grosswetterlagen* defined by Baur ...provide a valuable classification of the extended (duration longer than three days) weather types observed in Central Europe...28 large-scale weather types derived from about 70 years of observations.” Such weather regimes stimulated the second school of thought, which sought to identify non-linear interactions in the large-scale flow via highly-truncated solutions of the dynamical equations (Charney and DeVore, 1979; Charney and Straus, 1981). This approach sought to identify highly non-Gaussian (in fact multi-modal) probability distributions with weather regimes. That such multi-modal pdfs are possible in the context of atmospheric dynamics has been confirmed by recent work of Christiansen (2005), the latest of many papers over the years describing a simple index of large-scale wave activity in mid-latitudes from analyses (see Christiansen for details). This paper shows clearly that when the daily data are filtered to remove those periods of rapidly changing wave activity index, the resulting pdf is decidedly non-Gaussian and is in fact bi-modal.

Note that while the feedback of smaller, synoptic scales on the large-scale flow was neglected in the early highly truncated models, it of course is included in the observational results of Christiansen. The mutual feedback between the quasi-stationary large scale waves and the baroclinic, synoptic disturbances was developed theoretically by Reinhold and Pierrehumbert (1982) and Vautard and Legras (1988). This feedback can be parameterized purely dynamically (as in Reinold and Pierrehumbert), semi-empirically (as in Vautard and Legras) and completely statistically (as in Sura et al, 2005).

Attempts at diagnosing circulation regimes from reanalyses have been hampered by the short data record. Corti et al. (1999) examined Nov.-Apr. monthly means of 500 hPa height from the Northern Hemisphere (north of 20N) in EOF space. Retaining only 2 leading modes, they showed smoothed estimates of the two-dimensional pdf which indicate multiple maxima. However, Stephenson et al (2004) use statistical tests on the same monthly mean data set, and find that one cannot rigorously reject the null hypothesis of a multi-normal pdf in the two-dimensional phase space. The difficulty of rejecting a multi-normal null hypothesis was also emphasized by

*Correspondence to: David M. Straus, Center for Ocean-Land-Atmosphere Studies, 4041 Powder Mill Road, Suite 302, Calverton, MD 20705; E-mail: straus@cola.iges.org

Toth (1991), who used daily full-field 700 hPa height data from the Northern Hemisphere. However, *this oft-quoted result holds only for the phase-averaged pdf*, in which only the distance to the origin is considered. When the full pdf is taken into account, Toth (1993) did find significant departures from multi-normality if quasi-stationary data were used. (Quasi-stationarity means that periods when the daily rms change in the height field is largest are not used in the analysis. This filtering thus emphasizes episodes of persistent flow.)

2. Clusters in the NCEP Reanalysis and Methods of Regime Analysis

Straus et al (2007) are able to identify regimes in the wintertime 200 hPa height fields for 54 winters from the NCEP reanalysis (1948-49 through 2002-03). Daily data are filtered to retain only variability with periods of 10-90 days (but including the seasonal mean anomaly), and quasi-stationary filtering is applied. The partitioning method described by Michelangeli et al (1995) is applied to a subspace spanned by the leading six EOFs. For a choice of 3 or 4 regimes, the null hypothesis of multi-normality can be rejected at the 90% significance level (based on tests with synthetic data generated by a suitable Markov process), the patterns are reproducible using randomly drawn half-length samples, and it was demonstrated that the clusters arise due to “clumping” in phase-space and are not an artefact of skewness in the PCs. (Choices of 2 regimes, or 5 or greater, are shown to be less reproducible.) Figure 1 shows the patterns when 4 regimes are found. The Alaskan Ridge (Figure 1a) has been shown to be related to Alaskan blocking (Renwick and Wallace, 1996), and the Pacific Trough is reminiscent of the traditional “PNA” pattern. The Arctic High has a distinct signature of an annular mode or the North Atlantic Oscillation. The relationship of these regimes to synoptic blocking (diagnosed using potential temperature on the Potential Vorticity surface corresponding to the tropopause) was studied by Stan and Straus (2007).

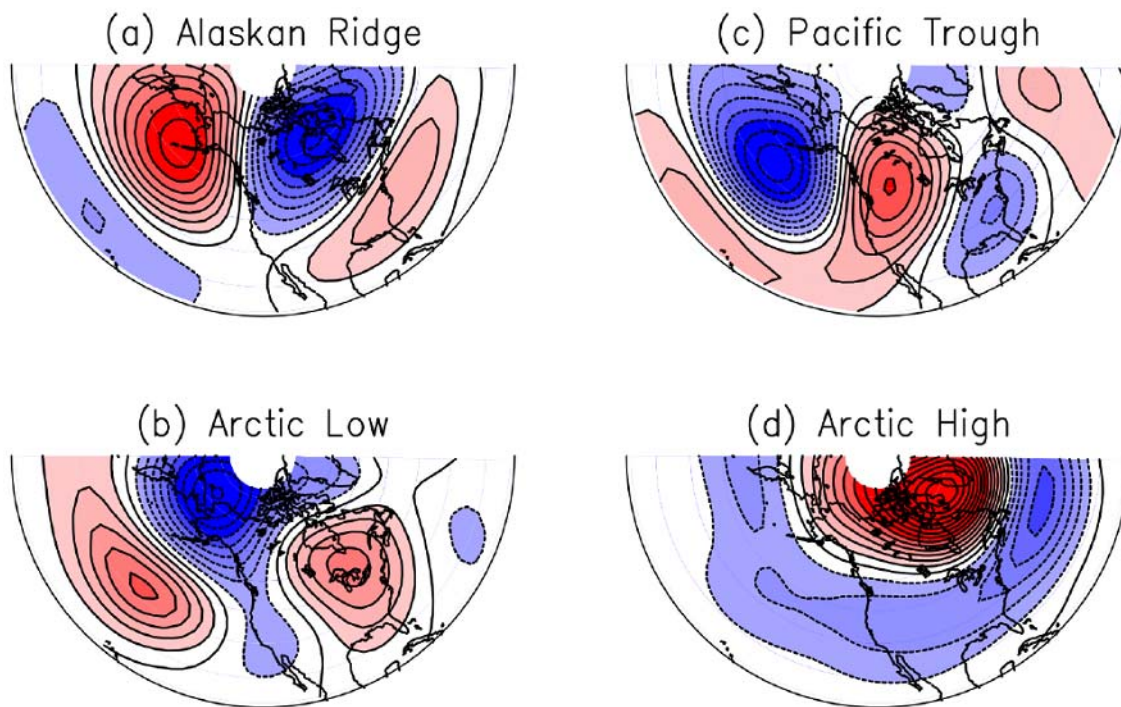


Figure 1 Four regimes identified from quasi-stationary periods during the 54 winters 1948/49 – 2002/03 from NCEP reanalysis. See text for details.

The need for long observed (reanalysis) data records in order to establish even modest statistical significance means that decadal changes in clustering properties are very hard to assess. Figure 2 shows the regimes obtained from the NCEP reanalysis for the 18 winters 1981-82 through 1997/98. From Figure 2 it is clear that the Alaskan Ridge is fairly robust with respect to period, while the Pacific Trough shows a change from a PNA-like pattern over the whole 54 years to a more ENSO-like response during the 18 years. Is this

change in pattern due to the differences in SST records for the two periods (see e.g. Straus and Shukla, 2002), or is the change simply due to differing sample sizes?

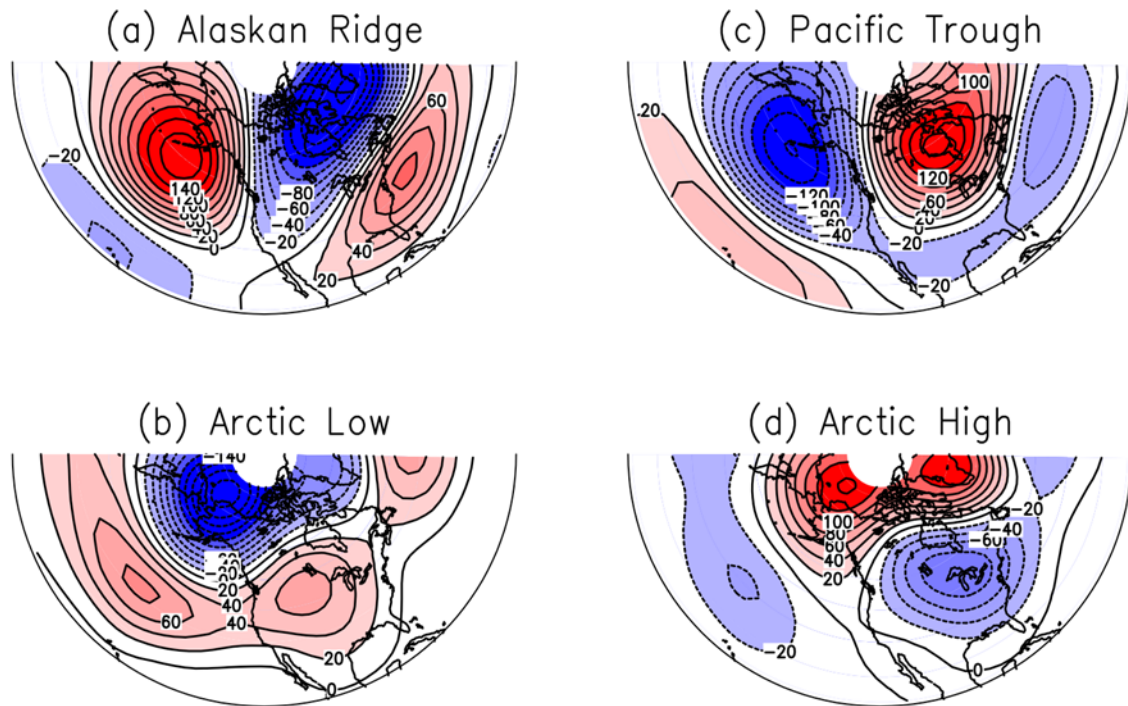


Figure 2 Four regimes identified from quasi-stationary periods during the 18 winters 1981/82 – 1998/99 from NCEP reanalysis. See text for details.

In order to assess the significance of the change in Pacific Trough, we need independent estimates of the sampling variability of the regimes. Such estimates are provided by an ensemble of wintertime atmospheric model simulations, constructed with the COLA atmospheric model forced by observed weekly SST. For each of the 18 above-mentioned winters, an ensemble of 55 simulations was run (see Straus and Molteni, 2004, for details). From this set of 55 x 18 simulations, we can construct a very large number of “samples” of simulations, each sample consisting of 18 simulations, one simulation chosen randomly per winter and so comparable to the observed record. (Call this sample Type A.) For each Type A sample, we construct an enhanced (Type B) sample of 54 winters, by augmenting the single simulation for each winter by 2 additional randomly chosen winters from the same winter. A pair of Type-A (18 members) and Type-B (18 x 3 = 54-member) samples thus represents atmospheric evolutions forced by identical SST histories, differing only in the number of simulations. For each of 100 such pairs of samples we repeat the regime analysis (as presented above), and obtain the pattern correlation between the regimes most strongly resembling the Pacific Trough. Thus a pdf of the pattern correlation between Pacific Trough regimes can be constructed. Against this pdf we evaluate the single pattern correlation between the Pacific Trough regimes shown in Figures 1 and 2 for the NCEP-54 and NCEP-18 samples, which did not see the same evolution of SST. The results (not shown) indicate that the observed pattern correlation (~ 0.6) lies well out into the tail of the pdf, indicating that the observed change in Pacific Trough between the NCEP-54 and NCEP-18 records is very likely to be due to the differences in SST, and not due to the differences in record length.

3. Regimes and Error Growth in the CFS Interactive Ensemble

It is widely accepted that ocean-atmosphere coupling is an important ingredient in the evolution of the climate system. Thus it is worthwhile diagnosing the regime behavior in coupled models. However, the dependence of regime properties on SST state discussed above and in Straus et al. 2007 indicates that evaluating regimes from coupled models may be difficult, since multiple atmospheric realizations with identical SST

evolutions are not available. The Interactive Ensemble (hereafter IE) configuration solves this problem however. In the IE, the ocean model communicates to six realizations of the atmosphere model started from slightly different initial conditions and run in parallel. The SST of the ocean model is felt by each atmospheric realization, but it is only the ensemble means of the atmospheric fluxes of heat, momentum and fresh water that are communicated to the ocean. The atmosphere ensemble – ocean coupling occurs once per day. (See Stan and Kirtman, 2007, and Kirtman and Shukla, 2002, for more details.)

The IE configuration of the CFS model was carried out with atmospheric resolution T62 and 64 levels in the vertical (Stan and Kirtman, 2007). IE forecasts were initiated from 1 January for the 11 years: 1980, 1981, 1982, 1983, 1984, 1985, 1986, 1987, 1989, 1990, 1998. For each calendar year, 5 slightly perturbed 1 January ocean states were used to generate 5 Interactive Ensembles. For each IE, we use the first 90 days of the forecast. The regimes of 200 hPa height are computed as in described in Section 2. [In this case quasi-stationary pre-filtering was not used, so that each forecast state could be uniquely assigned a regime.] The results shown in Figure 3 are comparable to those in Figure 2. The Pacific Trough (upper right), Alaskan Ridge (lower left) and Arctic Low (lower right) are all reasonably represented. However, the fourth regime resembles a wave train, and is clearly quite distinct from the Arctic High. Interestingly, the same failure occurs for the COLA atmospheric model (not shown). Why this particular regime is so hard to simulate is not understood.

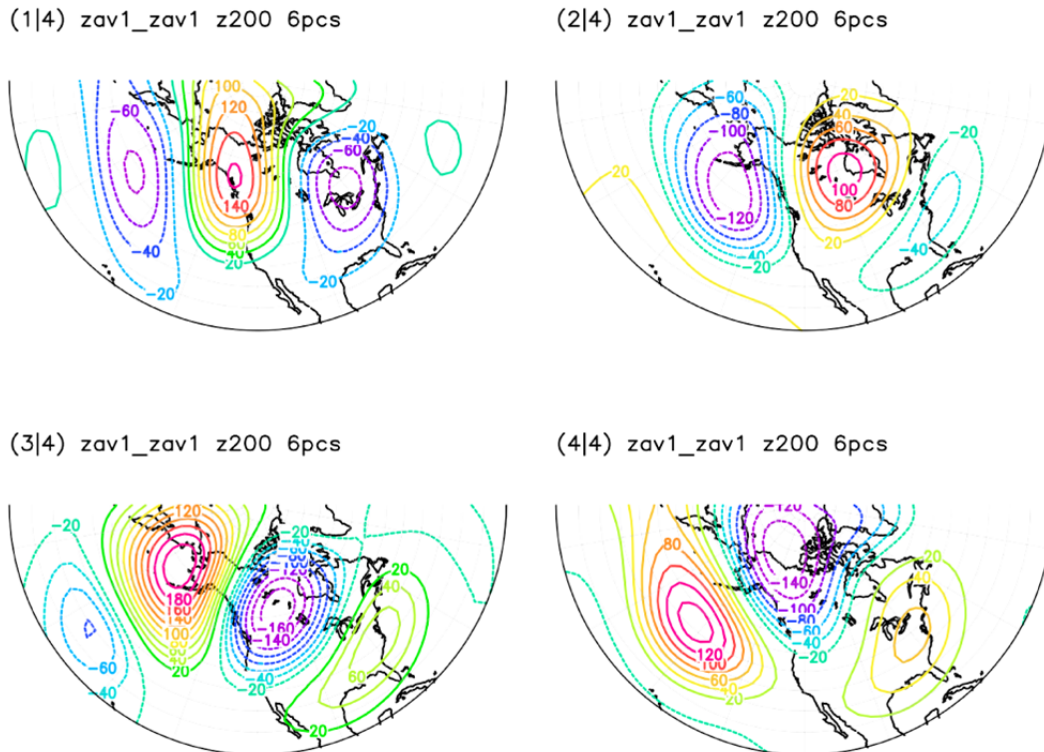


Figure 3 Four regimes identified from the CFS Interactive Ensemble forecasts. See text for details.

In order to show that these regimes correspond to preferred states in some sense, we evaluated the growth of the ensemble spread within each IE. Since Interactive Ensemble uses atmospheric initial conditions that are only slightly perturbed, we use the mean squared deviation of 200 hPa height for each atmosphere about the corresponding ensemble mean as a measure of “error.” This error is then evaluated as a function of forecast day, and averaged over the $11 \times 5 = 55$ distinct IEs. Following Trevisan (1993), we expect that a system showing strongly preferred regimes to lead to non-Gaussian pdfs of errors.

The pdfs of IE errors is shown as a function of forecast day in Figure 4. For each panel, three separate representations of the pdf (based on different degrees of smoothing in the kernel estimator algorithm) are shown in the bright colors, while the cumulative pdf is shown in the light green. All the pdfs have been standardized to

have zero mean and unit area. (This effectively normalized out the overall error growth.) The pdf at forecast day 5 looks qualitatively like that at day 1 – sharply peaked and positively skewed. However, by forecast day 10 the pdf has become much flatter (with a hint of bi-modality). Beyond forecast day 10 the pdf again relatively little change in shape. The timing of the change in error pdf, near day 10, corresponds roughly to the time when the average number of regimes represented in each ensemble starts to increase dramatically (not shown).

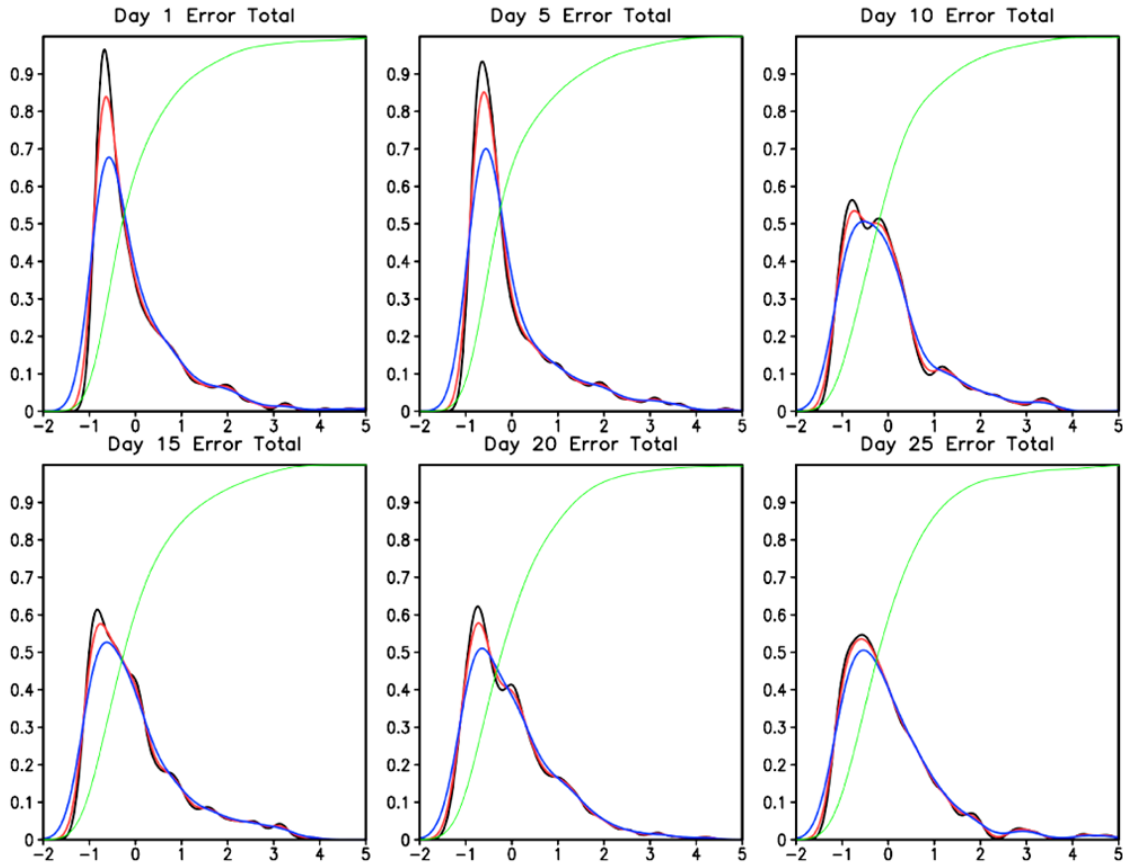


Figure 4 Standardized pdfs of error growth (ensemble spread) as a function of forecast day from the CFS Interactive Ensemble forecasts. See text for details.

4. Summary

There is enough evidence for significant circulation regimes in quasi-stationary data records of sufficient length for the concept to be taken seriously. However, statistical significance and reproducibility are still issues to be dealt with for each region, variable and period. Large ensembles of model simulations are very helpful in providing estimates of sampling statistics for regime properties. Regimes respond to changes in SST forcing both by changes in the structure of the regimes themselves, and in their population of occurrence. Preliminary results indicate that the regimes obtained from the CFS Interactive Ensemble forecasts are likely to be truly preferred states; more analysis of the CFS results is currently underway.

Acknowledgments. The help of Cristiana Stan in providing the data from the CFS Interactive Ensemble is acknowledged.

References:

- Baur, F., P. Hess and H Nagel, 1944; Kalendar der Grosswetterlagen Europas 1881-1969. Bad Homburg v.d.H.
 Charney J. G. and J. DeVore, 1979: Multiple flow equilibria in the atmosphere and blocking. *J. Atmos. Sci.*, **36**, 1205-1216.

- Charney J. G. and D. M. Straus, 1980: Form-drag instability, multiple equilibria, and propagating planetary waves in baroclinic, orographically forced, planetary wave systems. *J. Atmos. Sci.*, **37**, 1157-1176.
- Christiansen, B., 2005: Bimodality of the Planetary-Scale Atmospheric Wave Amplitude Index. *J. Atmos. Sci.*, **62**, 2528-2541.
- Corti, S., T. Palmer and F. Molteni, 1999: Signature of Recent Climate Change in Frequencies of Natural Atmospheric Circulations, *Nature*, **398**, 799-802
- Egger, J., 1981: Stochastically driven large-scale circulations with multiple equilibria. *J. Atmos. Sci.*, **38**, 2606-2618.
- Michelangeli, P.-A., R. Vautard, and B. Legras, 1995: Weather regimes: Recurrence and quasi-stationarity. *J. Atmos. Sci.*, **52**, 1237-1256.
- Reinhold, B., and R. T. Pierrehumbert, 1982: Dynamics of weather regimes: Quasi-stationary waves and blocking. *Mon. Wea. Rev.*, **111**, 2355-1272.
- Renwick, J. A., and J. M. Wallace, 1996: Relationships between North Pacific wintertime blocking and, El Nino and the PNA. *Mon. Wea. Rev.*, **124**, 2071-2076
- Stan, C. and B. P. Kirtman, 2008: The influence of atmospheric noise and uncertainty in ocean initial conditions on the limit of predictability in a coupled GCM. *J. Climate*, in press.
- Stan, C. and D. M. Straus., 2007: Is Blocking a circulation regime? *Mon. Wea. Rev.* **135**, 2406–2413
- Stephenson, D. B., A. Hannachi, and A. O’Neill, 2004: On the existence of multiple climate regimes. *Quart. J. Ro. Meteor. Soc.*, **130**, 583-605
- Straus, D. M., and J. Shukla, 2002: Does ENSO force the PNA? *J. Climate*, **15**, 2340-2358.
- Straus, D. M., S. Corti and F. Molteni, 2007: Circulation Regimes: Chaotic Variability versus SST-Forced Predictability. *J. Climate*, **20**, 2251–2272
- Straus, D. M., and F. Molteni, 2004: Circulation Regimes and SST Forcing: Results from Large GCM Ensembles. *J. Climate*, **17**, 1641-1656.
- Straus, D. M., S. Corti and F. Molteni, 2007: Circulation Regimes: Chaotic Variability versus SST-Forced Predictability. *J. Climate*, **20**, 2251–2272.
- Sura, P., M. Newman, C. Penland and P. Sardeshmukh, 2005: Multiplicative Noise and Non-Gaussianity: A Paradigm for Atmospheric Regimes? *J. Atmos. Sci.*, **62**, 1391-1409
- Toth, Z., 1991: Circulation patterns in phase space: A multinormal distribution? *Mon. Wea. Rev.*, **119**, 1501-1511.
- Toth, Z., 1993: Preferred and unpreferred circulation types in the Northern Hemisphere wintertime phase space. *J. Atmos. Sci.*, **50**, 2868-2888.
- Trevisn, A., 1993: Impact of Transient Error Growth on Global Average Predictability Measures. *J. Atmos. Sci.* **50**, 1016–1028.
- Vautard, R., and B. Legras, 1988: On the source of midlatitude low-frequency variability. Part II: nonlinear equilibration of weather regimes. *J. Atmos. Sci.*, **45**, 2845-2867.

MJO Monitoring and Assessment at the Climate Prediction Center and Initial Impressions of the CFS as an MJO Forecast Tool

Jon Gottschalck, Qin Zhang, Wanqui Wang

Michelle L'Heureux, Peitao Peng

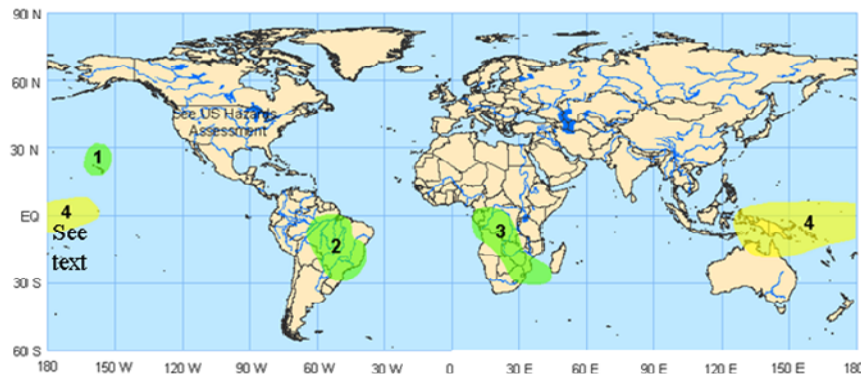
Climate Prediction Center, NOAA/National Weather Service

1. Introduction

The Madden-Julian Oscillation (MJO) is the leading mode of tropical intraseasonal climate variability and is characterized by organization on a global spatial scale with a period typically ranging from 30-60 days (Madden and Julian, 1971; 1972; 1994, Zhang, 2005). The MJO produces extensive periods of alternating enhanced and suppressed tropical rainfall, modulates tropical cyclone activity and monsoon systems and often impacts the extratropical circulation including over the US (Maloney and Hartmann, 2000a; 2000b; Kousky and Kayano, 1994; Higgins and Shi, 2001; Jones and Carvalho, 2002; Higgins et. al. 2000). The Climate Prediction Center (CPC) is committed to comprehensively monitoring, assessing and predicting the MJO in realtime operations. The CPC is particularly interested in and actively pursuing methods to better understand the MJO and include its potential predictability more effectively into CPC operations – both to improve the current forecasting capability in the week 2-4 time frame but also in the tropics through weekly hazard assessments. Not only is CPC the official NOAA source for MJO information to the National Weather Service (NWS) regions but also conducts

Issued: 12/3

Week 1 Outlook – Valid: December 4 – 10, 2007



1. An increased chance for above-average rainfall for Hawaii and nearby waters mainly to the north. An upper-level cutoff low is expected to become established to the west-northwest of the Hawaiian Islands and result in rather persistent surface low pressure and so the potential for enhanced rainfall in this region during the period. **Confidence: High**

2. An increased chance for above-average rainfall for east-central Brazil. Low-latitude frontal systems and a large-scale environment favorable for convection associated with the MJO is expected to continue to produce beneficial rains across this region during the period. **Confidence: High**

3. An increased chance for above-average rainfall for sections of interior and southern Africa. The enhanced phase of the MJO will produce a favorable environment for convection especially across interior Africa. Southern hemisphere frontal activity will likely increase the flow of moisture southeast towards southern Africa resulting in enhanced rainfall during the period. **Confidence: High**

4. An increased chance for below-average rainfall for the eastern Maritime continent, northern Australia, and the western Pacific Ocean. The suppressed phase of the MJO and cool sea surface temperatures associated with La Nina is expected to result in drier-than-average conditions across this region. **Confidence: High**

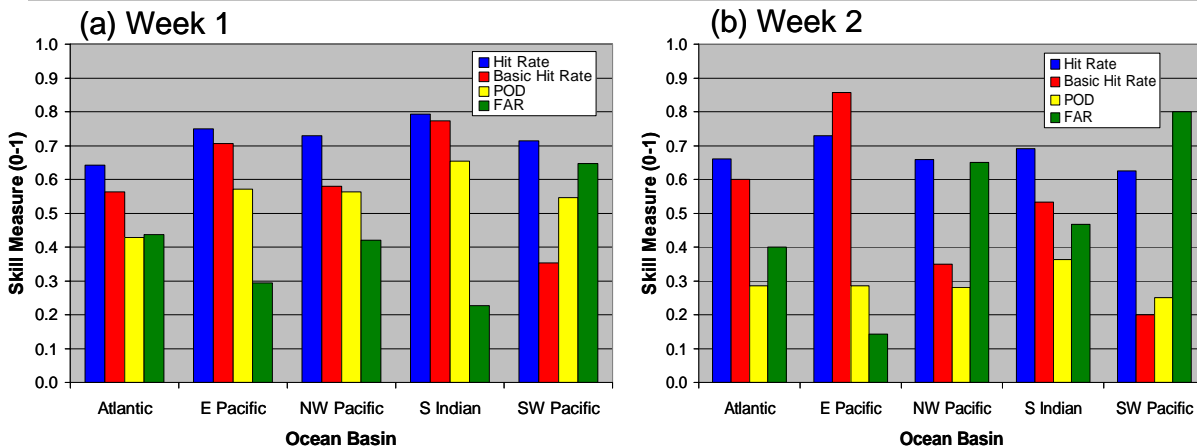
Figure 1 An example global tropics hazards/benefits assessment from December 2007. Highlighted areas depict elevated chances of above- or below-average rainfall (green/yellow) and favorable conditions for tropical cyclogenesis. Text is also given that provides some details for the type and basis of the hazard.

research towards the development of MJO related tools and is responsible for transferring this knowledge and expertise to NWS operations. An important current and especially future area of work is the development, evaluation, and implementation of MJO forecast tools related to the Climate Forecast System (CFS). This article describes current CPC MJO related monitoring and prediction activities and how CPC is currently using CFS within these work areas.

2. Operational Perspective and the MJO

The CPC monitors, assesses and predicts the MJO for three important reasons. First, the MJO alters the pattern of tropical convection substantially and can lead to extended periods of above- and below-average rainfall that can lead to flooding or exacerbate drought conditions. These periods of anomalous rainfall are very important in many regions across the global tropics where rainy seasons are generally short and can have far-reaching socio-economic impacts. The aforementioned effect on tropical cyclone activity and monsoon systems also result in economic consequences when they occur. Second, the MJO substantially modulates the extratropical circulation when it is active and can lead to large-scale transitional changes in the mid-latitudes resulting in extended periods of warmer or colder, wetter or drier conditions and also can lead to extreme events. Knowledge of circulation changes linked to the MJO increase predictability of subseasonal forecasts such as the CPC 6-10 day, 8-14 day, monthly, and hazard forecasts. Third, the MJO can also affect the onset, decay and evolution of the El Nino-Southern Oscillation (ENSO) as some of the most important characteristics of the MJO is its modulation of the low-level wind field that can produce important oceanic surface and sub-surface changes (Kessler and Kleeman, 2000; Zhang and Gottschalck, 2002).

Global Tropics Hazards/Benefits Assessment--Verification



		Observed	
		yes	no
Forecast	yes	a	b
	no	c	d

Figure 2 Verification of tropical cyclone hazard areas from Mar 2005 – February 2007 for (a) week 1 and (b) week 2. Refer to the 2x2 contingency table for bar plot explanation. The **Hit Rate** is the proportion of correct “yes” and “no” forecasts: $(a+d)/n$. The **Basic Hit Rate** is the proportion of correct “yes” forecasts: $a/(a+b)$. The **Probability of Detection (POD)** and **False Alarm Rate (FAR)** are calculated by $[a / (a+c)]$ and $[b / (a+b)]$ respectively. The total number of forecasts, n , is given by $n=(a+b+c+d)$.

The CPC monitors the MJO and its impacts through numerous web-monitoring products, the routine creation of a weekly MJO update and a global tropics hazards/benefits assessment (Figure 1). The weekly MJO update and global tropics hazards/benefits assessment are produced every Monday and released by 4 PM local time. The assessments incorporate input from all branches of CPC and collaboration from other NOAA centers including the National Hurricane Center (NHC) and the Earth Systems Research Laboratory (ESRL) among other national and international contributors. The purpose of the global tropics hazards/benefits assessment is to

1) assess and forecast changes in the distribution of tropical convection and communicate this information to NWS forecasters, 2) provide advance notice of potential hazards related to climate, weather and hydrological events across the global tropics, 3) serve as an additional resource for sectors of the US economy with international interests (finance, energy, agriculture, water resource management).

The assessment provides forecasts of extensive and persistent enhanced and suppressed tropical rainfall and areas where conditions are favorable or unfavorable for tropical cyclogenesis. The outlook spans the Week 1 - 2 time period. The physical basis for the assessment includes ENSO, the MJO and other coherent subseasonal tropical variability, interactions with the extratropical circulation, numerical weather forecast model guidance, boundary layer forcing (i.e. SST, soil moisture, etc.) and additional statistical forecasting tools.

The assessment is verified for both the precipitation areas and tropical cyclone regions (Figure 2). To date, both categories indicate useful skill and warrant continued development of the product. An emphasis on application of current, under development and planned objective tools is a goal during the next few years to make the assessment more objective in nature.

3. CFS MJO-Related Projects at CPC

The CFS is currently being utilized in intraseasonal monitoring and research in two primary ways at CPC. First, the CFS is being used as part of the MJO realtime monitoring activities in support of the weekly MJO update and global tropics hazards/benefits assessment products. Along these lines, we have applied the Wheeler and Hendon (2004, hereafter WH2004) MJO filtering methodology to realtime operational CFS forecasts. To briefly review, the technique is a spatial filter as opposed to a temporal filter which makes it very attractive to realtime operational applications and is based on a combined Empirical Orthogonal Function (EOF) analysis using Outgoing Longwave Radiation (OLR) and 850-hPa and 200-hPa zonal wind data. In order to pinpoint the MJO signal data pre-filtering is applied and includes removal of the seasonal cycle and ENSO associated variability. An MJO index is defined as the first two principal components (PCs) after projecting data (either observational or model) onto the above EOF structures and these are called realtime MJO mode 1 and 2 (RMM1 and RMM2). An example of the procedure as applied to the ensemble Global Forecast System (GFS), the atmospheric component of CFS, is shown in Figure 3.

The upgrade of operational CFS forecasts from 8-day to 1-day lag during late 2007 has now made it possible to realistically use CFS forecasts in realtime MJO monitoring and prediction applications. The CFS data available are operational forecasts (four members daily) and a lead dependent climatology in order to calculate bias corrected anomalies. The WH2004 methodology is applied and these data are projected onto observed EOFs and realtime CFS RMM1 and RMM2

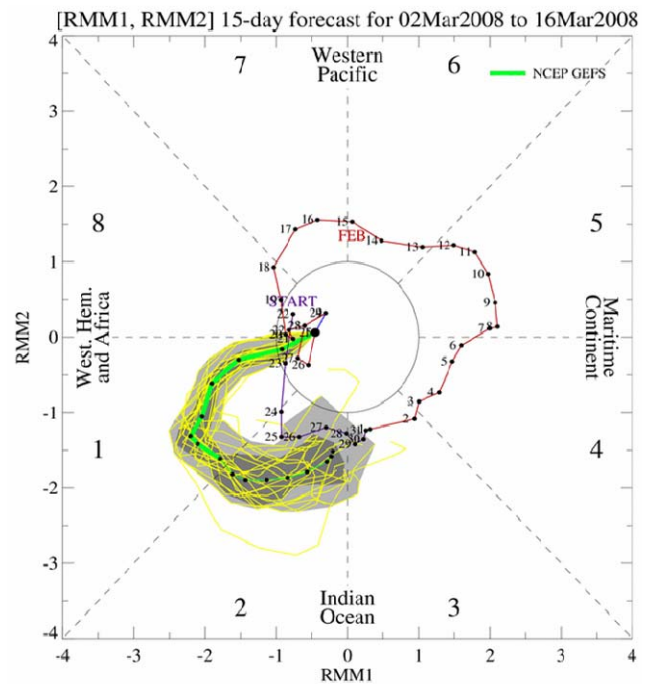


Figure 3 An example phase diagram illustrating the amplitude and phase of the MJO during January and February 2007. Description of this display can be found in WH2004. A few important details are 1) the counterclockwise trajectory shown here indicates eastward propagation through various phases of the enhanced phase of the MJO, 2) the greater the distance from the circle the greater the strength of the MJO. Observations are the red and purple lines. The extended green and yellow lines are forecasts from the ensemble Global Forecast System (GEFS). The yellow lines are the individual 20 members from the GFS and the green line is the ensemble mean. The dark gray shading indicates 90% of the members are included and the light gray indicates that 50% of the members are included.

MJO index values calculated. Figure 4 shows an example phase diagram from a CFS operational forecast along with the verification of the MJO index during the last few years. Anomaly correlation skill of the MJO index remains useful till approximately 7-10 days for operational forecasts ranging from 2005 to February 2008. Utilizing the CFS hindcast datasets, the MJO index was calculated for the historical data record of 1979-2004 and the anomaly correlation skill calculated (Figure 5). The skill here is lower – mainly a result of using daily forecasts only. The operational CFS forecasts do include more than one member per day (2 initially and 4 later during 2007).

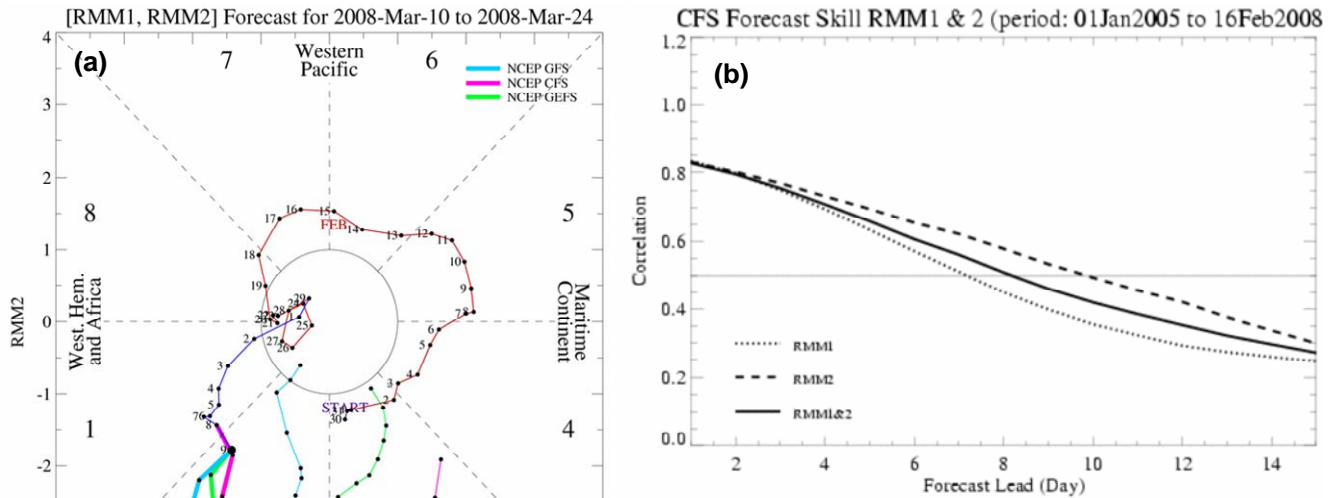


Figure 4 (a) Phase diagram illustrating an example from an operational CFS forecast (magenta line). (b) Anomaly correlation skill for RMM1, RMM2, and both RMM1 and RMM2 from January 2005 to February 2008.

In addition to the operational realtime CFS MJO index forecast, CFS data is being used as part of an objective MJO forecast tool consolidation activity. Products from this project will be used as objective forecast input for the CPC weekly MJO update and international hazards/benefits assessments. Several tools are available for MJO prediction and include both statistical and dynamical approaches.

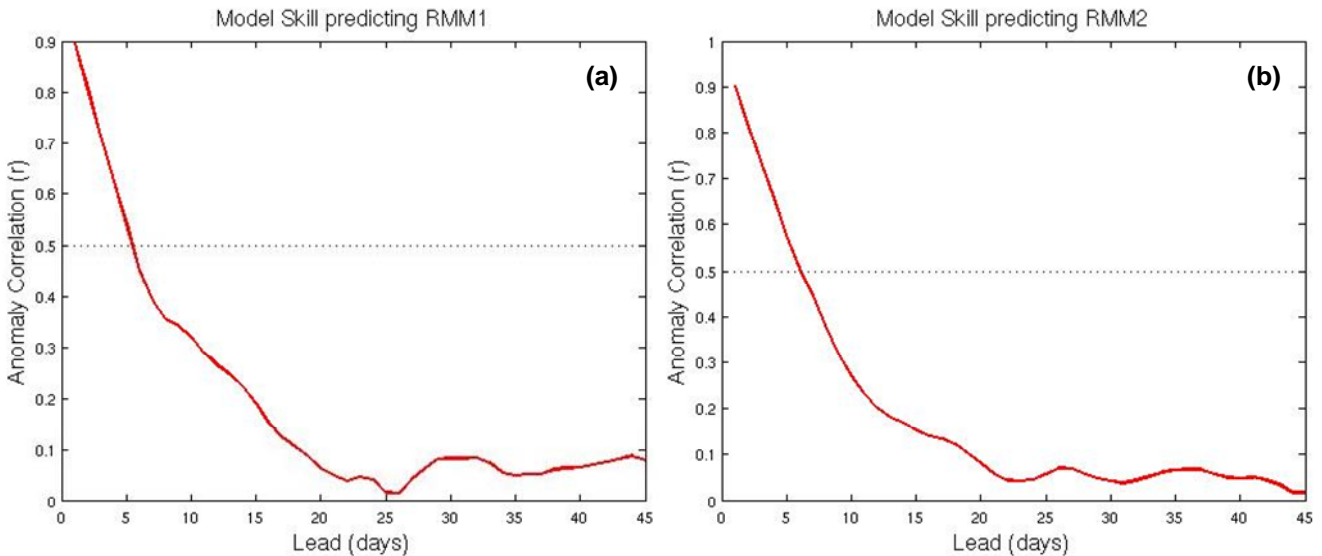


Figure 5 Anomaly correlation skill for (a) RMM1 and (b) RMM2 using the historical CFS hindcasts.

Hindcasts were derived from five MJO methods with the goal to choose a wide-spectrum of methods that vary in complexity and diversity. We utilized four statistical models and one dynamical model. These methods include (1) lagged linear regression model (PCL), (2) autoregressive model (ARM), (3) empirical phase propagation model (EPP), (4) constructed analogue model (ANL) and (5) the CFS. Due to length considerations, the technical details for the models are omitted. The hindcasts are forecasts of the first two PCs based on anomalous data filtered to the MJO time scale (WH2004) with low-frequency variability (i.e., ENSO) removed from both the observational and model datasets. The statistical models were “trained” on data from the period from 1979-1989 and a set of hindcasts created covering a period from 1990-2004 out to a lead of six pentads or 30 days. No training was necessary for the CFS hindcasts as this is a dynamical model.

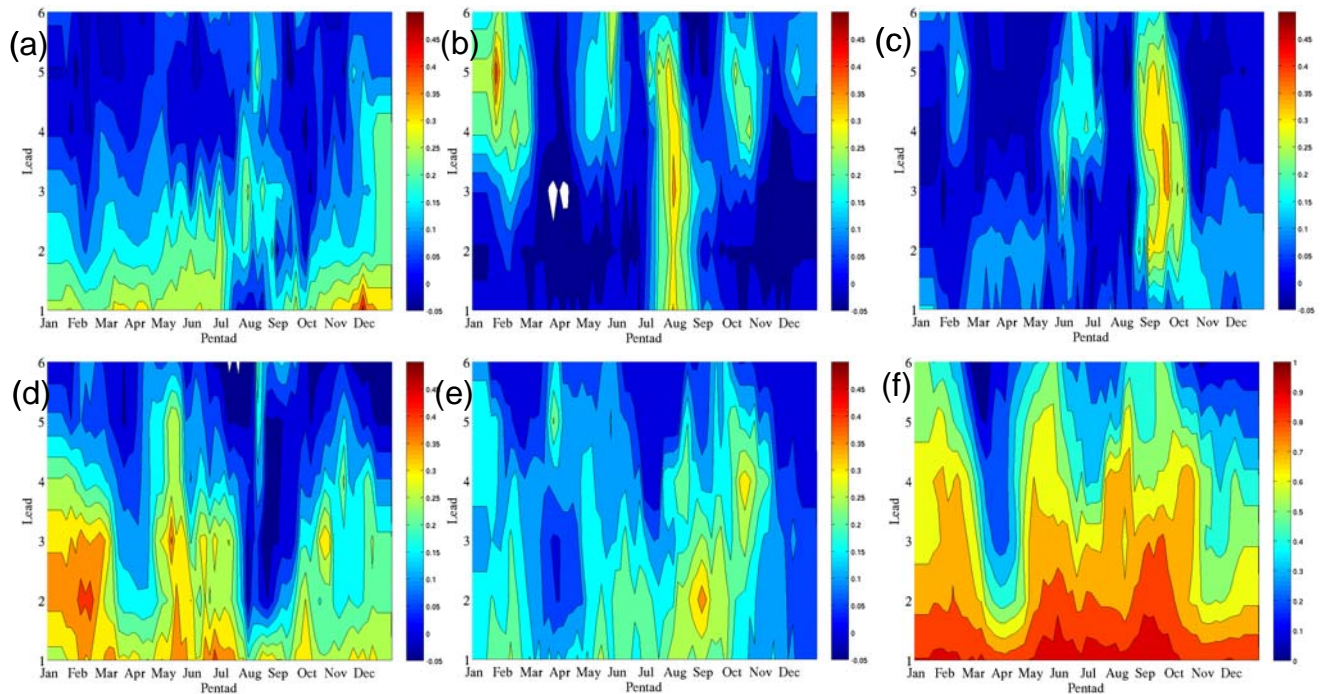


Figure 6 Weights based on historical data from 1990-2004 time period for (a) PCL, (b) ARM, (c) EPP, (d) ANL, (e) CFS, and (f) All forecast methods as a function of seasonal cycle and lead. Shading indicates the degree of weights.

A framework for objective consolidation of these forecasts has been developed and weights (to be used for the realtime forecasts) based on the historical data (hindcasts) determined. Two approaches for objective consolidation are used – (1) equal weights (CEQ) – all methods receive a weight of 0.20, and (2) skill-based weights that account for the independent skill of each method (CRR, co-linearity between methods accounted for). The approach used in (2) is the “ridge regression” approach. Figure 6 illustrates the weights [as determined by approach (2)] for the five methods as a function of lead and seasonal cycle and indicate when and how much each method contributes to the consolidation. The results show that the constructed analogue method (ANL) contributes the most to the consolidation during the majority of the year. The autoregressive model only contributes to the consolidation during the July-August period and at times longer leads. The CFS only contributes significantly to the consolidation during the September to November time period at generally earlier leads.

Figure 7 shows the anomaly correlation skill for each method and the two consolidation approaches as a function of lead. The results indicate only minor improvement over what can be expected on independent data (after cross-validation) over the best method at any given lead. The results indicate only a 2-4% improvement for pentads 1-3 and 8-18% for pentads 4-6. However, by the later leads, the skill improvement occurs at a time when the skill levels have dropped below what is commonly the cutoff for useful skill ($r = 0.5$). The CRR approach outperforms CEQ at short leads (pentad 1-3) while CEQ outperforms CRR at longer leads (pentad 4-6).

It is believed that the percent improvement of the consolidated “ridge regression” forecasts is small because the statistical MJO tool approaches offer similar and little independent information so that the consolidation does not substantially improve upon the best method. The CFS dynamical model, although offering useful independent information, has a historical skill level that is quite low and so does not aid the consolidation.

Despite the modest skill shown here by the CFS in prediction of the MJO index, the future of the CFS is bright. The next generation of the CFS is currently under development and evaluation and it offers changes that are expected to improve the skill of forecasts of the MJO index. These changes include 1) the use of more consistent initial conditions, 2) improved spatial resolution, 3) more frequent forecasts (every 30 hours) for a large ensemble, and 4) active MJO research within the Environmental Modeling Center (EMC) in order to improve our physical understanding of not only the MJO but model representations of the MJO. We expect the CFS skill to approach that shown by the Global Ensemble Forecast System after these changes are implemented.

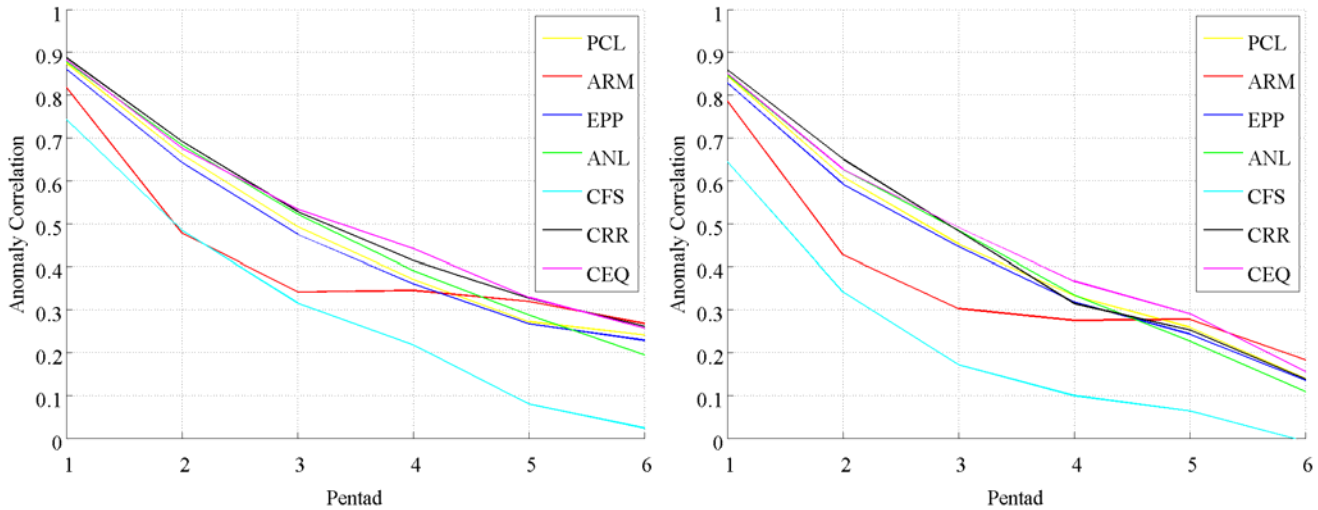


Figure 7 Anomaly correlation for RMM1 and RMM2 as a function of lead for the five methods individually (PCL) lagged linear regression, (ARM) autoregressive model, (EPP) empirical phase propagation model, (ANL) constructed analogue model, the Climate Forecast System (CFS) and the equal weights (CEQ) and ridge regression (CRR) consolidation approaches.

An important collaborative effort underway at CPC is the calculation of realtime MJO index forecasts (WH2004) from not only NCEP models (GFS and CFS) but also with other international operational center model output. The goal is to apply a standard methodology for calculation of the forecast MJO indices, their display, and for their verification. Current participating centers include the National Center for Environmental Prediction (NCEP), European Centre for Medium Range Weather Forecasting (ECMWF), United Kingdom Meteorology Office (UKMET), Canadian Meteorological Center (CMC), Bureau of Meteorology in Australia (BOM), Earth System Research Laboratory (ESRL) and Brazilian Center for Weather Forecasting and Climate Studies (CPTEC). CPC was chosen to lead, host, and disseminate these products.

4. MJO Impacts on CFS SST Prediction

Strong MJO activity developed during November 2007 and lasted through mid-February. It has been hypothesized that the MJO can substantially alter the intensity and timing of the ENSO cycle. Alternating periods of westerly and easterly wind anomalies across the western Pacific during the winter of 2007-2008 strongly affected the CFS SST forecast of La Nina conditions during this period. Figure 8 shows the sensitivity of the SST prediction during different phases of the MJO when the CFS forecast was initialized. Forecasts initialized during the November and early December period resulted in a forecast of cooling conditions for March 2008 while forecasts later during December 2007 and January 2008 resulted in a significantly warmer forecast during March 2008. In fact, the differences in the mean of the CFS SST forecasts during these two periods were large enough for a forecast of a moderate-strong La Nina by themselves (Figure 8).

5. Summary and Discussion

The CPC has a comprehensive MJO monitoring, assessment, and prediction activity as the MJO has large ramifications for a number of CPC operational forecasts and assessments. Operational considerations are important and should be kept in mind when conducting MJO-related research at the Center for Ocean-Land-Atmosphere Studies (COLA). Improved understanding and prediction of intraseasonal variability can improve CPC extended range prediction as the MJO can result in important extratropical transitions leading to extended periods of varying weather regimes. Also, CPC international hazard assessments are heavily influenced by the MJO. The CFS has an encouraging future but currently the skill in prediction of an MJO index is low to modest and useful skill extends out to approximately 7-10 days in this initial analysis and CFS version. The new CFS version is expected to improve the skill.

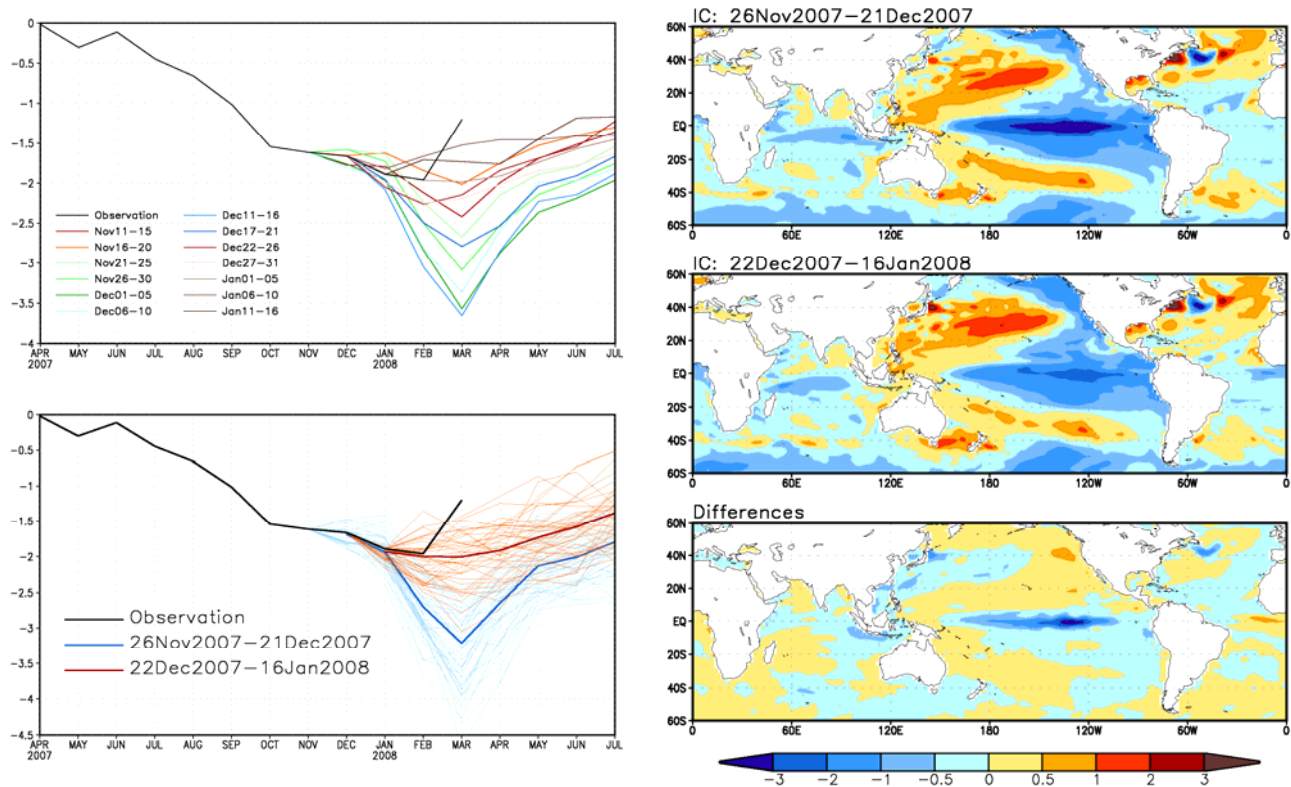


Figure 8 *Left panels:* CFS forecasts of Nino3.4 for a number of different initial conditions over the period from November to January. The black line is the subsequent observations. *Right panels:* SST differences during March 2008 between forecasts from two periods of CFS initial conditions.

An important area of research work that could significantly aid CPC forecast operations is an improved understanding of the MJO onset and decay periods (i.e., tropical transitions). Operations are often forced to wait for the MJO to develop or end before forecasts can respond effectively and appropriately. Although the dynamical model MJO index forecasts show some promise for MJO prediction (e.g., November 2007), operational forecasts at CPC can benefit from comprehensive, innovative research targeting MJO initiation and demise periods. For example, what role do extratropical-tropical exchanges play? How important are scale interactions (i.e., diurnal convection, mesoscale regional convection)? Is pre-conditioning of atmospheric moisture the primary player in regenerating the MJO evolution? These questions are quite difficult to answer and most likely will only be answered through a dedicated series of modeling studies. The MJO is a very complex phenomenon and encompasses multiple time and space scales and research in these areas may aid our understanding of the MJO and its operational prediction of US and global impacts.

References

- Higgins, W., J. Schemm, W. Shi, and A. Leetmaa, 2000: Extreme precipitation events in the western United States related to tropical forcing. *J. Climate*, **13**, 793-820.
- Higgins, W and W. Shi, 2001: Intercomparison of the principal modes of interannual and intraseasonal variability of the North American monsoon system. *J. Climate*, **14**, 403-417.
- Jones, C. and L. Carvalho, 2002: Active and Break phases in the South American Monsoon System, *J. Climate*, **15**, 905-914.
- Kessler, W. and R. Kleeman, 2000: Rectification of the Madden-Julian Oscillation into the ENSO cycle. *J. Climate*, **13**, 3560-3575.
- Kousky, V. and M. Kayano, 1994: Principal modes of outgoing longwave radiation and 250-mb circulation for the South American sector. *J. Climate*, **7**, 1131-1143.
- Madden R. and P. Julian, 1971: Detection of a 40-50 day oscillation in the zonal wind in the tropical Pacific, *J. Atmos. Sci.*, **28**, 702-708.
- Madden R. and P. Julian, 1972: Description of global-scale circulation cells in the tropics with a 40-50 day period. *J. Atmos. Sci.*, **29**, 1109-1123.
- Madden R. and P. Julian, 1994: Observations of the 40-50 day tropical oscillation: A review. *Mon. Wea. Rev.*, **112**, 814-837.
- Maloney E. and D. Hartmann, 2000a: Modulation of eastern North Pacific hurricanes by the Madden-Julian Oscillation, *J. Climate*, **13**, 1451-1460.
- Maloney E. and D. Hartmann, 2000b: Modulation of hurricane activity in the gulf of Mexico by the Madden-Julian Oscillation. *Science*, **287**, 2002-2004.
- Wheeler, M. and H. Hendon, 2004: An All-Season Real-Time Multivariate MJO Index: Development of an Index for Monitoring and Prediction. *Mon. Wea. Rev.*, **132**, 1917-1932.
- Zhang, C. and J. Gottschalck, 2002: SST anomalies of ENSO and the Madden-Julian Oscillation in the equatorial Pacific. *J. Climate*, **15**, 2429-2445.
- Zhang, C. 2005: Madden-Julian Oscillation. *Reviews of Geophysics*, **43**, 1-36

Dominant Daily Modes of the South Asian Summer Monsoon Rainfall in the NCEP Climate Forecast System

Deepthi Achuthavarier^{1,*} and V. Krishnamurthy^{1,2}

¹Department of Climate Dynamics, George Mason University, Fairfax, VA

²Center for Ocean-Land-Atmosphere Studies, Calverton MD

1. Introduction

Observational studies by Krishnamurthy and Shukla (2007, 2008; KS07 and KS08 hereafter) and Krishnamurthy and Kirtman (2008; KK08, hereafter) have demonstrated that the convective and rainfall anomalies associated with the south Asian summer monsoon consist of two intraseasonal oscillatory modes with periods around 45 and 28 days and two non-oscillatory or persistent components which are related to ENSO and Indian Ocean dipole sea surface temperature (SST). These results are based on a multi-channel singular spectrum analysis (MSSA) of daily anomalies of the observed outgoing long wave radiation (OLR) and rainfall data. The persistent modes are characterized by large scale patterns that prevail over most of the south Asian monsoon region with same sign anomalies throughout the summer monsoon season [June-September (JJAS)]. Their results also show that the seasonal anomalies are largely determined by the amplitude and sign of the persistent modes, emphasizing the role of low frequency variability of SST in climate predictability. Despite this potential, success in seasonal forecasts depends on the ability of the current general circulation models (GCMs) to correctly simulate the above-mentioned modes and their relationship with the SST.

The objective of the present study is to examine and document the dominant daily modes of the summer monsoon rainfall in a state-of-the-art coupled GCM. This study will provide an account of the intraseasonal variability in a coupled model as well as its seasonally persistent components that are shown to be pivotal in understanding the interannual variability of the monsoon. The ENSO-monsoon teleconnection in the model will be discussed from a new point of view opened by the recognition of the seasonally persistent components. The impacts of horizontal resolution and air-sea coupling will also be mentioned briefly at the end.

2. Models and methods of analysis

2.1 Models

The primary model used in this study is the Climate Forecast System (CFS) with a horizontal resolution of 62 waves, developed at the National Centers for Environmental Prediction (NCEP). The atmospheric component of the CFS is the NCEP's Global Forecast System (GFS) and its ocean component is the Modular Ocean Model version 3 (MOM3) of the Geophysical Fluid Dynamics Laboratory (GFDL). The atmosphere-ocean coupling in the CFS spans from 65°S to 50°N, and the coupling interval is once a day. No flux correction is employed in the CFS. A detailed description of the

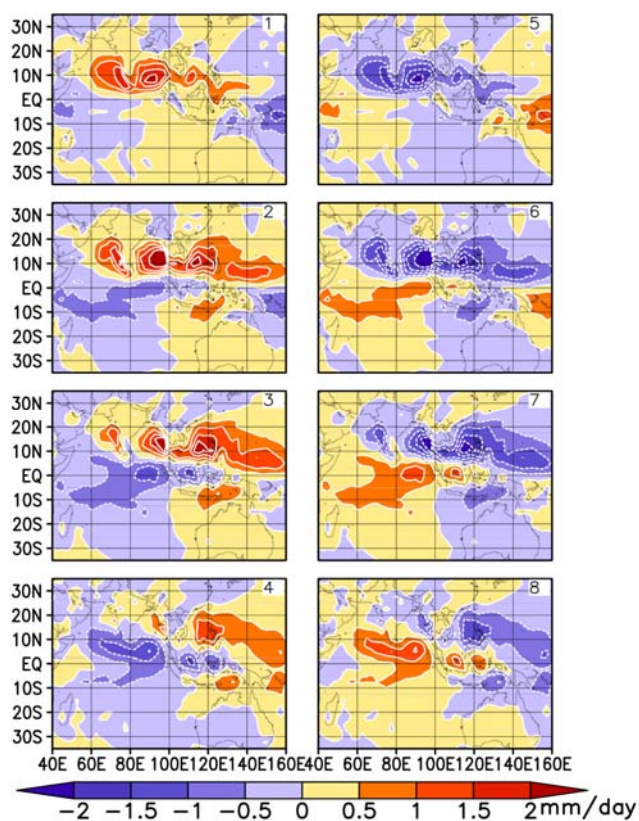


Figure 1 Phase composites of the 100-day oscillatory mode of the CFST62. One cycle is divided into 8 equally spaced intervals. Units are in mm day^{-1} .

*Correspondence to: Deepthi Achuthavarier, Department of Climate Dynamics, George Mason University, Fairfax, VA; E-mail: deepthi@cola.iges.org

model can be found in Saha et al. (2006). Daily mean precipitation data from a 52 year long simulation of the CFST62 (CFS with T62 resolution) (Pegion and Kirtman 2008) is used in this study. In order to examine the impact of horizontal resolution, a 100 year long simulation of the T126 version of the CFS (CFST126) is obtained from the NCEP. Additionally, data from an AMIP (Atmospheric Model Intercomparison Project) type simulation by the GFS is also considered (B. Jha, Personal Communication). The GFS, which is of T62 resolution (GFST62), is run from 1950 to 2002 (53 years) with prescribed monthly reconstructed SST. From all the three simulations, the last 30 years of data are analyzed. The results are compared with observational findings of KS08 and KK08.

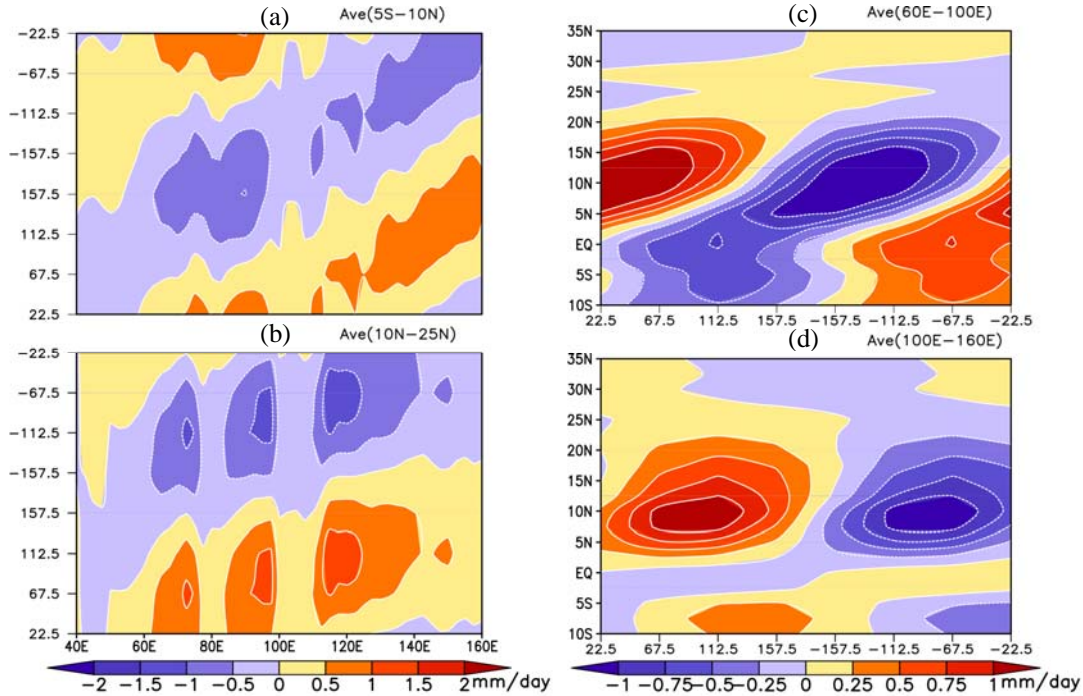


Figure 2 Longitude-time cross sections of the 100-day oscillatory mode of the CFST62 computed by averaging over the latitudes 5°S - 10°N (a) and 10°N - 25°N (b). Latitude-time cross sections of the 100-day oscillatory mode of the CFST62 computed by averaging over the longitudes 60°E - 100°E (c) and 100°E - 160°E (d). The y-axis in (a) and (b) and the x-axis in (c) and (d) represent phase angle. Units are in mm day^{-1} .

2.2 Methods

The analysis methods used in this study follow those of KS08. The dominant daily modes of monsoon are obtained by performing an MSSA on daily anomalies of rainfall for the JJAS season. No filters are applied on the data except for a 5-day running mean to remove synoptic scale fluctuations. While a traditional empirical orthogonal function (EOF) analysis provides the spatial patterns of maximum variance, MSSA isolates the spatial structure of the most dominant modes as well as their propagation in time (Plaut and Vautard 1994). In the context of a dynamical system, MSSA can be considered as a tool to isolate quasi-periodic and quasi-stationary orbits of the system. The computational procedure of MSSA can be briefly described as follows. Let the original data set contain L spatial points (channels) at N discrete time intervals. The lagged covariance matrices are constructed by choosing a certain lag window of length M for each L spatial point. The lagged covariance matrices for all spatial points are arranged to form a trajectory matrix of order $(LM, N-M+1)$, eigenanalysis of which yields LM eigenvalues and LM eigenvectors. The eigenvectors contain M sequences of spatial maps and are referred as space-time EOFs (ST-EOFs). The space-time principal components (ST-PCs), each of length $N-M+1$ are obtained by projecting the original data on to the corresponding ST-EOFs. The component of the original data corresponding to each eigenvalue can be reconstructed by projecting the ST-PC onto its respective ST-EOF, and is referred as the reconstructed component (RC). The RCs share the spatial and

temporal dimensions of the original dataset and can be considered as the filtered data corresponding to a particular mode.

3. Climatology and variability

Preliminary analysis shows that all three simulations (CFST62, CFST126 and GFST62) capture the general features of the JJAS seasonal climatology of rainfall over the south Asian monsoon region (40°E - 160°E , 35°S - 35°N). A few deficiencies to note are the overestimation of rainfall over the southwestern and northeastern parts of India and the underestimation over the central India, western Pacific and the south China Sea region. An erroneous patch of rainfall anomaly is seen over the western equatorial Indian Ocean in both the coupled models, but is not present in the GFS. The interannual and the intraseasonal variability of the three simulations are examined by computing the standard deviation of the JJAS seasonal and pentad anomalies. Although the models capture the spatial structure of variability, which includes maxima on either side of the Indian peninsula and over the western Pacific and minima over the southeastern parts of India, the amplitude of the variability is considerably overestimated. Comparing between the coupled models, there is no noticeable improvement in the CFST126 as far as the climatology and variability are considered. However, the uncoupled run fails to capture the rainfall maxima over the western Pacific and South China Sea region.

4. Dominant daily modes of rainfall in the CFS

Following the observational study of KS08, MSSA with a lag window of 61 days is performed on the daily anomalies of rainfall during the JJAS season for 30 years of model data from CFST62, CFST126 and GFST62. This analysis, which was performed exclusively on the JJAS season in order to isolate the summer modes, yielded only a single pair of intraseasonal modes of 30-day period. A closer examination of the other dominant non-oscillatory modes indicated that the dataset contained another intraseasonal mode probably with a longer period that was not resolved in the lag window used in this analysis. Therefore, a new MSSA was performed taking all days of the year and employing a longer lag window of 181 days. This analysis revealed two pairs of oscillatory modes with periods around 100 days in the coupled models, and a single pair of oscillatory mode of 70-day period in the uncoupled model. Out of the two 100-day modes, one is found to be dominant during the summer and another during the winter season. The winter mode is likely to be the Madden Julian Oscillation (MJO). This study will focus on the two summer modes mentioned above.

4.1 Oscillatory modes

As mentioned above, CFST62 shows two summer intraseasonal modes with periods 100 and 30 days. Figure 1 shows phase composites calculated from the RCs corresponding to the 100-day oscillatory mode. Since the MSSA isolates the oscillatory mode in a pair, RC of such a mode is obtained by adding the corresponding RCs constituting that pair; i.e., RC of 100-day mode, denoted by RC34 is the sum of RCs 3 and 4. Phase angles of the oscillations are calculated from the RCs, following Krishnamurthy and Shukla (2007). One complete cycle of oscillation is divided into eight intervals that are 45 degrees apart. The phase composite for a particular phase

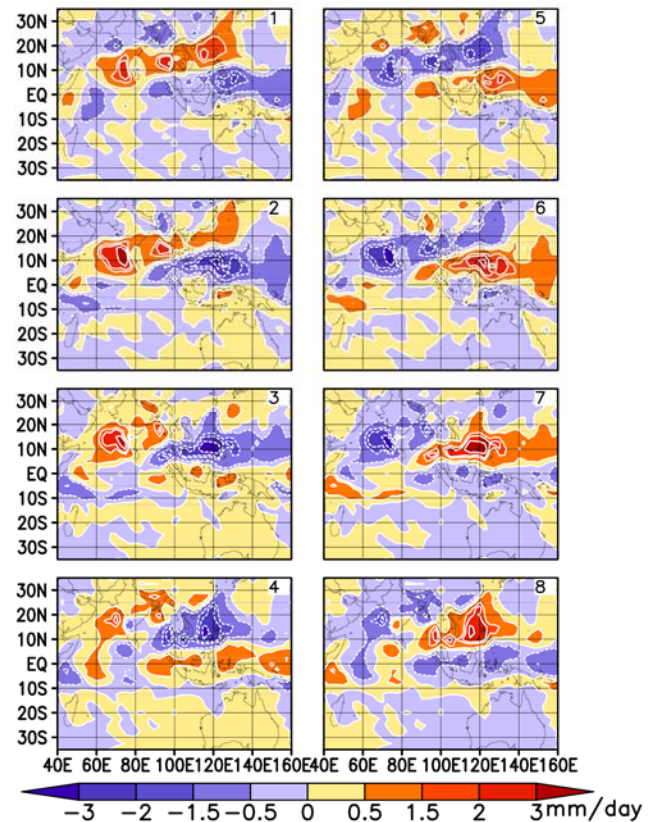


Figure 3 Phase composites of the 30-day oscillatory mode of the CFST62. One cycle is divided into 8 equally spaced intervals. Units are in mm day^{-1} .

is computed by averaging parts of the RC falling into that particular phase. Figure 1 shows that the anomalies developed over the equatorial Indian Ocean slowly propagate northeastward and develop into a large scale tilted pattern extending from 60°E to 140°E. This large-scale pattern is characteristic of the 45-day mode discussed in KS08 (their Figure 4).

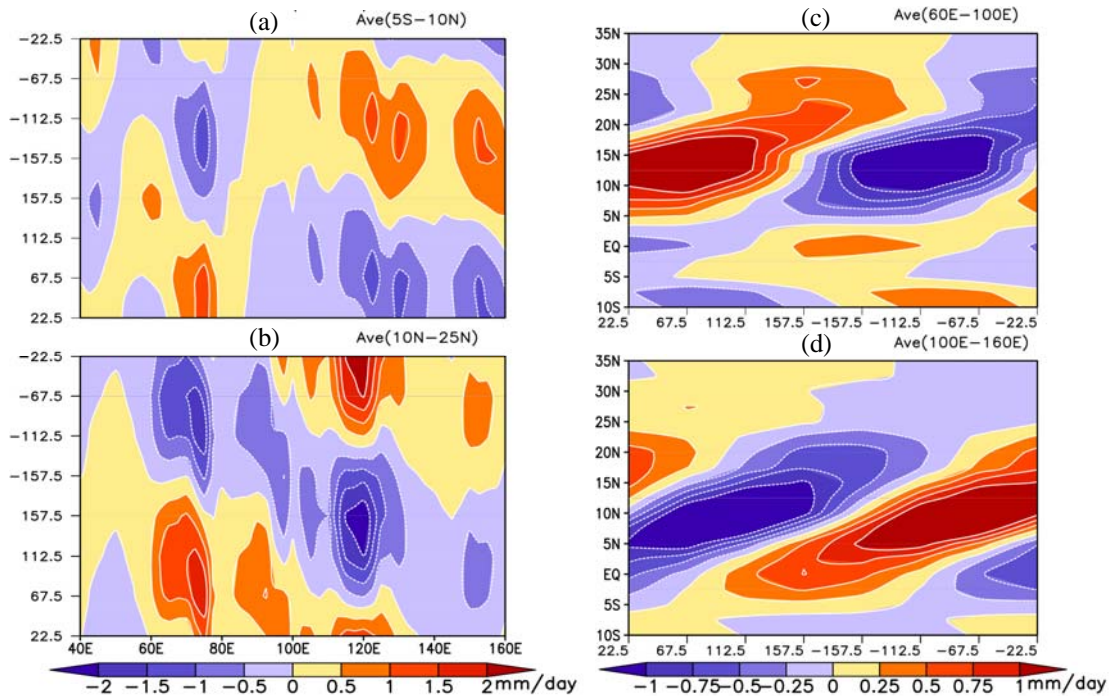


Figure 4 Longitude-time cross sections of the 30-day oscillatory mode of the CFST62 computed by averaging over the latitudes 5°S-10°N (a) and 10°N-25°N (b). Latitude-time cross sections of the 30-day oscillatory mode of the CFST62 computed by averaging over the longitudes 60°E-100°E (c) and 100°E-160°E (d). The y-axis in (a) and (b) and the x-axis in (c) and (d) represent phase angle. Units are in mm day^{-1} .

The propagation characteristics of the 100-day mode are examined by plotting longitude-time and latitude-time cross sections of the phase composites (Figure 2). It is seen that the 100-day mode has coherent eastward propagation between the latitudes 5°S and 10°N and northward propagation from 5°N to 20°N. These results are consistent with the observational findings except for that the model fails to capture northward propagation between 100°E and 160°E (see Figure 10 of KS08). Figures 1 and 2 suggest that the 100-day mode must be equivalent to the 45-day mode obtained in observations. An important point to note here is that, although the model captures the spatial structure and propagation characteristics of the mode, the intraseasonal oscillations in the model are considerably slower and extend well beyond the JJAS summer season. The phase composites and the propagation of the 30-day mode are shown in Figure 3 and 4. The spatial structure of the 30-day mode does not show the characteristic quadruple structure seen in its observational counterpart (see Figure 5 of KS08). However, longitude-time and latitude-time cross sections of the phase composites suggest coherent westward and northward propagation as seen in observations (Figure 4).

The relation between the intraseasonal modes and the SST is examined by computing daily point correlation between RCs averaged over the EIMR (Extended Indian Monsoon Region; covers the area 70°E-110°E, 10°N-30°N) and daily anomalies of the SST. The 100-day mode shows moderate dependence on the eastern Pacific and Indian Ocean SST where correlations values range up to 0.4. The 30-day mode shows little correlation (values below 0.1) with the SST over most of the ocean basins, which suggests that it might be an atmospheric-only mode. These results are consistent with the observations.

4.2. Non-oscillatory or persistent modes

This section examines the persistent components among the first 8 modes obtained from the 181-day-lag-window MSSA. Figure 5 shows the daily point correlation between the EIMR index computed from the RCs of the four persistent modes and daily SST anomalies. The spatial structure of the correlation patterns of the RCs 1, 5 and 8 have an ENSO-like structure in the Pacific and compare well with the correlation map of the observed ENSO mode (see Figure 4(c) of KK08). Daily rainfall anomalies corresponding to the modes 1, 5 and 8 are negatively correlated with the eastern Pacific SST, consistent with the findings of KK08 (their Figure 4(c)). Note that the sign of the correlation is opposite in KK08 since they used the OLR anomalies instead of the precipitation. Thus there are three modes showing possible links with the ENSO, while the observational analysis produced only a single ENSO mode. One explanation could be that, by performing the analysis on the entire data as opposed to only the summer season, the ENSO modes of different timescales might be captured here.

Another important point to note from Figure 5 is that the correlation map for RC2 has a pattern similar to the rest of the modes but with positive correlations over the eastern Pacific. It is not clear whether this is the model equivalent of the dipole mode. However, it is to be noted that this is the second mode resolved in the MSSA and its contribution to the seasonal anomalies is not negligible (Figure not shown).

It is widely known among the CFS users that the model has an apparent failure to capture the correct sign of the ENSO monsoon correlation in the interannual time scale. The relation between summer monsoon and the ENSO is often depicted as a lead lag correlation between the JJAS seasonal anomalies of the EIMR index and the monthly anomalies of the NINO3 index. (The NINO3 index is the SST anomalies averaged over the region 150°W - 90°W , 5°N - 5°S). Observational data show that the correlation between monsoon rainfall and NINO3 index stays close to zero during the months preceding the monsoon, but reaches a maximum of about -0.6 during the winter season following the monsoon season. A similar analysis performed on the CFST62 data produces an unrealistic curve that has positive correlations during and after the monsoon season (Figure 6(a)). The seemingly strange behavior of the RC2 discussed earlier prompted us to examine whether the RC2 offers any explanation for the lack of ENSO-monsoon teleconnection in the model.

Figure 6(b) shows the lead/lag correlation between the JJAS seasonal anomalies of EIMR index calculated from first two persistent modes (RCs 1 and 2) and the 100-day oscillatory mode (RC34) and monthly NINO3 index, all taken from the CFST62 run. The black line in Figure 6(b) represents the lead-lag correlation analysis performed for the total rainfall anomalies of CFST62 and is same as the black line in Figure 6(a). Although the total anomalies fail to capture the correct sign of the correlation, the MSSA mode RC1 captures the observed

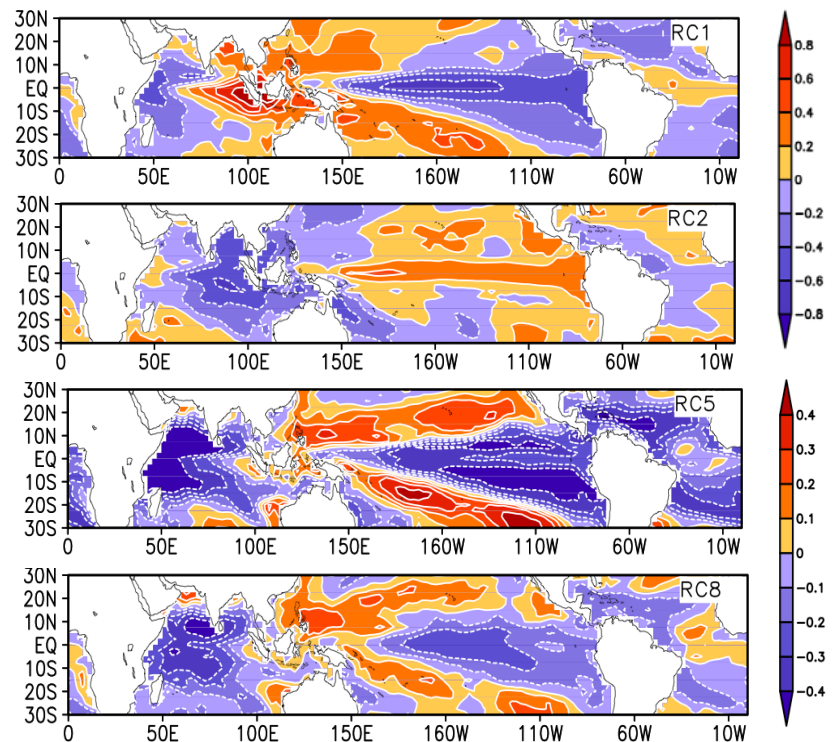


Figure 5 Daily point correlation between the EIMR index computed from RCs 1, 2, 5 and 8 and the daily anomalies of the SST using the CFST62 data. The top color bar applies to RC1 and RC2 and the bottom to RC5 and RC8.

ENSO-monsoon relationship. However RC2 and RC34 closely follow the total anomalies. From the above analysis, we would like to emphasize two points: Firstly, although not revealed in the conventional analysis, the CFS does contain a mode, which captures the correct ENSO-monsoon teleconnection in the interannual time scale. Secondly, the positive correlation between seasonal mean rainfall and monthly NINO3 anomalies in the CFS might be linked to other dominant modes such as RC2 and RC34 and their relationships with the SST.

5. Comparison with CFS T126

Two MSSA were performed on the CFST126 data, with lag windows 61 and 181 days, which isolated two summer intraseasonal modes with periods 30 and 100 days. The spatial structure of the oscillatory modes and their correlation with SST did not show any noticeable difference from those of the CFST62. The phase composites and the latitude-time and longitude-time cross sections for the oscillatory modes resembled well with those of the CFST62.

6. Comparison with GFS

The GFS produced two oscillatory modes with periods around 70 days and 30 days. The 70-day mode has clear northward propagation, but incoherent eastward propagation. The 30-day mode has northwestward propagation and is somewhat similar to its counterparts in the coupled models. One noticeable difference seen in the GFS is that none of its dominant persistent modes captured the correct ENSO mode i.e., a mode equivalent to the RC1 in CFST62. This emphasizes the importance of coupled processes in simulating the ENSO-monsoon correlation.

7. Summary

The dominant daily modes of the south Asian summer monsoon rainfall in the CFS are identified using the technique of the MSSA. The CFST62 has two dominant intraseasonal modes with periods 100 and 30 days. The 100-day mode has northeastward propagation and is similar to the 45-day mode found in observations. The 30-day mode propagates northwestward and can be considered the model equivalent of the 28-day mode seen in observations. Although the structure and behavior of the intraseasonal modes compare well with the observations, the dominant intraseasonal oscillation in CFS is considerably slower and extends well beyond the JJAS summer season. Out of the four persistent components analyzed, three of them are likely to be ENSO-related. The remaining persistent component shows strong links with the eastern Pacific SST, but has positive correlations over there. The impact of the horizontal resolution and the air sea coupling are examined briefly by performing the same analyses on a T126 version of the CFS and its atmospheric model (GFST62) respectively. While no noticeable differences were found between CFST62 and CFST126, the coupled models appear to have more realistic simulation of the oscillatory and persistent modes than the uncoupled one.

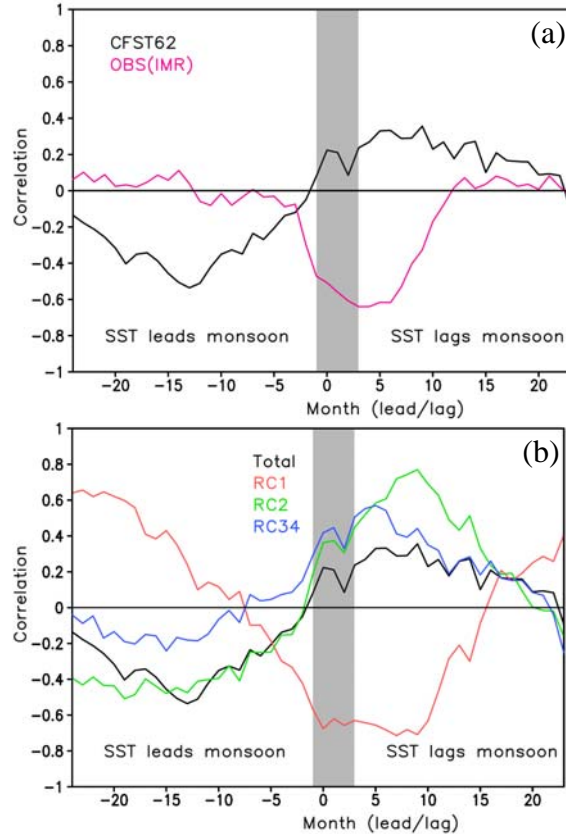


Figure 6 Lead/lag correlation between JJAS seasonal anomalies of the EIMR index and the monthly NINO3 values using the CFST62 data ((a) and (b); black curve). Pink curve in (a) shows similar analysis performed on the observational data (IMR index from CMAP precipitation and NINO3 from Reynolds SST). Similar analysis using RCs corresponding to first two persistent modes (RCs 1 and 2) and the 100-day oscillatory mode (RC34) from CFST62 run ((b); red, green and blue curves).

References

- Krishnamurthy, V., and J. Shukla 2007: Intraseasonal and seasonally persisting patterns of Indian monsoon rainfall. *J. Climate*, **20**, 3-20.
- Krishnamurthy, V., and J. Shukla, 2008: Seasonal persistence and propagation of intraseasonal patterns over the Indian monsoon region. *Clim. Dyn.*, **30**, 353-369.
- Krishnamurthy, V., and B. Kirtman, 2008: Relation between Indian monsoon variability and SST. *COLA Technical Reports*. 261.
- Pegion, K., and B. P. Kirtman, 2007: The Impact of Coupled Air-Sea Interactions on the simulation of Tropical Intraseasonal Variability. Submitted to *J. Climate*.
- Plaut, G., and R. Vautard, 1994: Spells of low frequency oscillations and weather regimes in the Northern Hemisphere. *J. Atmos. Sci.*, **51**, 210-236
- Saha, S. Nadiga, C. Thiaw, J. Wang, W. Wang, Q. Zhang, H. M. van den Dool, H.-L. Pan, S. Moorthi, D. Behringer, D. Stokes, M. Pena, S. Lord, G. White, W. Ebisuzaki, P. Peng, P. Xie, 2006: The NCEP Climate Forecast System. *J. Climate*, **19**, 3483 – 3517.

Summer Season Forecast Experiments with the NCEP Coupled Forecast System (CFS) Using Different Land Models and Different Initial Land States

Rongqian Yang, Ken Mitchell and Jesse Meng

Environmental Modeling Center, NOAA/National Weather Service

ABSTRACT

It is well known that in the N.H. summer season, the ENSO signal and influence across the continental U.S.(CONUS) is much weaker than in the winter season, hence seasonal predictions by coupled global climate models manifest significantly lower skill over CONUS in the summer than in the winter season. Research over the past decade has demonstrated that proper land state initialization (especially soil moisture) can be important to global model seasonal predictions for summer precipitation over CONUS. In this study, we use the state-of-the-art NCEP Coupled Forecast System (CFS) to examine the extent to which upgrades to the land model and land data assimilation component of the CFS can improve CFS summer season predictions over the CONUS.

The CFS, which is equipped with the modern Noah Land Surface Model (Noah LSM), is initialized with three different initial land states (GR2, GLDAS, and GLDAS climo), in comparison with a CFS control run using the older OSU Land Surface Model (OSU LSM) with the GR2 initial land state. (Herein, “GR2” denotes the NCEP-DOE Global Reanalysis 2, which utilizes the OSU LSM, and “GLDAS” denotes the Global Land Data Assimilation System, which utilizes the Noah LSM.) CFS seasonal forecast experiments have been carried out for 25 different summers (1980-2004), each with 10 CFS ensemble members, whose initial starting dates are from April 19 to May 3. We examined the impact of two different land surface models and three choices of different initial land states on seasonal precipitation, 2-meter air temperature, 200 mb and 500 mb heights, SSTs, and on land surface fields including latent heat and sensible heat fluxes, among others. (Due to limitation of length of this report, we only present CFS summer seasonal precipitation performance, including one special case – a strong Southwest U.S. monsoon in summer 1999.)

Results from the CFS experiments indicate that achieving improvement in CFS performance from a land model upgrade requires the execution of a companion global land data assimilation system (GLDAS) with the very same new land model as utilized in the land-component upgrade of the global climate model. Providing the land surface model with compatible and self-consistent land states is important to seasonal predictions. In contrast, improper initialization of the land surface model can degrade the global model performance, suggesting it is naive to merely upgrade the land component of a global climate model for seasonal forecasting without simultaneously upgrading the land component of the companion global data assimilation system.

1. Introduction

The research literature has rather firmly established that large-scale anomalies in the atmospheric general circulation on seasonally-averaged time scales are forced first and foremost by large-scale anomalies in SST (especially in the tropical Pacific Ocean). Additionally, research has strongly indicated that the next most important forcing (albeit secondary to SST) of such anomalies is large-scale anomalies in the land states of soil moisture, snowpack, and vegetation cover [Koster et al. 2004]. The linkage between land surface anomalies and the spawning of seasonal atmospheric circulation anomalies has been harder to confirm and quantify than that of SST. Being a secondary forcing source to that of SST anomalies, land-anomaly forcing is more difficult to

separate from the natural chaotic variability of seasonal circulations (i.e. land-anomaly impact has a smaller signal to noise ratio than SST impact). Therefore, harnessing the impact of land surface anomalies on seasonal prediction skill in operational practice, such as at NCEP, is a tremendous challenge that requires not only a large number of members in the ensemble set of seasonal predictions, but also special care in the treatment of land state initial conditions, especially root-zone soil moisture and seasonally persistent snow pack.

It is substantially more difficult to create global analyses of the initial land states from satellite and in situ observations than it is to apply satellite and in situ observations to create global analyses of initial SST state. For this reason, over the last three decades, global analyses of SST on say weekly intervals have been much more routinely available and sanctioned for use in global prediction models than the counterpart case for global soil moisture and snowpack analyses. During the past 8-10 years, a consensus is emerging [Dirmeyer et al. 1999; Mitchell et al. 2004; Rodell et al. 2004; Koster et al. 2004] that embraces the view that the best approach for providing global or continental-scale analyses of deep soil moisture and snowpack is to execute a continuously cycled, multi-year, global, uncoupled, temporal integration of a land surface model (LSM) forced by global analyses of observed atmospheric land surface forcing, especially global analyses of observed (non-model) precipitation and satellite observed (non-model) surface solar insolation. This approach is well illustrated in the Global Soil Wetness Project of the late 1990's [Dirmeyer et al. 1999]. Such approaches have become known as Land Data Assimilation Systems (LDAS), though many (not all) of these LDAS systems to date are so-called "open loop" systems that do not actually assimilate observations to directly update the land states, but rather let the LSM-simulated land states physically evolve freely in response to the external analyses of near-surface atmospheric forcing, especially precipitation analysis.

Additionally, it is now well established that the land surface model (LSM) component of any given global general circulation model (GCM) has its own inherent annual-cycle climatology of soil moisture (and snowpack at high latitudes) over each region of the global landmass. Moreover, this inherent LSM climatology can be quite different from one LSM to another [Dirmeyer et al. 2006; Koster and Milly 1997]. Therefore, the optimal land-state initial conditions for the LSM component of a given GCM should be generated by long-term multi-year (even multi-decade) executions of the given LSM in the LDAS mode described above. Long-term executions are essential to allow for the multi-year spin-up time scales of deep soil moisture.

The global Coupled Forecast System [Saha et al. 2006], or CFS, implemented by NCEP in 2004 represents NCEP's 2nd-generation seasonal forecast system, which is a global coupled atmosphere/ocean/land prediction system. Its development focused on upgrades to the ocean and atmospheric components and its Global Ocean Data Assimilation System (GODAS), but not land surface model upgrades. The currently operational CFS still executes the legacy Oregon State University (OSU) LSM (which is the old late 1980's ancestor of the Noah LSM) that was executed in NCEP's 1st generation seasonal forecast system.

There are two basic pathways for improving the representation of land surface processes in coupled global prediction models. One pathway is to advance the realism of the physical processes of the land surface component. A second pathway is to improve the specification of the initial conditions of the land states (e.g. soil moisture and snowpack) via global land data assimilation. In summary, the two pathways are:

- Improve and upgrade the physics of the LSM component of the GCM,
- Provide optimal initial conditions for the land states of the GCM's LSM component by executing the given LSM in global LDAS mode over multi-year periods.

To demonstrate the importance of each pathway, we proceed to improve the land representation in the global CFS along each of the two pathways. First off, we executed GLDAS to provide the CFS with optimal initial land states. Secondly, we employed the CFS to carry out a series of seasonal forecast experiments. The atmosphere component in these CFS experiments is taken from a recently operational version (August, 2007) of NCEP's global medium-range forecast system, known as the Global Forecast System (GFS) and the ocean model used in the CFS is GFDL MOM3. The CFS experiments are seasonal prediction experiments, in hindcast mode, described further next.

As described below, we set out to execute one set of seasonal prediction experiments for each of the two pathways above

1.1 Upgrade the LSM physics of the CFS

At NCEP, the Noah LSM was implemented in NCEP's operational GFS in late May 2005. Thus the Noah LSM is expected to be the land component of NCEP's next generation CFS for seasonal prediction. The current operational CFS at NCEP employs the OSU LSM, a respected but increasingly older and distance ancestor to the Noah LSM (see Table 1 for major differences between the two LSMs). The next generation CFS is anticipated to utilize the Noah LSM and execute at T126/L64 resolution. We employ the latter resolution in all CFS experiments here.

Noah LSM Features	OSU LSM Features
<ul style="list-style-type: none"> – 4 soil layers (10, 30, 60, 100 cm) – frozen soil physics included – surface fluxes weighted by snow cover fraction – improved seasonal cycle of vegetation cover – spatially varying root depth of 1-2 m – improved soil and snow thermal conductivity – higher canopy resistance – infiltration accounts for sub-grid variability in precipitation and soil moisture – More 	<ul style="list-style-type: none"> – 2 soil layers (10, 190 cm) – no frozen soil physics – fluxes not weighted by snow fraction – vegetation cover never less than 50% – spatially constant deep root depth of 2 m – poor soil and snow thermal conductivity – too low canopy resistance – infiltration does not account for sub-grid variability in precipitation and soil moisture

Table 1 Characteristics of Noah LSM versus OSU LSM

1.2 Provide optimal land state initial conditions

As a prerequisite to the T126 resolution CFS experiments to be carried out, a GLDAS was constructed and executed over the 28-year period of 1979-2006 using the Noah LSM as the land model and on exactly the same computational native grid as that of the T126 CFS. In so doing, we took care to use exactly the same terrain field and land mask as in the T126 CFS, as well as all the same specifications of land surface characteristics (soil class, vegetation class, etc), land physical parameters, and same version of the Noah LSM (2.7.1) as employed in the CFS/Noah experiments. This T126 GLDAS/Noah suite provided both the instantaneous and climatological GLDAS/Noah land states used in the CFS Cases C and D (see below about CFS Experimental Design).

The precipitation forcing for the GLDAS/Noah executions is CPC's CMAP pentad analysis of observed precipitation, partitioned to 6-hourly amounts using the global precipitation fields of the NCEP-DOE Global Reanalysis 2 (GR2). Aside from the precipitation forcing, all remaining land-surface forcings for the GLDAS/Noah executions are taken from the GR2. This surface forcing is adjusted for the terrain height differences between the T62 GR2 and the T126 CFS using adjustment algorithms that have been extensively and widely applied in EMC's longstanding N. American Land Data Assimilation System [Mitchell et al. 2004]. Additional details and background of the NCEP-NASA Global Land Data Assimilation System (GLDAS) is given in [Rodell et al. 2004].

Here are the steps we followed:

- Execute the collaborative NCEP-NASA, uncoupled, land-only, open loop Global Land Data Assimilation System (GLDAS) with the Noah LSM on the computational grid of the T126 CFS.
- Use these GLDAS-Noah land states to provide the optimum land-state initial conditions for the Noah LSM component of the CFS-Noah runs in the CFS experiment below.

- Characterize and depict the global distribution and magnitude of the differences between the Noah-LSM consistent land-state database of these GLDAS-Noah runs and the land states from the NCEP coupled atmosphere/land Global Reanalysis 2 (GR2), which employed the older OSU LSM.
- Characterize and depict the differences in terms of both the respective land-state climatology of each system (GLDAS versus GR2) and the interannual variability of anomalies of each with respect to their own climatology. The uncoupled NASA-NCEP Global Land Data Assimilation System (GLDAS) covers over a 25-year hindcast period (1979-2004) on the T126 Gaussian grid of the next generation CFS. The physics, parameters, and configuration of the Noah LSM in the GLDAS will exactly match that of the Noah LSM component of the CFS. Additionally, the GLDAS/Noah configuration and its forcing sources will be such that future real-time GLDAS executions are feasible for initializing operational CFS real-time forecasts.

1.3 CFS experimental design

To demonstrate whether the replacement of the OSU LSM with the Noah LSM yields meaningfully significant improvement in CFS seasonal prediction skill and test the impact of different initial land states on summer season prediction, the T126 CFS was executed and assessed using the following 4 configurations for each summer of 1980-2004, each with 10 members (for which the initial dates are April 19-23 and April 29-May 3, all at the initial time of 00Z). The time and dates of the initial conditions follow those used in NCEP's presently existing hindcast database of the presently operational T62 CFS/OSU).

- A - CFS/OSU/GR2: - OSU LSM, Land ICs from GR2 (CONTROL)
- B - CFS/Noah/GR2: - Noah LSM, Land ICs from GR2
- C - CFS/Noah/GLDAS: - Noah LSM, Land ICs from GLDAS/Noah
- D - CFS/Noah/GLDAS-Climo: - Noah LSM, Land ICs from GLDAS/Noah climatology

For our control case we execute the T126 CFS with the older OSU LSM used in the present operational CFS and initialized in the old manner from the land states of the NCEP-DOE Global Reanalysis 2 (denoted GR2), as done in the present operational CFS. In addition to the control, we execute three CFS experimental configurations, altogether giving the above four CFS configurations. We hereafter denote these four CFS configurations as Cases A-D. For all 4 cases, the atmospheric initial conditions are from GR2 and the ocean initial conditions are from NCEP's MOM3-based Global Ocean Data Assimilation (GODAS).

In Case B, we replace the old OSU LSM with the Noah LSM, but still use the old source of initial land states, which is the old Global Reanalysis 2 (GR2) that includes the older OSU LSM in its assimilating global background model. In Case C, we not only replace the OSU LSM with Noah, but we also replace GR2 with the Noah-based GLDAS as the source of initial land states. Finally, in Case D, we replace the instantaneous initial land-states from GLDAS/Noah with the 28-year daily climatology of the GLDAS/Noah land states.

Here GLDAS/Noah denotes a 28-year retrospective execution of the GLDAS (described above in Section 1.2) with the same Noah LSM as used in the CFS experiments, and on exactly the same T126 native computational grid as the CFS runs, with the same terrain field, land mask, and specification of land surface characteristics as used with the Noah LSM in the CFS.

Prior to launching the experiments, the working hypothesis was that Case C would yield the most skillful forecast, because Case C makes use of both a more modern LSM (Noah LSM) and the self-consistent initial land states of the Noah-based GLDAS. Case D sets out to examine the impact of using GLDAS/Noah soil moisture climatology rather than instantaneous soil moisture states. Case B intends to illustrate what degradation in CFS performance is realized if we had not developed the GLDAS suite and had to resort to using the land states of the NCEP-DOE Global Reanalysis 2 (GR2), which is based on the older OSU LSM. Finally Case A (control) represents the situation wherein we assume that neither the Noah LSM nor the GLDAS/Noah had been developed and applied to the CFS.

For each of the four cases above, we executed ten members of 6-month CFS forecasts for each summer during the 25-year period of 1980-2004. Hence the total number of 6-month CFS hindcasts we executed was 1000 ($4 \times 10 \times 25$), which represents a huge undertaking in managing model runs and output files. The 10 members differ in the start date of their initial conditions from late April and early May. The ten initial start

dates for each of the 25 summers are Apr 19-23, Apr 29-30, and May 1-3. Late-April/early-May initial conditions were chosen because in operational practice at NCEP, the operational CFS members from initial dates around late April represent the most important ensemble set of CFS runs used operationally by CPC in formulating the mainline CPC summer forecast, which is issued in mid-May.

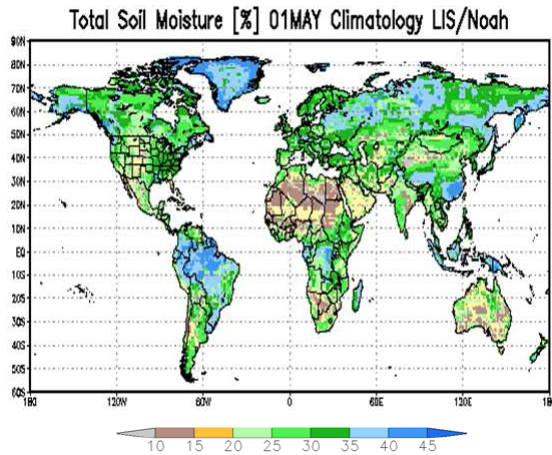


Figure 1 Climatology of total 2-m soil moisture (percent volumetric) of GLDAS/Noah on May 1.

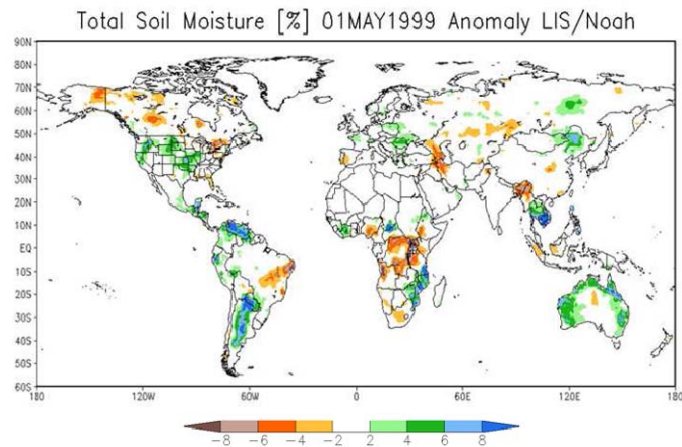


Figure 2 Anomaly of total 2-m soil moisture (percent volumetric) of GLDAS/Noah on May 1, 1999.

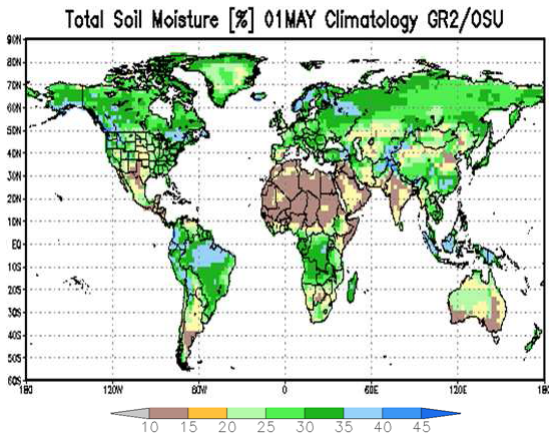


Figure 3 Climatology of total 2-m soil moisture (percent volumetric) of GR2/OSU on May 1.

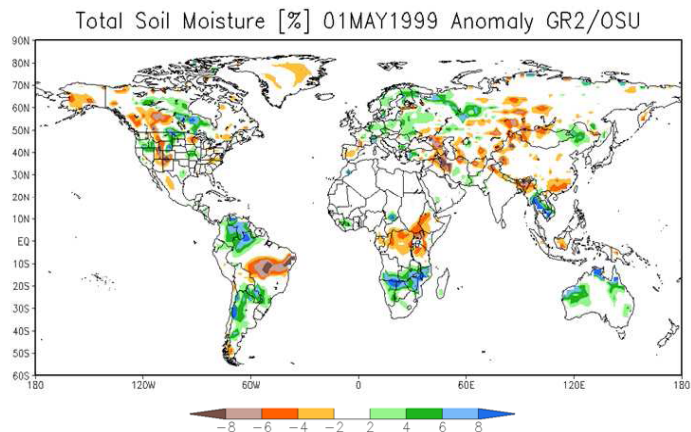


Figure 4 Anomaly of total 2-m soil moisture (percent volumetric) of GR2/OSU on May 1, 1999.

2. Results

2.1 The retrospective GLDAS for the CFS experiment and comparison with GR2

We first compare the land states of the 28-year retrospective T126 GLDAS/Noah, used in CFS cases C and D, with that of the NCEP/DOE Global Reanalysis 2 (GR2), used in CFS Cases A and B. The GR2 employed the older OSU LSM. Figure 1 and Figure 2, respectively, present global maps of the 01 May climatology and 01 May 1999 anomaly of the 2-meter soil moisture field from the GLDAS/Noah. Figures 3 and 4 are as in Figures 1 and 2, but from GR2/OSU. Figures 5-8 are as in Figures 1-4, but zoomed in over the CONUS domain. Both the GLDAS and GR2 simulate the soil moisture of a 2-meter soil column, albeit with four soil layers in GLDAS/Noah (0-10, 10-40, 40-100, 100-200 cm) and only two layers in GR2/OSU (0-10, 10-190 cm). We choose to depict 01 May conditions, as that time is within the 19 April - 03 May period from which the initial conditions are taken for the 10 members of the summer CFS hindcasts. Comparison between the two sources of

soil moisture shows that the climatological values in early May of the GR2/OSU soil moisture are pervasively lower than those of GLDAS/Noah over the vast majority of both the global and CONUS domains (some exceptions).

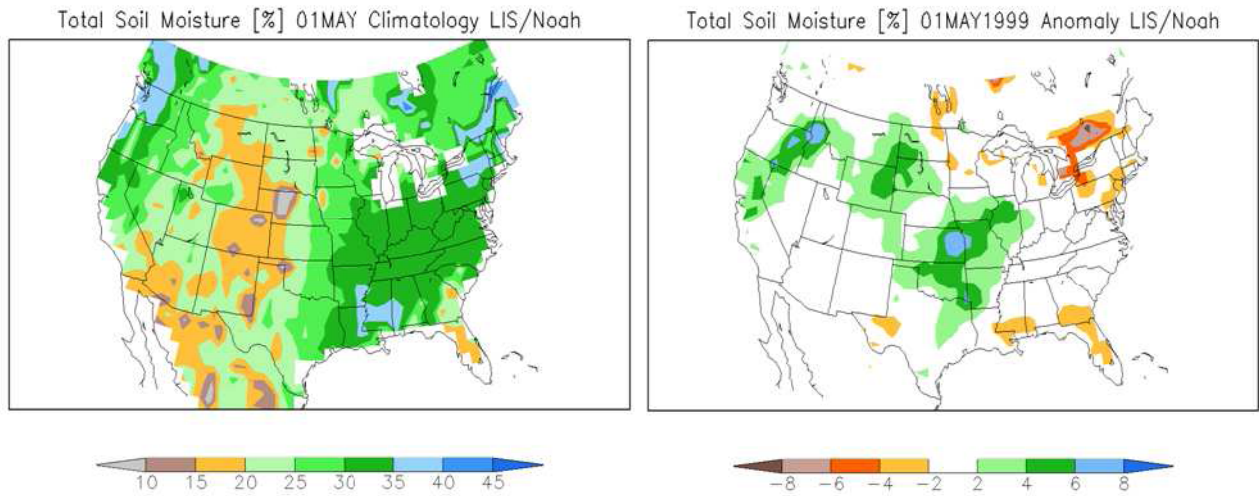


Figure 5 Climatology of total 2-m soil moisture (percent volumetric) over CONUS of GLDAS/Noah on May 1.

Figure 6 Anomaly of total 2-m soil moisture (percent volumetric) over CONUS of GLDAS/Noah on May 1, 1999.

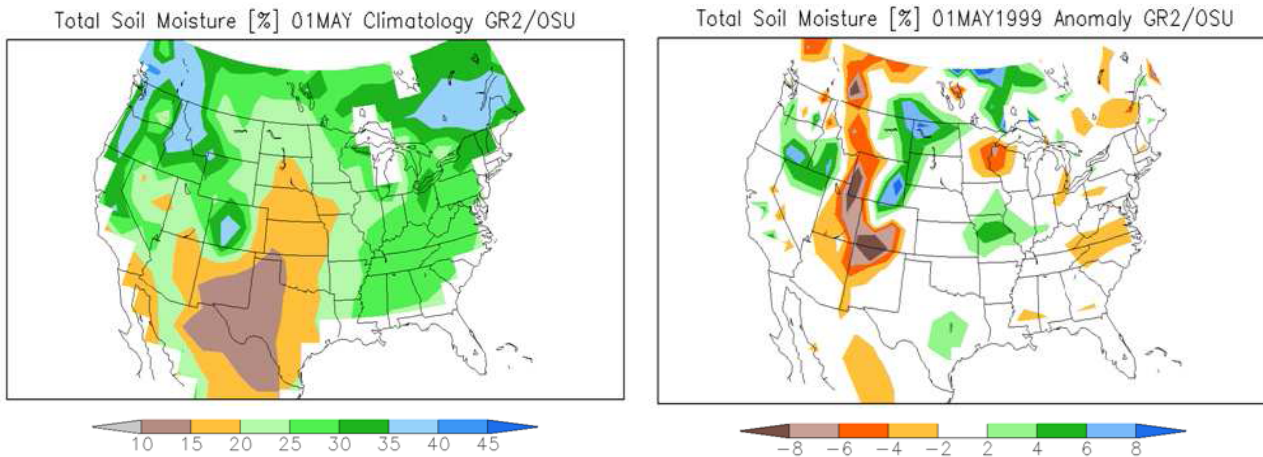


Figure 7 Climatology of total 2-m soil moisture (percent volumetric) over CONUS of GR2/OSU on May 1.

Figure 8 Anomaly of total 2-m soil moisture (percent volumetric) over CONUS of GR2/OSU on May 1, 1999.

The anomaly fields of GLDAS/Noah and GR2/OSU in Figures 2 and 4 show some similarities in some regions of the globe (S. America, Africa, Australia, Southeast Asia), but rather substantial differences over other regions (N. America and CONUS, southwest Asia, Europe). Focusing now on the latter substantial differences over CONUS, Figures 6 and 8 clearly reveal the large disagreement over CONUS between GLDAS/Noah and GR2/OSU soil moisture anomalies for the case of 01 May 1999. Figure 9 shows the observed precipitation anomaly for the 90-day period ending 30 April 99 (close in time to the 01 May 99 anomaly depicted in Figures 6 and 8). The GLDAS/Noah soil moisture anomaly in Figures 6 shows strikingly more spatial agreement with the observed precipitation anomaly than does GR2/OSU. This is because the GLDAS/Noah, unlike the GR2/OSU, uses an analysis of observed precipitation to force the land surface. To force its land surface, GR2/OSU uses the model precipitation from the background global model of the assimilation system. Over 5-day intervals, the GR2/OSU computes the errors in the model precipitation compared to the observed precipitation analysis (aside: the same precipitation analysis used directly by GLDAS above) and then subsequently applies a soil moisture

nudging scheme to try to offset the effects of the model’s precipitation errors, but Figures 5-8 strongly suggests that the GR2/OSU nudging scheme is not effective.

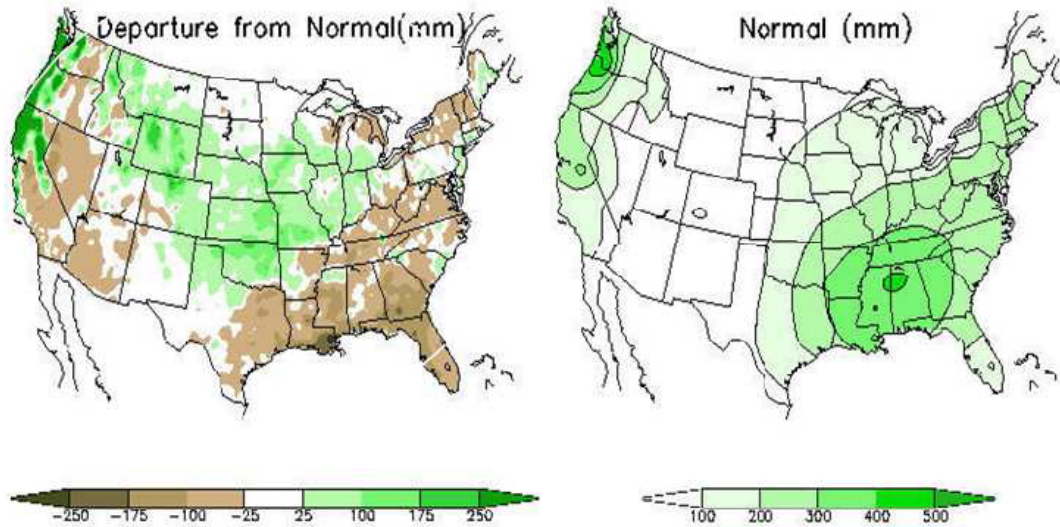


Figure 9 Observed 90-day of precipitation anomaly of 1999 (ended at April 30) (top) and climatology (bottom).

While Figures 1 to 8 are for a particular time of year, Figure 10 shows the multiyear time series and climatological annual cycle of monthly soil moisture (mm) from both the GLDAS/Noah and GR2/OSU for the 2-meter soil moisture (mm) spatially averaged over Illinois, plus the time series of the observed soil moisture derived from the Illinois network of soil moisture observations (Figure 9). Clearly in Figure 10, the soil moisture climatology of GR2/OSU remains consistently lower than that of GLDAS/Noah on a month-to-month basis year after year over the Illinois domain. Moreover in Figure 10, the higher GLDAS/Noah soil moisture is in closer agreement with the observations than that of GR2/OSU, though still exhibiting some low bias, but substantially less so than GR2/OSU.

One key implication to be drawn from Figure 10 and Figures 1 and 3 (climatology for 01 May from two sources of soil moisture) is that initializing the Noah LSM component of CFS from the notably drier states of the GR2/OSU soil moisture dataset will result in lower land surface evaporation in the CFS – a situation that is likely a significant contribution to the poor performance of the CFS/Noah/GR2 case (Case B) presented next in Section 2.2.

2.2 CFS experiments results

It is known that seasonal prediction climate models have substantial systematic error. To overcome systematic error and achieve useful prediction skill, seasonal predictions from climate models are depicted as predicted anomalies from the model’s own climatology. To derive the model climatology, it is necessary, as we do here, to execute a multi-decade ensemble-based reforecast of the climate model. Thus the first task after completing the 25-year summer-season reforecast set of 1000 members was to compute the CFS model climatology for each Case A-D.

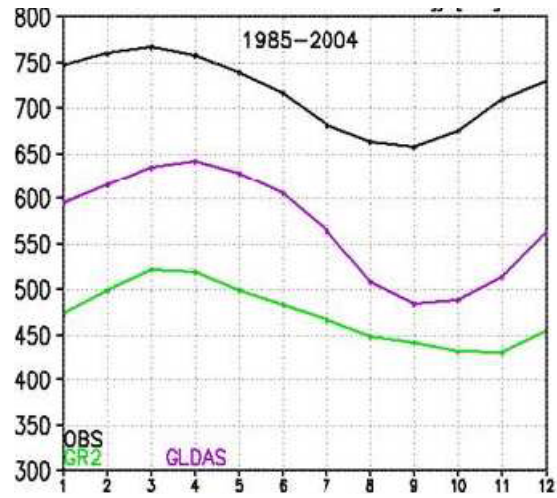


Figure 10 Climatology (1985-2004) of annual cycle of monthly 2-meter column soil moisture (mm) averaged over Illinois from GLDAS (purple), GR2 (green) and in situ observations (black).

The prior generation CFS manifested considerably useful skill in predicting tropical Pacific SST (ENSO anomalies), but showed virtually no skill for predicting anomalies

of summer precipitation total over CONUS. Therefore, we focus here on assessing Case A-D performance in predicting anomalies over CONUS of total 3-month precipitation for June-July-August (JJA). As our measure of CFS prediction skill for summer total precipitation, we will employ the primary CFS skill measure used by CPC, which is the anomaly correlation (AC) between CFS forecasts of precipitation anomalies and observed precipitation anomalies over the entire 25 years of the CFS reforecasts of Cases A-D. To defined the observed anomalies, we use the daily gauge-only 1/8th-deg CONUS precipitation analysis (with PRISM adjustment) produced by CPC for each day from 01 January 1979 to present. For application here, we spatially average this precipitation analysis to the T126 CFS grid (about 1-degree resolution) and compute the anomaly correlation (AC) score for precipitation on each CFS grid point over CONUS. This yields a CONUS map of AC score and this AC map is referred to as the CFS “skill mask”.

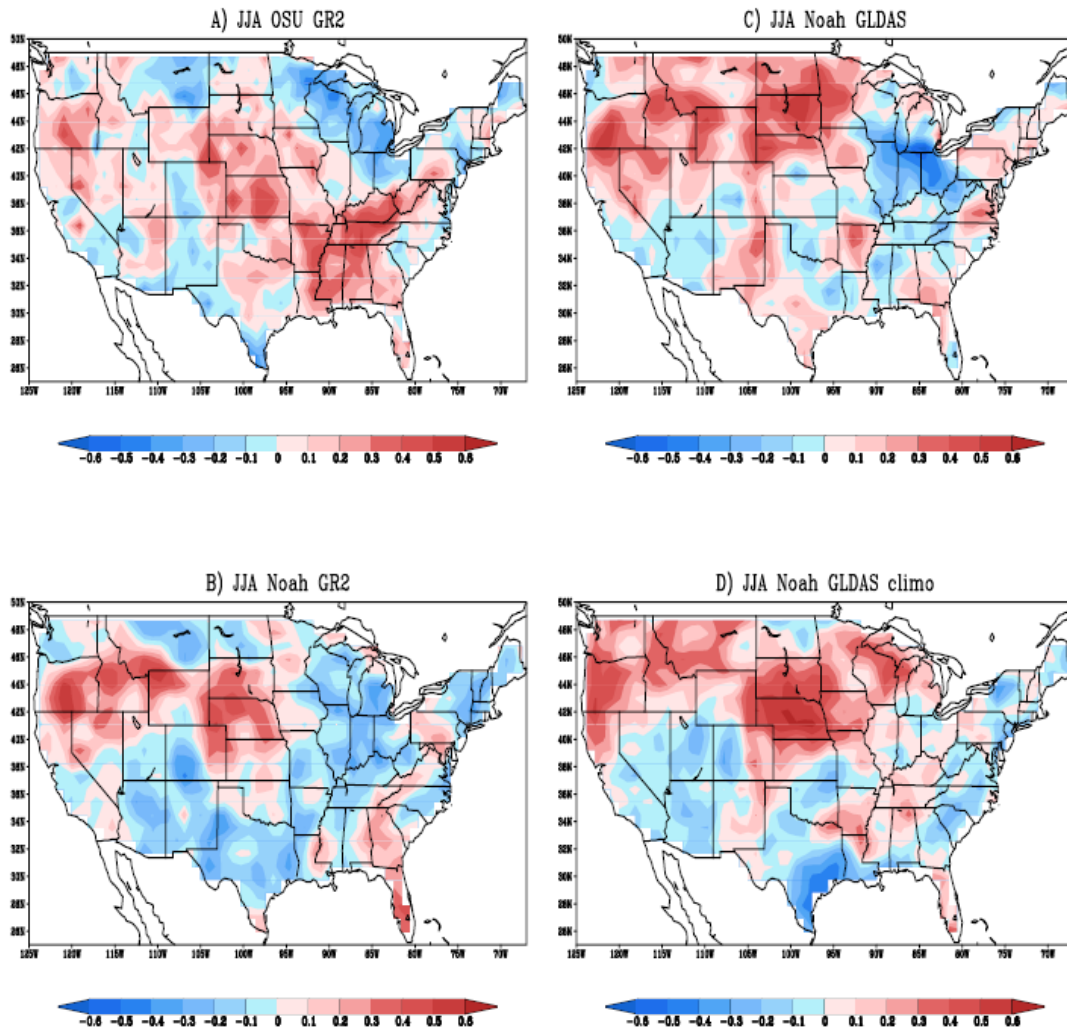
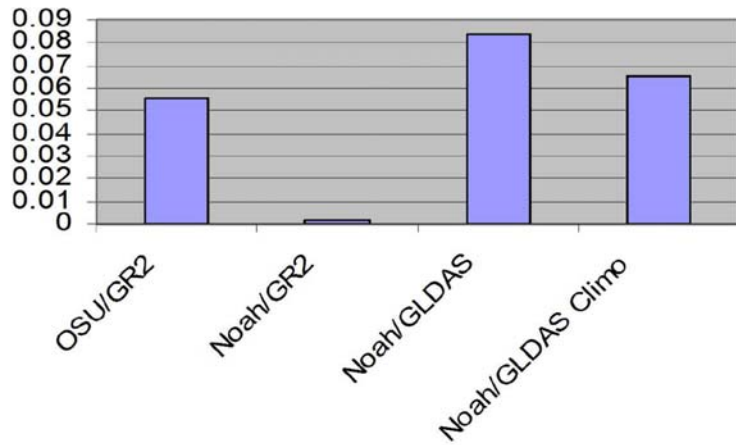


Figure 11 Anomaly correlation maps for 10-member ensemble mean seasonal forecasts of JJA precipitation from 25-year (1980-2004) reforecasts of four configurations of CFS using different land surface models and sources of initial land states. The ten members correspond to 10 different initial dates from 00Z of April 19-23 and April 30-May 3.



Here we present results from the extensive T126 CFS 25-year summer reforecast experiments of the four CFS configurations described above. The latter resolution of the new CFS is double the T62 resolution of the currently operational CFS. The CFS ocean model is the MOM-3 ocean model of GFDL. Specifically, the 10-member 6-month CFS reforecasts for each summer of the 25-year period of 1980-2004 were executed and assessed with four different land configurations (with and without the Noah LSM upgrade and with and without the Noah-based GLDAS) as described in Section 1.3. From the results of these experiments, we show below that the Noah LSM upgrade together with the Noah-based GLDAS improves the summer-season skill of CFS precipitation forecasts over the CONUS. The results illustrate that the Noah-based GLDAS is an important necessary component to realize the CFS

Figure 12 CONUS-wide spatial average anomaly correlation values from the four correlation maps presented in Figure 11.

forecast improvements from the Noah LSM upgrade.

The four panels of Figure 11 show the CONUS skill mask of AC score for JJA precipitation for each of the four CFS Cases A-D, as derived from the entire 25-year reforecast. The bar chart in Figure 12 shows the CONUS spatially averaged AC score. Figure 12 shows that Case C with both the Noah LSM upgrade and inclusion of the GLDAS/Noah does indeed yield the highest average AC score. Interestingly, Case D, which initializes the CFS Noah land states with the 25-year daily climatology of the 28-year GLDAS/Noah yields an AC score only modestly lower than that of Case C. Strikingly, and with far-reaching implications, Case B yields the lowest AC score by far (essentially zero). This result demonstrates that the real prediction benefit of upgrading the land model in a global model may likely not be realized if the global model is not provided with initial land states that are self-consistent with the inherent climatology and physics of the new land model. This strongly suggests that the global data assimilation system that is providing the initial land states for the global forecast model should be executing the same land model and same land surface characteristics and parameters as the global forecast model.

The spatial character of the AC skill masks of the four panels of Figure 11 are also very revealing. Case B is obviously far inferior to the other three cases. Also, each case yields different preferred regions for higher AC score, with Cases B-C showing a tendency to yield higher scores in the north central and northwest CONUS while Case A shows a different tendency toward higher scores in the south central and

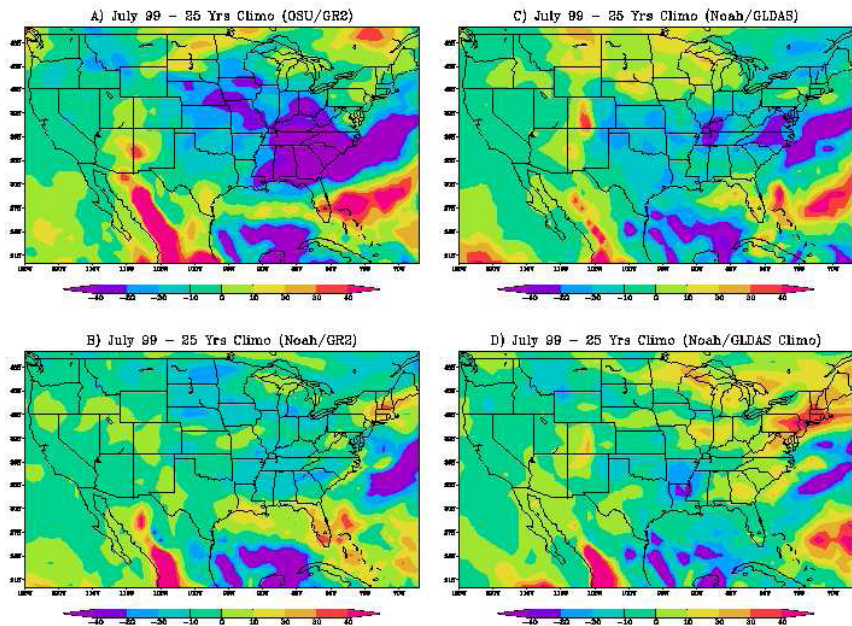


Figure 13 Ensemble mean CFS predicted precipitation anomaly (mm) for July 1999 from 10 CFS members of late April and early May initial conditions, using four different cases in CFS of choice of LSM and source of initial land states. The CFS anomalies are with respect to corresponding 25-year (1980-2004) reforecast climatology of each given CFS configuration.

southeast CONUS. For Cases A and C only, an additional 5 members (15 members total) were executed and no appreciable difference in the spatial patterns of Figure 11 for those two cases was evident (not shown).

We emphasize that even though Case C yields the highest AC score in Figure 12, even its value is distressingly low – of order 0.084 and hence not even reaching 0.1. Figure 11 reveals that even in the regions of positive AC values, the values usually do not exceed 0.4. Furthermore, even consistently predicting the correct sign of the anomaly over the entire CONUS remains illusive. Hence the seasonal prediction skill of summer precipitation over CONUS is still a major challenge, needing still much more effort (likely in CFS physics unrelated to the land surface).

We next turn in Figure 13 to examine the results for one specific summer, namely 1999, to gain more insight into the different performance of the four cases. The summer of 1999 was suggested for our examination by CPC. The precipitation observations (Figure 14) indicate that the southwest U.S. monsoon was strong that year, with July precipitation well above normal in Arizona and western New Mexico. Additionally, the northern Midwest experienced well above normal July precipitation, while the lower Mississippi River basin experienced substantially below normal precipitation.

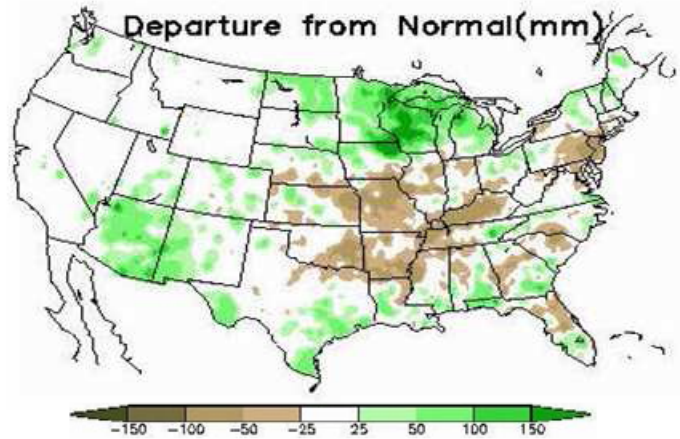


Figure 14 Observed precipitation anomaly of July 1999.

The four panels of Figure 13 show the CFS predicted precipitation anomaly of July 1999 for each Case A-D (wherein the anomaly depicted for each case is derived with respect to the CFS climatology of that case). Hence we are essentially looking for which CFS configurations can reproduce even the correct SIGN and SIGNGRADIENT of the observed precipitation anomaly. Thus, with respect to the sign of the anomaly, Figure 13 reveals that Case C (CFS with Noah LSM and GLDAS/Noah initial land states) indeed had the most consistently good performance among all four configurations.

Once again, Figure 13 shows how poorly Case B performed. This is the configuration where the CFS/Noah model configuration used GR2 initial land states. As indicated in Figures 1-8, the differences between the GR2/OSU and GLDAS/Noah initial land states indicates that both their climatology and spatial anomalies of soil moisture are quite different, with GLDAS/Noah having higher soil moisture values in the warm season over most non-arid regions worldwide, than that of GR2 with the OSU LSM from GR2.

Also noteworthy from Figure 13 is the degradation in Case D versus Case C, hence for July 1999 the CFS/Noah performance is worse if the climatology of GLDAS/Noah is used for initial land states in place of the instantaneous states of GLDAS/Noah.

Finally from Figure 13, the control Case A (with older OSU LSM and GR2 as source of initial land states) appears to yield somewhat better anomaly pattern in the southwest monsoon region, but clearly performs worse than Case C for the spatially large anomalies of the northern Midwest and lower Mississippi Valley.

3. Conclusions

The CFS experiments presented here demonstrate the positive impact from use of the Noah LSM and the GLDAS. Here are the main conclusions from these experiments.

- CFS prediction skill for CONUS summer season precipitation is marginally improved by the upgrade from OSU LSM to Noah LSM, provided that Noah-compatible initial land states are provided with properly spun-up land initial conditions (such as via a GLDAS executing the same Noah LSM).

- Even with improved prediction skill from combination of LSM upgrade and compatible GLDAS-generated initial conditions, the CONUS-average summer season prediction skill for precipitation remains low.
- A disturbingly inaccurate picture of the impact of an LSM upgrade can be obtained by not providing initial land states compatible with the new LSM.
- The climate model prediction skill was actually degraded by the new LSM if self-consistent initial land states were not provided.
- The use of initial soil moisture states with instantaneous soil moisture anomalies did not appear to provide a clear-cut advantage over climatological soil moisture states, provided the soil moisture climatology was produced by the same land model being tested in global forecast model.

4. Future works

We will execute and assess the corresponding winter season reforecasts of the new CFS over the same 25 years. To save computational resources, we will assess only Cases A and C.

For both the summer and winter reforecasts, we will expand our assessment of the CFS hindcasts experiments to include Asia, Europe and South America, plus assess other fields besides precipitation, such as near surface air temperature, large-scale height and circulation fields, and low-level jets. In particular, we will add assessment of the SST anomaly fields predicted by the four CFS cases to determine to what degree the changes in the land treatment effected the larger-scale global circulation patterns and hence the coupled SST prediction. A recent study [Schubert et al. 2004] has firmly established the important role of Pacific and Atlantic SST anomalies as substantial causes of significant warm-season drought over the CONUS. Additionally, we will focus on the CFS predictions of the 1988 major summer drought event and the 1993 major summer flood event, as well as the additional strong southwest U.S. monsoon event of summer of 1990.

Very importantly, we will enlist the CFS Assessment Team of the NOAA-NCEP Climate Test Bed to carry out their own independent evaluations of our CFS experiments.

Lastly, we will execute CFS impact tests for future Noah LSM upgrades not yet embodied in the Noah LSM version used in the CFS experiments here. Two anticipated Noah upgrades are a dynamic vegetation treatment and a multi-layer snowpack treatment. Noah currently employs a single bulk-layer treatment of the snowpack. Such CFS impact tests will require re-execution of the retrospective GLDAS/Noah in order to include the same Noah upgrades in GLDAS.

Acknowledgements. We would like to thank S. Saha, S. Moorthi, W. Wang, C. Thiaw and H. Wei for their helps during these experiments.

References

- Dirmeyer, A. P., Dolman, A., and Sato, N. 1999. The Global Soil Wetness Project: A Pilot Project for Global Surface Modeling and Validation. *Bull. Amer. Meteor. Soc.*, **80**, 851–878.
- Dirmeyer, A. P., Gao, X., Zhao, M., Guo, Z., Oki, T., and Hanasaki, N. 2006. GSWP-2: Multimodel Analysis and Implications for Our Perception of the Land Surface. *Bull. Amer. Meteor. Soc.*, **87**, 1381–1397.
- Koster, R., Dirmeyer, P. A., Guo, Z., Bonan, G., Chan, E., Cox, P., Gordon, C. T., Kanae, S., Kowalczyk, E., Lawrence, D., Liu, P., Lu, C.-H., Malyshev, S., McAvaney, B., Mitchell, K., Mocko, D., Oki, T., Oleson, K., Pitman, A., Sud, Y. C., Taylor, C. M., Verseghy, D., Vasic, R., Xue, Y., and Yamada, T. 2004. Regions of Strong Coupling between Soil Moisture and Precipitation. *Science*, **305**, 1138–1140.
- Koster, R. and Milly, C. 1997. The Interplay Between Transpiration and Runoff Formulations in Land Surface Schemes Used with Atmospheric Models. *J. Climate*, **10(7)**, 1578–1591.
- Mitchell, K., Lohmann, D., Houser, P. R., Wood, E. F., Schaake, J. C., Robock, A., Cosgrove, B. A., Sheffield, J., Duan, Q., Luo, L., Higgins, R. W., Pinker, R. T., Tarpley, J. D., Lettenmaier, D. P., Marshall, C. H., Entin, J. K., Pan, M., Shi, W., Koren, V., Meng, J., Ramsay, B. H., and Bailey, A. A. 2004. The Multi-institution North American Land Data Assimilation System (NLDAS): Utilizing Multiple GCIP Products

-
- and Partners in a Continental Distributed Hydrological Modeling System. *J. Geophys. Res.*, **109**, D07S90, DOI:10.1029/2003JD003823.
- Rodell, M., Houser, P. R., Jambor, U., Gottschalck, J., Mitchell, K., Meng, C.-J., Arsenault, K., Cosgrove, B., Radakovich, J., Bosilovich, M., Entin, J. K., Walker, J. P., Lohmann, D., , and Toll, D. 2004. The Global Land Data Assimilation System. *Bull. Amer. Meteor. Soc.*, **85**(3), 381–394.
- Saha, S., Nadiga, S., Thiaw, C., Wang, J., Wang, W., Zhang, Q., van den Dool, H. M., Pan, H.-L., Moorthi, S., Behringer, D., Stokes, D., Pena, M., Lord, S., White, G., Ebisuzaki, W., Peng, P., and Xie, P. 2006. The NCEP Climate Forecast System. *J. Climate*, **19**, 3483–3517.
- Schubert, S., Suarez, M., Pegion, P., Koster, R., and Bacmeister, J. 2004. Causes of Long-Term Drought in the U.S. Great Plains. *J. Climate*, **17**, 485–503.

Sensitivity of CFS Mean State and ENSO Variability to Changes in SST Bias

Julia V. Manganello^{1,*} and Bohua Huang^{1,2}

¹ Center for Ocean-Land-Atmosphere Studies, Calverton MD

² Climate Dynamics Department, College of Science
George Mason University, Fairfax, VA

1. Introduction

Tropical biases, including the Southeast Pacific (SEP) warm SST bias, have persisted in coupled general circulation models (CGCMs) for quite some time. It is generally believed that this tropical warm bias is a major factor that limits the interannual variability and predictability in current CGCMs (Li and Hogan 1999, Wittenberg et al. 2006, Manganello and Huang 2008). Therefore, it is important to understand its specific effects in the coupled systems.

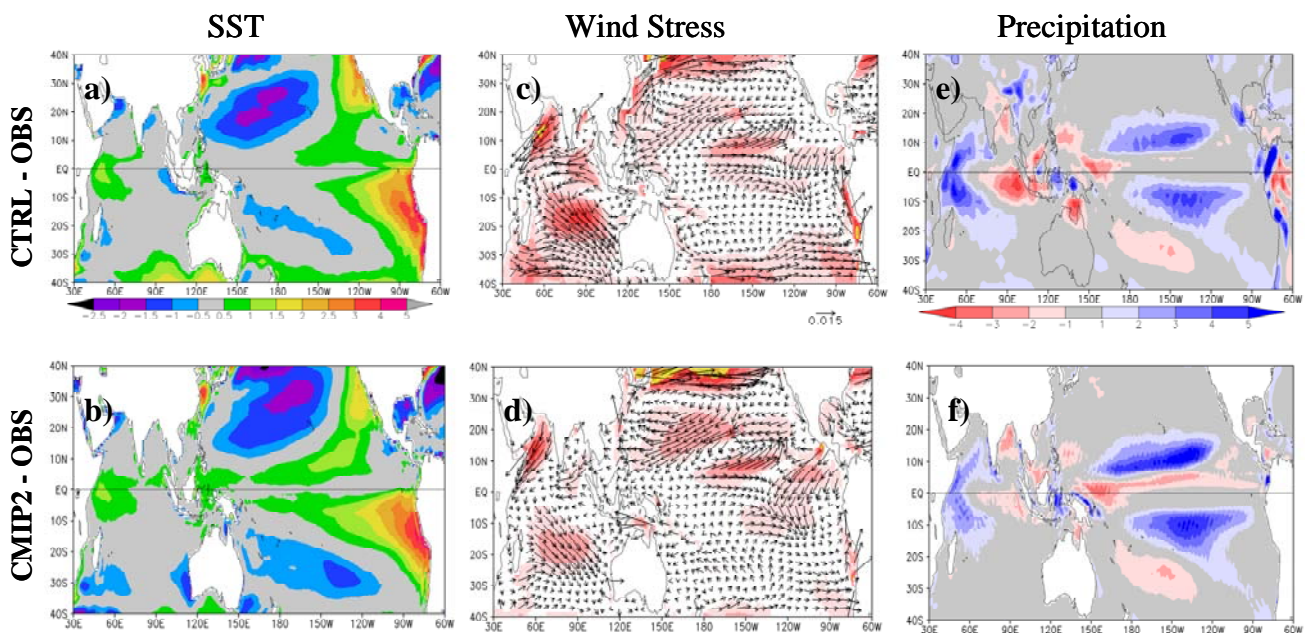


Figure 1 *Left Panel:* annual mean SST errors from the (a) fully coupled integration with CFS03 at T62L64 (CTRL) and (b) CMIP2 simulation relative to CPC SST data for 1950-2001. Units are °C. *Middle Panel:* annual mean surface wind stress errors from the (c) CTRL and (d) CMIP2 relative to ERS-1 data for 1991-2000. The arrow is 0.015 N/m², representing the unit vector. Shading indicates large magnitudes of error vector. *Right Panel:* annual mean precipitation error from the (e) CTRL and (f) CMIP2 relative to CMAP data for 1979-2005. Units are mm/day.

In the NCEP Climate Forecast System (CFS; Saha et al. 2006), SEP SST error reaches about 2-3°C (Fig. 1a) and is one of the largest in the Tropics. Associated with this error, surface wind stress shows an erroneous convergence over the region. Near the coast, the warm SST bias persists against the cooling effects of intensive evaporation and coastal upwelling induced by the overly strong alongshore southerlies (Fig. 1c). A wet bias in the SEP is consistent with the above-mentioned SST and wind stress errors (Fig. 1e). In general, CFS shows a double-ITCZ signature, where excessive precipitation is observed both north and south of the equator throughout the central and eastern Pacific. In the Indian Ocean the center of precipitation is shifted westward away from the Sumatra coast. Correspondingly, the Indian Ocean equatorial winds are too easterly while the off-

*Correspondence to: Julia V. Manganello, Center for Ocean-Land-Atmosphere Studies, 4041 Powder Mill Road, Suite 302, Calverton, MD 20705; E-mail: julia@cola.iges.org

equatorial southeasterly trade winds are too weak. In the CMIP2 integration with a new version of CFS at T126L64, Indian Ocean errors are reduced but the tropical Pacific biases are still present and are of the same magnitude, if not larger, with the exception of the coastal wind errors off South America (Figs. 1b, d and f). It further confirms that the coastal wind bias in CFS is an independent problem from the SEP SST bias because the latter persists without the coastal wind bias.

In this study, we present results from a set of heat and momentum flux correction experiments (HFC and MFC hereafter) that were designed to empirically reduce tropical SST biases in CFS. In the HFC experiment, heat flux correction term that was added to the surface heat flux into the ocean was set to vary spatially but remain constant in time. Its magnitude was proportional to the annual mean local SST error from the 52-year long fully coupled CFS integration (CTRL). Proportionality factor was set everywhere to $-15 \text{ W/m}^2/\text{K}$. Furthermore, heat flux correction was restricted only to the SEP and the Southeast Atlantic where SST errors were larger than 1.5°C . In the MFC experiment, momentum flux correction term was set to be equal to the annual mean CFS surface wind stress errors with respect to the remotely sensed scatterometer ERS-1 wind stress for the period of 1991-2001, taken with a negative sign. The correction was restricted to 30°S - 30°N , tapering off to zero at 40°S and 40°N . In both HFC and MFC experiments, CFS was integrated for 115 years starting from January 1, 1985 initial conditions with their corresponding corrections. Outputs from the last 100 years of each run were used for the analysis.

2. Mean climate in the tropical Pacific

HFC is found to be successful in reducing SEP SST bias and the associated precipitation bias, practically eliminating CFS precipitation errors in the South Pacific east of the dateline (Figs. 2a and 2c). However, these changes produce new errors in the model: cold SST bias at the equator and in the central South Pacific (Fig. 2a); stronger equatorial easterlies and southeasterlies compared to observations and further weakening of northeasterlies in the eastern Pacific with respect to the CTRL (Figs. 1c and 2b); as well as larger wet bias over the ITCZ compared to the CTRL (Figs. 1e and 2c).

According to the heat budget analysis, the cold SST errors south of the equator are a remote response to the heat flux correction and are due to cooling by anomalous Ekman transport in response to surface wind stress changes. On the other hand, the amplification of the wet bias in the ITCZ is likely due to increased divergence out of the SEP in the lower troposphere and the subsequent enhancement of moisture flux convergence over the ITCZ. To some extent, this response is expected as warm SST bias is reduced, which leads to reduction in convection and increase in sea level pressure (SLP), as well as the northward cross-equatorial flow. Since the precipitation in the northern branch of the double ITCZ is already excessive in CFS, the increased convergence inevitably amplifies this bias. The presence of overly active ITCZ could be traced to Global Forecast System (GFS), which is the atmospheric component of CFS. In fact, the wet ITCZ bias in the HFC is similar in magnitude to the corresponding bias in the AMIP-type simulation with GFS (not

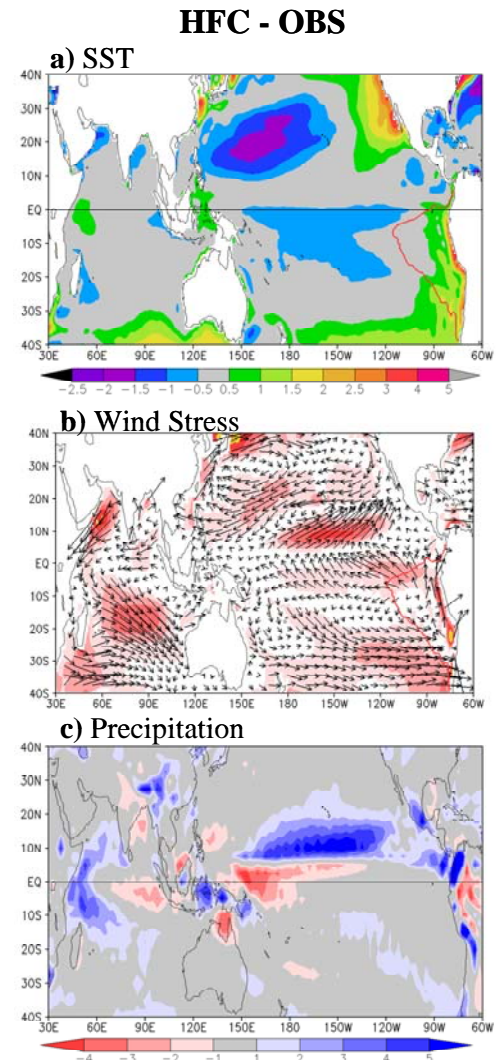


Figure 2 Annual mean errors of (a) SST, (b) surface wind stress and (c) precipitation from the HFC relative to CPC SST data for 1950-2001, ERS-1 data for 1991-2000 and CMAP data for 1979-2005 respectively. Units are $^\circ\text{C}$ and red contour shows the extent of heat flux correction in (a). In (b) the arrow is 0.015 N/m^2 , representing the unit vector. Shading indicates large magnitudes of error vector. Units are mm/day in (c).

shown). Weakening of the northeasterly surface wind stress in the eastern Pacific is directly linked to these ITCZ errors.

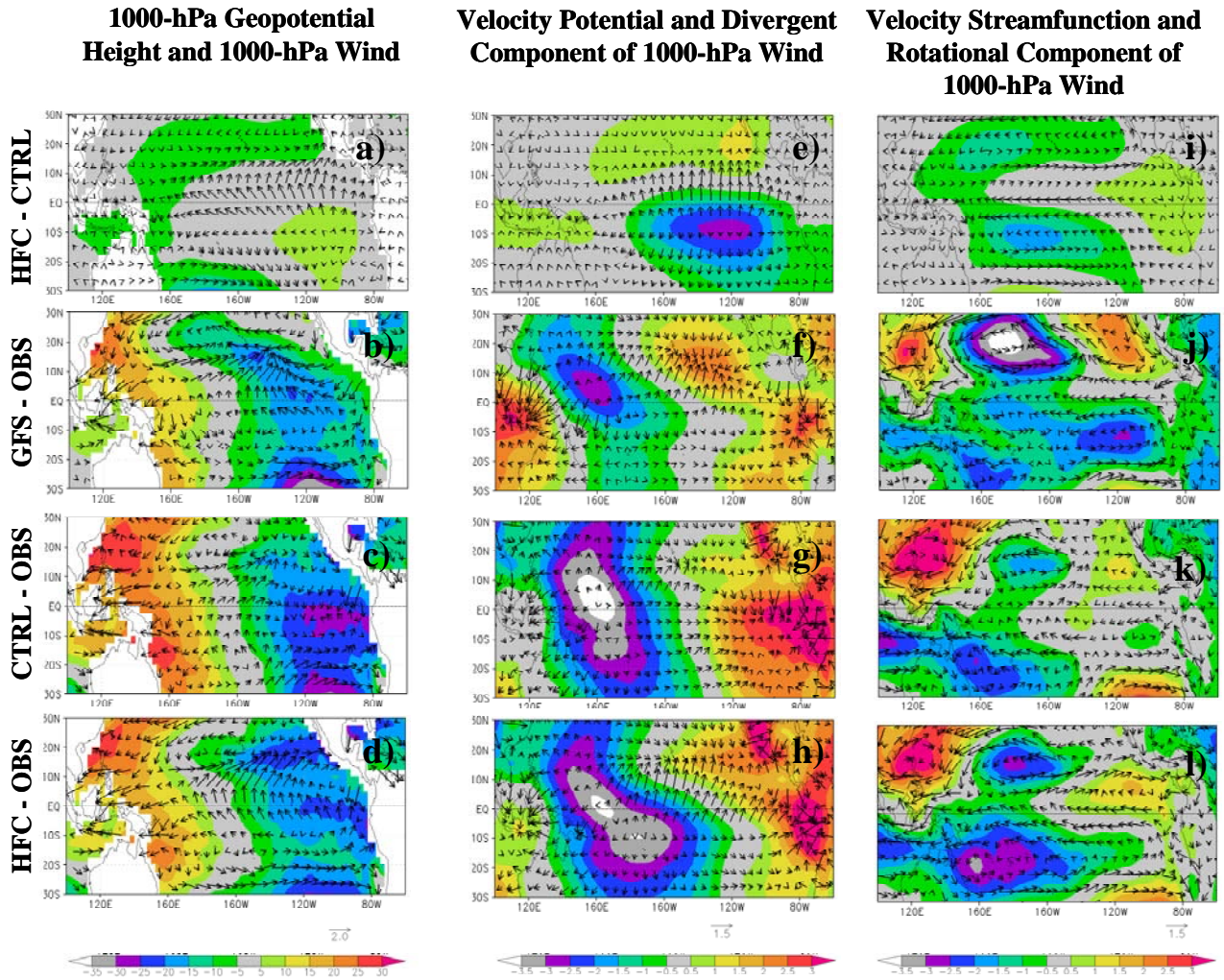


Figure 3 *Left Panel:* 1000-hPa geopotential height and 1000-hPa wind (a) response to the HFC; bias in the (b) GFS AMIP run, 1961-2002, (c) CTRL and (d) HFC relative to the NCEP/DOE Reanalysis-2 (R2). *Middle Panel:* velocity potential and divergent component of the 1000-hPa wind (e) response to the HFC; bias in the (f) GFS AMIP run, 1961-2002, (g) CTRL and (h) HFC relative to the R2. *Right Panel:* velocity streamfunction and rotational component of the 1000-hPa wind (i) response to the HFC; bias in the (j) GFS AMIP run, 1961-2002, (k) CTRL and (l) HFC relative to the R2. Units are m, m/s and 10^6 m²/s. The unit vectors are 2.0, 1.5 and 1.5 m/s respectively.

It is critical to understand the origin of the easterly wind bias at the equator in the HFC since the related cold SST bias could adversely affect El Niño-Southern Oscillation (ENSO) feedbacks by shifting the precipitation and wind stress anomalies westward, which could also change some properties of ENSO (e.g. Kirtman 1997, An and Wang 2000, Wittenberg et al. 2006). For this purpose, we decompose the summer-average (JJA) 1000-hPa wind response to the heat flux correction and the respective model bias into the divergent and rotational components (Fig. 3). (Analysis of the winter means leads to similar conclusions). First of all, equatorial easterly wind bias is already present in the GFS AMIP-type simulation and is due to rotational wind errors as a result of a large-scale too strong anti-cyclonic circulation present in the Southern Hemisphere Tropics (Figs. 3b, f and j). In the coupled mode (CTRL), the equatorial easterly wind is reduced. In fact, the equatorial wind bias becomes weakly westerly mostly as a result of additional convergence over the SEP because of low SLP bias there (associated with the warm SSTs), as rotational wind errors are weakened (Figs. 3e, g and k). Therefore, the

presence of the warm bias cancels out some of the model errors associated with an overly strong model ITCZ. In HFC, however, reduced SEP SST bias again increases regional SLP and the southeast trades. This change reinforces the anti-cyclonic circulation in the south Pacific and re-creates easterly wind bias at the equator to the level largely similar to the GFS AMIP run (Figs. 3d, h and l). (Divergent wind errors in the HFC actually lead to weaker equatorial easterlies (Fig. 3h)). The similarity between GFS AMIP and HFC experiments is rather astonishing. We therefore conclude that reducing SEP SST bias in CFS could expose and amplify other systematic errors that originate from the atmospheric component of CFS and appear to be related to an overly active ITCZ.

3. Mean climate in the Indian Ocean

The largest benefit of the MFC for the mean climate is found in the Indian Ocean. Since the overly strong alongshore winds off the Peru coast tend to cool the ocean down, reducing large southerly bias of alongshore winds in the SEP amplifies the existing warm SST bias by about 1.5°C near the coast and 0.5°C in the tropical Pacific.

The most significant effect of the momentum flux correction in the Indian Ocean amounts to reducing equatorial and coastal upwelling and improving upper ocean temperature distribution at the equator. As a result, the dipole errors in the SST and precipitation in the Indian Ocean (Figs. 1a and e) become much smaller (not shown).

4. El Niño-Southern Oscillation

ENSO in CFS is found to exhibit a high degree of sensitivity to the mean state changes imposed by heat and momentum flux corrections. In HFC, the variance of interannual SST anomalies (SSTA) in the equatorial Pacific is considerably reduced (Fig. 4c) and is barely statistically significant over the Niño-3.4 region (Fig. 5a). On the other hand, in the MFC SSTA variance is generally more in line with the observations compared to the CTRL (Fig. 4d). Besides weaker amplitude, ENSO is much less regular in this experiment (Fig. 5a). In addition, the duration of warm ENSO events is more realistic in both experiments, but more so in the MFC (Fig. 5b). It is found that the equatorial thermocline in the HFC is substantially deeper and more diffuse compared both to the CTRL and MFC, which could partly explain the loss of ENSO strength in this simulation (Meehl et al. 2001).

Zonal wind stress and precipitation responses to the Niño-3 SSTA also show certain differences. Although regression patterns in the HFC exhibit the highest degree of zonal asymmetry including the easterly wind response in the eastern equatorial Pacific (Figs. 6c and g), the bulk of the response is shifted to the west of the dateline likely due to the equatorial cold SST bias, where it is slightly east of the dateline in the observations (Figs. 6a and e). This change could in turn shift the subsurface response westward away from the region of strong air-sea coupling. Regression of subsurface temperature onto the Niño-3 Index (not shown) indicates that indeed in the eastern equatorial Pacific subsurface temperature variability is much weaker in the HFC compared to other simulations. The center of variability is located further westward, and the mixing appears to occur more along the isopycnals, rather than across them, and deeper than in the CTRL and MFC. Notable difference in the regression patterns of zonal wind stress in the MFC vs. CTRL is significant reduction of anomalous easterlies to the west of 160°E north of the equator (Figs. 6f and h). This change could be responsible for the increase in ENSO irregularity in the MFC according to Wang et al. (2005)

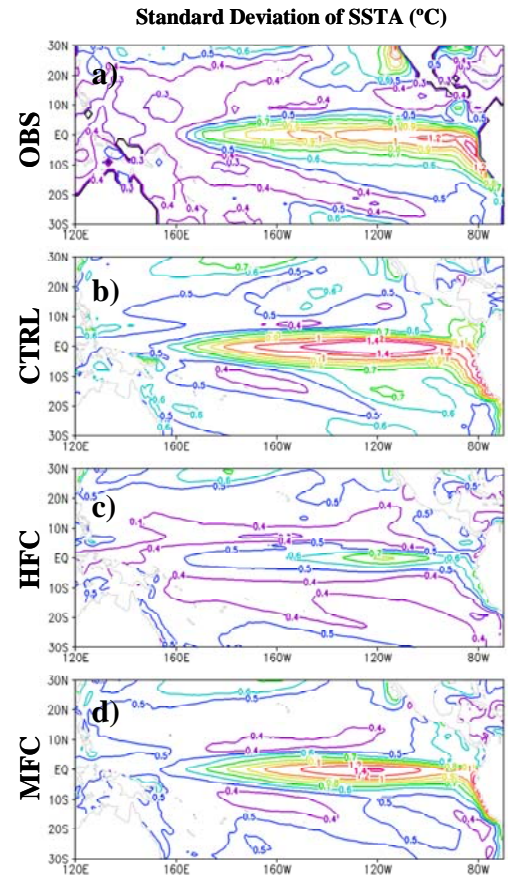


Figure 4 Standard deviation of the interannual SSTA from (a) CPC SST data for 1950-2001, the (b) CTRL, (c) HFC and (d) MFC experiments. Units are $^{\circ}\text{C}$.

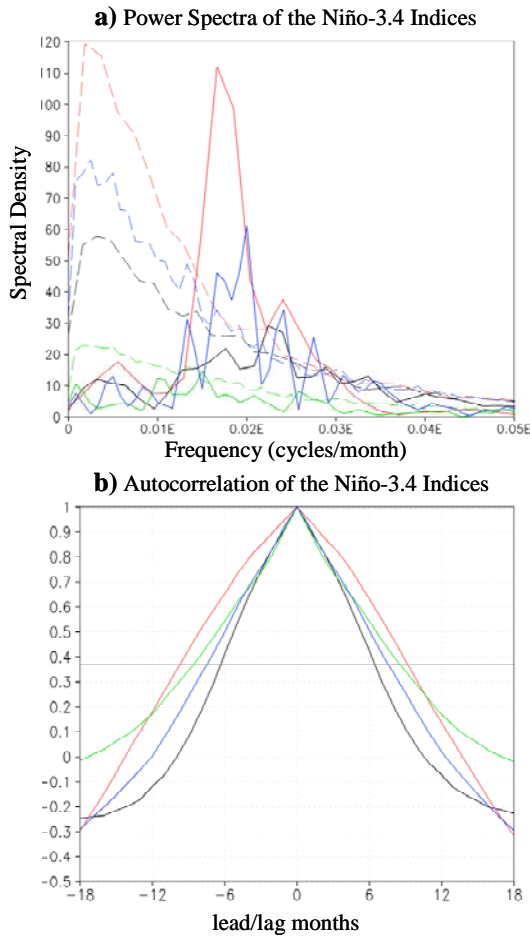


Figure 5 (a) Power spectra and (b) autocorrelation of the Niño-3.4 indices (SST anomalies averaged over 5°S-5°N, 120°-170°W) from the CPC SST data for 1950-2001 (black), the CTRL (red), HFC (green) and MFC (blue). Dashed lines in the upper plot indicate 95% significance levels.

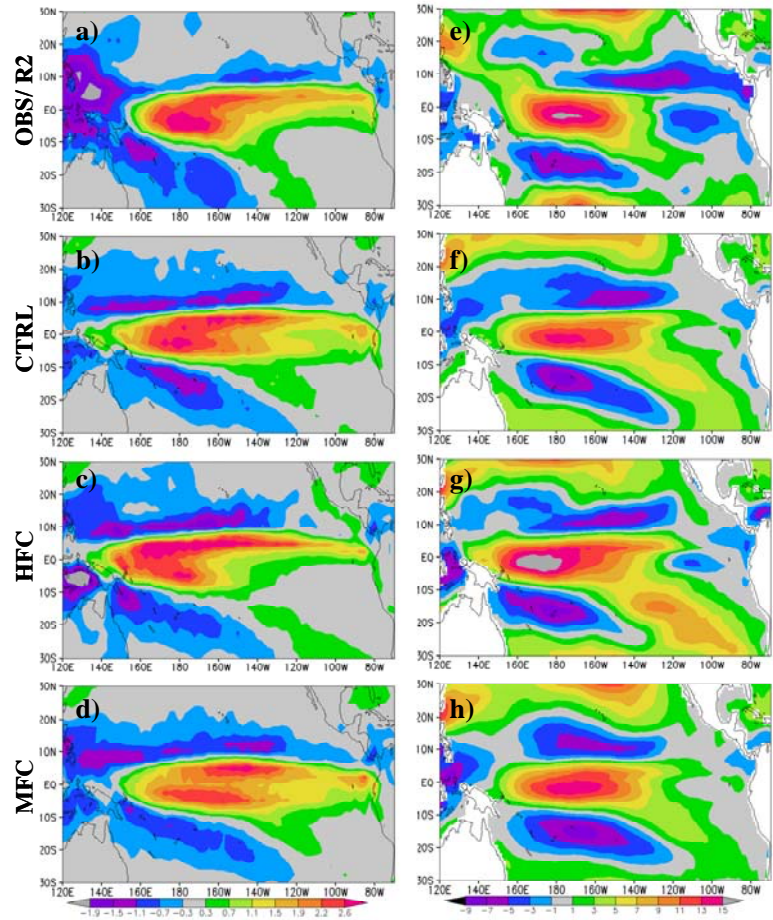


Figure 6 Linear regression coefficient of monthly mean precipitation anomalies from (a) CMAP data for 1979-2001, (b) CTRL, (c) HFC, (d) MFC and zonal wind stress anomalies from (e) NCEP-DOE Reanalysis-2 for 1979-2001, (f) CTRL, (g) HFC and (h) MFC onto the Niño-3 Index from CPC SST data for 1979-2001 for (a) and (e) and respective model simulations otherwise. Units are mm/(day*°C) and 10⁻³ N/(m²*°C).

5. Summary

Both the ocean-atmosphere mean circulation and its annual and interannual variability in CFS exhibit a high degree of sensitivity to the Southeast Pacific SST bias. Reduction of this bias generally increases regional sea level pressure and the southeast trade winds. This change, however, exposes and amplifies other systematic errors in CFS, such as an excessive cross-equatorial flow in the eastern Pacific, that appear to be related to an overly active ITCZ. As a result, the heat flux corrected model demonstrates too strong equatorial easterlies and further weakening of northeasterlies in the eastern Pacific. The ITCZ errors to a varying extent are also present in the AMIP-type simulation with GFS and probably not directly linked to the SST; SEP bias therefore acts as a means to compensate for them.

As a consequence of surface wind stress errors in the heat flux correction experiment, CFS develops a cold SST bias at the equator and the central South Pacific. Equatorial thermocline becomes too deep and diffuse. These changes have a major impact on the model's ENSO simulation, considerably reducing its amplitude.

Largest improvements in the simulation of the mean climate due to momentum flux correction are found over the Indian Ocean. Moreover, with the reduction of the mean errors in the surface wind stress, amplitude and duration of ENSO events become more realistic in this simulation than directly coupled CFS integration.

References

- An, S.-I., and B. Wang, 2000: Interdecadal change of the structure of the ENSO mode and its impact on the ENSO frequency. *J. Climate*, **13**, 2044-2055.
- Kirtman, B. P., 1997: Oceanic Rossby wave dynamics and the ENSO period in a coupled model. *J. Climate*, **10**, 1690-1704.
- Li, T., and T. F. Hogan, 1999: The role of the annual-mean climate on seasonal and interannual variability of the Tropical Pacific in a coupled GCM. *J. Climate*, **12**, 780-792.
- Manganello, J. V., and B. Huang, 2008: The influence of systematic errors in the Southeast Pacific on ENSO variability and prediction in a Coupled GCM. *Clim. Dyn.* DOI 10.1007/s00382-008-0407-5 (available online).
- Meehl, G. A., P. R. Gent, J. M. Arblaster, B. L. Otto-Bliesner, E. C. Brady and A. Craig, 2001: Factors that affect the amplitude of El Niño in global coupled climate models. *Clim. Dyn.*, **17**, 515-526.
- Wang, W., S. Saha, H.-L. Pan, S. Nadiga and G. White, 2005: Simulation of NESO in the new NCEP Coupled Forecast System model (CFS03). *Mon. Wea. Rev.*, **133**, 1574-1593.
- Wittenberg, A. T., A. Rosati, N.-C. Lau, and J. J. Ploshay, 2006: GFDL's CM2 global coupled climate models. Part III: Tropical Pacific climate and ENSO. *J. Climate*, **19**, 698-722.

Global Ocean Monitoring: A Synthesis of Atmospheric and Oceanic Analysis

Yan Xue, Boyin Huang, Arun Kumar, Wanqui Wang
Climate Prediction Center, NOAA/National Weather Service

1. Introduction

Given the importance of the El Niño and Southern Oscillation (ENSO) on global climate variability on seasonal-to-interannual time scale, NOAA's Climate Prediction Center (CPC) actively engages in the real-time monitoring of oceanic and atmospheric conditions in the equatorial tropical Pacific (<http://www.cpc.ncep.noaa.gov/products/precip/CWlink/MJO/enso.shtml>). An important component of monitoring and predicting ENSO evolution is the oceanic sub-surface conditions. The subsurface ocean monitoring at CPC is based on the Global Ocean Data Assimilation System (GODAS; Behringer and Xue 2004). The GODAS is one component of the NCEP Climate Forecast System (CFS), and it provides the oceanic initial conditions for CFS (Saha et al. 2006).

The retrospective global ocean analysis for 1979-2004 and its near real-time extension (with a 7-day delay) produce pentad and monthly mean ocean fields on a 1x1 degree grid. To gain a broader dissemination of the GODAS data, and to increase involvement of the research community in the assessment of GODAS, the Climate Observation Division of Climate Program Office of NOAA supports CPC to maintain and to enhance a web based dissemination for the GODAS products for the purpose of ocean monitoring (<http://www.cpc.ncep.noaa.gov/products/GODAS>). The web site provides the users interested in various aspects of the evolution of the ocean state an easy access to the documentation, data link, data validation and global ocean monitoring products derived from GODAS.

To support CPC's mission in monitoring, assessing and predicting short-term climate variability, the ocean monitoring at CPC has been significantly expanded recently, from monitoring the tropical Pacific ENSO alone to monitoring the global oceanic variability on intraseasonal-to-interannual time scales. The global ocean monitoring efforts have two components: 1) the real time plots and animations and 2) Monthly Ocean Briefing (MOB), which was initiated in May 2007. The MOB provides a synthesis view of the current state of the global ocean based on the GODAS and the NCEP/NCAR atmospheric analysis. This synthesis includes a real time assessment of the state of the global ocean and its interaction with atmosphere. The MOB is composed of a conference call and PowerPoint Presentation and is usually held around the 7th day of each month. Both internal and external colleagues are encouraged to participate and contribute to the MOB, which is becoming a valuable product for both operational and research communities.

2. GODAS web site

CPC's subsurface ocean monitoring for the ENSO was initially based on the Pacific Ocean Data Assimilation System (ODAS) (Ji et al. 1995). The Pacific ODAS was replaced by a Global Ocean Data Assimilation System (GODAS) (Behringer and Xue 2004). The major changes included 1) an extension to a quasi-global domain (75°S-65°N), 2) replacement of the Geophysical Fluid Dynamics Laboratory's Modular Ocean Model version 1 with version 3, 3) change from momentum flux forcing only to momentum flux, heat flux and fresh water flux forcings of the NCEP/DOE reanalysis, and most importantly, 4) data input changes from temperature only to temperature and synthetic salinity that is constructed from temperature and a local temperature/ salinity climatology. Currently only temperature observations are assimilated into GODAS and they are from XBTs, Argo profiling floats and TAO moorings.

An extensive validation of GODAS against independent observations suggests that the temperature field in the GODAS is closer to observations than that in the Pacific ODAS, and the poor salinity field in the latter is

dramatically improved. Although this version of the GODAS does not assimilate the Altimetry sea level, GODAS compares reasonably well with the Altimetry and tide gauge sea level records. Note that the operational GODAS has been updated in March 2007 with inclusion of the Altimetry sea level. Large biases still exist in velocity fields, probably due to assimilation of synthetic salinity that severely underestimates salinity variability. The results on the validation of GODAS can be accessed at the GODAS web site.

A comprehensive web site (<http://www.cpc.ncep.noaa.gov/products/GODAS>) has been constructed to display the extensive information that is available from the GODAS. The web site contains numerous plots and animations that describe not only the seasonal-to-interannual variability but also the subseasonal variability. In addition, the web site provides a technical report describing the GODAS, a link to the GODAS binary data, a validation of GODAS, a climatology calculated for the base period 1982-2004 and the observational data distribution for each month in 1979-present. Since the goal of the web site is to serve a broad user community that includes operational forecast centers, scientific research groups, and the general public, we solicit feedback from all users, strive to answer their questions in a timely manner, and improve the web site based on the suggestions from the user community.

3. Monthly Ocean Briefing

Although the GODAS web site provides extensive set of plots and animations that are updated in near real time, a synthesis of the available information connects various aspects of the ocean-atmosphere coupled variability, and is a succinct way to summarize a wide array of available information. In addition, such a synthesis also highlights the roles of the ocean beyond the tropical Pacific ENSO on climate variability and predictability, and raises questions about the climate variability that not well understood. Such an expert assessment synthesizes what has happened, whether the atmospheric and oceanic analysis are consistent in describing what has happened, whether the recent evolution is within the normal range, and what is the interaction with atmosphere. This product is expected to be useful for researchers, forecasters, and the general public.

CPC started to make a real time expert assessment of the global ocean, referred to as Monthly Ocean Briefing (MOB), in May 2007. We invite outside colleagues to participate in MOB through a conference call. A PowerPoint Presentation is prepared and distributed through an email list one day before the ocean briefing, which is held around the 7th day of each month. Anyone who is interested in the ocean briefing can join the conference call, or access the PPT archive through the GODAS web site.

The following data sets are used in the construction of the ocean briefing PPT:

- NCEP/NCAR atmospheric analysis: 850 mb winds, 200 mb velocity potential, latent and sensible heat flux, short and long wave radiation at the surface
- NOAA's Outgoing Longwave Radiation
- Weekly Optimal Interpolation SST version 2 (Reynolds et al. 2002)
- NCEP Global Ocean Data Assimilation System: subsurface temperature, heat content (temperature average in the top 300 meters), Tropical Cyclone Heat Potential
- TAO subsurface temperature gridded analysis (personal communication with Dr. Mike McPhaden at PMEL)
- Aviso Altimetry Sea Surface Height (http://www.jason.oceanobs.com/html/donnees/welcome_uk.html)
- Ocean Surface Current Analyses – Real-time (OSCAR, <http://www.oscar.noaa.gov/datadisplay>)

The briefing PPT contains two parts. The first part describes the recent evolution and current conditions of the ocean in different basins. An SST heat budget analysis is used to explain the SST tendencies for the major air-sea coupled modes such as ENSO. The influences of the MJO-related winds on oceanic Kelvin waves and ENSO are discussed. The impacts of extra-tropical winds on the ocean are monitored in the North Pacific and North Atlantic. The second part discusses the biases in GODAS and their potential impact on the recent performance of ENSO predictions by NCEP's CFS. Some of the plots used in the latest ocean briefing, January 2008 Ocean Briefing, are presented in the Appendix.

4. Annual Ocean Briefing

CPC conducted its first Annual Ocean Briefing on February 8, 2008. The purpose of the briefing was to provide an overview of oceanic variability in the past year, and its potential impacts on annual mean atmospheric circulations. The PPT can be accessed at

http://www.cpc.ncep.noaa.gov/products/GODAS/ocean_briefing_gif/ocean_briefing_annual_2007.ppt

5. Future additions

We will continue to add new items to MOB, some of which are listed below:

- GODAS/TAO subsurface temperature and salinity comparison in real time
- Indonesian Throughflow
- Integrated meridional transports along 9S and 9N in Pacific
- Meridional Overturning Circulation in Atlantic
- Atmospheric impacts of SST anomalies
- Intercomparison with other ocean analysis products

References

Behringer, D. W., and Y. Xue, 2004: Evaluation of the global ocean data assimilation system at NCEP: The Pacific Ocean, *Eighth Symposium on Integrated Observing and Assimilation System for Atmosphere, Ocean, and Land Surface*, AMS 84th Annual Meeting, Washington State Convention and Trade Center, Seattle, Washington, 11-15.

Ji, M., A. Leetmaa, and J. Derber, 1995: An ocean analysis system for seasonal to interannual climate studies, *Mon. Wea. Rev.*, **123**, 460-481.

Reynolds, R. W., N. A. Rayner, T. M. Smith, D. C. Stokes and W. Wang, 2002: An improved in situ and satellite SST analysis for climate, *J. Climate*, **15**, 1609-1625.

Saha, S., S. Nadiga, C. Thiaw, J. Wang, W. Wang, Q. Zhang, H. M. van den Dool, H.-L. Pan, S. Moorthi, D. Behringer, D. Stokes, G. White, S. Lord, W. Ebisuzaki, P. Peng, P. Xie, 2006: The NCEP climate forecast system, *J. Climate*, **19**, 3483-3517.

Appendix: CPC Ocean Briefing Samples

Global Ocean

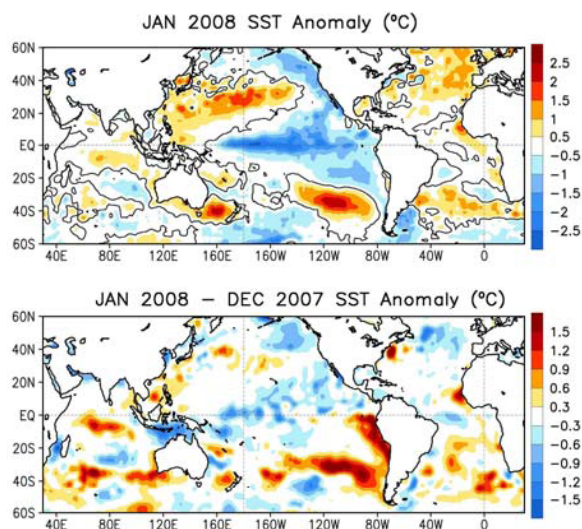


Figure 1 Global SST anomaly in January 2008 (top) and its tendency (low).

Pacific Ocean

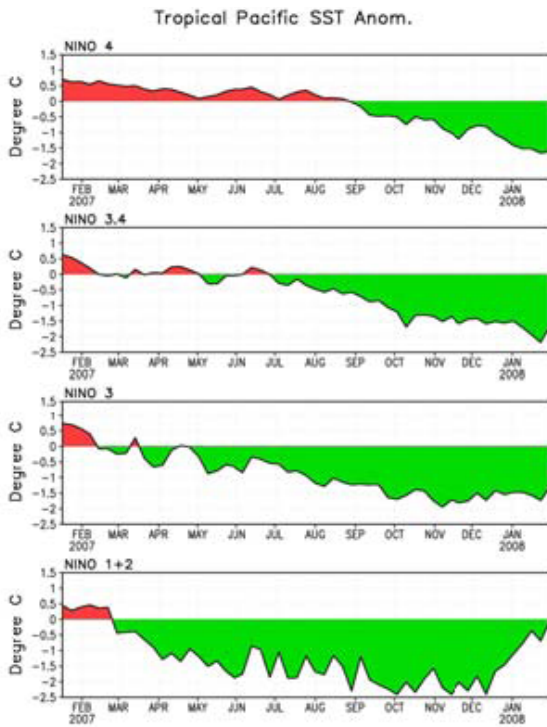


Figure 2 NINO indices.

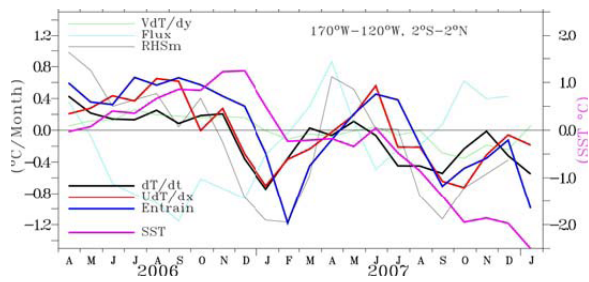


Figure 4 Mixed layer heat budget analysis derived with GODAS (Courtesy of Dr. Dongxiao Zhang from PMEL).

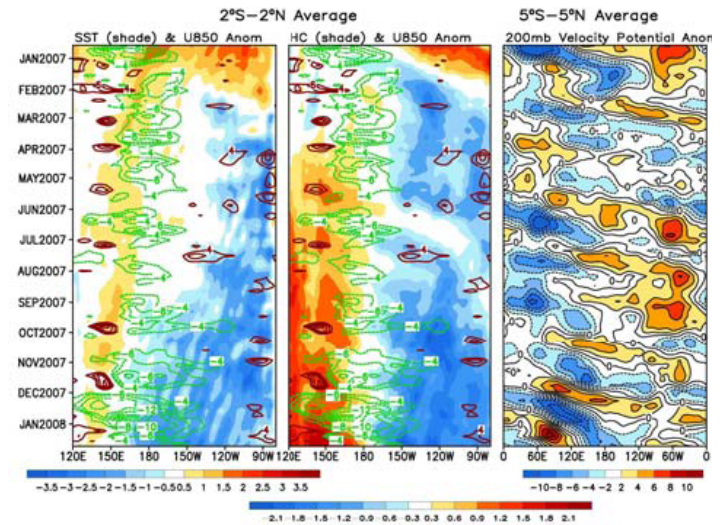


Figure 3 Time-Longitude of SST (shade) and 850 mb zonal wind (contour) anomaly (left), heat content (shade) and 850 mb zonal wind (contour) anomaly (middle), and 200 mb velocity potential anomaly (right).

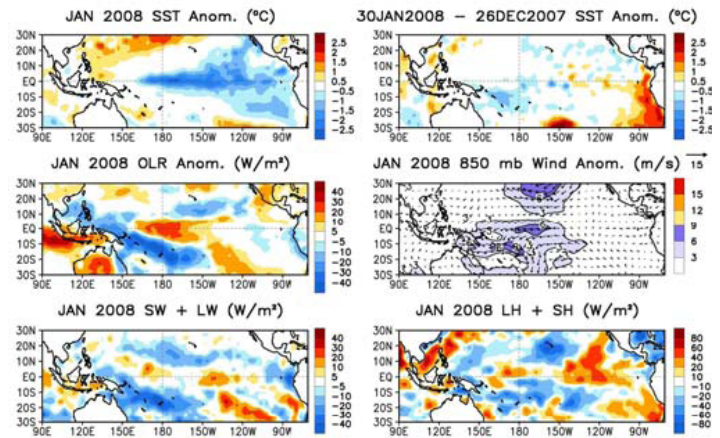


Figure 5 SST (upper left), SST tendency (upper right), OLR (middle left), 850 mb wind (middle right), short and long wave (lower left) and latent and sensible heat flux (lower right) anomalies in January 2008.

Indian Ocean

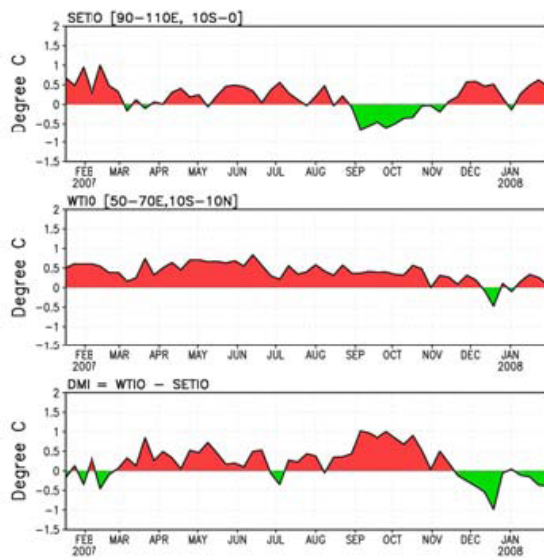


Figure 6 Indian Ocean Dipole indices.

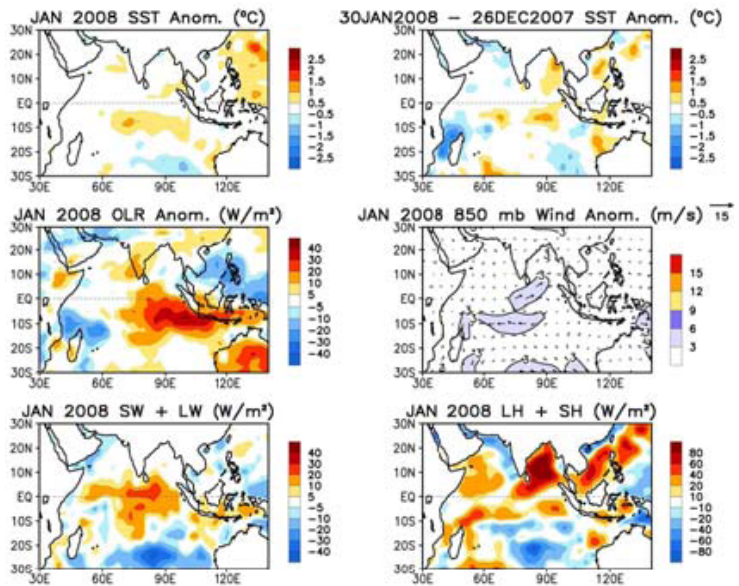


Figure 7 Same as Figure 5 except for the tropical Indian.

Atlantic Ocean

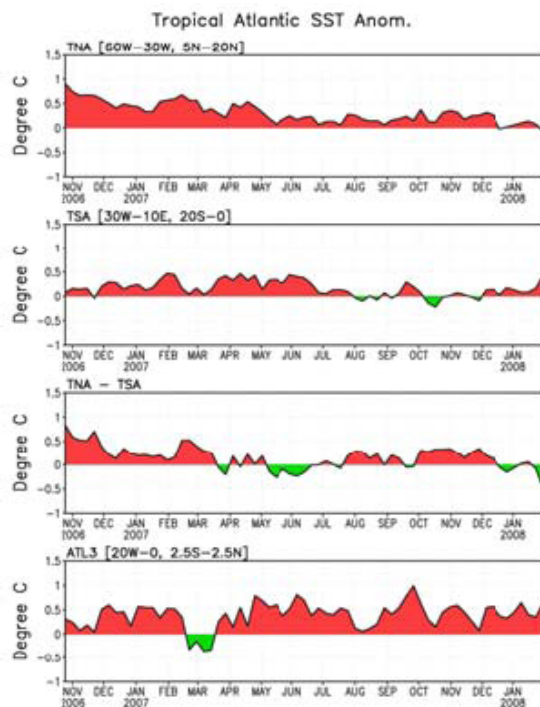


Figure 8 Atlantic Ocean SST indices.

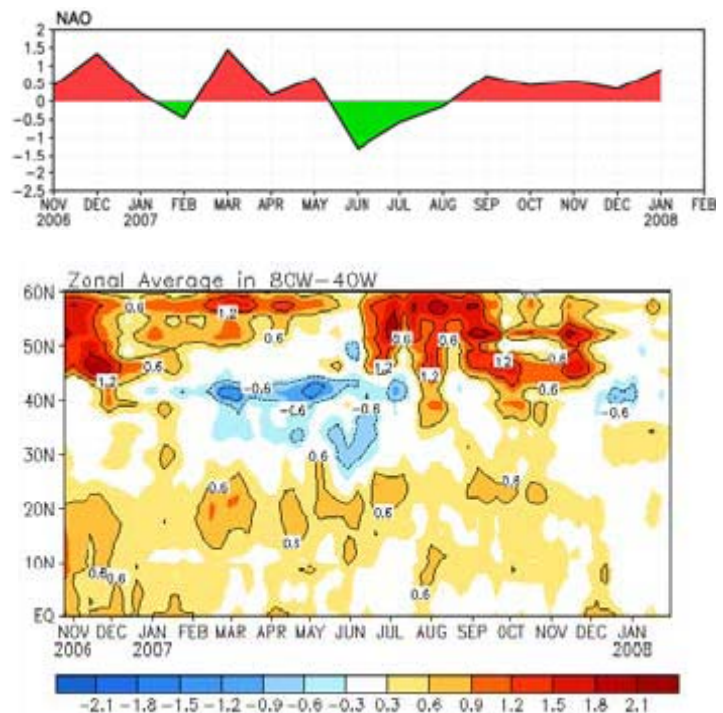


Figure 9 North Atlantic Oscillation index (top) and zonal average of SST anomaly as functions of latitude and time (low).

GODAS biases

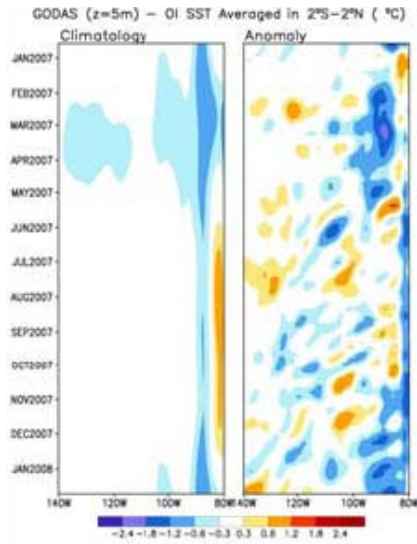


Figure 10 Differences between GODAS temperature at 5 meter depth and OI SST. Climatology (left) and anomaly (right).

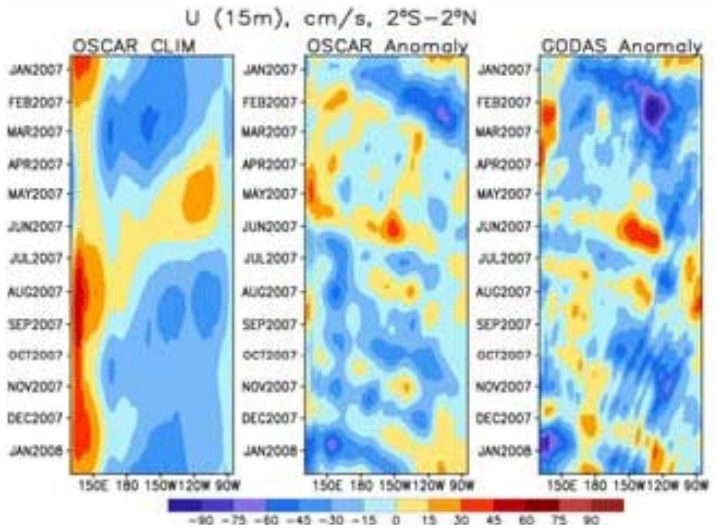


Figure 11 Zonal current at 15 meter depth. OSCAR climatology (left) and anomaly (middle), and GODAS anomaly (right).

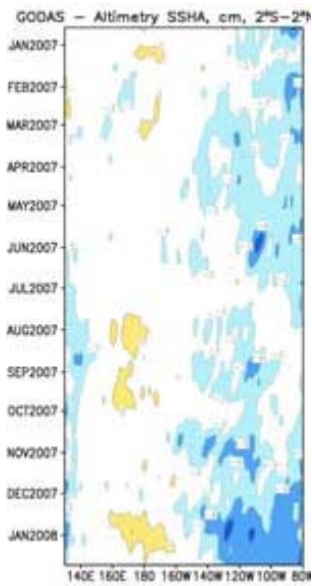


Figure 12 Differences between GODAS and Altimetry sea surface height anomaly.

CFS ENSO prediction

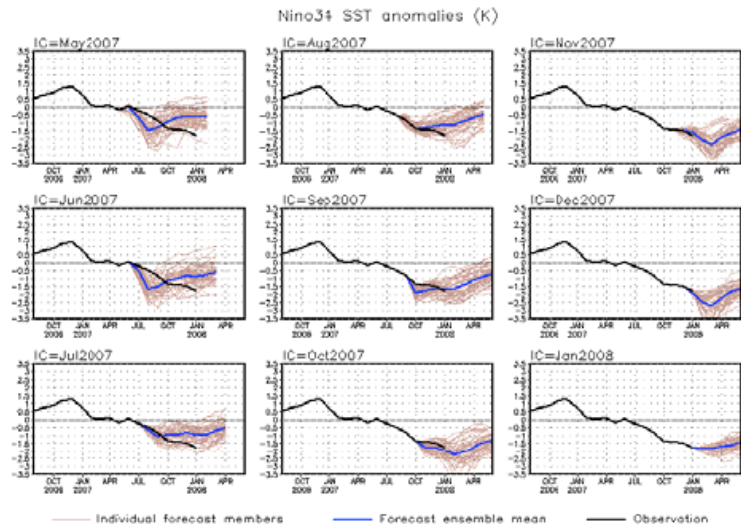


Figure 13 NINO3.4 SST forecast by the NCEP CFS model in the past nine months.

Assessment of the CFS on the Predictability of the North American Monsoon

Lindsey N. Long⁽¹⁾, Jae-Kyung E. Schemm⁽¹⁾, Suranjana Saha⁽²⁾

NOAA/NWS/NCEP

⁽¹⁾ Climate Prediction Center

⁽²⁾ Environmental Modeling Center

1. Introduction

The North American Monsoon (NAM) is a difficult region for weather and climate prediction because although it encompasses a small region, it has an intricate terrain. The region stretches from central Mexico into Arizona and New Mexico with the Gulf of California and Baja peninsula to the west and the Gulf of Mexico to the east. In addition, the Sierra Madre Occidental stretches along the west coast of Mexico with the Sierra Madre Oriental to the east. This combination of mountains, water bodies, and the Baja peninsula make the NAM an interesting system.

Two similar studies focusing on the NAM system have been compiled. The first study investigates the ability of NCEP's Climate Forecast System (CFS) to simulate the NAM using different atmospheric physics, horizontal resolutions, and lead times. The second study highlights results gathered during the NAM Experiment Model Assessment Project 2 (NAMAP2). For NAMAP2, six global models, including NCEP's CFS and Global Forecast System (GFS), and four regional models were gathered and analyzed. The results presented for both studies focus only on precipitation and the general circulation in the region. These studies aim to determine 1) how the predictability of the monsoon system by the CFS changes with different variations of the model and 2) how the CFS compares to other global and regional models.

2. CFS Variations Simulating the NAM

In the first study, a test version of the CFS (Saha et al. 2006), which may be used for the next generation CFS, is run at three different horizontal resolutions: T62, T126, and T382. These single runs use May 15th for their initial condition. In addition, the current operational CFS forecast, run at T62, is used. These operational runs are 15-member ensemble means using both a 1-month lead (May) and a 3-month lead (March). For observational comparison, a Unified Rain Gauge Dataset (URD) for North America (Higgins et al. 2000) is used for precipitation and the North American Regional Reanalysis

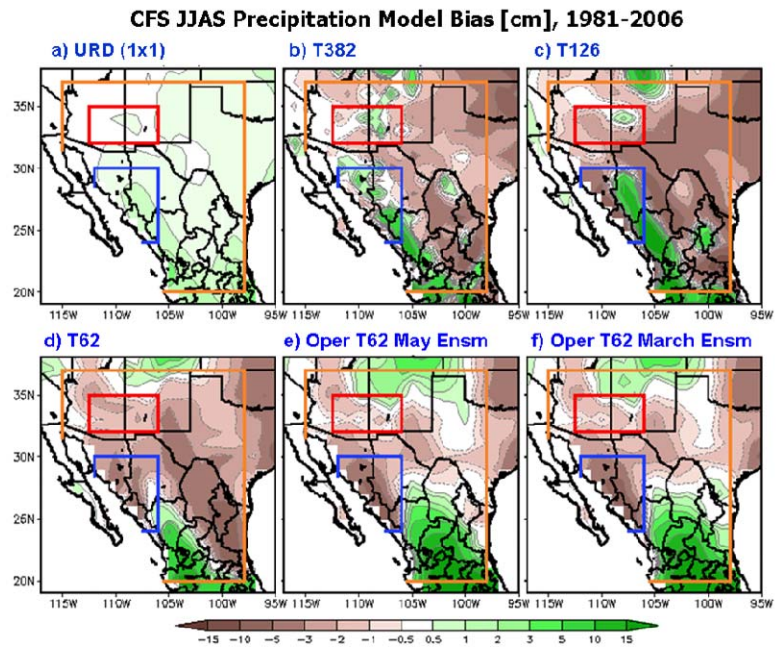


Figure 1 Spatial maps of the JJAS Precipitation Model Bias [cm] for CFS from 1981-2006 for b) CFS at T382, c) CFS at T126, d) CFS at T62, e) Operational T62 CFS Ensemble with May initial conditions, and f) Operational T62 CFS Ensemble with March initial conditions. The total observed precipitation from which the bias is calculated is shown in a), the URD 1981-2006 climatology. Orange boxes represent the TIER 1.5 region. Blue boxes represent the CORE region. Red boxes represent the AZNM region.

(NARR) is used for wind velocities (Mesinger et al. 2006).

a) Precipitation

In order to compare the different versions of the CFS, we first look at the model precipitation bias compared to the total rainfall represented by the URD (Figure 1). The bias shows that both operational versions of the CFS (Fig 1e and 1f) have a wet bias in central Mexico and a slight dry bias in northern Mexico into the southwest U.S. Also unlike observed climatology (Fig 1a), the precipitation is not contained in a swath following the mountains along the west coast (CORE region, blue box). Instead, this region is extremely dry. Figure 1d shows that the T62 CFS (next generation) is more organized along the mountain range and begins to bring rain into this CORE region, although not far enough north. In addition, the dry bias in Texas is more extreme, reaching down into northern Mexico. Finally, the T382 and T126 runs (Figs 1b and 1c) continue to have this dry bias in Texas and northern Mexico, but the precipitation becomes more organized along the western coast, bringing a healthy swath of precipitation northward. The high resolution of the T382 run leaves a small patch of wet biases along this swath; however, it is important to note that the observations are based on rain gauges and therefore may miss small areas of intense rainfall. Overall, finer resolution and model upgrades are more accurate in simulating precipitation variability in the NAM region.

Moving to the seasonal cycle, Figure 2 shows area averages of monthly precipitation from May to September over the three NAM sub-regions. Focusing now on the CORE region (Fig 2b), a clear progression occurs in the CFS model runs, reinforcing the spatial maps in Figure 1. The two operational CFS ensembles at T62 show a much drier monsoon than seen in observations (black line). The T62 with updated physics (red) shows an improvement in the precipitation magnitude, but maintains a precipitation peak in August. The T126 and T382 runs more accurately predict the amount of precipitation; however, only the T382 run correctly simulates the peak in July (versus T126 in August). The T382 does well simulating the monsoon onset from June to July in all three regions, with the onset in the AZNM region being right with observations. In the larger Tier 1.5 region, the two operational CFS ensembles do a better job with the onset and amount of precipitation in the early season than in the AZNM and CORE regions. As seen in Figure 1 by the extreme wet bias to the south, the precipitation is present in these T62 runs, but restricted to the southern NAM region of central Mexico.

Unfortunately, although the CFS does well in predicting the seasonal variability, it does poorly when simulating the interannual variability. Figure 3 shows the correlations for the interannual variability of each model run compared to the URD for each month (left) and seasonal averages (right). Plots of the interannual variability (not shown) are extremely chaotic as can be surmised from the very low or even negative correlations. The next generation CFS at T62 shows improvement over the operational CFS at T62. Increased horizontal resolution also shows improved correlations. Surprisingly, the T382 is not always the most skilled model run. While the T382 run exhibits the most skill in the small AZNM region (Fig 3a and 3d), reaching close to 0.45, it is the T126 run that does better in the larger regions. The T126 run reaches the peak correlation for any CFS run

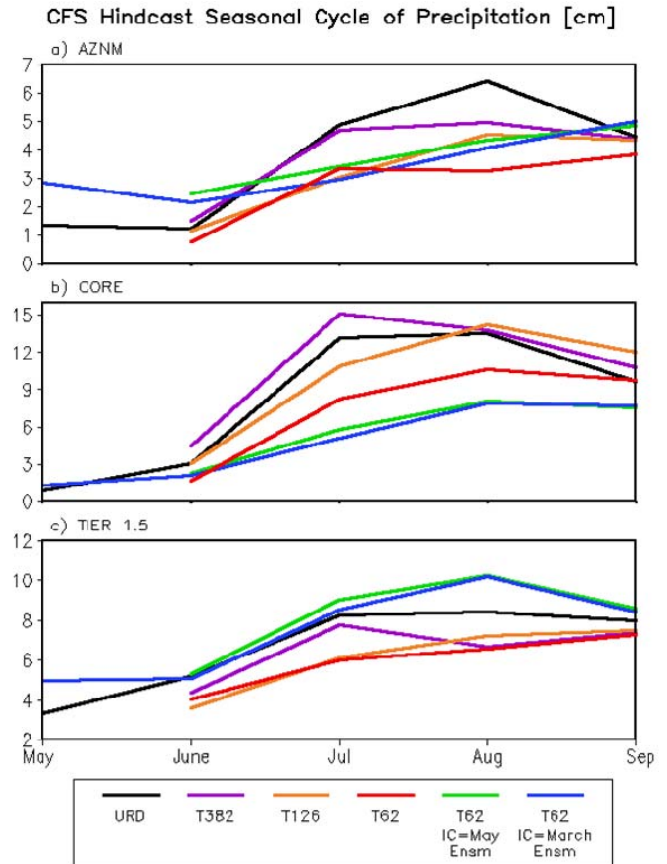


Figure 2 Seasonal Cycle of precipitation [cm] for the a) AZNM, b) CORE, and c) TIER 1.5 Regions from May to September.

at 0.51 in the Tier 1.5 region for August. Obviously with these very low correlations, few are actually statistically significant.

b) Winds

The NAM region has three distinct upper and lower level wind features. The first is a large anticyclonic flow located off the west coast of Mexico at 300 mb. This anticyclonic flow seems to come and go throughout the JJA and JAS seasons (not shown). The T382 run correctly produces an intense anticyclone slightly too far south during JJA, but this disappears during JAS. The two operational T62 runs do the opposite. An anticyclonic flow appears late in the monsoon season in JAS. This is consistent with earlier analysis that shows the operational CFS has a tendency to have a late onset of the monsoon. The remaining runs show little to no evidence of the anticyclone near Mexico, but most produce a slight anticyclonic flow far from the area in the southwest Pacific.

The other two important wind features are low-level jets located over the Gulf of Mexico (GoM LLJ) and the Gulf of California (GoC LLJ). At 925 mb, all runs of the CFS produce a robust GoM LLJ bringing warm, moist air into Texas and eastern and central Mexico; however, the CFS does poorly simulating the GoC LLJ. The GoC LLJ brings moist air from the Gulf of California directly into the monsoon region (Figure 4, left). Winds turn from northerly in the Pacific to southerly in the Gulf of California. The CFS produces the northerly flow over the Pacific, but instead of turning to southerly flow over the Gulf, the CFS produces a weak westerly flow. The T382 run is the only run shown in Figure 4 (right), but the wind direction and magnitude is surprisingly consistent between all CFS runs analyzed in this study.

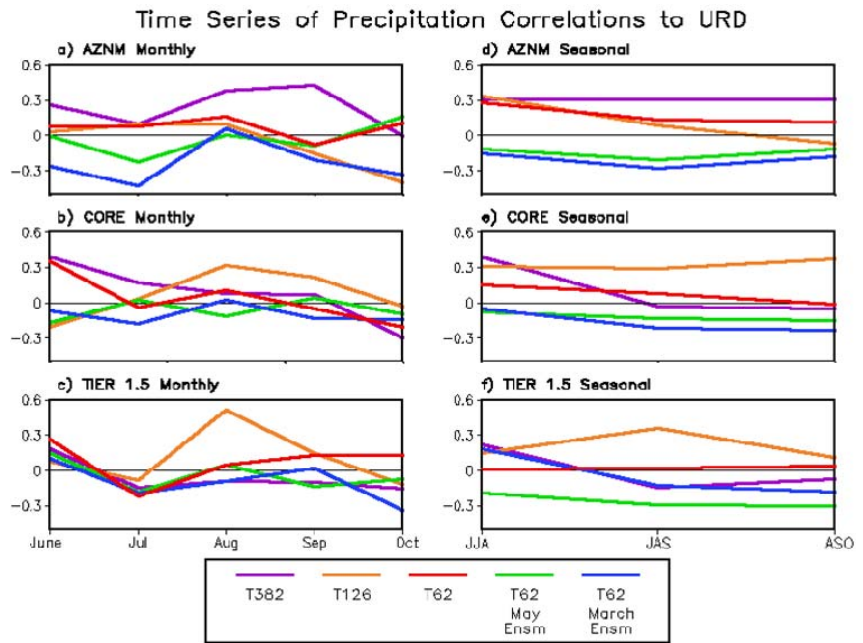


Figure 3 Time series of precipitation correlations to URD for the interannual variability of the NAM from 1981-2006. Correlations are for each month in a) AZNM, b) CORE, and c) TIER 1.5 and for each season in d) AZNM, e) CORE, and f) TIER 1.5.

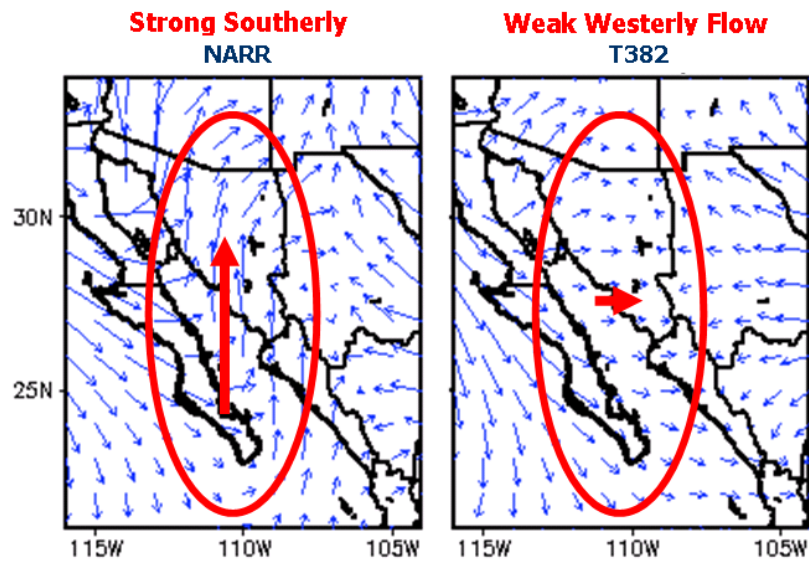


Figure 4 Spatial map of 925mb winds over the Gulf of California region for NARR and CFS T382 averaged for JJA. The main direction of the Gulf of California Low-Level Jet is highlighted by the red vector.

3. NAMAP2

The second study is a snapshot of results gathered during NAMAP2. NAMAP2 is an international collaboration between the United States and Mexico which focuses on the 2004 monsoon season. For this project, modelers were asked to submit simulations for the 2004 summer season from May 15th to September 30th using a new high resolution Multiplatform-Merged (MPM) SST analysis (Wang and Xie, 2007). Ten modelers submitted runs for the study consisting of six global models and four regional models. Model details are illustrated in Table 1 (more complete information on the different models can be obtained from the NAMAP2 web page at <http://www.eol.ucar.edu/projects/name/namap2>). Most modelers used our requested SST analysis, but a few used their own (RAMS, CAM3b). One modeler submitted two sets of runs, one using the MPM SSTs and one using Era-40 (CAM3c and CAM3a, respectively). There is also a wide range in model resolution and ensemble members.

Model Name	Affiliation / Contact	Horizontal Resolution	Ensemble Size	SST prescription
CFS	NOAA CPC / Schemm	T126 (~1°)	5	MPM
GFS	NOAA CPC / Mo & Wei	T126 (~1°)	4	MPM
CAM3_a	UCSD SIO / Collier & Zhang	T42 (~2.8°)	1	Era-40
CAM3_b	NCAR / Lawrence	1.0°×1.25°	1	Hadley
CAM3_c	UCSD SIO / Collier & Zhang	T42 (~2.8°)	3	MPM
Finite Volume	NASA GSFC / Bosilovich	0.25°×0.36°	2	MPM
GEOS5	NASA GSFC / Lee & Schubert	0.5°	5	MPM
<i>RAMS</i>	<i>Duke U / Roy</i>	<i>64 km</i>	<i>1</i>	<i>NOAA OI</i>
<i>RSM</i>	<i>UCSD SIO / Nunes & Roads</i>	<i>30 km</i>	<i>1</i>	<i>MPM</i>
<i>MM5_a</i>	<i>IMTA / Lobato</i>	<i>30 km</i>	<i>3</i>	<i>MPM</i>
<i>MM5_b</i>	<i>UNM / Ritchie</i>	<i>15 km</i>	<i>1</i>	<i>MPM</i>

Table 1 Listing of models participating in NAMAP2 and their key characteristics. The six global models are indicated in non-italic type; the four regional models in italics.

a) Precipitation

Spatial maps of the NAM region show a large discrepancy between models in precipitation magnitude and scope. Figure 5 shows the spatial precipitation maps for each global model and the URD for JJAS in 2004. As in the prior study, three regions are boxed off (AZNM, CORE, and TIER 1.5). The top row (Fig 5a – 5d) shows the URD for comparison and each CAM3 simulation. The two CAM3 simulations from UCSD show precipitation occurring too far south and to the east. The rainfall is not well organized and shows a lack of topographic forcing. These CAM3 simulations are at T42 whereas the NCAR simulation of the CAM3 model (Fig 5d) is at a much finer resolution (~1 degree). At this finer resolution, the CAM3 is able to produce a more accurate representation of the NAM rainfall. Rainfall is confined to a thin region along the western coast of Mexico, moving into the CORE region (blue box). One feature lost in the NCAR contribution is the rainfall present in Texas, Oklahoma, and Arkansas.

Looking now at the bottom row of global model simulations (Fig 5e – 5h), we see a very similar pattern. Here the CFS, FV GCM, GEOS 5, and GFS all capture the swath of precipitation stretching into the CORE region; however, the exact swath location, swath width, and rainfall magnitude vary between models. In addition to the similar precipitation swath, these models all show a dry bias in Texas, Oklahoma and Arkansas.

Only the GEOS 5 from NASA shows some significant precipitation in the AZNM region (red box) for the global models.

Figure 6 is the same as Figure 5 but for the regional model contributions. Here the effect of increased resolution is evident by the increased detail to the rainfall pattern; however, in addition to this increased detail, the regional models are producing significantly more precipitation than observed. The exception is the RAMS model from Duke which is the coarsest of the regional models and has a more conservative amount of precipitation produced over the NAM region. Northward in the United States, the regional models more accurately simulate the presence of precipitation (albeit too wet), both in the AZNM region and farther east.

Focusing now on the CORE region, the seasonal cycle of precipitation from May to September is shown in Figure 7. For 2004, many different observational tools were available for the NAM region. For comparison, three different products (black lines) are used: a rain gauge dataset, URD, used in the previous study; TRMM, a satellite product (Huffman et al. 2007); and RMOPRH, a satellite-gauge blend (Janowiak et al. 2007). One interesting result of NAMAP2 is the large discrepancy between precipitation products. Although the magnitude of these three products differs greatly, the overall structure is consistent. Each product shows a pronounced increase in precipitation from June to July. All global and regional models, with the exception of one, capture this increase. This is a marked improvement over the previous NAMAP results which indicated delayed onset for most global models. The lone model with delayed onset is the CAM3a submission (dark blue) which produces precipitation too far east

GLOBAL Models - JJAS Precipitation [cm], 2004

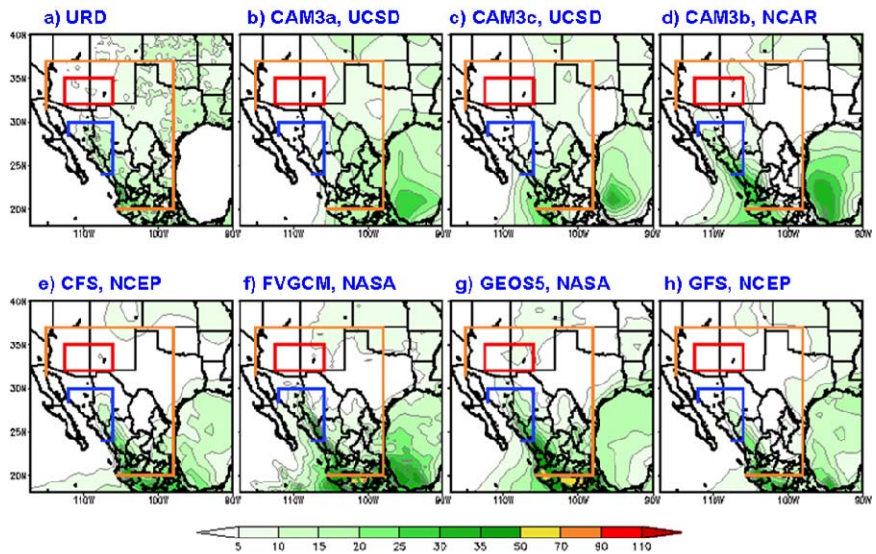


Figure 5 Spatial maps for Global NAMAP2 models and URD. Maps depict JJAS total precipitation [cm] for 2004. Orange boxes represent the TIER 1.5 region. Blue boxes represent the CORE region. Red boxes represent the AZNM region.

REGIONAL Models - JJAS Precipitation [cm], 2004

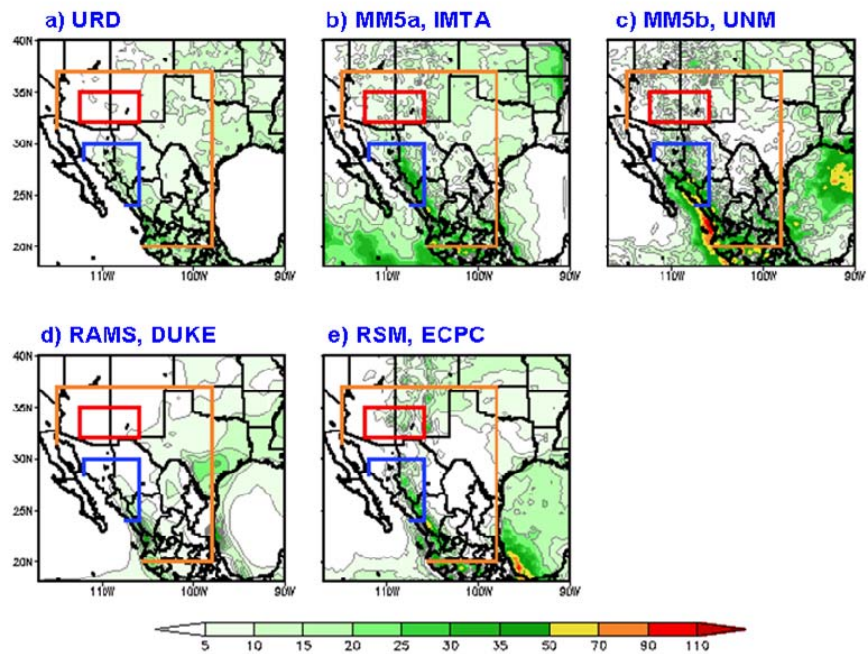


Figure 6 Same as Figure 5, but for Regional Models.

and then slowly moves it into the CORE region late in the season.

Of the global models, only the CFS (red) and GFS (purple) peak in July and then show a decrease in precipitation for the remainder of the season. These two submissions simulate the 2004 monsoon seasonal cycle extremely well. The other five model runs peak in August. This is also true for one regional model (MM5b); however, the other three regional models peak in July. Both the RAMS and RSM simulate the seasonal cycle well. Another interesting feature is the large wet bias in both MM5 submissions seen earlier in the spatial maps. Note the change in scale for the y-axis between the global to regional models.

2004 Seasonal Cycle of Precipitation [cm], CORE Region

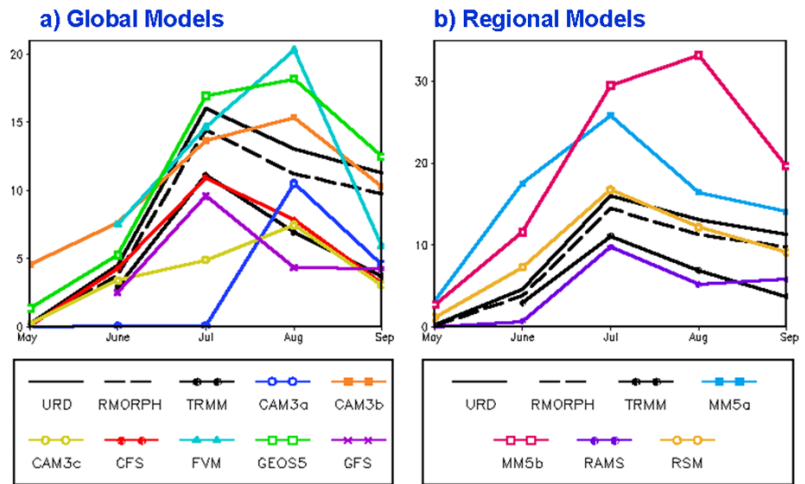


Figure 7 Time Series of Monthly Precipitation [cm] averaged over the CORE Region for a) Global models and b) Regional models for May to September. Observations are in black.

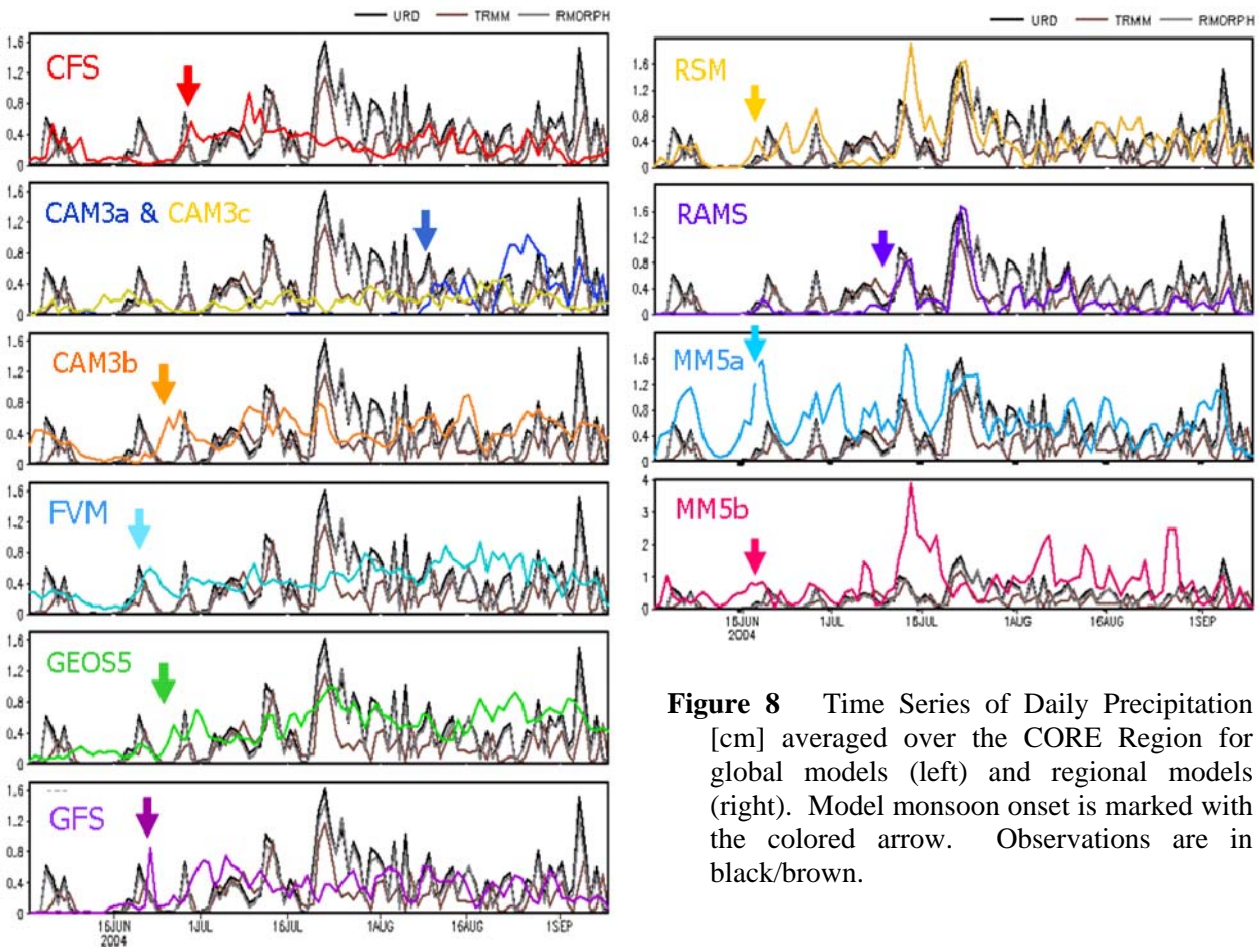


Figure 8 Time Series of Daily Precipitation [cm] averaged over the CORE Region for global models (left) and regional models (right). Model monsoon onset is marked with the colored arrow. Observations are in black/brown.

Figure 8 takes a closer look at the monsoon onset for the CORE region by showing the daily precipitation amounts simulated by each model. Again the same three observational products are shown in the dark colors. Thick colored arrows indicate the monsoon onset for each model, defined as three days of precipitation over 0.5

mm/day after June 1st. This again shows how well the models are doing at simulating the monsoon onset. In fact, some models even capture the false onset taking place in early June. The CFS, CAM3b, FVM, RSM, and both MM5 simulations show a definite peak in precipitation in early June and then a true onset around June 21st. In addition, the regional models tend to accurately simulate the noisy rainfall pattern throughout the season. Note that the two heavy rainfall events during mid and late July are captured extremely well by the RSM, RAMS, and MM5a (Figure 8, right).

b) Winds

The anticyclonic feature associated with the NAM is represented differently by each model in NAMAP2. At 300 mb, each submission has some anticyclonic flow present in the NAM region; however, many are not located off the western coast of Mexico as seen in observations (not shown). Instead, the center of circulation is found throughout the NAM region including near the US/Mexico border (CAM3 submissions and GEOS5), in eastern Texas (FV GCM), and in central Mexico (MM5a). Both the GFS and CFS produce the anticyclonic flow in the correct location, but with a latitudinally elongated circulation. The RSM produces the most accurate representation of this anticyclonic flow. In addition, as seen in the earlier study, all models do well at simulating the GoM LLJ. The jet shows consistent strength from model to model, but with a slight difference in the angle of flow onto land between model submissions.

Also as seen in the previous study, it is difficult to find a good representation of the GoC LLJ in the NAMAP2 model simulations. Only the MM5b submission from the University of New Mexico shows some sign of the GoC LLJ (not shown). This submission shows a westerly flow that does manage to turn to a southerly flow, albeit weakly, in the very northern portions of the gulf at around 18 UTC.

However, it is important to note some obstacles faced by the models in correctly simulating the GoC LLJ. For NAMAP2, only data at 300, 500, and 850 mb was requested; however, low-level jets are best viewed at pressure levels lower than 850 mb. The GoC LLJ is strongest at approximately 925 mb. Therefore, although the models may not show a jet at 850 mb, there may be one present at lower levels. In addition, the GoC LLJ was weak during the 2004 season which makes it even harder to see at 850 mb. Because the GoM LLJ is such a strong jet, it is easily seen at 850 mb and there is no such problem.

Even with the limitations described above, it is surprising that none of the models can correctly simulate the GoC LLJ. Because of the topography of the region, model resolution was thought to be a main contributor to model weaknesses in simulating the jet. However, with this group of model simulations, many regional models are at considerably fine resolutions. Therefore, limitations in horizontal resolution may not be the actual cause of model error.

Although only total precipitation and general circulation is mentioned here, many other variables were analyzed during NAMAP2. Spatial maps, plots of seasonal and diurnal cycles, and much more are available on the NAMAP2 Online Atlas. This atlas is hosted by the University of Miami located at

<http://www.rsmas.miami.edu/personal/pkelly/Research.html>.

4. Conclusions

Overall, the CFS has been doing fairly well in simulating seasonal precipitation during the warm season NAM. With horizontal resolutions T126 and finer, the CFS is able to create the swath of precipitation up the west coast of Mexico along the Sierra Madres in the CORE region. The CFS at T62 using the new, test version of the CFS also shows great improvement over the current operational CFS. This test version of the CFS is able to capture the monsoon onset occurring between June and July with greater accuracy as resolution increases. In comparison to other global models examined in NAMAP2 for 2004, the T126 CFS is doing as good if not better than the other submissions.

Even though the CFS correctly predicts this seasonal precipitation, the upper and lower level circulations have serious deficiencies. Because both the GoC LLJ and the upper level anticyclonic flow off the Mexican coast are poorly simulated by the CFS, they bring into question the skill shown by the CFS in predicting precipitation in the NAM region. Although the CFS seems to capture the seasonal cycle of the monsoon, including both magnitude and onset, it seems to be correctly capturing these features for the wrong reasons. The

GoC LLJ is the main source for NAM moisture, and although there is some westerly flow produced over the Gulf of California by the CFS, it is too weak and not pulling from the warmest waters in the southern gulf.

As seen in NAMAP2, this error with the GoC LLJ is also produced by all global and regional models examined. Although complex terrain can be blamed for not capturing the jet at coarse resolutions, when simulations using a grid scale as fine as 15 km fail to capture the jet, other model issues must be responsible. If an additional NAMAP-type study is performed in the future, it would be advantageous to redo the analysis on the GoC LLJ while looking at the correct pressure level of 925 mb to see if this is in fact hampering the analysis.

Finally, the CFS is doing poorly at simulating the interannual variability of the NAM. Although the CFS does well for the 2004 season in NAMAP2, the low correlations presented in Figure 3 show that there is still a significant amount of work to be done on the CFS in the NAM region. Future work involves looking at the general circulation during high and low correlation years to find if there is a connection between a correctly located anticyclone off the west coast of Mexico and a more accurate precipitation simulation. Because there was an anticyclonic flow consistent with observations during the 2004 season, and the CFS correctly predicted the monsoon magnitude and onset, this is a viable analysis.

References

- Higgins, R.W., W. Shi, E. Yarosh and R. Joyce, 2000: *Improved United States Precipitation Quality Control System and Analysis*. NCEP/Climate Prediction Center ATLAS No. 7, 40 pp. [Available from NOAA Climate Prediction Center, 5200 Auth Road, Camp Springs, MD 20746]
- Huffman, G. J., R. F. Adler, D. T. Bolvin, G. Gu, E. J. Nelkin, K. P. Bowman, Y. Hong, E. F. Stocker, and D. B. Wolff, 2007: The TRMM Multi-satellite Precipitation Analysis (TMPA): Quasi-global, multi-year, combined-sensor precipitation at fine scales. *J. Hydrometeorol*, **8**, 38–55.
- Janowiak, J.E., V.J. Dagsostaro, V.E. Kousky and R.J. Joyce, 2007: An examination of precipitation in observations and model forecasts during NAME with emphasis on the diurnal cycle. *J. Climate*, **20**, 1680–1692.
- Mesinger, F., G DiMego, E. Kalnay, K. Mitchell, P. C. Shafran, W. Ebisuzaki, D. Jovic, J. Woollen, E. Rogers, E. H. Berbery, M. B. Ek, Y. Fan, R. Grumbine, W. Higgins, H. Li, Y. Lin, G. Manikin, D. Parrish, W. Shi, 2006: North American Regional Reanalysis. *Bull. Amer. Meteor. Soc.*, **87**, 343–360.
- Saha, S., S. Nadiga, C. Thiaw, J. Wang, W. Wang, Q. Zhang, H. M. van den Dool, H.-L. Pan, S. Moorthi, D. Behringer, D. Stokes, G. White, S. Lord, W. Ebisuzaki, P. Peng, P. Xie, 2006: The NCEP climate forecast system. *J. Climate*, **19**, 3483–3517.
- Wang, W., and P. Xie, 2007: A Multiplatform-merged (MPM) SST analysis. *J. Climate*, **20**, 1662–1679.

Surface Latent Heat Flux and Relationships with SST in CFS

Renguang Wu^{1,*}, Ben P. Kirtman^{1,2} and Kathy Pegion¹

¹ Center for Ocean-Land-Atmosphere Studies, Calverton MD

² RSMAS/MPO, University of Miami, Miami, FL

1. Introduction

The surface latent heat flux (LHF) is an important quantity in atmosphere-ocean interactions, of which studies show the surface evaporation-sea surface temperature (SST) feedback could contribute to the development of several climate modes (the Atlantic meridional mode, Chang et al. 1997; the Indian Ocean dipole/zonal mode, Saji et al. 1999 and Webster et al. 1999). The NCEP Climate Forecast System (CFS) is an ocean-land-atmosphere fully coupled dynamical system designed for short-term climate prediction (Saha et al. 2006). Since the CFS became operational in August 2004, it has been increasingly used for various climate studies. The CFS retrospective forecast data lend themselves to many studies beyond seasonal forecasts. Thus, it is important to evaluate the CFS performance in both simulation and forecast modes to learn how closely to the reality the atmosphere and ocean interact in the model. This can be done by diagnosing the LHF-SST relationship (Barsugli and Battisti 1998; Wu et al. 2006).

The present study compares mean and interannual variability of LHF and the LHF-SST correlation in a 50-year CFS simulation and in 24-year CFS retrospective forecasts (Saha et al. 2006) against proxies derived from observational datasets, including the Goddard Satellite-based Surface Turbulence Fluxes version 2 (GSSTF2) for the period 1988-2000 (Chou et al. 2003) and the NOAA optimum interpolation (OI) version 2 monthly mean SST starting from November 1981 (Reynolds et al. 2002). A 30-year SST forced simulation of the atmospheric model of the CFS, i.e., the Global Forecast System (GFS), is also analyzed to give the information of how different the coupled and forced simulations are regarding the LHF variability and the LHF-SST relationship. The SST forcing for the forced simulation is from the CFS simulation.

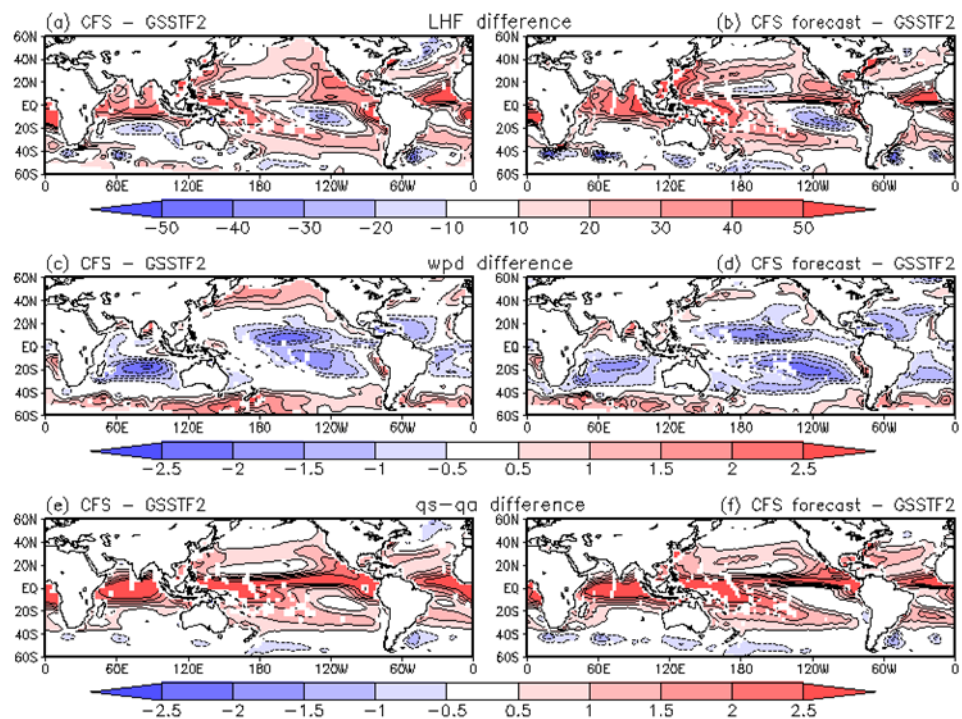


Figure 1 CFS simulation minus GSSTF2 differences of mean LHF (Wm^{-2}) (a), mean surface wind speed (m/s) (c), and mean sea-air humidity difference (g/kg) (e). (b), (d), and (f) are the same to (a), (c), and (e) except for the CFS retrospective forecasts with 1-month lead.

*Correspondence to: Renguang Wu, Center for Ocean-Land-Atmosphere Studies, 4041 Powder Mill Road, Suite 302, Calverton, MD 20705; E-mail: renguang@cola.iges.org

2. Mean and interannual variability

The distribution of mean LHF in GSSTF2 has been documented in previous studies (Chou et al. 2003; Feng and Li 2006). Large mean LHF is seen in trade wind belts and in the western boundary warm current regions of Kuroshio and Gulf Stream due to high surface winds coupled with large sea-air humidity differences. The LHF is also large in the Arabian Sea and the Bay of Bengal region in relation to the monsoon activity. Small LHF is seen in the eastern equatorial Pacific and Atlantic due to weak winds and upwelling-induced cold SSTs, and in high latitudes due to poleward decrease of SSTs. The LHF is also small in the equatorial eastern Indian Ocean-western Pacific warm pool region, mainly due to weak surface winds.

The CFS simulation and forecasts produces much larger LHF in the equatorial Indian Ocean-western Pacific, eastern equatorial Pacific, eastern tropical North Pacific, equatorial Atlantic, north of equatorial Atlantic, and in the western boundary current regions of Kuroshio and Gulf Stream (Figs. 1a-b). The difference of mean LHF in these regions exceeds 30 Wm^{-2} . In trade wind belts, the CFS produces smaller LHF, especially in the South Pacific where the difference reaches about 20-30 Wm^{-2} .

Higher LHF in the warm pool, cold tongue, and warm current regions is due to larger sea-air humidity difference (Figs. 1e-f). This, in turn, is attributed to lower surface air humidity (not shown). Higher LHF in the Bay of Bengal and northern Arabian Sea is due to higher wind speed (Figs. 1c-d). The wind speed in trade wind belts is weaker in the CFS, leading to smaller LHF in the subtropical South Indian and Pacific Oceans. In the mid-ocean part of the Pacific Inter-tropical Convergence Zone and western tropical North Atlantic, the effects of weaker trade winds are nearly cancelled by the effects of larger sea-air humidity difference.

Large LHF variability tends to occur in regions of high mean LHF because high mean wind speed and large sea-air humidity difference not only lead to high mean LHF, but also favor large LHF variability. In GSSTF2 (Fig. 2a), the variability is large over subtropical regions and western boundary warm current regions. The variability is small in eastern tropical Atlantic, eastern equatorial Pacific, and in high latitudes. The variability is relatively low in the equatorial eastern Indian Ocean and western Pacific.

Compared to GSSTF2, the CFS simulation (Fig. 2b) displays larger LHF variability in the equatorial Indian Ocean-western Pacific, coastal southeast China, tropical eastern North Pacific, tropical eastern North Atlantic. This is related to larger mean sea-air humidity difference in the CFS (Fig. 1e). The larger variability in high latitudes may be due to higher mean wind speed (Fig. 1c) and larger wind speed variability in the CFS. The

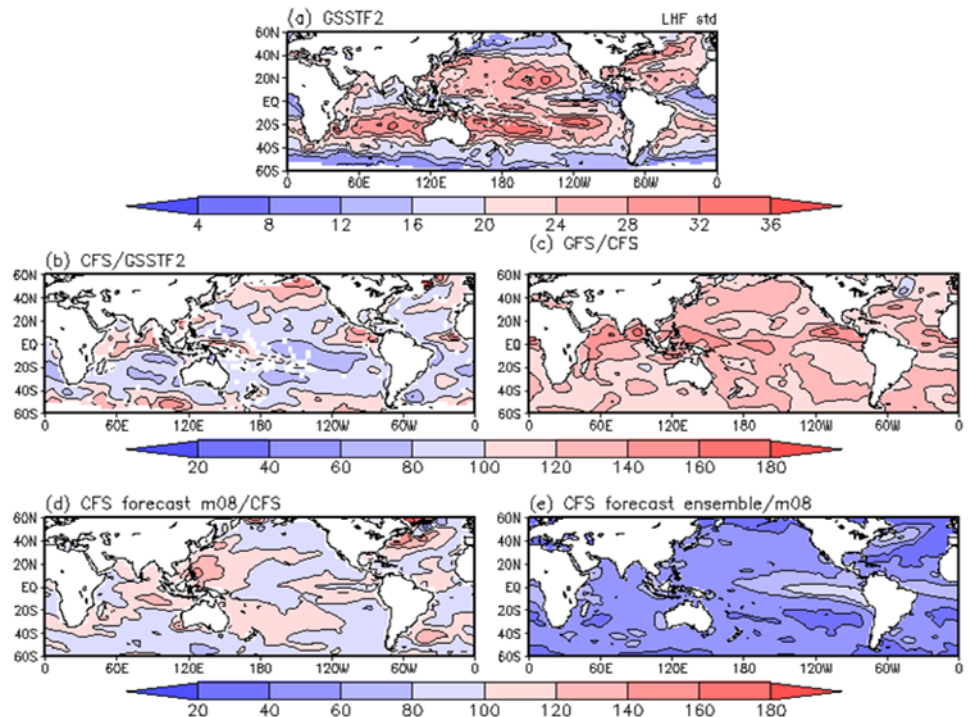


Figure 2 Standard deviation of monthly mean LHF anomalies (Wm^{-2}) from GSSTF2 (a), standard deviation ratio (%) of CFS simulation to GSSTF2 (b), GFS to CFS simulation (c), CFS individual forecast of 1-month lead to CFS simulation (d), and CFS ensemble forecast to individual forecast with 1-month lead (e).

variability in trade wind belts is smaller in the CFS compared to GSSTF2, which is related to weaker mean wind speed (Fig. 1c) and smaller variability of sea-air humidity difference in the CFS.

Compared to the CFS coupled simulation, the SST forced GFS simulation (Fig. 2c) displays larger variability globally. The most pronounced variability increase is seen in the tropical Indian Ocean-western Pacific, eastern tropical North Pacific and Atlantic. The increase of variability in these regions reaches 40%. This increase is due to the lack of atmospheric negative feedback in the forced simulation, which increases the persistence of atmospheric anomalies and leads to excessively large seasonal mean rainfall and surface LHF anomalies (Wu and Kirtman 2005). This is most pronounced in regions of warm SST and high mean rainfall where the atmospheric internal dynamics is active and contributes to SST variations.

The individual CFS retrospective forecast displays a spatial distribution of LHF variability similar to the CFS coupled simulation. The difference in the magnitude of the LHF variability is within 20% in most regions (Fig. 2d). An increase over 20% is seen in the eastern tropical Indian Ocean, the western North Pacific and Atlantic.

The CFS forecast ensemble shows significantly reduced LHF variability, presumably due to ensemble averaging. The ensemble mean LHF variability is less than 60% of individual member in most of the regions (Fig. 2e). This suggests that the LHF has a large component of high frequency variations driven by atmospheric internal dynamics. The effects are smallest in the eastern equatorial Pacific, equatorial Atlantic, and mid-latitude western North Atlantic where the ocean forcing of the atmosphere dominates.

3. Latent heat flux-SST correlation

In observations (Fig. 3a), positive LHF-SST correlation is seen in the eastern equatorial Pacific and Atlantic, western North Pacific, western North Atlantic, tropical North Atlantic, southwest coast of Australia, and south of Africa. In the equatorial central-western Pacific and most of the tropical Indian Ocean, the correlation is negative. The LHF-SST tendency correlation is negative in mid-latitudes, equatorial central-western Pacific, north Indian Ocean, and coastal Sumatra (Figure 6c of Wu et al. 2006). The above distribution of correlation indicates the dominance of oceanic forcing of the atmosphere in the eastern equatorial Pacific and Atlantic, and the dominance of atmospheric forcing of the ocean in mid-latitudes and the contribution of atmospheric forcing to SST variations in the eastern Indian Ocean-western Pacific.

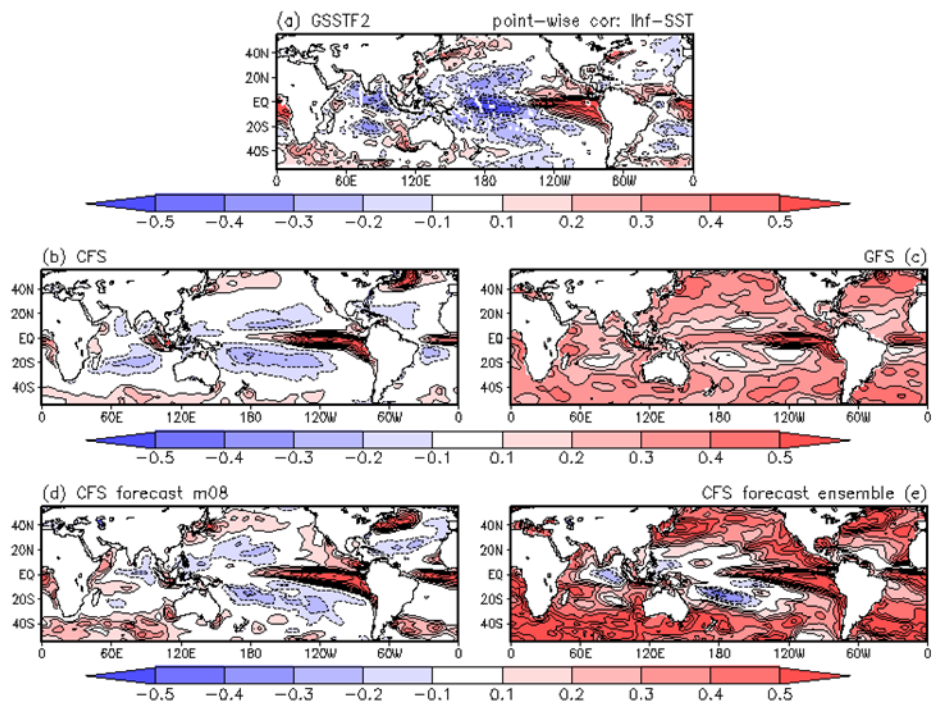


Figure 3 Point-wise and simultaneous LHF-SST correlation derived from GSSTF2 and OI version 2 SST (a), the CFS coupled simulation (b), the GFS forced simulation (c), an individual member of CFS forecasts of 1-month lead (d), and CFS ensemble forecasts of 1-month lead (e).

The CFS coupled simulation (Fig. 3b) captures the positive correlation in the eastern equatorial Pacific and Atlantic, and in the western North Pacific and North Atlantic, but misses the negative correlation in the

equatorial western-central Pacific. In particular, the simulation produces a positive correlation in the coastal Sumatra-Java region, which is in sharp contrast with observations. This positive correlation suggests the dominance of oceanic forcing of the atmosphere, as in the eastern equatorial Pacific and Atlantic. This disagrees with observations.

The GFS forced simulation (Fig. 3c) displays the dominance of positive LHF-SST correlation. This contrasts with the coupled simulation and indicates that the forced simulation produces spurious oceanic forcing of the atmosphere, consistent with previous studies (Wu et al. 2006).

The CFS individual forecast (Fig. 3d) displays LHF-SST correlation similar to the CFS simulation. There are, however, some regional differences. In the eastern tropical Indian Ocean, the positive LHF-SST correlation is limited in spatial coverage compared to the coupled simulation. When the forecast lead time increases, the positive correlation in the eastern Indian Ocean becomes more similar to the coupled simulation (not shown).

In the CFS ensemble forecasts (Fig. 3e), the LHF-SST correlation displays large differences from the individual forecast; the ensemble forecast has a much larger and broader positive correlation. This difference occurs because the ensemble averaging removes the high-frequency LHF variations that are weakly correlated with SST variations. The remaining low frequency LHF variations are largely induced by SST variations and thus have a positive correlation with SST. With the increase of forecast lead time, the spatial coverage of positive LHF-SST correlation is reduced in particular in mid-latitudes (not shown).

The discrepancy in the LHF-SST correlation is mainly due to excessive dependence of sea-air humidity difference on SST in the CFS simulation and forecast. This is confirmed by comparing the correlation between the sea-air humidity difference and SST. In the CFS coupled simulation and retrospective forecasts, the correlation between sea-air humidity difference and SST is very high (correlation coefficient > 0.7) (not shown). The corresponding correlation based on observations is below 0.5 except for eastern tropical Pacific and Atlantic.

4. Latent heat flux-SST relationship in the eastern equatorial Indian Ocean

Observational evidence indicates that the development of the Indian Ocean dipole/zonal mode during boreal summer involves a positive wind-evaporation feedback (Wang et al. 2003; Wu and Kirtman 2007). Can the CFS simulation or retrospective forecasts capture the positive wind-evaporation feedback in the above region? To address this question, we have calculated monthly simultaneous correlation with respect to SST anomalies for the region of 0°-10°S, 90°-105°E (Fig. 4).

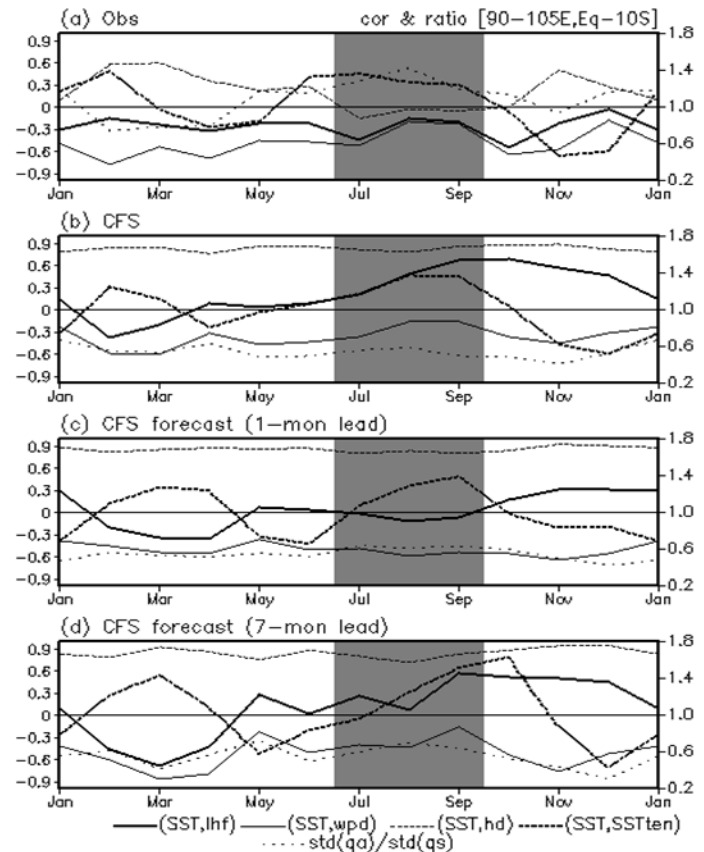


Figure 4 Point-wise and simultaneous correlation (scale at left) of LHF (thick solid), surface wind speed (thin solid), sea-air humidity difference (thin dashed), and SST tendency (thick dashed) with respect to SST, and ratio (dotted; scale at right) of standard deviation of surface air humidity to that of sea humidity, area averaged over the region of 5°S-5°N and 170°-90°W and derived from GSSTF2 and OI version 2 SST (a), the CFS coupled simulation (b), and CFS ensemble forecasts of 1-month lead (c) and 7-month lead (d).

The CFS simulation and CFS retrospective forecasts capture the SST warming during boreal summer although the positive SST tendency appears about 1-2 months later in the CFS forecasts. In observations, the LHF is reduced due to a decrease in wind speeds, indicating a positive feedback of evaporation on SST. In the CFS simulation, however, LHF anomalies are positive, i.e., surface evaporation has a damping effect on the existing warm SST anomalies, which is opposite to observations. This occurs because of the large positive correlation between sea-air humidity difference and SST. In the 1-mon lead CFS forecasts, LHF anomalies are weak because of the cancellation of sea-air humidity difference effects on the wind speed effects. When the forecast lead time increases to 7 months, LHF anomalies become positive as in the CFS simulation.

A common feature of the CFS simulation and retrospective forecasts is that the sea-air humidity difference follows closely the SST variation, whereas in observations the sea-air humidity difference is not as closely related to SST. This discrepancy occurs because the CFS has a dry bias in the eastern equatorial Indian Ocean that leads to smaller variability in the surface air humidity compared to that of sea humidity (Figs. 4b-d). As such, the sea-air humidity difference anomalies follow the sea humidity (or SST) anomalies. In observations, the variability of the air humidity is larger than that of the sea humidity (Fig. 4a).

5. Summary

The CFS mean LHF is higher than satellite estimates in the tropical Indo-western Pacific, tropical Atlantic, eastern tropical Pacific, and Kuroshio and Gulf Stream regions. This discrepancy is due to larger sea-air humidity difference. In the South Indian and Pacific Ocean trade wind belts, the CFS mean LHF is lower than satellite estimate due to weaker winds. The forced simulation produces a larger variability of LHF due to the lack of atmospheric negative feedback. The CFS ensemble forecasts have much smaller variability of LHF due to reduced high frequency variability.

The CFS simulations and retrospective forecasts display large discrepancy from observations in the local LHF-SST correlation in the eastern equatorial Indian Ocean and western-central equatorial Pacific. This discrepancy is due to an excessively large contribution of sea-air humidity difference to the LHF-SST correlation. The ensemble averaging in retrospective forecasts significantly increases the LHF-SST correlation in mid-latitudes.

The CFS simulation fails to capture the LHF-SST relationship in the eastern equatorial Indian Ocean. In observations, the wind-evaporation feedback contributes to the development of SST anomalies in the eastern pole of the Indian Ocean Dipole/Zonal Mode during boreal summer. In the CFS simulation, surface LHF acts as a damping term due to an excessive SST dependence in the sea-air humidity difference anomalies. While the short-lead CFS retrospective forecasts appear better than the CFS simulation in this aspect, this problem shows up when the forecast lead time increases.

The discrepancies between the CFS and observations in the eastern Indian Ocean-western Pacific are related to a dry bias in the CFS. The dry bias leads to lower variability in the surface air humidity because the interaction between convection and circulation depends on the mean state. As a result, the CFS underestimates the atmospheric forcing of SST, and overestimates the SST forcing of the atmosphere in the above regions. This suggests the importance of improving the simulation of mean moisture fields. The specific reasons for the dry bias remain to be uncovered.

References

- Barsugli, J. J., and D. S. Battisti, 1998: The basic effects of atmosphere-ocean thermal coupling on midlatitude variability, *J. Atmos. Sci.*, **55**, 477-493.
- Chang, C.-P., L. Ji, and H. Li, 1997: A decadal climate variation in the tropical Atlantic Ocean from thermodynamic air-sea interactions. *Nature*, **385**, 516-518,
- Chou, S.-H., E. Nelkin, J. Ardizzone, R. M. Atlas, and C.-L. Shie, 2003: Surface turbulent heat and momentum fluxes over global oceans based on the Goddard Satellite retrievals, version 2 (GSSTF-2), *J. Climate*, **16**, 3256-3273.
- Feng, L., and J. Li, 2006: A comparison of latent heat fluxes over global oceans for ERA and NCEP with GSSTF2, *Geophys. Res. Lett.*, **33**, L03810, doi:10.1029/2005GL024677.

- Reynolds, R. W., N. A. Rayner, T. M. Smith, D. C. Stokes, and W. Wang, 2002: An improved in situ and satellite SST analysis for climate, *J. Climate*, **15**, 1609-1625.
- Saha, S. and Coauthors, 2006: The NCEP Climate Forecast System, *J. Climate*, **19**, 3483-3517.
- Saji, N. H., B. N. Goswami, P. N. Vinayachandran, and T. Yamagata, 1999: A dipole mode in the tropical Indian Ocean, *Nature*, **401**, 360-363.
- Wang, B., R. Wu., and T. Li, 2003: Atmosphere-warm ocean interaction and its impacts on the Asian-Australian monsoon variation, *J. Climate*, **16**, 1195-1211.
- Webster, P. J., A. M. Moor, J. P. Loschnigg, and R. R. Leben, 1999: Coupled ocean-atmosphere dynamics in the Indian Ocean during 1997-98, *Nature*, **401**, 356-360.
- Wu, R., and B. P. Kirtman, 2005: Roles of Indian and Pacific Ocean air-sea coupling in tropical atmospheric variability, *Clim. Dyn.*, **25**, 155-170.
- Wu, R., B. P. Kirtman, and K. Pegion, 2006: Local air-sea relationship in observations and model simulations, *J. Climate*, **19**, 4914-4932.
- Wu, R., and B. P. Kirtman, 2007: Regimes of seasonal air-sea interaction and implications for performance of forced simulations, *Clim. Dyn.*, **29**, 393-410.

Mean, Variability and the Most Predictable Patterns in CFS over the Tropical Atlantic Ocean

Zeng-Zhen Hu¹, Bohua Huang^{1,2}, and Kathy Pegion¹

¹Center for Ocean-Land-Atmosphere Studies, Calverton, MD

²Department of Climate Dynamics, George Mason University, Fairfax, VA

(1) Model and Model Output

As a state-of-the-art coupled system, the National Centers for Environmental Prediction (NCEP) Climate Forecast System (CFS) is now being used at NCEP for operational seasonal climate predictions. It has been demonstrated that the CFS reproduces the major features of the El Niño-Southern Oscillation (ENSO) (Wang et al. 2006; Saha et al. 2006) and the Asian and Australian monsoon (Liang et al. 2008). The atmospheric component of the CFS has horizontal resolution of T62 and 64 vertical sigma levels. The oceanic component is configured from the version 3 of the Modular Ocean Model of Geophysical Fluid Dynamics Laboratory (Pacanowski and Griffies 1998). The ocean model has 40 levels vertically, with 27 of them in the upper 400 meters. The domain of the ocean model extends from 74°S to 64°N with a horizontal grid of 1°x1° poleward of 30°S and 30°N, and with gradually increased meridional resolution to 1/3° between 10°S and 10°N. The atmospheric and oceanic components exchange surface fluxes on a daily interval without flux adjustment.

The NCEP CFS hindcasts analyzed in this work were initialized in all calendar months from 1981 to 2003. In a given start month, 15 nine month predictions were produced. The oceanic initial conditions (ICs) were taken from the NCEP Global Ocean Data Assimilation (GODAS) (Behringer et al. 1998, Behringer and Xue 2004) analyses on 11th and 21st of lead-month 0 and 1st of lead-month 1 (Saha et al. 2006). The atmospheric ICs were from the NCEP reanalysis II (Kanamitsu et al., 2002). For each of the three chosen oceanic ICs, five atmospheric ICs from 2 days before to 2 days after at daily interval were chosen to form 15 ocean-atmosphere ICs. The details about the ICs were given in Saha et al. (2006) and Huang et al. (2007). The monthly mean of the 15 individual member predictions and their ensemble mean are available from the NCEP website at

<http://nomad6.ncep.noaa.gov/cfs/monthly>.

In addition, a 52-year coupled integration using CFS was conducted at the Center for Ocean-Land-Atmosphere Studies (COLA). The ocean-atmospheric IC is from January 1, 1985. The monthly data of the last 42 years, after a 10-year spin-up, are used in this analysis.

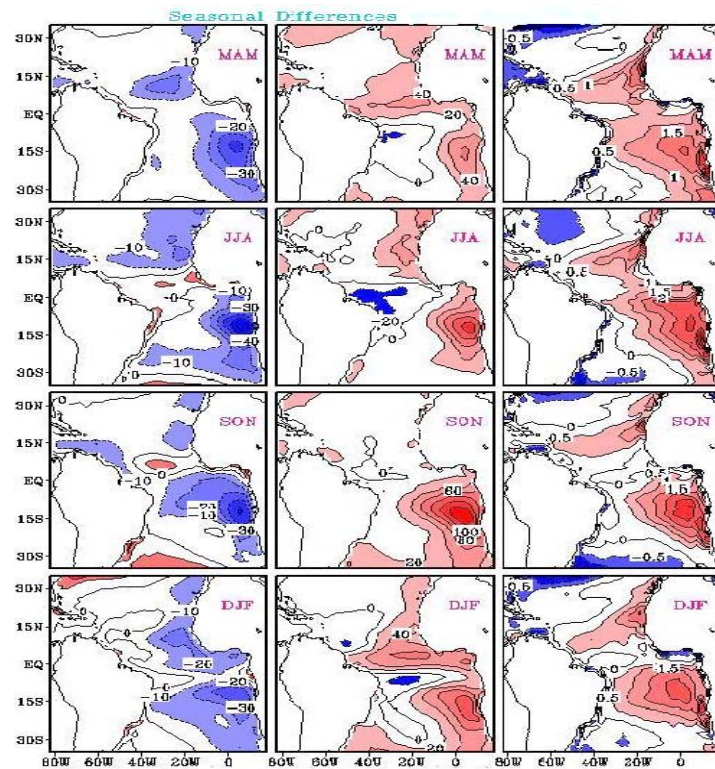


Figure 1 Seasonal mean climatology differences of low clouds (left column), downward short-wave radiation (central column), and SST (right column) between CFS simulation and corresponding analyses.

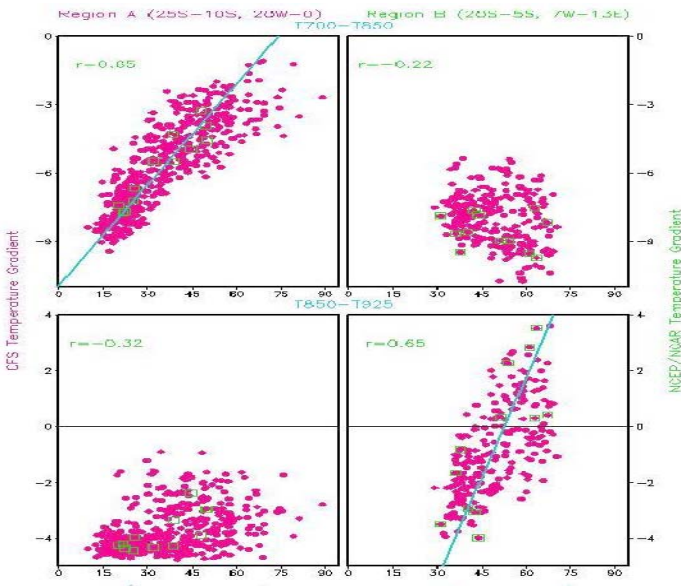


Figure 2 Scatter plot of low-level clouds (%) vs. T700–T850 ($^{\circ}\text{C}$, top panels), and vs. T850–T925 ($^{\circ}\text{C}$, bottom panels) averaged in the region of (25°S – 15°S , 20°W – 0) in the CFS (left column) and in the region of (20°S – 5°S , 7°W – 13°E) in the observations (right column). The circles represent individual monthly mean.

southeastern Atlantic could be a cause of the warm SST biases in this region.

The low-level clouds are linked to a stable or inversion layer between 850 hPa and 925 hPa in the observation, but found to be associated with a stable layer between 700 hPa and 850 hPa in the CFS (Fig. 2). On average, the lower troposphere is less stable in the CFS than in the observation over the tropical Atlantic, a condition more favorable for the development of deeper convection. Moreover, in the observation, the low-level cloud variability in the South Atlantic is mainly associated with anomalies in the southeastern Atlantic and along the African coast, but in the CFS prediction the anomalies are moved to the subtropical South Atlantic.

Overall, the interactive processes among the low-level clouds, vertical inversion layer, and SST are important. The inadequate low-level cloud (left column of Fig. 1) and excessive short-wave radiation (central column of Fig. 1) are associated with the warm SST biases in the southeastern Atlantic (right column of Fig. 1). In return, the warm biases do not favor an inversion layer and low cloud formation (Fig. 2). Details about this part are given in Hu et al. (2008a).

(3) Leading Modes and Physics

The mean annual cycle, interannual variability, and leading patterns of the tropical Atlantic Ocean simulated in a long-term integration of CFS are examined (Hu et al. 2008b). Besides the warm biases in the tropical southeastern Atlantic, it is found that the seasonal transition from warm to cold phase along the equator is delayed one month in the CFS compared with the observations. This delay might be related to the failure of the model to simulate the cross-equatorial meridional wind associated with the African monsoon.

The CFS realistically simulates both the spatial structure and spectral distributions of the three major leading patterns of the SST anomalies in the tropical Atlantic Ocean: the south tropical Atlantic pattern (STA), the North tropical Atlantic pattern (NTA), and the southern subtropical Atlantic pattern (SSA) (Fig. 3). The CFS simulates the seasonal dependence of these patterns and partially reproduces their association with ENSO. The dynamical and thermodynamic processes associated with these patterns in the simulation and the observations are similar.

Based on the results from the above CFS hindcasts and the long-term integration, we examined the model mean climate, variability (Hu et al. 2008a), leading modes and their physics (Hu et al. 2008b), as well as the predictive skill and the most predictable patterns (Hu and Huang 2007) in the tropical Atlantic. The main conclusions are listed in the following.

(2) Mean Climate and Variability

By comparing the CFS simulation with corresponding observation-based analyses/re-analyses, it is shown that the CFS captures the seasonal mean climate, including the zonal gradients of sea surface temperature (SST) in the equatorial Atlantic Ocean, even though the CFS produces warm mean biases and underestimates the variability over the southeastern ocean (right column of Fig. 1). It is also found that the CFS produces too few low-level clouds (left column of Fig. 1) and too many high-level clouds (not shown) over the southeastern part of the tropical Atlantic. The center of the low clouds in the model is also shifted westward, away from the cold tongue region, to the central ocean. The underestimation of low-level clouds in the

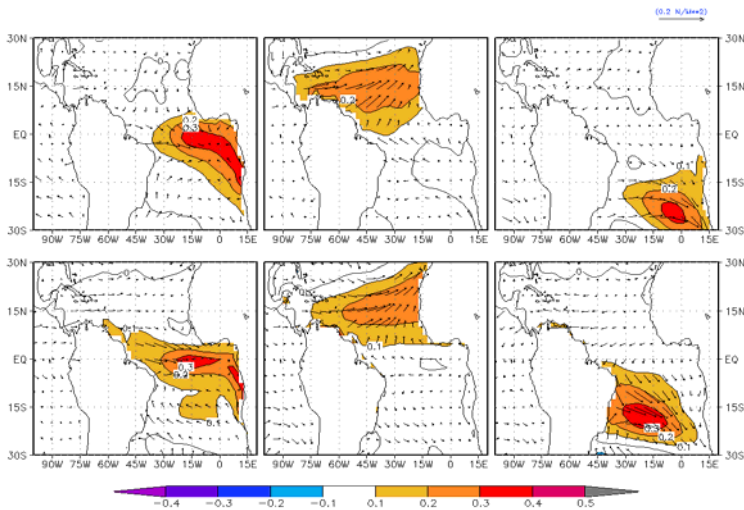


Figure 3 Spatial patterns (shading and contour) of REOFs of ERv2 (top panels) and the CFS simulated (bottom panels) seasonal mean SST in the tropical Atlantic (30°S–30°N, 100°W–20°E). The vectors represent the simultaneous regression of seasonal mean wind stress onto the corresponding time series of the REOF. The contour interval is 0.1°C. The percentages of the variance explained by each pattern are 16%, 15%, 10% (top panels from left to right), 10%, 11%, and 12% (bottom panels from left to right).

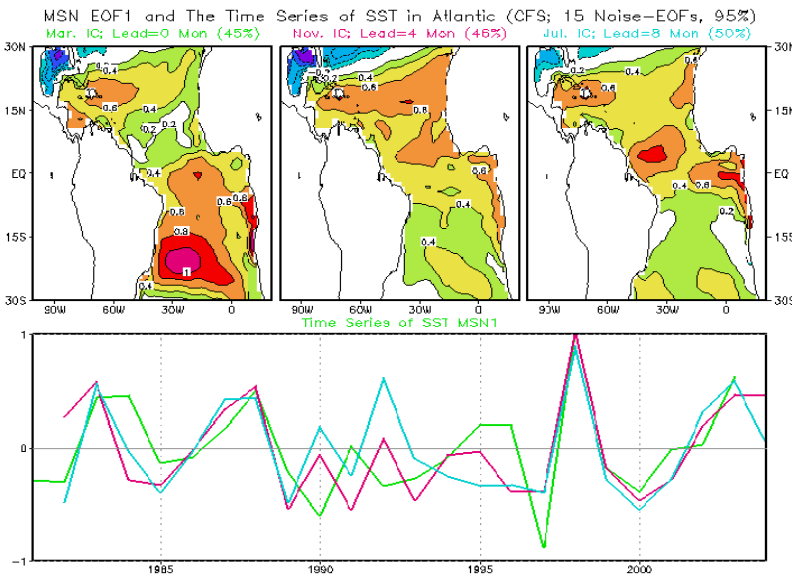


Figure 4 Spatial patterns (top panels) and time series (bottom panels) of MSN EOF1 of March SST, lead 0 month and March IC (top left), lead 4 months and November IC (top central), and lead 8 months and July IC (to right). The contour interval is 0.2, the zero lines are omitted, and the shading is for values larger than 0.2 or smaller than -0.2 for the spatial patterns. The real magnitude of the SST anomalies (°C) can be restored by multiplying the values in the spatial patterns with the corresponding time series. The percentage of the explained variance for the ensemble mean anomalies is indicated in each panel.

The air-sea interaction processes associated with the STA pattern are well simulated in the CFS. The primary feature of the anomalous circulation in the Northern Hemisphere (NH) associated with the NTA pattern resembles that in the Southern Hemisphere (SH) linked with the SSA pattern, implying a similarity of the mechanisms in the evolution of these patterns and their connection with the tropical and extratropical anomalies in their respective hemispheres. The anomalies associated with both the SSA and NTA patterns are dominated by atmospheric fluctuations of equivalent-barotropic structure in the extratropics including zonally symmetric and asymmetric components. The zonally symmetric variability is associated with the annular modes, the Arctic Oscillation in the NH and the Antarctic Oscillation in the SH. The zonally asymmetric part of the anomalies in the Atlantic is teleconnected with the anomalies over the tropical Pacific. The misplaced teleconnection center over the southern subtropical ocean may be one of the reasons for the deformation of the SSA pattern in the CFS.

(4) Predictive Skill and Most predictable Patterns

The predictive skill and most predictable patterns in the tropical Atlantic Ocean are studied using the CFS hindcasts (Hu and Huang 2007). The skill is measured by SST anomaly correlation between the predictions and the corresponding analyses. On average, for predictions with IC of all months, the predictability of SST is higher in the west than in the east. The highest skill is near the tropical Brazilian coast and in Caribbean Sea, and the lowest skill

occurs in the eastern coast. Seasonally, the skill is higher for predictions with IC in summer or autumn and lower for those with IC in spring. CFS poorly predicts the meridional gradient in the tropical Atlantic Ocean. The superiority of the CFS predictions to the persistence forecasts depends on IC month, region, and lead-time. The CFS prediction is generally better than the corresponding persistence forecast when lead-time is longer than 3 months.

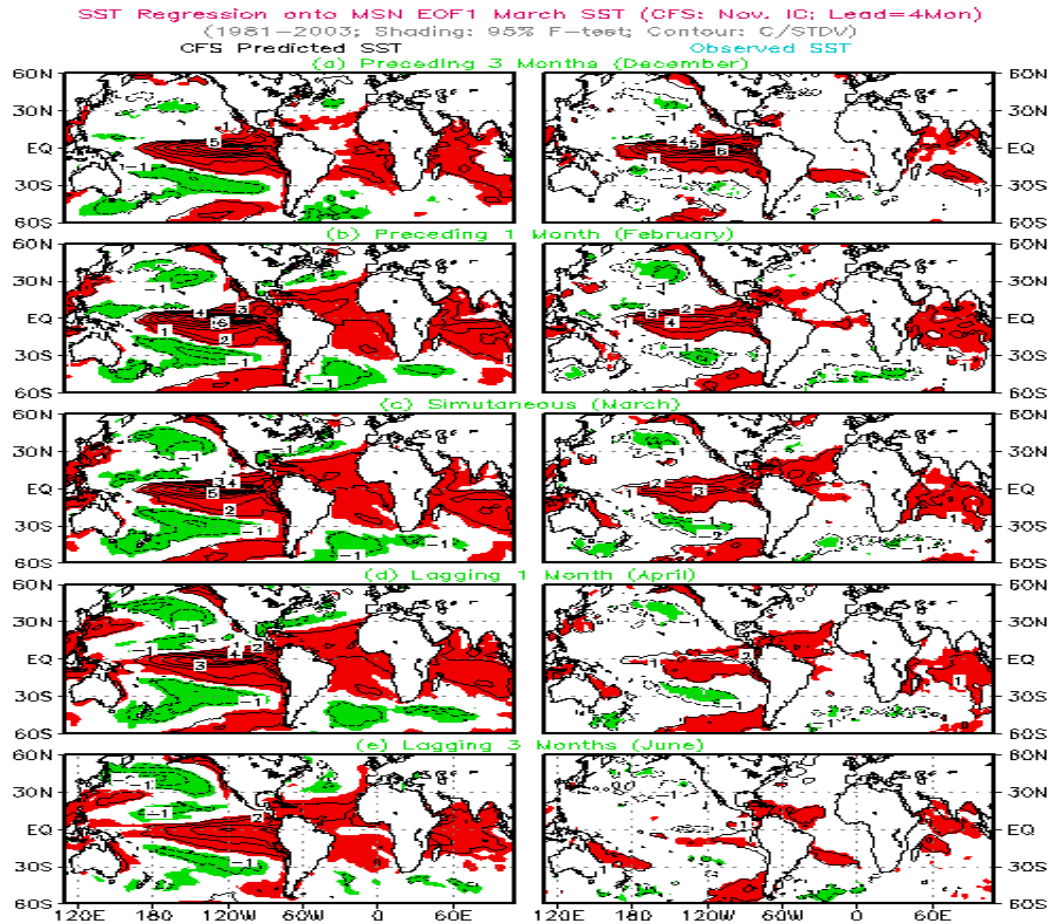


Figure 5 CFS predicted (left column) and OIv2 analyzed (right column) SST regression onto SST MSN EOF1 time series for lead 4 months and November IC (Fig. 4) at different leading and lagging months. The contour interval is 1.0°C per standard deviation of the MSN EOF1 time series, the zero lines are omitted, and the shading indicates the significance of the regression at the 95% confidence level.

The predictable patterns are identified by applying an empirical orthogonal function (EOF) analysis with maximized signal-to-noise ratio (MSN EOF hereafter) to the predicted time series of 1981–2003 with given lead-time of the hindcasts. The most predictable pattern of SST in March has the same sign in almost the whole tropical Atlantic (Fig. 4). The corresponding pattern of geopotential height at 200 hPa (H200) is dominated by the same sign in most of the domain, while the corresponding precipitation pattern showed a distinct opposite variation between the northwestern tropical North Atlantic and the regions from tropical South America to the southwestern tropical North Atlantic (not shown). The time series of the most predictable pattern of SST (Fig. 4), as well as the H200 and precipitation, are highly correlated with the SST in the eastern tropical Pacific (Fig. 5), implying that the predictable signals mainly result from the ENSO influence. The significant values in the most predictable precipitation pattern in the regions from tropical South America to the southwestern tropical North Atlantic in March are associated with the regional excessive divergence (convergence) at low (high) level in the

CFS hindcast. Due to the strong connection between ENSO and the most predictable patterns in the tropical Atlantic in the model, the predictive skill of the CFS in the tropical Atlantic is largely determined by its ability to predict ENSO. The relative high predictive skill of the tropical North Atlantic SST is consistent with the CFS ability of predicting ENSO on interseasonal time scales, particularly for the ICs in warm months from March to October. In the southeastern ocean, the systematic warm bias is considered as a crucial factor causing the low skill in that region.

Acknowledgements We appreciate the suggestions and comments of Drs. S. Saha, S. Yang, K. Campana, and Mr. B. Jha.

References

- Behringer, D., M. Ji, A. Leetmaa, 1998: An improved coupled model for ENSO prediction and implications for ocean initialization. Part I: The ocean data assimilation system. *Mon. Wea. Rev.*, **126**, 1013-1021.
- Behringer, D., and Y. Xue, 2004: Evaluation of the global ocean data assimilation system at NCEP: The Pacific Ocean. *Eighth Symposium on Integrated Observing and Assimilation Systems for Atmosphere, Ocean, Land Surface. AMS 84th Annual Meeting*, Seattle, Washington, January 11-15, 2004.
- Hu, Z.-Z., B. Huang, and K. Pegion, 2008a: Low cloud errors over the southeastern Atlantic in the NCEP CFS and their association with lower-tropospheric stability and air-sea interaction. *J. Geophys. Res. (Atmosphere)* (submitted).
- Hu, Z.-Z., B. Huang, and K. Pegion, 2008b: Leading patterns of the tropical Atlantic variability in a coupled general circulation model. *Clim. Dyn.*, DOI 10.1007/s00382-007-0318-x (in press).
- Hu, Z.-Z. and B. Huang, 2007: The predictive skill and the most predictable pattern in the tropical Atlantic: The effect of ENSO. *Mon. Wea. Rev.*, **135** (5), 1786-1806.
- Huang, B., Z.-Z. Hu, and B. Jha, 2007: Evolution of model systematic errors in the tropical Atlantic basin from the NCEP coupled hindcasts. *Clim. Dyn.*, **28** (7/8), 661-682, DOI 10.1007/s00382-006-0223-8.
- Kanamitsu, M., W. Ebisuzaki, J. Woollen, S.-K. Yang, J. J. Hnilo, M. Fiorino, and G. L. Potter, 2002: NCEP-DOE AMIP-II Reanalysis (R-2). *Bull. Amer. Meteor. Soc.*, **83**, 1631-1643.
- Liang, J., S. Yang, Z.-Z. Hu, B. Huang, A. Kumar, and Z. Zhang, 2007: Predictable patterns of the Asian and Indo-Pacific summer climate in NCEP CFS. *Clim. Dyn.*, (revised).
- Pacanowski, R. C., and S. M. Griffies, 1998: MOM 3.0 manual, NOAA/Geophysical Fluid Dynamics Laboratory, Princeton, New Jersey, USA 08542, 668 pp.
- Saha, S, S. Nadiga, C. Thiaw, J. Wang, W. Wang, Q. Zhang, H. M. van den Dool, H.-L. Pan, S. Moorthi, D. Behringer, D. Stokes, M. Pena, S. Lord, G. White, W. Ebisuzaki, P. Peng, and P. Xie (2006), The NCEP climate forecast system. *J. Climate*, **19**, 3483-3517.
- Wang, W., S. Saha, H.-L. Pan, S. Nadiga, and G. White, 2005: Simulation of ENSO in the new NCEP coupled forecast system model. *Mon. Wea. Rev.*, **133**, 1574-1593.

Sensitivity of the MJO to SST: A Simulation and Predictability Study of the MJO using the CFS and GFS

Kathy Pegion^{1,*} and Ben P. Kirtman^{1,2}

¹ Center for Ocean-Land-Atmosphere Studies, Calverton MD

² RSMAS/MPO, University of Miami, Miami, FL

1. Introduction

This study addresses the following two questions: 1) What is the impact of air-sea coupling on the simulation and predictability of the Madden-Julian Oscillation (MJO)? and 2) How sensitive is the predictability of the MJO to forcing by different SST variability. These questions can be viewed in terms of the forecast problem by asking at what lead time should coupled models be used to make forecasts and if a coupled model is not used, what the potential impact on skill is.

2. Model and Experiment Design

a) Model Description

This study investigates the impact of air-sea coupling on the simulation and predictability of tropical intraseasonal variability using the NCEP Climate Forecast System (CFS; Saha et al. 2006). Here, we give a brief description of the model. A more extensive description of the CFS is provided by Saha et al. (2006) and Wang et al. (2005). The CFS is a fully coupled atmosphere-ocean general circulation model used operationally by the NCEP for climate forecasts. It is composed of the NCEP Global Forecast System 2003 (GFS) as the atmospheric component and the Geophysical Fluid Dynamics Laboratory (GFDL) Modular Ocean Model version 3 (MOM3; Pacanowski and Griffies 1998) as the oceanic component. The GFS has a resolution of T62 in the horizontal and 64 layers in the vertical. The ocean model has a quasi-global domain ranging from 74°S to 64°N latitude. It has 40 layers in the vertical and a resolution of 1/3°x1° in the tropics and 1°x1° in the extratropics. The atmosphere and ocean exchange fluxes and sea surface temperatures once per day without flux correction. The sea ice extent is taken as climatology.

b) Simulation Experiments

A series of experiments are conducted to determine the impact of coupled air-sea feedbacks on the simulation of tropical intraseasonal variability in the CFS. These experiments are described in detail in Pegion and Kirtman 2007a. First, a control experiment is used to assess the ability of the CFS to simulate tropical intraseasonal variability. The control experiment is a freely coupled simulation initialized on Jan 1, 1985, and run for 52 years. The initial conditions for the atmosphere are from the NCEP Reanalysis-2 (Kanamitsu et al. 2002). The ocean is initialized from the Global Ocean Data Assimilation System (GODAS).

Second, to determine the impact of air-sea coupling on the simulation of tropical intraseasonal variability, an uncoupled experiment is performed using the atmospheric component of the CFS forced by prescribed, daily SST from the control simulation. The initial conditions are perturbed using atmospheric initial conditions from a different year of the control simulation. If the initial conditions are not perturbed, the control run is reproduced exactly. The uncoupled experiment is run for 32 years with the SSTs from the last 32 years of the control simulation.

c) Predictability Experiments

Since the goal is to estimate the impact of coupled air-sea feedbacks and on the predictability of the MJO and the sensitivity to SST, a series of predictability experiments are performed using both the coupled and uncoupled models. In the case of the uncoupled experiments, experiments are performed with different SST forcing including: “perfect” SST, forecast SST, monthly SST, persisted SST anomalies, and climatological SST.

*Correspondence to: Kathy Pegion, Center for Ocean-Land-Atmosphere Studies, 4041 Powder Mill Road, Suite 302, Calverton, MD 20705; E-mail: kpegion@cola.iges.org

The predictability experiments are performed for ten strong ($>2\sigma$) intraseasonal events selected from the coupled control simulation and the atmospheric initial conditions of these events are perturbed. The events are chosen according to the amplitude of the principal component (PC) time series of an extended empirical orthogonal function (EEOF) analysis of precipitation from the control simulation (Pegion and Kirtman 2007a). It is possible that the phase of the El Niño–Southern Oscillation (ENSO) may affect the propagation of the intraseasonal oscillation (Tam and Lau 2005) and its predictability. Therefore, in an attempt to reduce this impact, the selected events span the phases of the ENSO.

After the events are selected, ensembles are created by perturbing the atmospheric initial conditions to produce nine initial states. The coupled predictability experiments are initialized with the nine atmospheric states and the ocean initial conditions from the control simulation. They evolve with their own SSTs. The coupled predictability experiments by design have different SST evolutions than the control. On the other hand, the uncoupled experiments are initialized with the same nine atmospheric states and are forced by the different SSTs described above. All of the SSTs used to force the uncoupled model are derived from the coupled control simulation. These experiments are described in more detail in Pegion and Kirtman 2007.

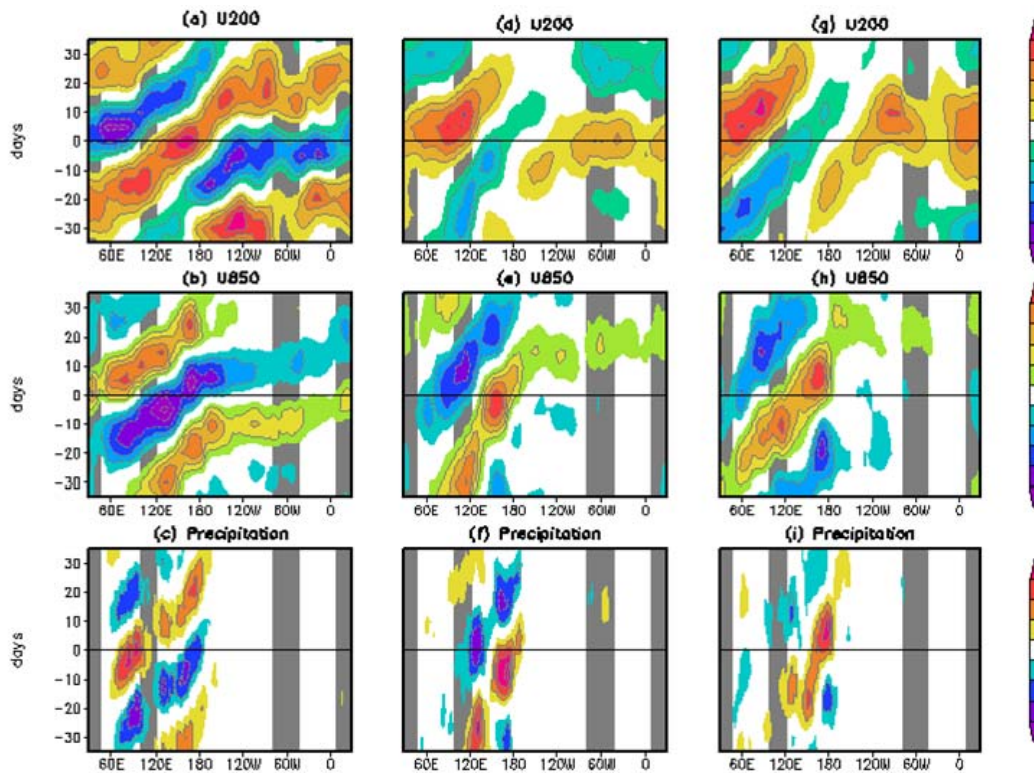


Figure 1 Time-longitude diagram of composite intraseasonal events averaged over 10°S – 10°N calculated from observed and reanalysis fields (a,b,c), 30 years of the CFS control simulation (d,e,f), and 30 years of the uncoupled simulation forced with daily SST (g,h,i). Composites are calculated by averaging events with PC timeseries amplitude $>2\sigma$. Twelve (twenty-one) events are averaged to make the observed (CFS) composite and twenty events are averaged to make the uncoupled composite. Time zero represents the average peak amplitude of precipitation. The top panels (a,d,g) are U200 (m/s), the middle panels (b,e,h) are U850 (m/s), and the bottom panels (c,f,i) are precipitation (mm/day).

3. The Impact of Air-Sea Interactions on the Simulation of the MJO

The simulation of the MJO is evaluated, by calculating composite events for U200, U850, and precipitation. Time-longitude diagrams of these composites are shown in Fig 1. In the composites from the coupled control simulation, the basic characteristics of the MJO are evident. There is eastward propagation from the Indian Ocean into the western Pacific Ocean in both U200 and U850. Additionally, eastward propagation is also

evident in precipitation; however it is weak in the Indian Ocean. In the region of enhanced (suppressed) precipitation, the lower level zonal winds are convergent (divergent) and the upper level zonal winds are divergent (convergent), consistent with observations. Also evident is a change in the phase speed once the convection becomes decoupled from the surface and the precipitation ceases near the dateline. The uncoupled model also has many of the characteristics of the observed MJO. There is eastward propagation from the Indian Ocean into the western Pacific Ocean in both U200 and U850. In the region of enhanced (suppressed) precipitation, the lower level zonal winds are convergent (divergent) and the upper level zonal winds are divergent (convergent), consistent with observations. The uncoupled model is also able to simulate the change in phase speed near the dateline. Similar to the coupled simulation, no precipitation anomalies are evident in the Indian Ocean because they remain too far south ($\sim 20^{\circ}\text{S}$; not shown). The main difference between the coupled and uncoupled composites (Fig 1, middle and right columns) is the organization of the precipitation. The precipitation in the uncoupled simulation is less organized. Although the precipitation propagates eastward from about 150°E to the dateline, it propagates westward near the Maritime Continent at about 120°E . These differences in propagation can be attributed to coupled air-sea interactions.

4. The Sensitivity of MJO Predictability to SST

a) Predictability Metrics

The predictability of intraseasonal precipitation is estimated in terms of the ability of each model to “forecast” the events from the control simulation. For this calculation, we calculate the pattern correlation precipitation anomalies in the Indo-Pacific region (30°S - 30°N ; 32.5°E - 92.5°W) over the nine ensemble members for the ten events between the predictability experiments and the control. The precipitation anomalies are first subject to a 30-day filter in order to remove the high frequency, synoptic variability. In order to apply the filter, 15-days from the control experiment are appended to the beginning of each of the predictability experiments. We also calculate correlations between the ensemble mean of the predictability experiments and the control over all 10 events. The ensemble mean is used in an attempt to reduce the “noise” and isolate any “signal” associated with the intraseasonal oscillation that is common among all ensemble members. Over lead-time, correlations will be reduced as the difference between the predictability experiment and the control simulation becomes larger. The limit of predictability for the correlations is subjectively defined as the time at which correlations fall below 0.5. We use this de-correlation time as a measure of predictability in order to mimic the way in which operational forecasts are verified. These predictability estimates are calculated for the coupled and uncoupled predictability experiments and their results are compared.

b) Predictability Estimates

The predictability estimates based on the ensemble members with the control are presented Fig. 2a as a function of lead-time. These estimates indicate that the coupled model has the longest predictability at about 18 days. The uncoupled model forced with perfect SST, forecast SST, and persisted SST anomalies all perform similarly with predictability estimates around 16-17 days. While most of the SST experiments have correlation coefficients that are very close together out to about 10 days, the monthly and climatological SST experiments both appear to lose skill more rapidly with estimates around 14 days and 9 days respectively. This is likely due to the fact that the initial SSTs for these experiments are out of balance with the initial atmospheric state whereas the other SST sensitivity experiments are initialized with SSTs that are the same as the coupled control run although the SSTs evolve differently. This underscores the importance of the balance between the atmosphere and ocean initial conditions as well as the importance of the initial SST containing the intraseasonal variability in SST.

The predictability estimates based on the correlation of the ensemble mean with the control shows a marked increase in predictability compared with the previous correlations with the exception of the climatological SST and monthly SST experiments (Fig. 2b). Both the forecast SST and perfect SST experiments show increases of about 7-8 days, when the ensemble mean is used. The largest increase as well as the longest predictability is seen in the coupled model, which has predictability estimates of about 36 days when the ensemble mean is used. By comparing the predictability estimates between the coupled and perfect SST experiments, it appears that coupled air-sea interactions provide about 12 days of additional predictability. However, perfect SST is not realistic for an operational forecast. Therefore, if a coupled model is not used, then the potential loss of forecast

skill is based on the predictability estimates from the forecast (~13 days less than coupled) or persisted SST anomaly (~16 days less than coupled) cases.

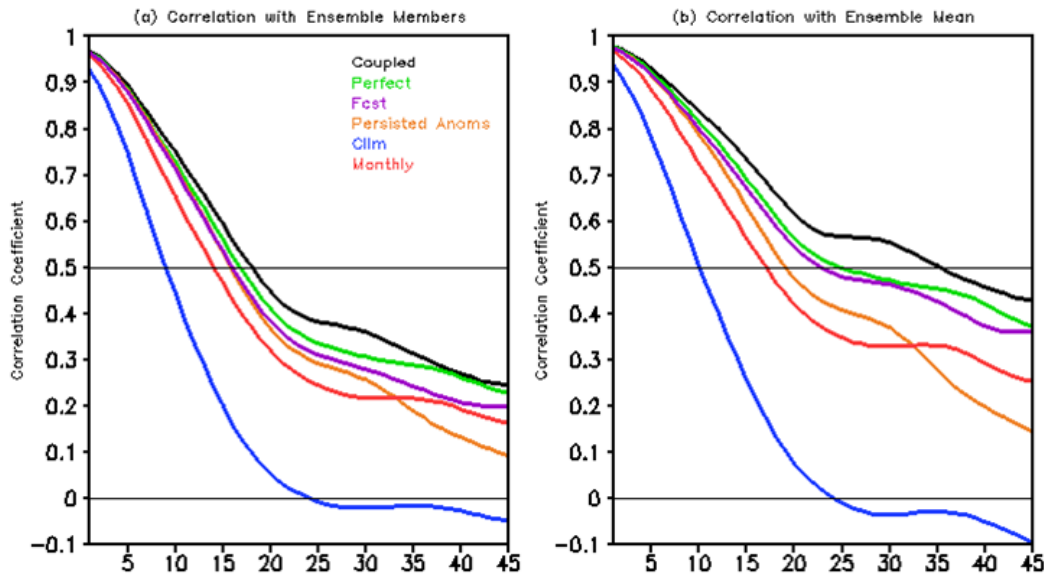


Figure 2 Predictability curves of filtered precipitation in terms of correlations between the ensemble members with the control (a) and correlations of the ensemble mean with the control (b) for the coupled experiment (black), the uncoupled experiment (green), the forecast SST experiment (purple), the persisted SST anomaly experiment (orange), the climatological SST experiment (blue), and the monthly SST experiment (red).

c) Implications for extended range forecasts

In the previous predictability calculations, the predictability is calculated over the entire Indo-Pacific region. Therefore, it is not possible to ascertain the specific locations that contribute to the “skill” of the forecasts. In this section, we focus on understanding the regions that potentially contribute to the skill of a week-3 forecast. The correlations over the nine ensemble members for all ten events are calculated at each point in the Indo-Pacific region for unfiltered precipitation anomalies averaged over a week-3 forecast. These correlations are calculated for the SST sensitivity experiments (excluding the climatological SST case) and shown in Fig 3. The bottom right panel (Fig 3f) shows the composite precipitation anomalies over all ten events from the control simulation for week-3. This is a composite picture of what the predictability experiments are trying to forecast. It is assumed that the “skill” in the predictability “forecasts” should be primarily due to the MJO-related precipitation. In general, the predictability experiments show skill in the region of positive precipitation anomalies with correlations exceeding 0.5. However, the region of highest correlations in all the experiments is located in the central Pacific Ocean with correlations exceeding 0.7. This indicates that ENSO may contribute strongly to forecast skill for week-3. In comparing the correlation maps for the different SST experiments, it is clear that degrading the SSTs produces a reduction in skill in the central Pacific and in the Indian Ocean for a week-3 forecast. Similar results are also seen for a week-4 forecast (not shown), although the correlations are weaker.

5. Conclusions

This study investigates the impact of coupled air-sea interactions on the simulation and predictability of the MJO and further attempts to understand the sensitivity of the predictability of the MJO to different SST variability. These questions are addressed by performing both simulation experiments and perfect model predictability experiments using the CFS. The main conclusions of this work are:

1. The CFS and GFS are able to simulate some of the major characteristics of the MJO, but there are deficiencies.

2. There is potential to improve forecasts of the MJO by using ensembles and a coupled model for week-2 and beyond. The loss of potential skill by not using a coupled model is approximately 18 days.
3. Forecasts for the MJO need to be initialized with atmospheric and oceanic initial conditions that contain intraseasonal variability and are in balance with each other.
4. There is potential skill for lead times of up to 4-weeks even without intraseasonal filtering. This skill comes from both ENSO and the MJO.

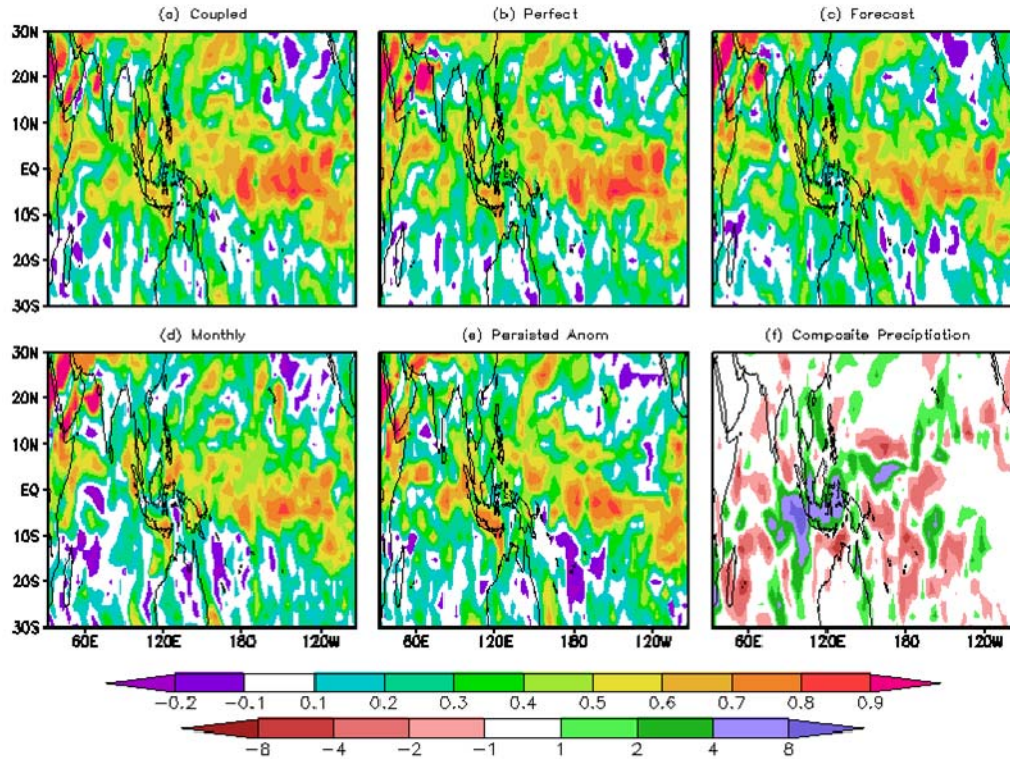


Figure 3 Correlation of unfiltered precipitation for a week-3 forecast calculated over the nine ensemble member for each of the ten events for the (a) coupled, (b) perfect SST, (c) forecast SST, (d) monthly SST, and (e) persisted SST experiments. The bottom right panel (f) shows the composite precipitation (mm/day) over all events from the control simulation for a week-3 forecast.

References

- Kanamitsu, M., W. Ebisuzaki, J. Woollen, S.-K. Yang, J. J. Hnilo, M. Fiorino, and G.L. Potter, 2002: NCEP-DOE AMIP-II Reanalysis (R-2). *Bull. Amer. Meteor. Soc.*, 83, 1631-1643.
- Pacanowski, R. C., and S. M. Griffies, 1998: MOM3 Manual, NOAA/Geophysical Fluid Dynamics Laboratory, Princeton, USA, 08542.
- Pegion, K. and B. P. Kirtman, 2007a: The Impact of Air-Sea Interactions on the Simulation of Tropical Intraseasonal Variability. *J. Climate.*, under revision.
- Pegion, K. and B. P. Kirtman, 2007b: The Impact of Air-Sea Interactions on the Predictability of the Tropical Intraseasonal Oscillation. Submitted to *J. Climate.*
- Saha, S., S. Nadiga, C. Thiaw, J. Wang, W. Wang, Q. Zhang, D. Behringer, W. Ebisuzaki, S. Lord, S. Moorthi, H. L. Pan, P. Peng, D. Stokes, H. M. van den Dool, G. White, P. Xie, 2006: The NCEP Climate Forecast System. *J. Climate*, 19, 2483-2516.

Tam, C. -Y., and N. -C. Lau, 2005: Modulation of the Madden-Julian Oscillation by ENSO: Inferences from Observations and GCM Simulations. *J. Met. Soc. Japan.*, 83, 727-743.

Wang W, Saha S, Pan HL, Nadiga S, White G (2005) Simulation of ENSO in the New NCEP Coupled Forecast System Model (CFS03). *Mon. Wea. Rev.*, 133, 1574–1593.

Evaluation of the Stratosphere in the Operational CFS and CFS-Next

Craig S. Long, Shuntai Zhou, Peitao Peng, S.K. Yang
Climate Prediction Center, NOAA/National Weather Service

An evaluation of the operational Climate Forecast System (CFS, T62L64) and a test version of the model, which may be used as the next version of the CFS (CFS-Next), has been conducted over the past 12 months. The purpose of this evaluation was to assess if the CFS forecasts are producing the basic state of the stratosphere correctly. The evaluation of the operational CFS was based upon 23 year averages of the monthly mean forecasts from 1982 through 2005. The multiyear CFS averages were compared against the Reanalysis-2 (R2) and the Climate Prediction Center (CPC) height, temperature and ozone analyses whenever possible. The focus was upon the 50 hPa heights, total ozone, zonal winds, and particularly the Quasi-Biennial Oscillation (QBO).

Beginning with 50 hPa heights, in comparison with R2 and CPC heights, we want to see if there is a bias between the CFS and these two standards, if the bias is uniform at all latitudes, and if the bias changes with forecast lead time. No bias or a constant bias is preferable, a variable bias with time, latitude, and/or initiating season indicates problems with the model dynamics and parameterizations. Figure 1 presents the average zonal mean 50 hPa heights at various lead times validating during the DJF time period. The average zonal mean R2 50 hPa heights for this same time period are plotted as well. There is an initial bias between the 0-month lead and the R2 heights at all latitudes, with the bias being greater in the SH, which is the summer hemisphere. This bias continues to grow until the 2-month lead, then seems to stabilize in the Northern Hemisphere (NH), but continues to grow in the Southern Hemisphere (SH). An evaluation of height field on other levels indicates that a bias between R2 and the CFS forecasts is present even at 500 hPa. This bias increases in magnitude, as does in the high latitude, and spreads from 500 to 50 hPa. The largest increase in the height bias occurs between 200 and 100 hPa.

Next, we evaluate the ozone field forecasts to see whether the equator to pole Brewer-Dobson circulation is correct and also if the parameterized chemistry is correct. Figure 2 presents the average zonal mean total ozone from the CFS forecasts validating during DJF. The average zonal mean total ozone from the Solar Backscatter Ultraviolet spectrometer (SBUV/2) is also plotted. Two features are apparent, large surpluses of ozone in the high latitudes and a deficit of ozone in the tropics. This implies that either the Brewer-Dobson

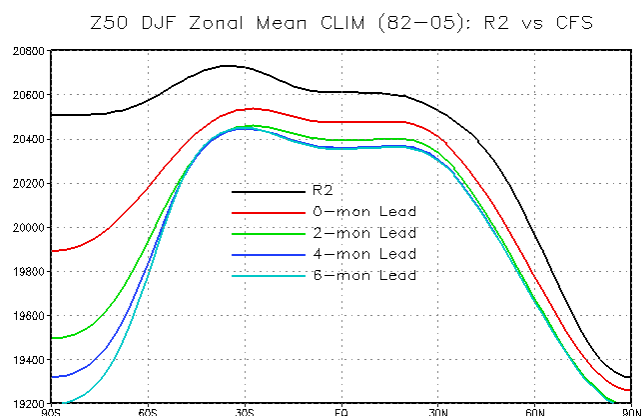


Figure 1 DJF climatology (1982-2005) of zonal mean 50 hPa height from Reanalysis 2 and CFS hindcasts at 0, 2, 4, and 6 months lead. (unit: m)

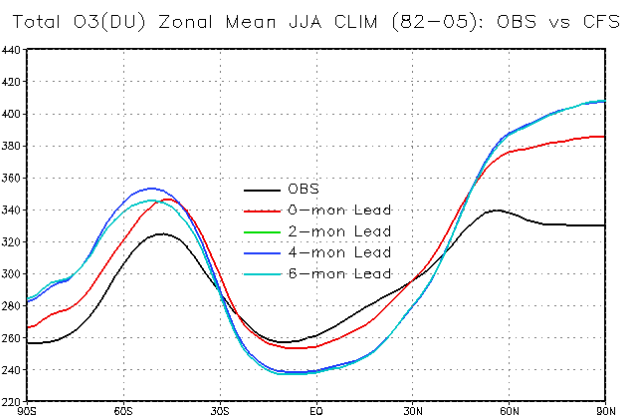


Figure 2 JJA climatology (1982-2005) of zonal mean total ozone from SBUV/2 and CFS hindcasts at 0, 2, 4, and 6 months lead. (unit: DU).

circulation is too aggressive or that the model's ozone Production/Loss parameterization is in error. These same features are also present in the JJA forecasts.

Reanalysis and CFS Zonal Winds at 30 hPa

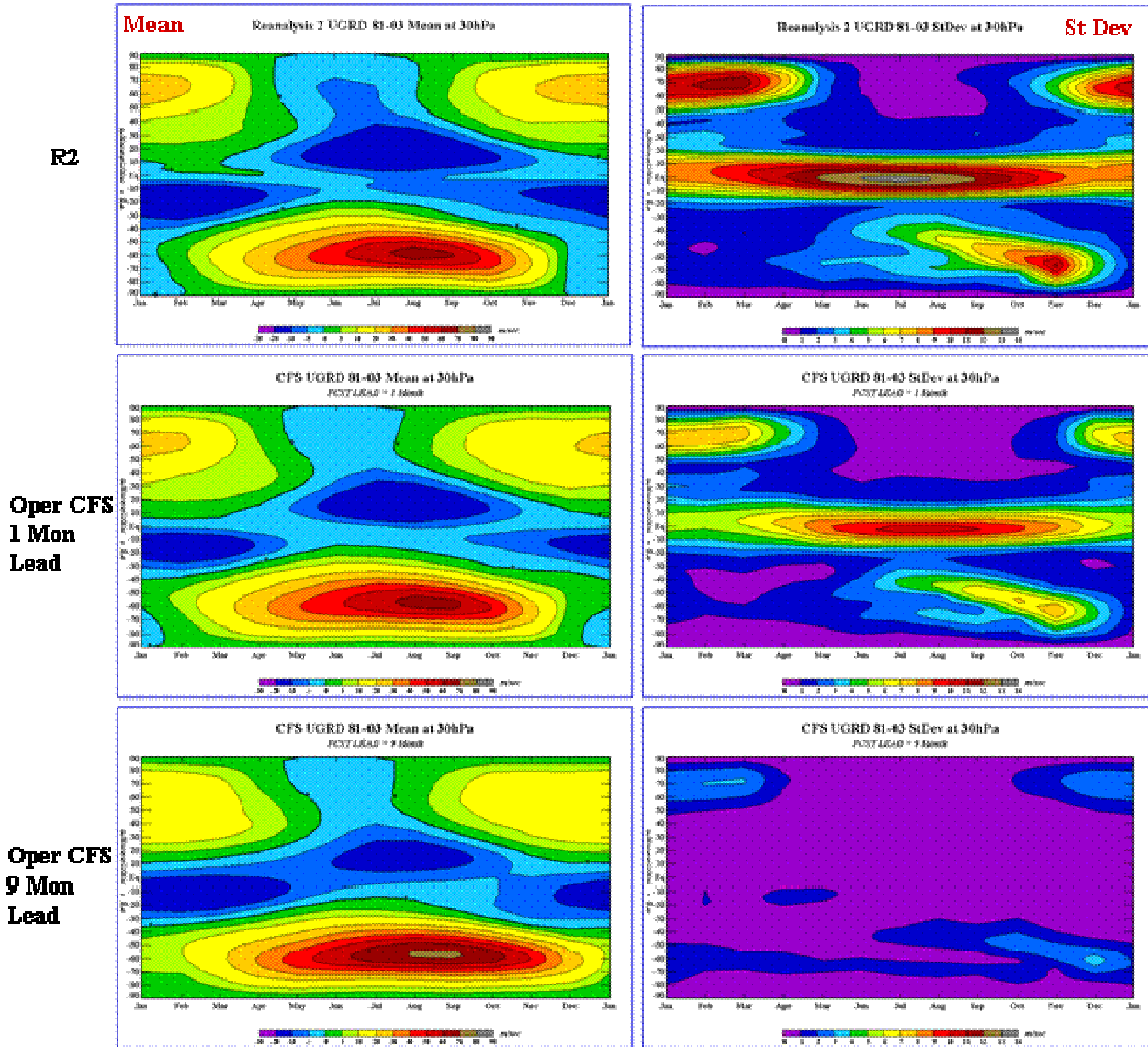


Figure 3 Annual cycle of 30 hPa zonal mean zonal winds (m/s) and their variability over the 1981-2003 period from Reanalysis 2 and CFS hindcasts at 1 month lead and 9 month lead.

If the height fields have an increasing bias, this must show up in the wind field differences. An evaluation of the CFS zonal mean wind fields from 100 hPa to 10 hPa and their variability from one year to the next (Figure 3) reveals that as the forecast time increases, the interannual variability decreases dramatically, particularly, for the equatorial winds and the SH polar jet. The winds in the SH also indicate that for longer forecasts there is no transition from winter to summer circulation, rather the circulation remains westerly, which is consistent with the strong height biases shown in Figure 1.

A closer look at the maintenance of the QBO revealed that the amplitude of the easterly and westerly zonal mean winds decreases with increasing forecast time (Figure 4). By the 5-month lead, the easterly winds are eliminated and by the 9-month lead the quasi-biennial nature of the winds has changed to a semiannual pattern.

The atmospheric component of the operational CFS uses the 2004 version of the Global Forecast System (GFS). Since then the operational GFS has had several modifications, of importance are changes to its long wave radiation code, the ozone production/loss scheme, its vertical coordinate system (from sigma to sigma-pressure hybrid), and now use of a Gridpoint Statistical Interpolation assimilation scheme. With these changes and improvements to what may be used for the CFS-Next, there were expectations of an improved basic state to the stratosphere. These expectations were assessed using output from a test experiment, which consists of 1 member runs initialized on May 15 for 25 years (from 1981-2006) using the T382L64 version of this model. This set of runs allows us to examine the model performance in the SH winter and spring period. Compared with the T62L64 15 member ensemble runs initialized in May for the same period (1981-2006), the bias in the JJA mean heights is greatly reduced at 50 hPa in the NH. However, there does not appear to be any improvement in the height bias in the SH. An examination of the JJA zonal mean temperatures (Figure 5) from the surface to 1 hPa reveals that the CFS and R2 agree with each other to within 1° C from the surface up to 200 hPa. Above 200 hPa the CFS is 6-9° C colder than R2 north of 30°S. While in the SH polar regions the bias between the CFS and R2 ranges from 6° C (at 70 hPa) to greater than 20° C above 5 hPa. The same is true for September-October (SO) temperatures except that the SH polar temperatures differ by 6° C at 150 hPa and the maximum cold bias has lowered to between 30 and 2 hPa. In the NH a warm bias shows up between 10 and 5 hPa poleward of 60° N.

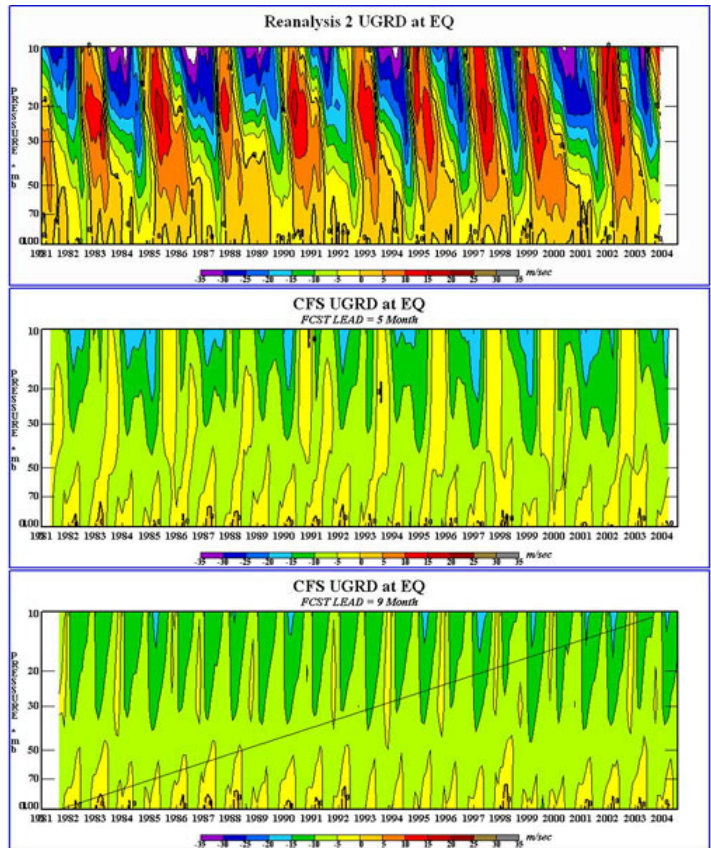


Figure 4 Pressure-time plots of the zonal wind (m/s) averaged between 10N and 10S from Reanalysis 2 (upper panel), CFS at 5 month lead (middle panel), and CFS at 9 month lead (lower panel).

The same is true for September-October (SO) temperatures except that the SH polar temperatures differ by 6° C at 150 hPa and the maximum cold bias has lowered to between 30 and 2 hPa. In the NH a warm bias shows up between 10 and 5 hPa poleward of 60° N.

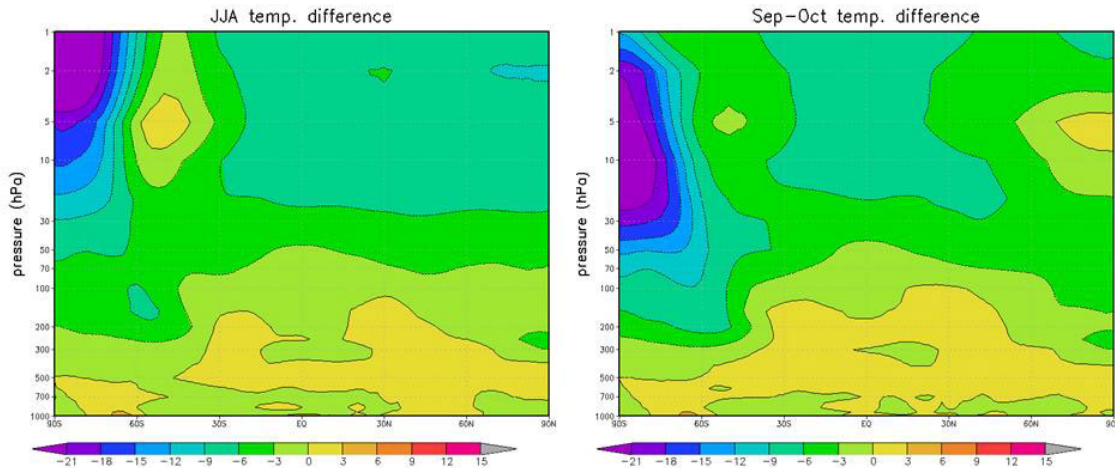


Figure 5 1000-1 hPa zonal mean temperature differences between CFS and R2 for JJA (left) and SO (right).

The impacts of the temperature bias upon the heights and consequently upon the wind fields reveal that the differences upon the wind fields occurs equatorward of the SH polar jet, beginning at 200 hPa and extending to lower pressures as forecast time increases.

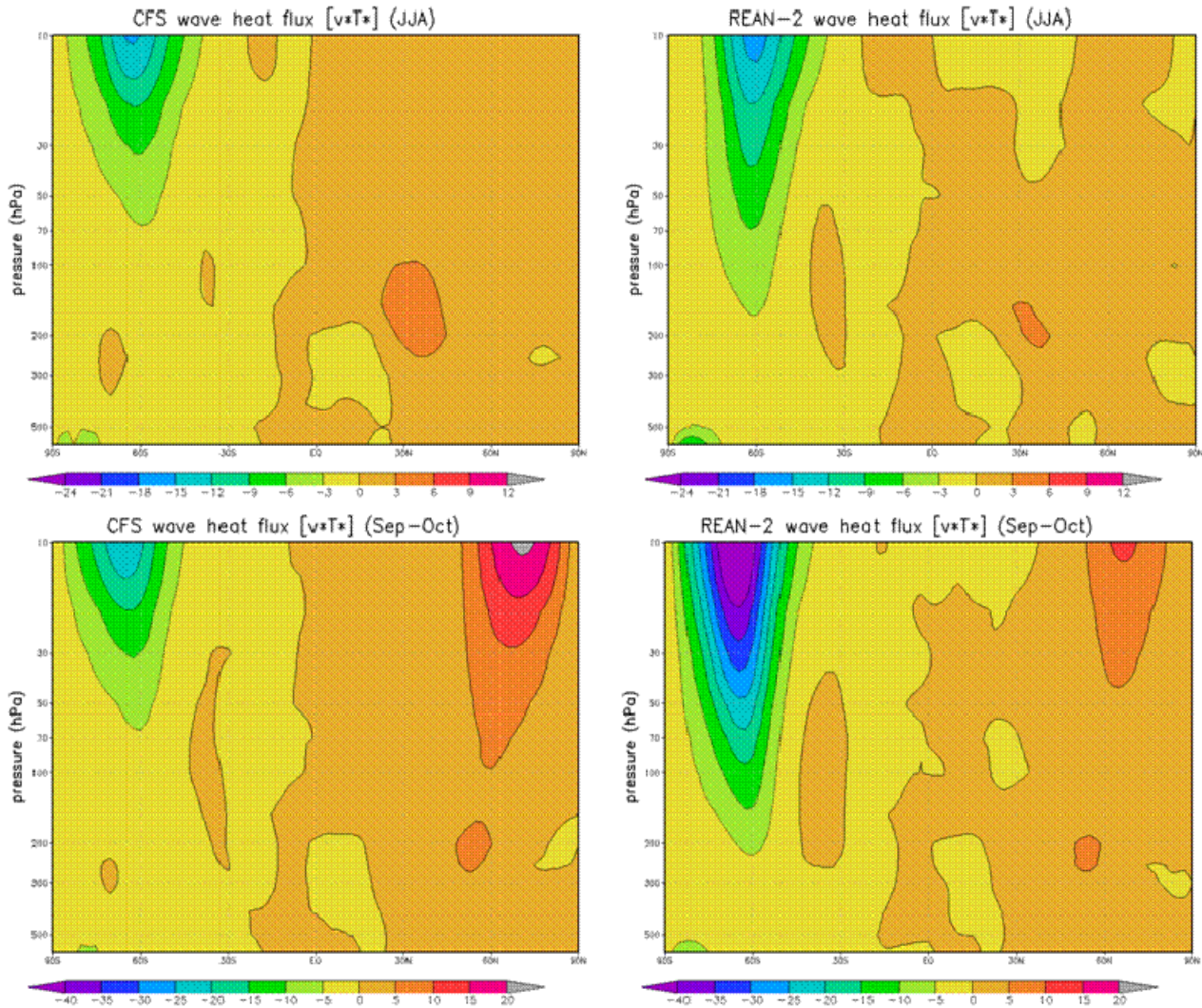


Figure 6 600-10 hPa zonal mean stationary wave heat flux (v^*T^*) (km/s). (a) CFS for JJA, (b) R2 for JJA , (c) CFS for SO, and (d) R2 for SO.

An examination of the poleward heat flux by stationary waves (v^*T^*) (Figure 6) indicates that in JJA the south poleward heat flux is weaker than R2 and does not extend towards the surface beyond 70 hPa. While the heat flux in R2 extends down to almost 200 hPa. In SO the CFS south polar heat flux is much less than R2 (-20 K m s⁻¹ vs < -40 K m s⁻¹). However, the CFS has a stronger northward north polar heat flux (>20 K m s⁻¹ vs. 10 K m s⁻¹). This would explain why the CFS has a positive temperature bias between 10 and 5 hPa poleward of 60° N.

Vertical-longitudinal cross-sections of height anomalies are useful to detect the baroclinicity of the atmosphere. A westward tilt of the anomalies with height (decreasing in pressure) is indicative of poleward heat flux. Such a cross-section at 50° S was taken of the 25 year mean R2 and CFS (Figure 7). The R2 cross-section shows a negative tilt of the primary wave from 0°E at the surface to 60°W at 10 hPa. Besides having quite different wave structures, the CFS waves are vertically stacked, indicative of a barotropic atmosphere with weak polar heat flux.

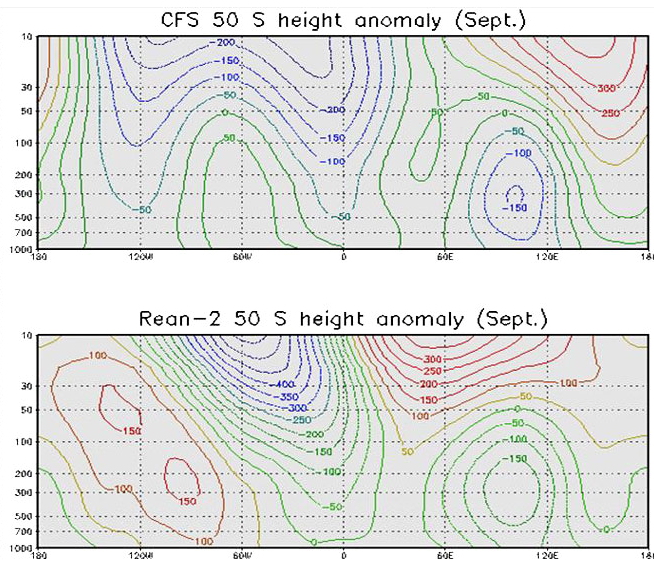


Figure 7 September mean height anomalies (m) from 1000-10 hPa at 50S. Top: CFS and bottom: R2.

parameterization need to be conducted. One thing that came out of this evaluation was that the horizontal resolution did not seem to make much of an improvement. Tests should be conducted to see if increasing the vertical resolution in the upper troposphere and lower stratosphere, raising the model top, or a combination of the two will make an improvement in the forecasts.

The ozone in the T382 CFS runs was much improved over the T62 CFS. There is no evidence of equatorial deficits or large polar surpluses.

Finally, the variability and predictability of extreme SH polar temperatures was examined. The warm SO that occurred in 1986, 1988, and 2002 do not show up in the time-latitude plot.

Problems are revealed:

1. Too little SH poleward heat flux,
2. Too little interannual variability in temperature, heights and winds,
3. Height differences begin above 200 hPa and continue to grow,
4. Insufficient vertical wave propagation is suspected.

These evaluations indicate that a closer examination of the upper troposphere-lower stratosphere dynamics, wave propagation and

US National Multi-Model ENSO Prediction with CFS and CCSM3

Ben P. Kirtman^{1,2,*} and Dughong Min¹

¹ *Center for Ocean-Land-Atmosphere Studies, Calverton MD*

² *RSMAS/MPO, University of Miami, Miami, FL*

1. Introduction

Seasonal-to-interannual climate predictions are now made routinely at a number of operational centers around the world, using comprehensive coupled models of the atmosphere, oceans, and land surface (e.g. Leetmaa and Ji 1989, Ji et al., 1994; Stockdale et al. 1998, Kanamitsu et al. 2002, Wang et al., 2002, Alves et al. 2002, Saha et al. 2006). These comprehensive coupled models are also being used for prediction and predictability research at various research centers around the world (Kirtman et al., 1997; Rosati et al. 1997, Schneider et al., 1999; Kirtman 2003; Schneider et al., 2003; DeWitt 2005; Stan and Kirtman 2007). This rapid growth in the use of comprehensive coupled models is due to the convergence of many factors including a concerted international effort to observe (i.e., McPhaden et al. 1998) and understand coupled ocean-atmosphere dynamics (Philander et al., 1984, Schopf and Suarez 1988, Battisti and Hirst 1989; Kirtman 1997). These efforts have led to the development and application of models that accurately simulate the observed variability (Neelin et al. 1992, Mechoso et al., 1995, Schneider et al. 1997; Davey et al., 2001, Kirtman et al. 2002, Collins et al., 2006, Delworth et al., 2006, Wittenberg et al., 2006).

Despite the advances noted above, real-time seasonal-to-interannual prediction efforts have not met expectations. For example, according to Barnston et al. (1999) and Landsea and Knaff (2000), the performance of many different prediction systems during the 1997-1999 ENSO episode was mixed. Arguably, there were substantial qualitative forecasting successes - almost all the models predicted that the boreal winter of 1997/98 would be a warm event one to two seasons in advance. But, there were also some striking quantitative failures. For instance, none of the models predicted the early onset or the amplitude of that event, and many of the forecast systems had difficulty capturing the demise of the warm event and the development of cold anomalies that persisted through 2001. Many models failed to predict the three consecutive years (1999-2001) of relatively cold conditions and the development of warm anomalies in the central Pacific during the boreal summer of 2002.

One approach for improving forecast skill that has received considerable international attention emphasizes the use of multiple forecast systems. For example, the studies by Krishnamurti et al. (1999), Palmer et al. (2004), and others have provided compelling evidence that the forecast skill of a multi-model ensemble (MME) system is higher than that of the individual models regardless of whether the skill measure is probabilistic or deterministic. The MME methodology is emerging as a clear strategy for reducing the impact of model error and quantifying forecast uncertainty associated with uncertainty due to differences in model formulation, and has become operational at the European Centre for Medium-Range Weather Forecasts (ECMWF; i.e., Eurosis), the International Research Institute for Climate and Society (IRI) and at the Asia-Pacific Climate Center (APCC). In fact, it is our assertion that the implementation of a MME prediction system at NOAA is the most direct path to improving operational seasonal-to-interannual prediction given current dynamic modeling capabilities. However, we emphasize that a multi-model prediction strategy does not remove the need to improve models, data streams or initialization strategies. It is important that the members of a multi-model ensemble be of comparably high quality.

There is ample evidence of the need for a US national multi-model seasonal-to-interannual prediction system. It is in the Nation's interest to have a multi-model seasonal-to-interannual prediction capability independent of information that may be available from outside sources. The advantage of a MME prediction system is that it, in addition to providing additional forecast information for the surface air temperature and

*Correspondence to: Ben Kirtman, RSMAS/MPO, University of Miami, 4600 Rickenbacker Causeway, Miami, FL 33149; E-mail: bkirtman@rsmas.miami.edu

precipitation outlooks that are currently products of the Climate Prediction Center (CPC), the MME can also provide information about fields and phenomena that the US has specific interest in predicting (i.e., ENSO cycle, monsoons, intraseasonal variability, the Madden-Julian Oscillation, among others). Finally, by subjecting the CCSM3 to the rigors of routine seasonal-to-interannual prediction, we can calibrate, and potentially gain additional confidence in, our climate change projections (assuming the model performs reasonably well).

2. CCSM as a Seasonal-to-Interannual Prediction System

Both models used in this study, the CCSM3 and the CFS, are coupled ocean-atmosphere-land models whose formulations of dynamics and subgrid-scale physical parameterizations, in both the atmospheric and oceanic component models, are considered state-of-the-art for this generation of models.

a. CCSM3.0

The CCSM3.0 is a global coupled climate model descended from its predecessor version, the Community Climate System Model version 2 (CCSM2; Kiehl and Gent 2004). However, as described by Collins et al. (2006), a number of changes and improvements have been made to the CCSM3.0. In this proposal we use the T85 version of CCSM3.0, with grid points in the atmospheric model [Community Atmospheric Model version 3 (CAM3)] roughly every 1.4° latitude and longitude, and 26 levels in the vertical. The ocean is a version of the Parallel Ocean Program (POP) with a nominal latitude-longitude resolution of 1° ($1/2^\circ$ in the equatorial Tropics) and 40 levels in the vertical, with Gent-McWilliams and *K*-profile parameterization (KPP) mixing. The land surface model is the Community Land Model (CLM), and the elastic-viscous-plastic (EVP) dynamic and thermodynamic sea ice component is the Community Sea Ice Model version 4 (CSIM4). No flux adjustments are used in the CCSM3.0.

b. CFS

Forecasts made with the operational version of CFS (Saha et al 2006) are used for comparisons and for the multi-model combination. The CFS data (i.e., retrospective forecasts) have been made available by NOAA (see <http://cfs.ncep.noaa.gov/>). The AGCM is the spectral T62 (triangular truncation at total wavenumber 62) version of the NCEP Global Forecast System (GFS; Moorthi et al., 2001) with a finite-differencing discretization on 64 sigma vertical layers between the Earth's surface and 0.2 hPa. The solar radiation parameterization is the scheme developed by Chou (1992); Chou and Lee (1996) and Chou and Suarez (1999). The parameterized physical processes include horizontal and vertical diffusion (Kanamitsu et al., 1991; Troen and Mahrt, 1986), gravity wave drag (Alpert et al., 1988; Kim and Arakawa, 1995). Deep convection is an implementation of Arakawa-Schubert as reported in Hong and Pan (1998). The model documentation is given in the technical note by the Global Climate and Weather Modeling Branch, EMC (2003) and in Wang et al., 2005.

The OGCM is the GFDL modular Modular Ocean Model version 3 (MOM3) described in Pacanowski and Griffies (1998). The numerical model is a finite-difference treatment of the primitive equations describing the oceanic circulation in spherical coordinates. The domain is that of the World Ocean between 74° S and 65° N. The coastline and bottom topography are realistic except that the ocean depths less than 100 m are set to 100 m. The zonal resolution is 1.0° and the meridional resolution is variable. Between 10° S and 10° N is $1/3^\circ$, gradually increasing poleward throughout the tropics. Beyond 30° N and 30° S the meridional grid spacing is fixed at 1.0° . In the vertical there are 40 time-independent levels with 27 layers in the upper 400 m. The vertical resolution is 10 m from the surface to the 240-m depth, gradually increasing to 511 m in the bottom layer. The vertical mixing scheme is the non-local *K*-profile parameterization of Large et al. (1994). The horizontal mixing of tracers and momentum is Laplacian. The momentum mixing uses the space-time-dependent scheme of Smagorinski (1963) and the tracer mixing uses Redi (1982) diffusion along with Gent and McWilliams (1990) quasi-adiabatic stirring.

c. Ocean Initialization

Here we briefly describe how we have initialized the ocean component of CCSM3 (POP) in our preliminary retrospective prediction experiments. The ocean initialization uses data assimilation products made available by GFDL (Rosati and Harrison, 2002; personal communication). The GFDL ocean data assimilation system is

based on MOM3 using a variational optimal interpolation scheme (Derber and Rosati, 1989). The GFDL ocean initial states are interpolated to the POP grid, and since the CFS Reanalysis and Reforecast (CFSRR) project uses MOM4, we expect that the overall process will be similar in the proposed experiment, although some modifications may be required.

The following is the procedure to produce the POP restart file converted from the MOM3 ocean data assimilation restart. The fields of the MOM3 restart file have values at time levels τ and $\tau+1$, while POP has data at time levels $\tau-1$, τ , and $\tau+1$. The $\tau-1$ time level is simply taken from the time level τ data. Both restart files have different resolutions in horizontal and vertical. The MOM3 meridional domain covers 75S to 65N, while the POP domain is global. The MOM3 fields have been interpolated horizontally and vertically using a bi-linear interpolation scheme, which has also been used previously to reduce the resolution in MOM3-based prediction experiments (Kirtman 2003). Climatological data from long simulations of CCSM3 are used in regions where MOM3 data is undefined (i.e., poleward of 65N and 75S). The surface pressure for POP is estimated using the sea surface height and the pressure gradient terms are estimated using centered differencing. As part of the proposed research we will modify the ocean initialization strategy to use the data from the 30-year NCEP CFSRR project.

d. Atmospheric Initialization

The atmospheric initial states are taken from an extended atmosphere-only (CAM3) simulation with observed, prescribed SST. The atmospheric ensemble members were obtained by resetting the model calendar back one week and integrating the model forward one week with prescribed observed SST. In this way, it is possible to generate an unlimited sample of initial conditions that are synoptically independent (separated by one week) but have the same initial date. This procedure was also used by Kirtman (2003) for ENSO prediction and Kirtman et al. (2001) to generate a 100-member ensemble for atmospheric seasonal prediction experiments.

e. Land Initialization

We have adopted an approach that is analogous to the procedure implemented with CAM, namely we use “AMIP”-type initial conditions.

f. Sea Ice Initialization

The sea-ice initial conditions set to the climatological monthly condition based on a long simulation of CCSM3.0. No observational information is included in the sea-ice initial conditions. As part of the proposed research we will modify the sea-ice initialization strategy to use the results from the 30-year NCEP CFSRR project.

g. Retrospective Forecast Experiments

To assess the potential predictive skill of the CCSM3.0, a large sample of retrospective forecast experiments have been made and compared to available observations. The retrospective forecasts cover the period 1982–1998. A 12-month hindcast is initialized each 1 January and 1 July during this 17-yr period. For each initial month, an ensemble of six hindcasts is run, yielding a total of 204 retrospective forecasts to be verified. The hindcast ensembles are generated by atmospheric perturbations only and no attempt has been made to find optimal perturbations. The ocean initial state for each ensemble member is identical. We acknowledge that with this approach we may underestimate the uncertainty in any individual forecast. We emphasize that these particular hindcasts were designed as a “proof of concept” in terms of developing a national multi-model prediction system.

Throughout the ENSO prediction literature there is some confusion regarding the appropriate definition of forecast lead-time. In this discussion, forecast lead-time is defined as in the following example. A CCSM3.0 forecast, initialized on 0000Z 1 January 1982, is labeled as being initialized in January 1982. The first monthly mean (i.e., the average of 1–31 January 1982) of the forecast is defined as the 0-month lead forecast. Similarly, the second monthly mean (i.e., 1–28 February 1982) is defined as the first month lead forecast. The CFS hindcast lead-times are defined similarly, but there are notable differences. For example, the forecast where January 1982 is lead-time zero (February 1982 is lead-time one month) is made up of 15 ensemble members.

Five ensemble members are initialized during 9–13 December 1981, 5-members are initialized 19–23 December and 5-members are initialized December 30–January 3, 1982. The remaining lead-times are defined analogously. In the CFS hindcast archive this forecast is referred to the January 1982 case. We have in the deterministic verification discussed below (i.e., Fig. 2) to combine, for example, the five CFS forecasts initialized on 30 December – January 3 with the six CCSM3.0 forecasts initialized on 1 January. There is a trade off here; we have chosen a sub-ensemble so that the multi-model combination is as “clean” as possible. As part of the proposed research the initial condition time and lead-time will follow the CFSRR project strategy thus removing the above confusion and difficulty in formulating the MME.

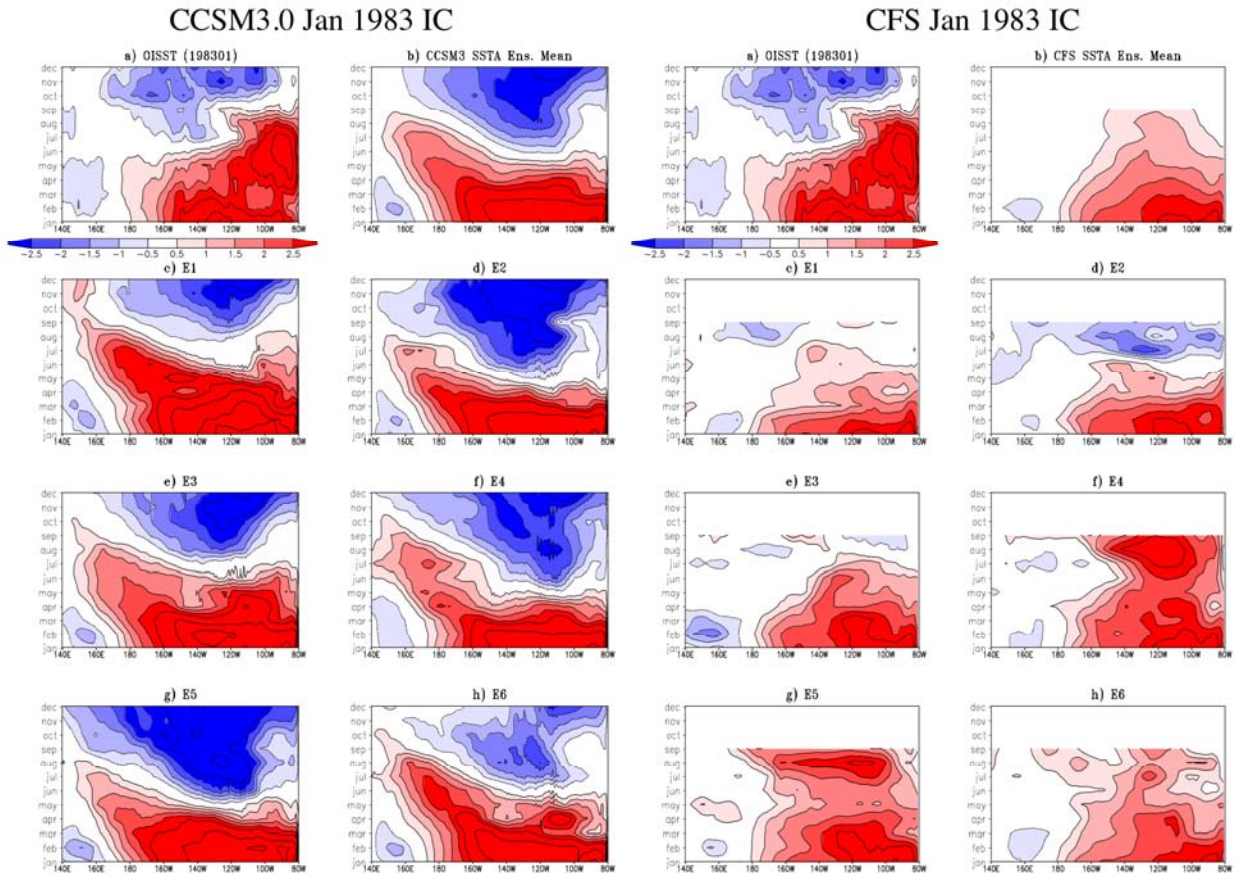


Figure 1 Time-longitude equatorial Pacific SSTA cross-sections for each CCSM3.0 ensemble member and for six randomly chosen ensemble members from the CFS hindcast data set. In each set of panels the top left is the observed SSTA and the top right is the ensemble mean model SSTA. In this example, the first full forecasted month is January 1983.

h. Deterministic Verification

Figure 1 shows the evolution of the SSTA along the equator in the Pacific in 1983 as an example. The figure has time-longitude sections for each of the six CCSM3.0 ensemble members and for six CFS ensemble members randomly chosen from the 15 hindcast members verifying at the same target month and lead time. The CCSM3.0 SSTA forecasts have notable westward phase propagation, which *may* be ameliorated in CCSM3.5. This is consistent with the errors in the “free running” model. Other examples (not shown), suggest that the CCSM3.0 forecasts appear to do a better job on the transition from warm to cold SSTA. This is probably due to the fact that the CFS tends to persist warm events longer than observed. The CCSM3.0 also appears to be more confident in forecasting cold events. This may be a weakness. Both models are quite weak for the forecast of the 1997 warm event (not shown).

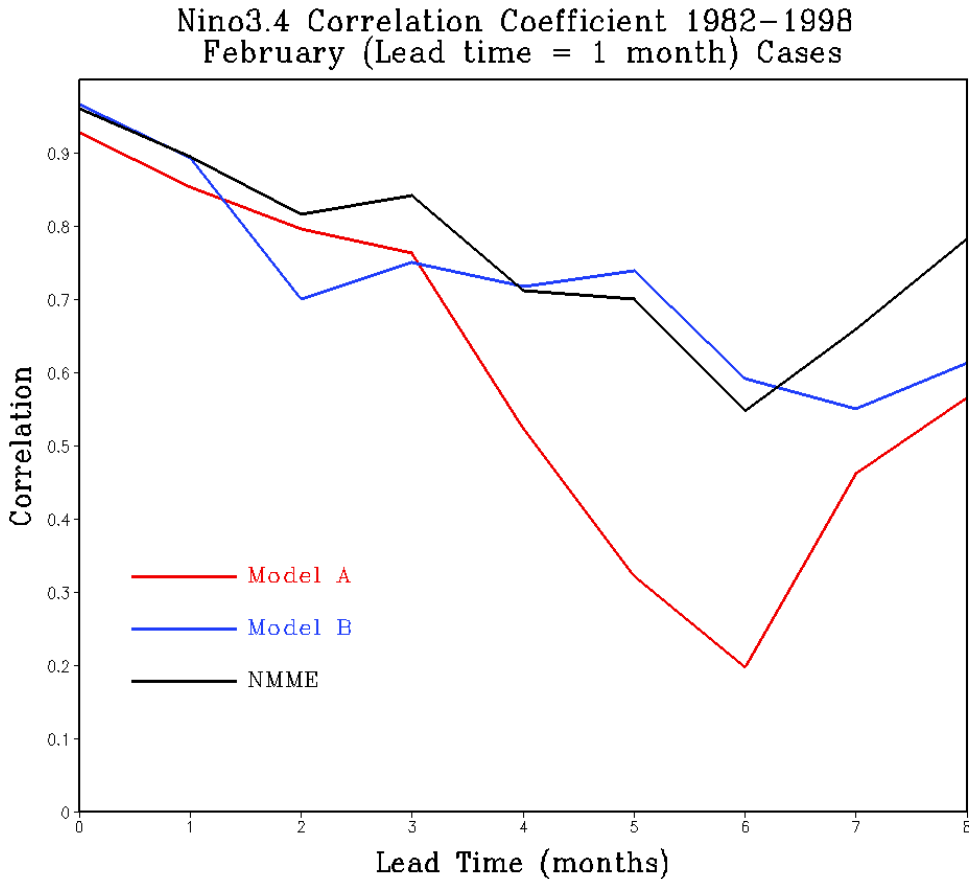


Figure 2 Correlation coefficient of Nino3.4 as a function of lead-time for both models (red and blue curves) and the National Multi-Model Ensemble (NMME; black curve). The removal of the systematic error is based on all 18-years of data for each model.

To form a multi-model ensemble, we use the six CCSM3.0 members initialized on 1 January for each year 1982-1998, and for CFS we use the five ensemble members initialized on 30 December – 3 January for each year 1982-1998. Figure 2 shows the correlation coefficient for each model (we have chosen not to identify which model is which) and the 11-member multi-model ensemble. The systematic error for each model is calculated in the same way as is based on the limited sample from 1982-1998. In calculating the correlation coefficients we use the ensemble means. There are several points to note:

- (i) The multi-model ensemble mean (black curve) has the highest correlation for most lead times;
- (ii) The multi-model correlation is higher than simply averaging the correlation from the two different models;
- (iii) Most notably the large drop in skill for Model A for lead times 4-6 has only a small impact on the multi-model skill;
- (iv) Based on 11-member sub-sampling of the CFS data (not shown), the overall multi-model improvement is better than a same-sized ensemble from a single model (this is consistent with the results from the DEMETER project).

This suggests that the correlation coefficient for the multi-model ensemble is generally higher than either model alone, although we need to use larger ensembles, more forecast cases and ensure consistent use of lead-time. Moreover, as lead-time increases the multi-model ensemble has a larger impact on the correlation. Similar results are found with the root mean square error. These results are quite encouraging in terms of developing a US national multi-model ensemble prediction system.

References

- Alpert, J. C., and co-authors, 1988: Mountain induced gravity wave drag parameterization in the NMC medium-range model. Preprints. Eight Conf. on Numerical Weather Prediction, Amer. Meteor. Soc., 429-432.
- Alves, O., G., and co-authors, 2002: POAMA: Bureau of Meteorology Operational Coupled Model Seasonal Forecast System. Proceedings of the ECMWF Workshop on the Role of the Upper Ocean in Seasonal Forecasting.
- Barnston, A. G., M. Glantz, and Y. He, 1999: Predictive skill of statistical and dynamical climate models in SST forecasts during the 1997-98 El Niño and the 1998 La Niña onset. *Bull. Amer. Meteor. Soc.*, **80**, 217-243.
- Battisti, D., and A. C. Hirst, 1989: Interannual variability in a tropical atmosphere-ocean model: Influence of the basic state, ocean geometry and nonlinearity. *J. Atmos. Sci.*, **46**, 1687-1712.
- Chou, M. D., 1992: A solar radiation model for use in climate studies. *J. Atmos. Sci.*, **49**, 762-772.
- Chou, M. D. and K. T. Lee, 1996: Parameterization for the absorption of solar radiation by water vapor and ozone. *J. Atmos. Sci.*, **53**, 1204-1208.
- Chou, M. D. and M. Suarez, 1999: A solar radiation parameterization for atmospheric studies. NASA/TM-1999-104606, Vol 15. 40pp.
- Collins, W. D., and co-authors, 2006: The Community Climate System Model version 3 (CCSM3). *J. Climate*, **19**, 2122-2143.
- Davey, M. K., and Coauthors, 2001: STOIC: A study of coupled model climatology and variability in tropical ocean regions. *Climate Dyn.*, **18**, 403-420.
- Delworth, T.L., and co-authors, 2006: GFDL's CM2 Global Coupled Climate Models. Part I: Formulation and Simulation Characteristics. *J. Climate*, **19**, 643-674.
- DelSole, T., 2007: A Bayesian Framework for Multimodel Regression. *J. Climate*, **20**, 2810-2826.
- Derber, J., and A. Rosati, 1989: A global oceanic data assimilation system. *J. Phys. Oceanogr.*, **19**, 1333-1347.
- DeWitt, D.G., 2005: Retrospective Forecasts of Interannual Sea Surface Temperature Anomalies from 1982 to Present Using a Directly Coupled Atmosphere-Ocean General Circulation Model. *Mon. Wea. Rev.*, **133**, 2972-2995.
- Dirmeyer, P.A., Gao, X., Zhao, M., Guo, Z., Oki, T., Hanasaki, N., 2005: The Second Global Soil Wetness Project (GSWP-2): Multi-Model Analysis and Implications for our Perception of the Land Surface, CTR 185, 46 pp.
- Gent, P. R. and J. C. McWilliams, 1990: Isopycnal mixing in ocean circulation models. *J. phys. Oceanogr.*, **20**, 150-155.
- Hong, S. Y. and H. L. Pan, 1998: Convective trigger function for a mass-flux cumulus parameterization scheme. *Mon. Wea. Rev.*, **124**, 2322-2339.
- Ji, M., A. Kumar, and A. Leetmaa, 1994: An experimental coupled forecast system at the National Meteorological Center: Some early results. *Tellus*, **46A**, 398-418.
- Kanamitsu, M., and co-authors, 1991: Recent changes implemented into the global forecast system at NMC. *Wea. and Forecasting*, **6**, 425-435.
- Kanamitsu, M., and coauthors, 2002: NCEP-DOE AMIP-II Reanalysis (R-2). *Bull. Amer. Meteor. Soc.*, **83**, 1631-1643.
- Kiehl, J. T. and P. R. Gent, 2004: The Community Climate System Model, version 2. *J. Climate*, **17**, 3666-3682.
- Kim, Y. J. and A. Arakawa, 1995: Improvement of orographic gravity wave parameterization using mesoscale gravity wave model. *J. Atmos. Sci.*, **52**, 1875-1902.
- Kirtman, B. P., 1997: Oceanic Rossby wave dynamics and the ENSO period in a coupled model. *J. Climate*, **10**, 1690-1704.
- Kirtman, B. P., J. Shukla, B. Huang, Z. Zhu and E. K. Schneider, 1997: Multiseasonal predictions with a coupled tropical ocean global atmosphere system. *Mon. Wea. Rev.*, **125**, 789-808.
- Kirtman, B. P., 2003: The COLA anomaly coupled model: Ensemble ENSO prediction. *mon. Wea. Rev.*, **131**,

- 2324–2341.
- Kirtman, B. P. and P. S. Schopf, 1998: Decadal variability in ENSO predictability and prediction. *J. Climate*, **11**, 2804–2822.
- Kirtman, B. P., D. A. Paolino, J. L. Kinter III and D. M. Straus, 2001: Impact of tropical subseasonal SST variability on seasonal mean climate. *Mon. Wea. Rev.*, **129**, 853–868.
- Kirtman, B. P., Y. Fan and E. K. Schneider, 2002: The COLA global coupled and anomaly coupled ocean-atmosphere GCM. *J. Climate*, **15**, 2301–2320.
- Kirtman, B. P., and J. Shukla, 2002: Interactive coupled ensemble: A new coupling strategy for GCMs. *Geophys. Res. Lett.*, **29**, 1029–1032.
- Kirtman, B. P., K. Pegion, and S. Kinter, 2005: Internal atmospheric dynamics and climate variability. *J. Atmos. Sci.*, **62**, 2220–2233.
- Krishnamurti, T. N., and co-authors, 1999: Improved weather and seasonal climate forecasts from multi-model superensemble. *Science*, **285**, 1548–1550.
- Landsea, C. W., and J. A. Knaff, 2000: How much skill was there in forecasting the very strong 1997–98 El Niño? *Bull. Amer. Meteor. Soc.*, **81**, 2107–2120.
- Large, W. G., J. C. McWilliams, and S. C. Doney, 1994: Oceanic vertical mixing: A review and a model with a nonlocal boundary layer parameterization. *Rev. Geophys.*, **32**, 363–403.
- Leetmaa, A., and M. Ji, 1989: Operational hindcasting of the tropical Pacific. *Dyn. Atmos. Oceans*, **13**, 465–490.
- McPhaden, M. J., and co-authors, 1998: The Tropical Ocean-Global Atmosphere observing system: A decade of progress, *Journal of Geophysical Research*, **103(C7)**, 14,169–14,240 (1998).
- Mechoso, C. R., and Coauthors, 1995: The seasonal cycle over the tropical Pacific in coupled ocean-atmosphere general circulation models. *Mon. Wea. Rev.*, **123**, 2825–2838.
- Moorthi, S., H.-L. Pan, and P. Caplan, 2001: Changes to the 2001 NCEP operational MRF/AVN global analysis forecast system. NWS Tech. Procedures Bulletin 484, 14pp. (Available online at <http://www.nws.noaa.gov/om/tpb/484.htm>).
- Neelin, J. D., and and Coauthors, 1992: Tropical air-sea interaction in general circulation models. *Climate Dyn.*, **7**, 73–104.
- Pacanowski, R. C. and S. M. Griffies, 1998: Mom3.0 manual. NOAA/Geophysical Fluid Dynamics Laboratory, 638pp.
- Palmer, T. N., and Coauthors, 2004: Development of a European multimodel ensemble system for seasonal to interannual prediction (DEMETER). *Bul. Amer. Met. Soc.*, **85**, 853–872.
- Philander, S. G. H., T. Yamagata, and R. C. Pacanowski, 1984: Unstable air-sea interactions in the Tropics. *J. Atmos. Sci.*, **41**, 603–613.
- Pegion, K. and B. P. Kirtman, 2007: Internal atmospheric variability and the Madden-Julian Oscillation. *J. Climate* (submitted).
- Pena, M. and H. van den Dool, 2008: Consolidation of Multi Model Forecasts by Ridge Regression: Application to Pacific Sea Surface Temperature. Submitted to *J. Climate*.
- Rosati, A., R. Gudgel, and K. Miyakoda, 1997: The impact of ocean initial conditions on ENSO forecasting with a coupled model. *Mon. Wea. Rev.*, **125**, 754–772.
- Redi, M. H., 1982: Oceanic isopycnal mixing by coordinate rotation. *J. Phys. Ocean.*, **12**, 1155–1158.
- Saha, S., S., and co-authors, 2006: The NCEP Climate Forecast System. *J. Climate*, **19**, 3483–3517.
- Schneider, E. K., and co-authors, 1997: ENSO variability in a coupled general circulation model. *Mon. Wea. Rev.*, **125**, 680–702.
- Schneider, E. K., and co-authors, 1999: Ocean data assimilation, initialization and prediction with a coupled GCM. *Mon. Wea. Rev.*, **127**, 1187–1207.
- Schneider, and co-authors, 2003: Retrospective ENSO forecasts: Sensitivity to atmospheric model and ocean resolution. *Mon. Wea. Rev.*, **131**, 3038–3060.

- Schopf, P. S., and M. J. Suarez, 1988: Vacillations in a coupled ocean– atmosphere model. *J. Atmos. Sci.*, **45**, 549–566.
- Smagorinski, J., 1963: General circulation experiments with the primitive equations. I. The basic experiment. *Mon. Wea. Rev.*, **91**, 99–164.
- Stan, C., and B. P. Kirtman, 2007: Internal atmospheric dynamics and tropical Pacific predictability in a coupled GCM. *J. Climate* (in press).
- Stockdale, T. N., D. L. T. Anderson, J. O. S. Alves, and M. A. Balmaseda, 1998: Global seasonal rainfall forecasts using a coupled ocean–atmosphere model. *Nature*, **392**, 370–373.
- Troen, I. and L. Mahrt, 1986: A simple model of atmospheric boundary layer; Sensitivity to surface evaporation. *Bound.-Layer Meteor.*, **37**, 129–148.
- Uppala, S.M., and co-authors, 2005: The ERA-40 re-analysis. *Quart. J. R. Meteorol. Soc.*, **131**, 2961–3012. doi:10.1256/qj.04.176
- Vikhliaev, Y., and B. P. Kirtman, 2007: Understanding the role of instability and stochastic forcing of ENSO dynamics using the breeding method. *J. Climate*, in press.
- Wang, G., R. Kleeman, N. Smith, and F. Tseitkin, 2002: The BMRC coupled general circulation model ENSO forecast system. *Mon. Wea. Rev.*, **130**, 975–991.
- Wang, W., S. Saha, H.L. Pan, S. Nadiga, and G. White, 2005: Simulation of ENSO in the New NCEP Coupled Forecast System Model (CFS03). *Mon. Wea. Rev.*, **133**, 1574–1593.
- Wheeler, M.C., and H.H. Hendon, 2004: An all season real-time multivariate MJO index: Development of an index for monitoring and prediction. *Mon. Wea. Rev.*, **132**, 1917–1932.
- Wittenberg, A.T., A. Rosati, N.C. Lau, and J.J. Ploshay, 2006: GFDL's CM2 Global Coupled Climate Models. Part III: Tropical Pacific Climate and ENSO. *J. Climate*, **19**, 698–722.
- Wu, Z., E. K. Schneider and B. P. Kirtman, 2004: Causes of low frequency North Atlantic SST variability in a coupled GCM. *Geophys. Res. Lett.*, **31**, L09210, doi:10.1029/2004GL019548.
- Wu, R., and B. P. Kirtman, 2004a: The tropospheric biennial oscillation of the monsoon-ENSO system in an interactive ensemble coupled GCM. *J. Climate*, **17**, 1623–1640.
- Wu, R., and B. P. Kirtman, 2004b: Understanding the impacts of the Indian Ocean on ENSO variability in a coupled GCM. *J. Climate*, **17**, 4019–4031.
- Wu, R., and B. P. Kirtman, 2004c: Impacts of the Indian Ocean on the Indian summer monsoon-ENSO relationship. *J. Climate*, **17**, 3037–3054.
- Wu, R., and B. P. Kirtman, 2005: Role of Indian and Pacific Ocean air-sea coupling in tropical atmospheric variability. *Climate Dyn.* **25**, 155–170.
- Wu, R., and B. P. Kirtman, 2006: Changes in spread and predictability associated with ENSO in an ensemble coupled GCM. *J. Climate*, **19**, 4378–4396.
- Yeh, S.-W., and B. P. Kirtman, 2003: On the relationship between the interannual and decadal SST variability in the North Pacific and the Tropical Pacific Ocean. *J. Geophys. Res.*, **108(D11)**, 4344, doi:10.1029/2002JD002817
- Yeh, S.-W., and B. P. Kirtman, 2004a: The impact of internal atmospheric dynamics for the North Pacific SST variability. *Climate Dyn.* doi:10.1007/s00382-004-0399-8.
- Yeh, S.-W., and B. P. Kirtman, 2004b: The North Pacific oscillation-ENSO and internal atmospheric variability. *Geophys. Res. Lett.*, **31**, doi:10.1029/2004GL019983, 2004.
- Yeh, S.-W., B. P. Kirtman, and Soon-il An, 2007: Local versus non-local atmospheric weather noise and North Pacific SST variability. *Geophys. Res., Lett.*, **34**, doi:10.1029/2007GL030206, 2007.
- Yeh, S.-W., and B. P. Kirtman, 2004c: Tropical Pacific decadal variability and ENSO amplitude modulation in a CGCM. *J. Geophys. Res. – Oceans*, **109**, C11009, doi:10.1029/2004JC002442.
- Yeh, S.-W., and B. P. Kirtman, 2004d: The North Pacific oscillation-ENSO and internal atmospheric variability. *Geophys. Res. Lett.*, doi:10.1029/2004GL019983.

On the Importance of Horizontal Resolution and Initial Conditions to Forecasting Tropical Intraseasonal Oscillations: the Maritime Continent Prediction Barrier

Augustin Vintzileos^{1,2} and Hua-Lu Pan²

¹ *Science Applications International Corporation*

² *Environmental Modeling Center, NOAA/NWS/NCEP*

1. Introduction

There is an increasing societal need for forecast at lead times between week 3 and month 2 (e.g., Toth et al., 2007). Probabilistic information about Monsoon onsets and breaks and perhaps of heat waves and intensification/suppression of tropical storm activity could clearly benefit many sectors of the economy. The major phenomenon allowing for subseasonal forecasts is the Madden-Julian Oscillation (Madden and Julian, 1971; Zhang 2005). Subseasonal forecasting is a new challenge and as such many questions are still open or even not yet well defined. Current state-of-the-art numerical models are not representing adequately all aspects of the Tropical Intraseasonal Oscillation (TIO) in free simulations (Lin et al. 2006). Many questions are still open on effectively using dynamical models in forecast mode. How important in respect to MJO forecast is adequate initialization of these models and how far into the future can these models propagate the initial information in a useful sense? What are the sources for error growth? Can these sources be attributed to model deficiencies or to intrinsic physical reasons? Would forecast at higher horizontal resolution i.e., with improved scale interactions, be better?

Here we answer these questions using a version of the NCEP Climate Forecasting System (CFS) in a series of experiments conducted under the Climate Test Bed (CTB). After introducing a simplified measure of tropical intraseasonal oscillation activity we show that, for the CFS and for resolutions up to T254, forecast skill of the TIO is independent of horizontal resolution. The element that is crucial is atmospheric initial conditions. By ameliorating the atmospheric initial state from the Reanalysis-2 (CDAS2) to the NCEP operational analysis we improved forecast of the TIO by 3-5 days. We also show that the forecast skill of the TIO in CFS depends on the phase of the oscillation with the fastest drop in pattern correlation occurring as the convectively active phase of the MJO approaches the Maritime Continent.

2. Model and experiment description

The model that we use here is the CFS (Wang et al., 2005; Saha et al., 2006). This is a fully coupled model of the ocean-land-atmosphere system. The atmospheric component is run at three different resolutions: T62, T126 and T254 respectively 200 km X 200 km, 100 km X 100 km and 50 km X 50 km. Experiments are initialized using atmospheric initial states from both Reanalysis-2 and the operational NCEP analysis (GDAS) every five days apart from May 23 to August 11. Initial conditions from GDAS are a better representation of the state of the atmosphere as this analysis is based on the constantly improving atmospheric model, observing system and assimilation methodology. The 5-day interval between initializations is chosen because while it adequately samples Intraseasonal Oscillations can yet fit to computational limitations. In what follows we will consider experiments initialized on the following dates in 2002 to 2006: May 23 and 28, June 3, 8, 13, 18, 23 and 28, July 2, 7, 12, 17, 22 and 27 and August 1, 6 and 11. This is a total of 105 summer hindcast experiments from 2002 to 2006 (21 runs per year) for each horizontal resolution and for each initial condition which is equivalent to about 200 years of a free coupled experiment with an atmospheric model at a resolution of T126. The ocean model is used at the operational CFS resolution and initialized by the operational ocean analysis (GODAS).

3. A measure for Tropical Intraseasonal Oscillations

There are numerous metrics for quantifying the intensity and phase of the MJO. One of the most used at present is defined in Wheeler and Hendon (2004). This index represents the coupling between the large scale circulation and organized diabatic forcing by combining winds at 200 hPa and 850 hPa and precipitation or OLR. However, in this analysis due to the constraint of a small number of years (5) which we use for computing the mean annual cycle and model drift we had to introduce a simplified version of the Wheeler and Hendon index as a measure for the MJO. This measure had to be based on a smooth field relevant to the MJO and not containing information from fields with strong variability in high frequencies like outgoing longwave radiation (OLR) or precipitation.

We construct the simplified MJO index using the observed (Reanalysis-2) 6-hourly zonal wind at 200 hPa averaged between 20°S - 20°N. We first compute the mean annual cycle using monthly mean data. Then we interpolate the mean annual cycle to 0, 6, 12 and 18 UTC and we subtract it from the raw data at each longitudinal grid point. Then we subtract the zonal mean at each time step and from each grid point.

After subtracting the annual mean cycle and the zonal mean from the original data we perform an EOF analysis. It has to be noticed that no time filtering is used here. The first and second modes are shown on Figure 1. Their respective principal components (not shown) present a maximum lag correlation of 0.6 at 10 days apart with mode 1 leading mode 2. It follows that these two first modes represent an eastward propagating wave with a period of 40 days. We repeated this analysis using only winter or summer data and the resulting modes were very similar.

In the following section we use these modes in order to extract the TIO modes from the forecast and from the observations. Figure 2 compares the observed anomalies of zonal wind at 60°E (thin dashed line) with the observed anomalies projected to the modes of Figure 1. It is clear that this projection method filters higher

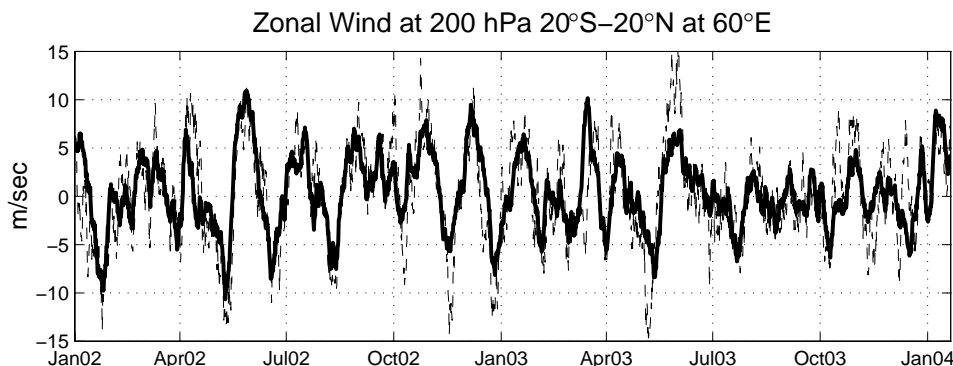


Figure 2 Zonal wind anomalies averaged between 20°S - 20°N at 60°E. The thin dashed line is the observed anomalies and the thick line shows the reconstruction of the signal as projected to the first two EOF modes of Figure 1.

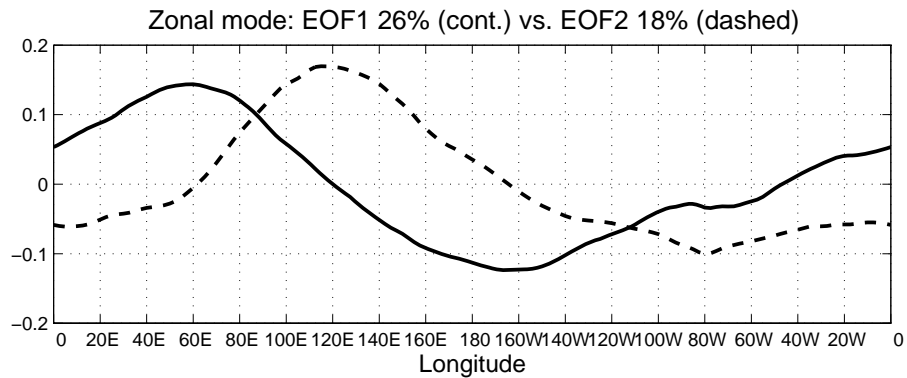


Figure 1 The first and second EOFs of the zonal wind at 200 hPa averaged 20°S - 20°N. Percentages of explained variance are 26% and 18% for the first and second mode respectively.

frequencies without decreasing the amplitude of intraseasonal oscillations. We therefore do not use time filtering of forecast and observed zonal wind data.

4. Forecast skill

The dependence of the forecast capacity of the CFS as a function of horizontal model resolution and initial conditions is shown on Figures 3 for pattern correlation and 4 for root mean square error. In both figures results for the

persistence forecast is shown by the thick continuous magenta line. Black, red and blue colors correspond to resolutions of T254, T126 and T62 respectively. Continuous/dashed lines show forecast initialized by GDAS/CDAS2. All resolutions and all initializations are more skilful than persistence forecast. Inspection of both Figures 3 and 4 shows clustering of pattern correlation and error. The separation criterion for the two clusters is initial conditions. Skill does not show any significant dependence on model resolution. The better and more compatible to the CFS initial conditions show an improvement that ranges between 3 and 5 days.

5. Reasons for the drop in forecast skill

In the previous paragraph we have shown that the anomaly correlation between the observed and forecast MJO modes is monotonically decreasing as a function of lead time. In order to understand reasons for this drop we present the pattern correlation as a function of initialization day (x-axis) and lead time (y-axis) in Figures 5 for (a) persistence forecast, (b) forecast initialized by the CDAS2 initial conditions and (c) forecast initialized by the GDAS initial conditions. Although Figures 5 present only forecasts initialized from the end of May to the beginning of August 2002 (for simplicity of the presentation) results are similar in all other initialization periods and thus the conclusions that follow can be generalized.

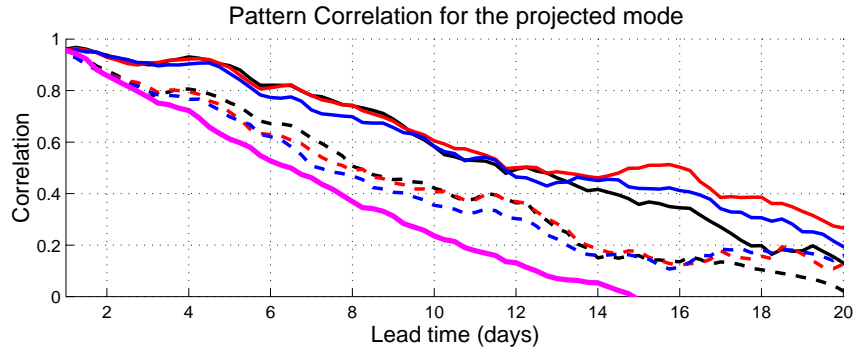


Figure 3 Pattern correlation between forecast and observations of a measure of TIO activity (see text). Model resolution is indicated by the different colors T62, T126 and T254 for respectively Blue, Red and Black. Initial conditions are indicated by dashed lines for and Black. Initial conditions are indicated by dashed lines for Reanalysis-2 and continuous lines for the operational analysis. The thick magenta line is the persistence forecast

Figure 5a shows pattern correlation obtained for a persistence forecast. Red colors represent a good forecast while dark blue colors indicate a forecast with opposite phase from the observed quantity. A good persistence forecast (vivid red colors) indicates a rather stationary pattern while a bad forecast (light red to deep blue colors) points to a progressive pattern. Increase in skill with lead time occurs due to the oscillatory behavior of the observed quantity (eventually the phase of the oscillation will reach again its values at initialization).

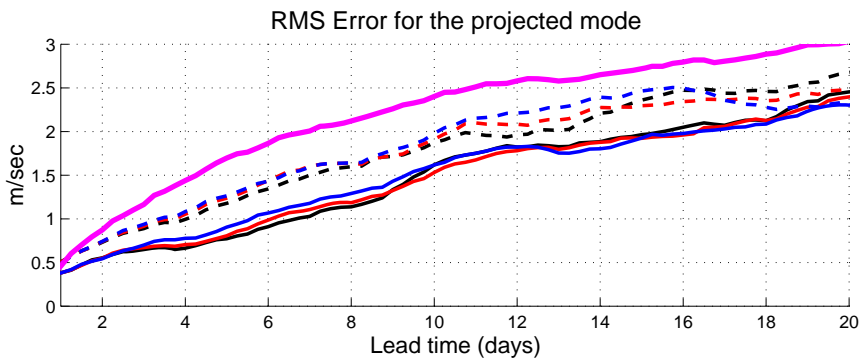


Figure 4 As in Figure 3 except for the RMS error.

In Figure 6 we show a longitude-time graph of the observed zonal velocity at 200 hPa projected to the MJO EOFs. Due to the incapacity of persistence forecast to capture changes, Figure 5a indicates that a progressive pattern exist from May to the third week of June followed by a rather stationary pattern until the beginning of August, followed by a progressive pattern in August. This succession of progressive and stationary patterns is clearly seen on the reconstructed upper troposphere MJO signal.

Figures 5b and 5c show forecast obtained with the CFS initialized by the CDAS2 and the GDAS products respectively. There is a clear improvement in forecast skill for predictions initialized after the first couple of weeks in June 2002. Inspection of Figure 6 shows that this period of improved skill coincides with the propagation of the enhanced convective phase of the MJO from the western Pacific eastwards and of the suppressed convective phase of the MJO over the Indian Ocean eastwards. However, during periods when the actively convective phase of the MJO is over the Indian Ocean and enters the Maritime Continent i.e., at the beginning of July and August (Fig. 6) there is no improvement in skill (against the persistence forecast). We define this drop in skill during the phase of the MJO when enhanced convection is over the Indian Ocean and enters the Maritime Continent as the Maritime Continent Prediction Barrier. Similar behavior has been observed in other operational forecasting systems like at ECMWF (Frederic Vitard, personal communication).

6. Conclusions

We demonstrated that the CFS present a good forecast capacity of the MJO up to week 3 (for pattern correlations of 0.4) when the model is initialized by the best initial conditions available – this is a skill similar to other operational forecasting centers. In fact, improving initial conditions from the CDAS2 to GDAS improves the forecast by 3-5 days. This improvement is due to two reasons. First, the atmospheric model used in this version of the CFS is more compatible with the model used to produce GDAS than with the model used to produce CDAS2. It follows (not shown here) that initialization shocks are more important when CDAS2 initial conditions are used. Further, GDAS has a better representation of the state of the atmosphere due to additional improvements of assimilation methodologies and the observing system.

We have shown that the skill of the CFS depends on the phase of the MJO. The worst forecasts are obtained when the active convective phase of the MJO is over the Indian Ocean and enters the Maritime Continent. Despite the improvement in forecast skill of the MJO conveyed by the better initial condition we were not able to break this Maritime Continent Barrier. The fact that similar behavior was noted in other forecasting systems suggests that there is either a physical reason for this barrier or that these forecasting systems present some

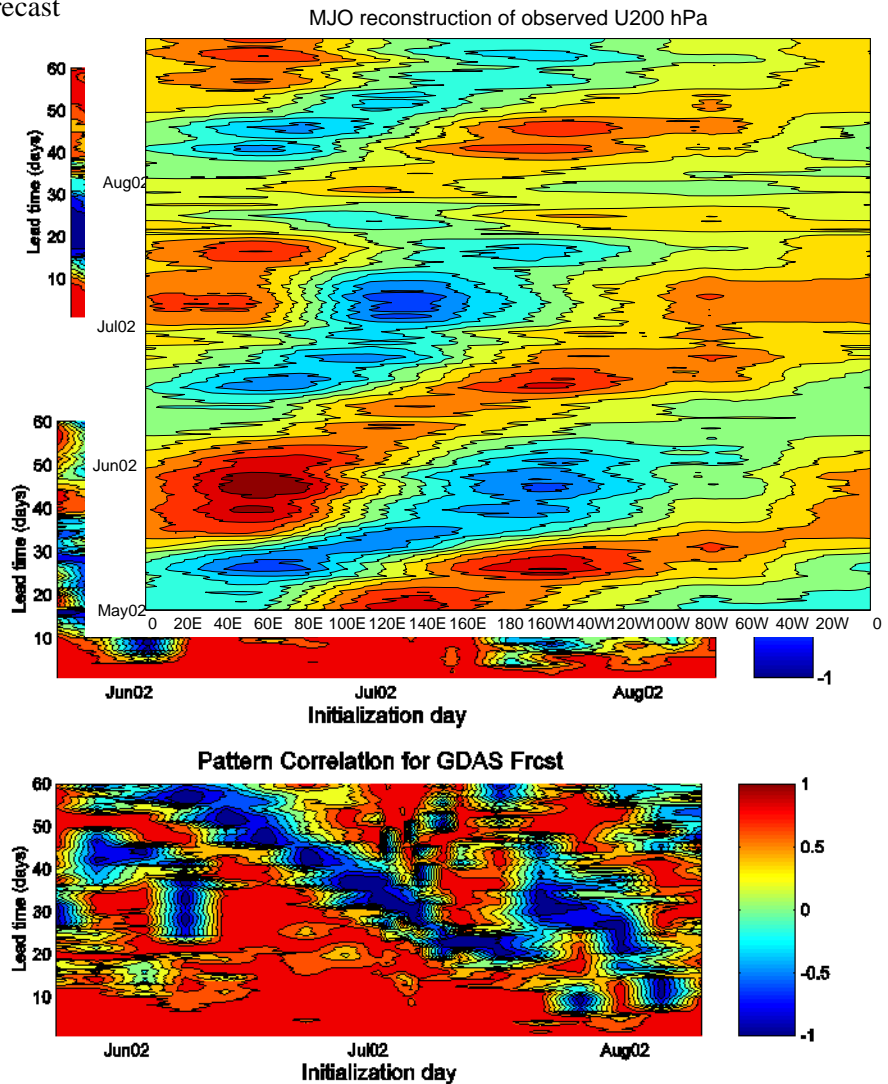


Figure 5 Pattern correlation between the EOF filtered MJO signal for forecast and observations: (a) persistence forecast, (b) CFS forecast initialized by CDAS2 and (c) CFS forecast initialized by GDAS.

similar shortcomings in their design. We currently examine actively the second possibility by investigating the role of ocean initial conditions on the MJO forecast. In fact, preliminary analysis on observed fields suggest coupling between the MJO and SST. Currently, the ocean analysis system (GODAS) which was designed and optimized for seasonal forecasting is not representing adequately periodicities relevant to the MJO. Therefore, we are now investigating an experimental version of GODAS with a more realistic behavior at subseasonal periodicities and the impact that this has on MJO forecasts.

References

- Lin, J.-L., and co-authors, 2006: Tropical Intraseasonal Variability in 14 IPCC AR4 Climate Models. Part I: Convective Signals. *J. Climate*, **19**, 2665-2690.
- Madden, R. A., and P. R. Julian, 1971: Detection of a 40–50 Day Oscillation in the Zonal Wind in the Tropical Pacific. *J. Atmos. Sci.*, **28**, 702-708.
- Saha, S., and co-authors, 2006: The NCEP Climate Forecast System. *J. Climate*, **19**, 3483–3517.
- Toth, Z., M. Pena, and A. Vintzileos, 2007: Bridging the gap between weather and climate forecasting - Research priorities for intraseasonal prediction. *Bull. Amer. Meteor. Soc.*, **88**, 1427-1429.
- Wang, W., S. Saha, H. Pan, S. Nadiga, and G. White, 2005: Simulation of ENSO in the New NCEP Coupled Forecast System Model (CFS03). *Mon. Wea. Rev.*, **133**, 1574–1593.
- Wheeler, M. C., and H. H. Hendon, 2004: An All-Season Real-Time Multivariate MJO Index: Development of an Index for Monitoring and Prediction. *Mon. Wea. Rev.*, **132**, 1917-1932.
- Zhang, C., 2005: The Madden Julian Oscillation. *Reviews of Geophysics*, **43**, RG2003, doi:10.1029/2004RG000158.

Figure 6 Longitude–time graph of the projection of the observed zonal velocity at 200 hPa averaged between 20S–20N on the two EOFs shown in Figure 1.

Estimation of the Limit of Predictability in the Stratosphere versus Troposphere Using CFS

Cristiana Stan^{1,*}, David M. Straus^{1,2} and Ben P. Kirtman^{1,2}

¹Center for Ocean-Land-Atmosphere Studies, Calverton MD

²George Mason University, Fairfax VA

1. Motivation of the Study

The NCEP Climate Forecast System (CFS) shows a good forecast skill for the variability of large-scale circulation in the troposphere but a low skill for the stratosphere. Sudden stratospheric warming events are among the tests that not only CFS but also its contemporary coupled general circulation models (GCM) have yet to pass. Why this is a surprising result? Because most of the theories aimed to explain the mechanism of formation and maintaining of stratospheric warming events involve propagation of planetary waves from the troposphere up in the stratosphere. The realistic representation of the troposphere and stratosphere in the CFS confers the potential of a successful prediction of these events.

2. Model Description

This study used the NCEP Climate Forecast System (CFS). The atmospheric GCM has a horizontal resolution of T62 of about 200 km with 64 sigma levels and the top at 0.2 hPa. Above 150 hPa there are 27 levels. The oceanic GCM is MOM3. The coupling between the atmosphere and ocean is realized through the interactive ensemble (Stan and Kirtman, 2007). In this coupling strategy the ocean model is coupled to the ensemble average of 6 atmospheric models that in turn are forced by the same SST. There are 30 atmospheric ensembles corresponding to 5 interactive ensembles. Each atmospheric model is initialized on January from slightly different initial conditions, so that the 6 realizations of the atmosphere give a good sample of internal variability. The atmospheric initial conditions are taken from the NCEP/DOE AMIP R2 reanalyses, and are 6 hours apart. Thus, the atmospheric realizations can be interpreted as equally likely responses of the atmosphere to the same SST.

For predictability studies, the atmospheric realizations in a single interactive ensemble represent outcomes of so called “identical twin experiments,” with 15 pairs of twins available. For each January in the 10-year period (1981-1990), 5 interactive ensemble forecasts (of length one year) were run from the same ocean initial condition representative of 1 January. Thus for each calendar year we have essentially 5 sets of identical twin experiments.

3. Sudden Stratospheric Warming

Figure 1 shows the ensemble forecasts of the polar cap temperature at 10hPa and the zonal mean zonal wind at 60°N and 10hPa around an episode of sudden stratospheric warming event with the central date on 23 January 1987 (Charlton and Polvani). This figure shows that while some individual forecasts capture the strong easterlies, few if any capture the extent of the polar warming. The ensemble means clearly do not have any prediction skill for this sudden stratospheric warming event. Results from other warming events that occur near the start of the forecasts are similar.

Before we investigate why the model is not able to consistently forecast these events, it is useful to check if the model climatology agrees with the observed counterpart. We want to eliminate the possibilities that in the model the stratosphere is already too warm so it cannot get warmer, or that it is too cold and if it warms up, the temperature raise is not enough to catch up with the observations. Figure 2 shows the temperature bias in January and February. While the 10 hPa temperature bias in January is small poleward of 60°N, it does grow fairly substantially in February when CFS temperature is too cold by over 8 degrees. The zonal-mean zonal wind for observations and the model are shown in Figure 3; it is clear that the model generally simulates the jet

*Correspondence to: Cristiana Stan, Center for Ocean-Land-Atmosphere Studies, Calverton, MD20705
E-mail: stan@cola.iges.org

structure well, although the 10 hPa winds near the pole are somewhat weak during January.

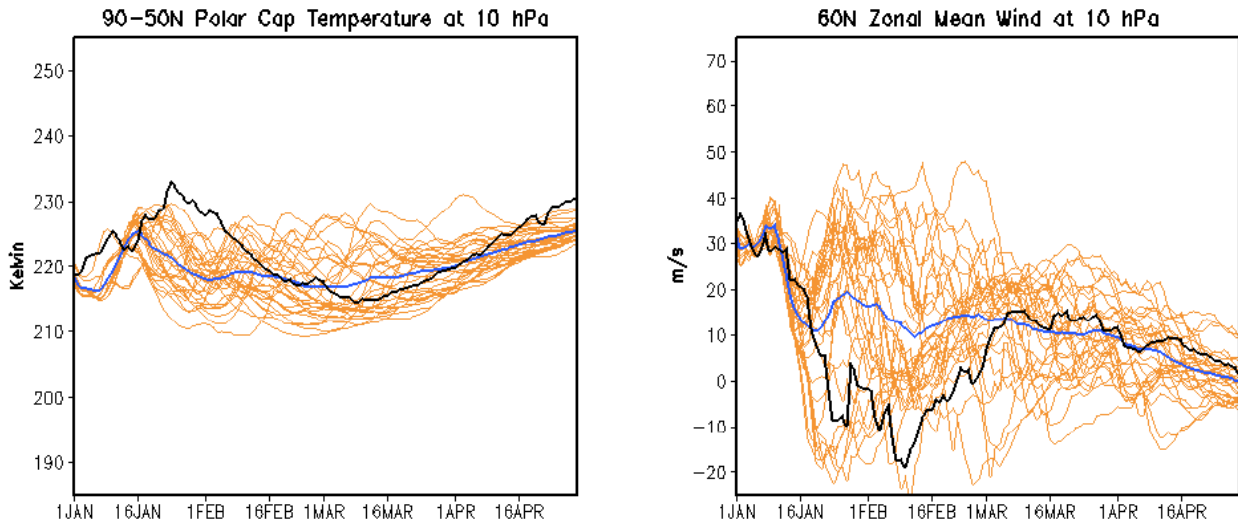


Figure 1 Left: Temperature averaged over the Polar Cap north of 50°N at 10hPa in 1987. Right: Zonal mean of U wind at 60°N at 10 hPa. The orange curves denote the 30 atmospheric realizations corresponding to the 5 interactive ensembles, the blue curve is the ensemble mean and the black curve corresponds to observations.

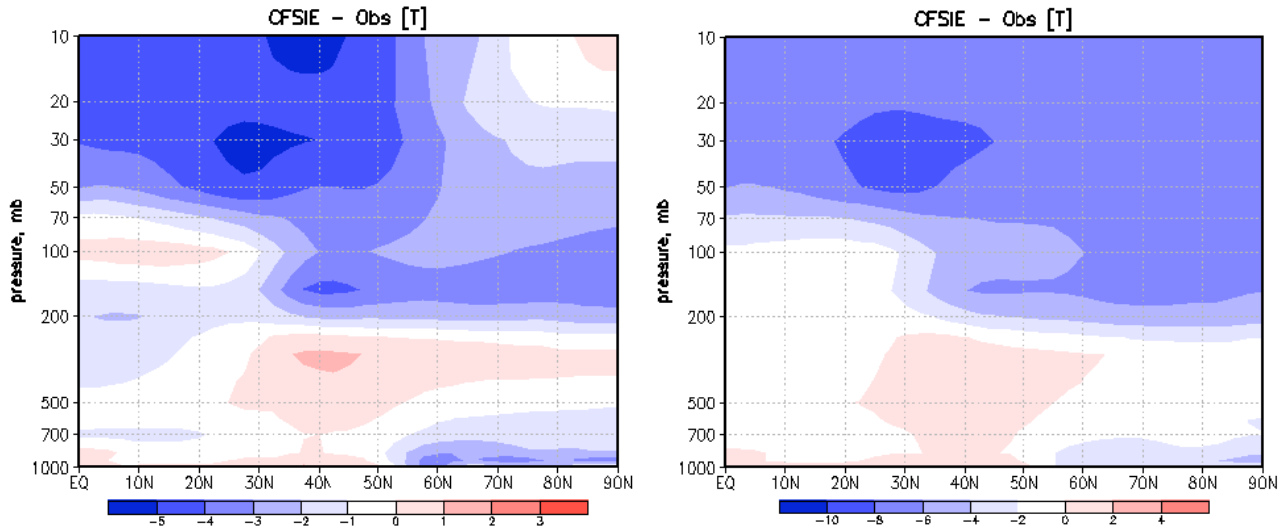


Figure 2 Model error of the zonal mean temperature simulation during January (left) and February (right).

4. Predictability

Another possible explanation for the model failure might be related to the intrinsic nature of stratospheric predictability. The experimental design offers the perfect opportunity to look into the limit of predictability in the stratosphere versus troposphere. For each interactive ensemble, the atmospheric realizations in a single interactive ensemble represent outcomes of so called “identical twin experiments”. There are 15 pairs of twins available for which the squared error of any quantity may be computed. Averaging the squared error over all pairs, then over all 5 interactive ensembles, and finally over 10 years, yields a good estimate of error growth due solely to differences in the initial conditions. This error growth is driven by the degree of deterministic chaos that characterizes the dynamics of the region in which the prediction is made. Zonally averaging the mean squared error allows for an expansion in terms of zonal wave numbers.

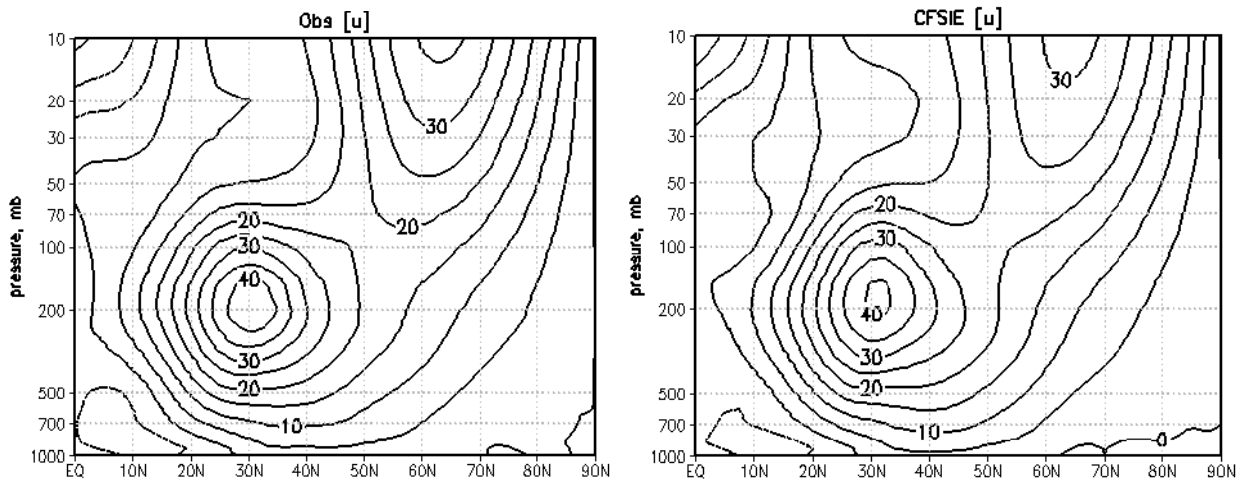


Figure 3 Meridional cross-section of the January zonal mean zonal wind climatology from observations (left) and model simulations (right).

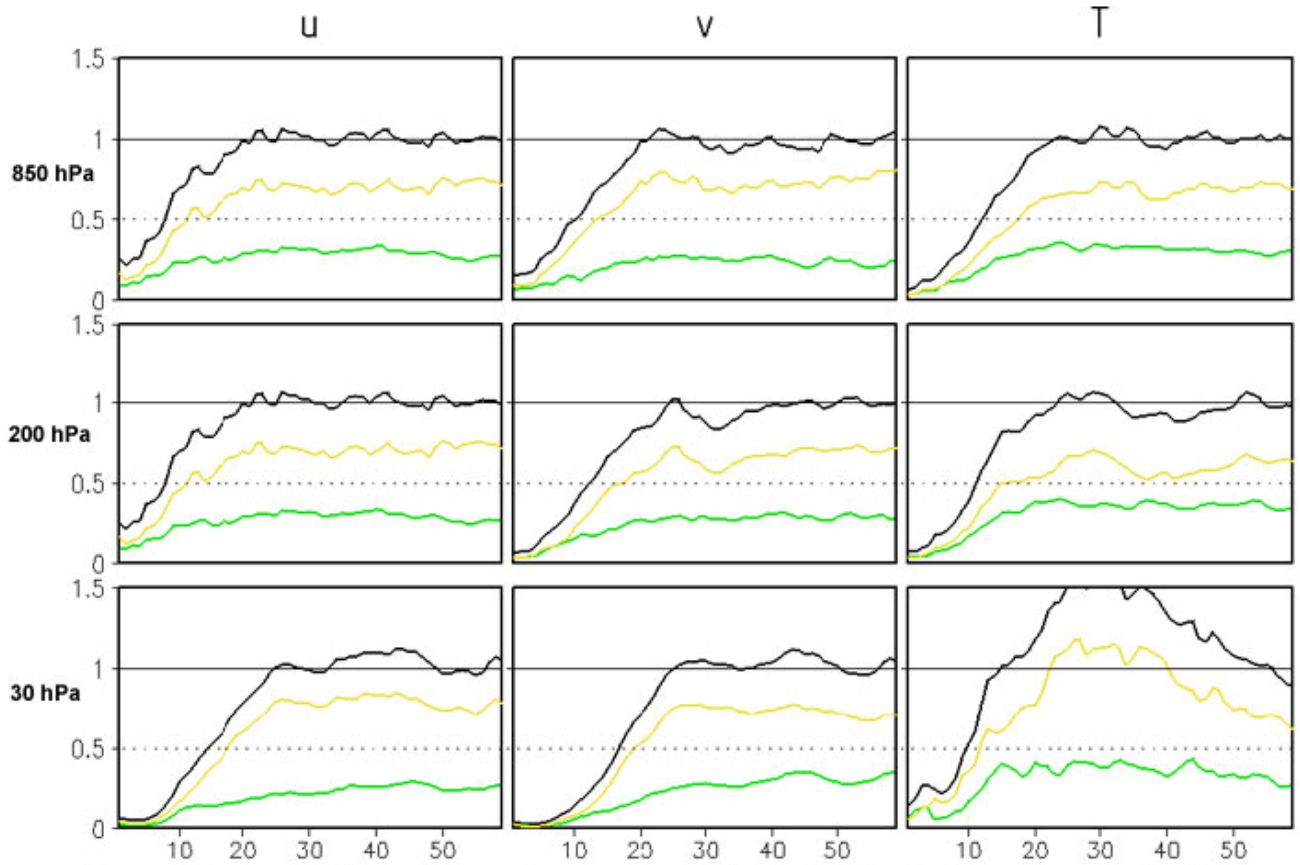


Figure 4 The normalized forecast errors in the zonal wavenumber 1 field of zonal wind, meridional wind and temperature for three different levels: 850, 200 and 30 hPa. The black line denotes the total amplitude, the yellow line represents the squared error due to the phase difference between the waves and the green line denotes the error due to the amplitude difference between the waves.

Figure 4 shows the normalized forecast errors in the zonal wave number 1 field of zonal wind, meridional wind and temperature for three different levels: 850, 200 and 30 hPa. The saturation value (which provides the normalization) is calculated as the 10-day mean at the end of February. The squared errors are averaged between 50° and 70°N. The black line denotes the total amplitude, which can be written as a sum of two terms, one giving the squared error due to the phase difference between the waves (shown in the yellow line) and the

second giving the error due to the amplitude difference between the waves (shown in the green line). A first important result is that the magnitude of the (squared) error is dominated by the magnitude of the phase error. This suggests that the phase of the wave is an important factor in limiting the predictability. For wave number 1, the predictability time (defined here as the time at which the normalized error reaches 0.75) is comparable at all levels, about 20 days. For wave number 2 (shown in Figure 5), the predictability time appears to become somewhat shorter at higher levels. Another interesting, and likewise surprising result, is the shape of the error curve in temperature at 30 hPa. Rather than simply growing and saturating, the error decreases at large time, indicating a systematic decrease in variability towards the end of the winter season.

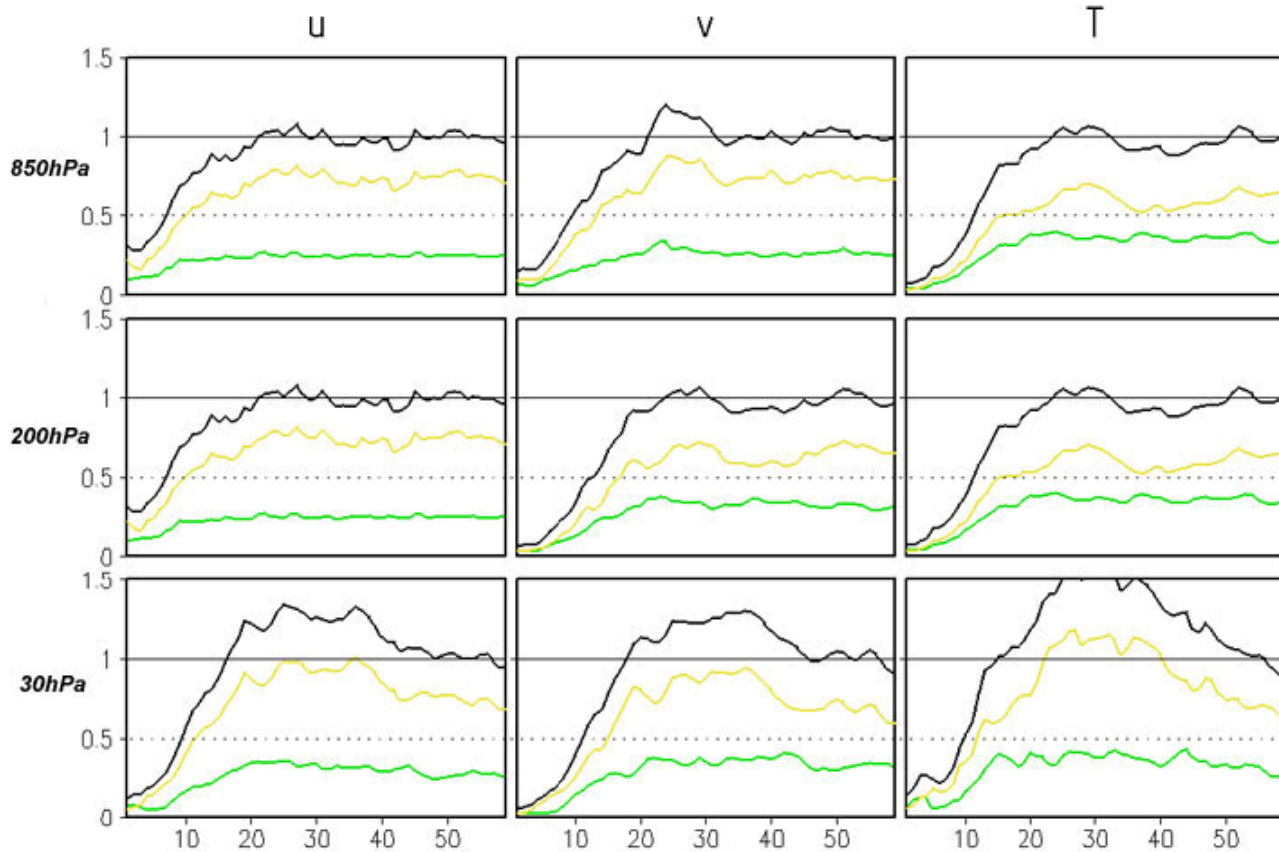


Figure 5 Same as Figure 8, but for zonal wavenumber 2.

As we know, sudden stratospheric warming events occur as a result of a special pattern in the wind and temperature fields. A good measure of the wave activity flux is the Eliassen-Palm (EP) flux and its divergence. Since the EP flux and its divergence are by definition zonally averaged quadratic quantities in the eddy fields, they can also be expressed as a sum over zonal wave numbers. For each zonal wave number separately, we computed the squared error of EP flux divergence averaged over all 15 identical twin pairs in each ensemble, over each ensemble and over all 10 years.

Figure 6 shows the result for wave numbers 1 and 2. The errors are also normalized by the saturation value, which is calculated as the last 10-day time average. The black curve corresponds to the 850 hPa level, the blue curve to the 500 hPa level, green to the 200 hPa level, yellow to the 100 hPa level, red to the 50 hPa level and purple to the 30 hPa level. The first feature of note is the large value of the initial error when compared to errors in the individual fields, and this is true for all levels. This result indicates that small errors in individual fields lead to large errors in the wave fluxes and their divergence. One might be tempted to say that this is an obvious result because the EP flux involves derivatives of second-order quantities.

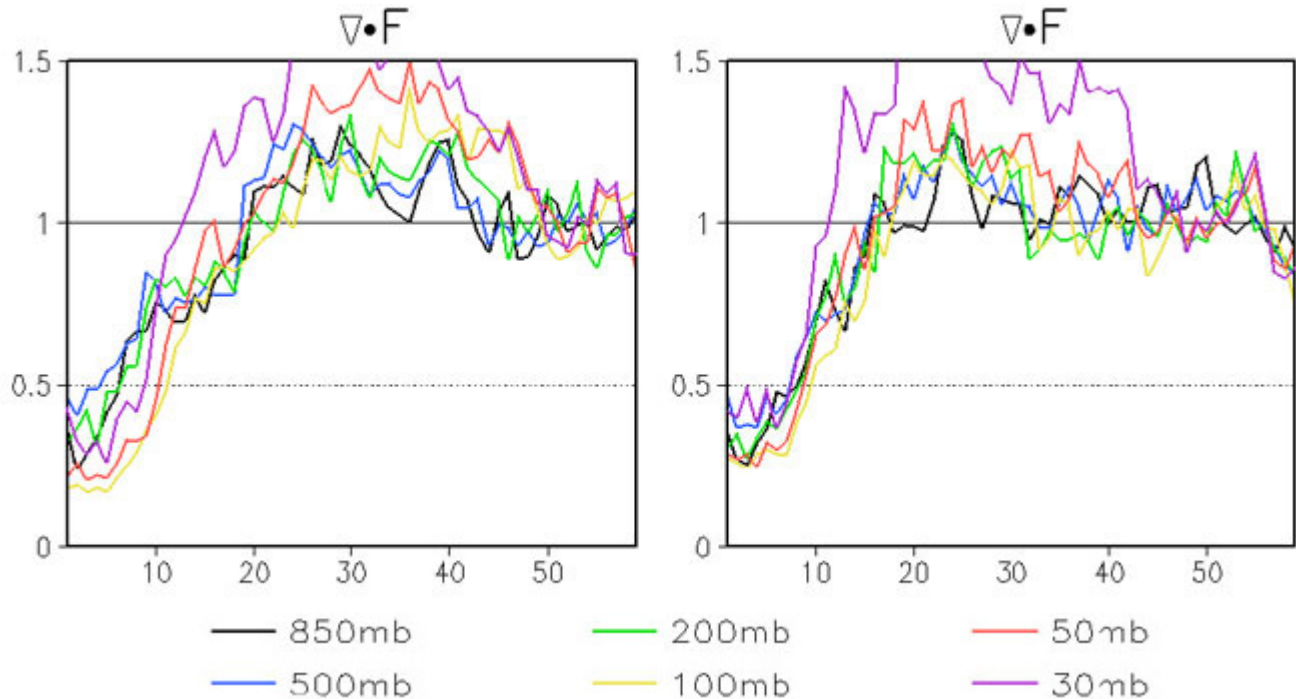


Figure 6 The squared error of EP flux divergence for wavenumbers 1 (left) and 2 (right).

5. Summary

The results suggest that *the predictability of sudden stratospheric events is low* because small errors in individual fields lead to large errors in the EP flux. The connection between the behavior of the temperature and EP flux divergence is consistent with previous work, which emphasizes that the vertically propagation of planetary waves in the stratosphere depends on the permeability of the tropopause. The second feature worth emphasizing is *the systematic decrease in variability towards the end of boreal winter seen at upper levels*. In the individual fields, this type of variation is characteristic mostly of the temperature field. The non-stationarity of the variability poses challenges for predictability theory, because it makes difficult to define the saturation value of the error growth. The last aspect we like to point out is *the shorter time of predictability in the stratosphere when compared to the troposphere*. At lower levels, the predictability time is around 20 days for wave number 1 and 15 days for wave number 2. At upper levels, the predictability time is reduced to about 10-12 days.

References

- Charlton, A. J. and L. M. Polvani, 2007: A new look at stratospheric sudden warming events: Part I. Climatology benchmarks. *J. Climate*, 20, 449-469.
- Stan, C. and B. P. Kirtman, 2007: The influence of atmospheric noise and uncertainty in ocean initial conditions on the limit of predictability in a coupled GCM. (under revision for *J. Climate*).